

**INVESTIGATION OF NEW
REACTION CHEMISTRIES
FOR Zn AND Ge ALD**

SYNTHESIS AND DEVELOPMENT OF PRECURSOR MOLECULES
AND REACTIONS FOR ATOMIC LAYER DEPOSITION (ALD) OF
ELEMENTAL ZINC AND GERMANIUM

By

KASUNI C. WEDISINGHE, B. Sc.

A Thesis

Submitted to the school of Graduate Studies

in Partial Fulfillment of the Requirements

for the Degree

Master of Science

McMaster University

© Copyright by Kasuni C. Wedisinghe, April 2021

Master of Science (2021)

McMaster University

(Chemistry)

Hamilton, Ontario

TITLE: Synthesis and Development of Precursor Molecules and
Reactions for Atomic Layer Deposition (ALD) of Elemental Zn
and Ge

AUTHOR: Kasuni C. Wedisinghe, B. Sc. (University of Kelaniya, Sri Lanka)

SUPERVISOR: Dr. D. J. H. Emslie

NUMBER OF PAGES: xxxiii, 215, III

ABSTRACT

Ultra-thin films of pure elements are important in microelectronics due to their wide range of applications. Atomic Layer Deposition (ALD) has drawn increasing attention as the thin films deposition technique for applications in microelectronics, due to its ability to deposit thin films with high conformality with atomic level control of the thickness of the film. However, due to the limited number of suitable precursor/co-reactant pairs available, only a few pure elements have been deposited successfully by ALD to date.

The current study involves the synthesis and identification of potentially suitable precursor and co-reactant molecules for ALD of elemental Zn and Ge, neither of which have previously been achieved. MeZnO^iPr , $\text{Zn}(\text{O}^i\text{Pr})_2$, and ZnEt_2 were investigated as Zn precursors while $\text{GeCl}_2(\text{Dioxane})$, $\text{Ge}\{\text{N}(\text{SiMe}_3)_2\}_2$, and $\text{Ge}(\text{OCH}_2\text{CH}_2\text{NMe}_2)_2$ were investigated as Ge precursors. Co-reactants of interest were, 4,4,5,5-tetramethyl-1,3,2-dioxaborolane (HBpin), PhSiH_3 , $[\text{H}_2\text{Al}(\text{tBuNCH}_2\text{CH}_2\text{NMe}_2)]$ (LAlH_2), $\text{BH}_3(\text{NMe}_3)$, and $\text{AlH}_3(\text{Quinuclidine})$. Ligand-exchange reactions between precursors and co-reactants were expected to produce unstable zinc or germanium hydride species, which would then reductively eliminate to produce the pure element. Solution reactivity studies were employed to identify potential precursor/co-reactant pairs.

Solution reactions of Zn precursors with the selected co-reactants indicated that unstable ZnH_2 is produced during the reactions, and will dissociate into its elements (Zn and H_2) at room temperature. These solution reactivity studies revealed that, HBpin and LAlH_2 were more reactive as co-reactants than $\text{BH}_3(\text{NMe}_3)$, $\text{AlH}_3(\text{Quinuclidine})$, and PhSiH_3 .

Additionally, MeZnO^iPr and ZnEt_2 exhibited the highest reactivity as precursors, although the lower reactivity of $\text{Zn}(\text{O}^i\text{Pr})_2$ may simply be due to low solubility.

Solution reactions of Ge precursors produced a polymeric mono-germanium hydride species $(\text{GeH})_x$, which will only dissociate into its elements upon heating at elevated temperatures. While LiAlH_2 indicated high reactivity with all Ge precursors, it was difficult to arrange co-reactants in order of reactivity as most reactions immediately produced insoluble $(\text{GeH})_x$ upon mixing reagents at room temperature. $\text{Ge}(\text{OCH}_2\text{CH}_2\text{NMe}_2)_2$ found to be the most reactive precursor out of all Ge precursors investigated.

ACKNOWLEDGMENTS

I would like to express the deepest appreciation to my supervisor, Dr. D. J. H. Emslie for giving me this incredible opportunity to carry out this project under his supervision and for his valuable guidance, supervision, and constant support throughout the course of this research project. Without his expert guidance and persistent help this dissertation would not have been possible.

I am highly grateful to all the group members for their companionship, especially Dr. J. Price for all his assistance with running X-ray experiments, Majeda Al Hareri for training me in the lab, Maia Murphy and Dr. Y. D. Yu (Kevin) for all their support without hesitation whenever I ask them for help.

Furthermore, I would also like to express my gratitude to Dr. I. Vargas-Baca for all his assistance and for being on my committee. I also convey my sincere gratitude to Dr. J. Britten for all his support with X-ray structure determination.

I am using this opportunity to thank my Sri Lankan family in Hamilton, Drs. D. Wijayarathne and P. Rupasinghe, Gayan, Guvanthi and Tharindu, who never let me feel homesick and made my stay in Canada memorable.

Finally, I would like to extend my deepest thanks to my family; my mother, Indra and my sister Kalani for their continuous love, encouragement, and emotional backing. Completion of this research project would not have been possible without them.

Above all I would like to thank my husband, Thenuka, for the endures love and for countless sacrifices made to be with me in Canada, for being extremely supportive and for always standing behind me when times get hard.

TABLE OF CONTENTS

| | |
|--|----------|
| Descriptive Note | ii |
| Abstract | iii |
| Acknowledgments..... | v |
| Table of Contents | vi |
| List of Figures | xiii |
| List of Tables | xxiv |
| List of Schemes..... | xxv |
| List of Symbols and Abbreviations..... | xxix |
| Declaration of Academic Achievement | xxxiii |
| Chapter 1- INTRODUCTION..... | 1 |
| 1.1 Microelectronics and their applications in current world | 1 |
| 1.2 Miniaturization of device features | 1 |
| 1.3 Thin films and their applications in microelectronics | 3 |
| 1.3.1 Thin film growth techniques | 3 |
| 1.3.2 Physical vapor deposition (PVD)..... | 4 |
| 1.3.3 Chemical vapor deposition (CVD)..... | 6 |
| 1.4 Atomic layer deposition (ALD) | 9 |
| 1.4.1 Plasma enhanced ALD (PEALD) | 16 |

| | |
|---|----|
| 1.4.2 Thermal ALD | 17 |
| 1.4.3 Substrate selection..... | 17 |
| 1.4.4 Precursor properties and reactivity..... | 18 |
| 1.4.5 Co-reactant chemistry | 23 |
| 1.5 Characteristics and advantages of thin films deposited by ALD | 25 |
| 1.5.1 Atomic scale deposition | 25 |
| 1.5.2 Low temperature deposition..... | 25 |
| 1.5.3 High uniformity and conformality | 26 |
| 1.6 Applications of ALD in microelectronics | 28 |
| 1.7 Limitations and disadvantages of ALD | 30 |
| 1.8 Overview of materials deposited by ALD | 31 |
| 1.9 Zn precursors used in CVD/ALD processes | 34 |
| 1.10 Ge precursors used in CVD/ALD processes | 39 |
| 1.11 Overview of pure elements deposited by ALD | 44 |
| 1.11.1 Zinc | 49 |
| 1.11.2 Germanium..... | 50 |
| 1.11.3 Thesis objective..... | 52 |

CHAPTER 2 - SOLUTION REACTIVITY STUDIES OF ZINC (Zn)

| | |
|--|-----------|
| PRECURSORS. | 54 |
| 2.1 Selection of precursors-Stability and volatility | 54 |
| 2.2 Precursor Synthesis | 57 |
| 2.3 Solution reactivity studies | 60 |
| 2.3.1 Solution reactivity studies of MeZnO ⁱ Pr..... | 61 |
| 2.3.1.1 Reaction of MeZnO ⁱ Pr with LAIH ₂ | 62 |
| 2.3.1.2 Reaction of MeZnO ⁱ Pr with HBpin..... | 66 |
| 2.3.1.3 Reaction of MeZnO ⁱ Pr with AlH ₃ (Quinuclidine)..... | 72 |
| 2.3.1.4 Reaction of MeZnO ⁱ Pr with BH ₃ (NMe ₃)..... | 75 |
| 2.3.2 Solution reactivity studies of Zn(O ⁱ Pr) ₂ | 77 |
| 2.3.2.1 Reaction of Zn(O ⁱ Pr) ₂ with LAIH ₂ | 78 |
| 2.3.2.2 Reaction of Zn(O ⁱ Pr) ₂ with HBpin | 81 |
| 2.3.2.3 Reaction of Zn(O ⁱ Pr) ₂ with AlH ₃ (Quinuclidine) | 84 |
| 2.3.2.4 Reaction of Zn(O ⁱ Pr) ₂ with BH ₃ (NMe ₃)..... | 88 |
| 2.3.2.5 Reaction of Zn(O ⁱ Pr) ₂ with PhSiH ₃ | 89 |
| 2.3.3 Solution reactivity studies of ZnEt ₂ | 92 |
| 2.3.3.1 Reaction of ZnEt ₂ with LAIH ₂ | 94 |
| 2.3.3.2 Reaction of ZnEt ₂ with HBpin..... | 97 |

| | |
|--|-----|
| 2.3.3.3 Reaction of ZnEt ₂ with BH ₃ (NMe ₃) | 100 |
| 2.3.3.4 Reaction of ZnEt ₂ with PhSiH ₃ | 101 |
| 2.4 Further characterization of by-products formed in solution reactions with HBpin and LAIH ₂ | 102 |
| 2.4.1 MeBpin, (ⁱ PrO)Bpin, and EtBpin | 102 |
| 2.4.2 (^t BuNCH ₂ CH ₂ NMe ₂)Al(O ⁱ Pr) ₂ (LAl(O ⁱ Pr) ₂)..... | 109 |
| 2.4.3 (^t BuNCH ₂ CH ₂ NMe ₂)AlEt ₂ (LAlEt ₂)..... | 112 |
| 2.5 Summary, conclusions, and future work | 115 |

CHAPTER 3 - SOLUTION REACTIVITY STUDIES OF GERMANIUM (Ge)

| | |
|--|------------|
| PRECURSORS | 120 |
| 3.1 Selection of precursors-Stability and volatility | 120 |
| 3.2 Precursor Synthesis | 124 |
| 3.3 Solution reactivity studies | 127 |
| 3.3.1 Solution reactivity studies of GeCl ₂ (Dioxane)..... | 128 |
| 3.3.1.1 Reaction of GeCl ₂ (Dioxane) with LAIH ₂ | 129 |
| 3.3.1.2 Reaction of GeCl ₂ (Dioxane) with HBpin | 132 |
| 3.3.1.3 Reaction of GeCl ₂ (Dioxane) with AlH ₃ (Quinuclidine)..... | 134 |
| 3.3.1.4 Reaction of GeCl ₂ (Dioxane) with BH ₃ (NMe ₃)..... | 137 |
| 3.3.1.5 Reaction of GeCl ₂ (Dioxane) with PhSiH ₃ | 140 |
| 3.3.2 Solution reactivity studies of Ge{N(SiMe ₃) ₂ } ₂ | 142 |
| 3.3.2.1 Reaction of Ge{N(SiMe ₃) ₂ } ₂ with LAIH ₂ | 144 |
| 3.3.2.2 Reaction of Ge{N(SiMe ₃) ₂ } ₂ with HBpin | 147 |
| 3.3.2.3 Reaction of Ge{N(SiMe ₃) ₂ } ₂ with AlH ₃ (Quinuclidine) | 149 |
| 3.3.2.4 Reaction of Ge{N(SiMe ₃) ₂ } ₂ with BH ₃ (NMe ₃)..... | 150 |
| 3.3.2.5 Reaction of Ge{N(SiMe ₃) ₂ } ₂ with PhSiH ₃ | 151 |
| 3.3.3 Solution reactivity studies of Ge(OCH ₂ CH ₂ NMe ₂) ₂ | 152 |
| 3.3.3.1 Reaction of Ge(OCH ₂ CH ₂ NMe ₂) ₂ with LAIH ₂ | 153 |

| | | |
|---------------------------------------|---|------------|
| 3.3.3.2 | Reaction of $\text{Ge}(\text{OCH}_2\text{CH}_2\text{NMe}_2)_2$ with HBpin | 157 |
| 3.3.3.3 | Reaction of $\text{Ge}(\text{OCH}_2\text{CH}_2\text{NMe}_2)_2$ with AlH_3 (Quinuclidine) | 160 |
| 3.3.3.4 | Reaction of $\text{Ge}(\text{OCH}_2\text{CH}_2\text{NMe}_2)_2$ with $\text{BH}_3(\text{NMe}_3)$ | 163 |
| 3.3.3.5 | Reaction of $\text{Ge}(\text{OCH}_2\text{CH}_2\text{NMe}_2)_2$ with PhSiH_3 | 165 |
| 3.4 | Attempts to obtain Ge from GeH_x precipitates | 170 |
| 3.5 | Further characterization of products formed in the solution reactions | 178 |
| 3.5.1 | $(^t\text{BuNCH}_2\text{CH}_2\text{NMe}_2)\text{AlCl}_2$ (LAICl_2) | 178 |
| 3.5.2 | $(\text{Me}_2\text{NCH}_2\text{CH}_2\text{O})\text{Bpin}$ | 182 |
| 3.5.3 | $\{(\text{Me}_3\text{Si})_2\text{N}\}\text{Bpin}$ | 188 |
| 3.6 | Summary, conclusions, and future work | 190 |
| CHAPTER 4 - EXPERIMENTAL | | 195 |
| 4.1 | General procedures | 195 |
| 4.2 | Solution reactions of Zinc | 196 |
| 4.2.1 | The 1:1 reaction of MeZnO^iPr with LAH_2 | 196 |
| 4.2.2 | The 1:1 reaction of $\text{Zn}(\text{O}^i\text{Pr})_2$ with LAH_2 | 197 |
| 4.2.3 | Powder X-ray diffraction (PXRD) sample preparation | 198 |
| 4.3 | Solution reactions of Germanium | 199 |
| 4.3.1 | The 1:1 reaction of GeCl_2 (Dioxane) with LAH_2 | 199 |
| 4.3.2 | The 1:1 reaction of $\text{Ge}\{\text{N}(\text{SiMe}_3)_2\}_2$ with LAH_2 | 200 |

| | |
|---|------------|
| 4.3.3 Powder X-ray diffraction (PXRD) sample preparation..... | 202 |
| 4.3.4 Sample preparation for GeH _x studies | 202 |
| 4.4 (tBuNCH ₂ CH ₂ NMe ₂)Al(O ⁱ Pr) ₂ (LAl(O ⁱ Pr) ₂)..... | 203 |
| 4.5 (tBuNCH ₂ CH ₂ NMe ₂)AlEt ₂ (LAlEt ₂) | 204 |
| 4.6 (NMe ₂ CH ₂ CH ₂ O)Bpin..... | 205 |
| REFERENCES..... | 206 |
| APPENDIX | I |

List of Figures

| | |
|--|----|
| Figure 1.1: Moore's Law: Number of transistors per microprocessor..... | 2 |
| Figure 1.2: Schematic diagram of physical vapor deposition (PVD); a) evaporative PVD, b) sputtering PVD | 6 |
| Figure 1.3: Schematic diagram of a chemical vapor deposition (CVD)..... | 8 |
| Figure 1.4: Film coverage and conformality illustration of (a) CVD/PVD growth (b) ALD growth on a narrow trench (width < 22 nm), (c) SEM cross sectional image of an ALD grown conformal Al ₂ O ₃ film in trenches | 10 |
| Figure 1.5: Schematic diagram of one ALD cycle of Al ₂ O ₃ film growth using (CH ₃) ₃ Al and H ₂ O | 12 |
| Figure 1.6: Plot of growth rate vs precursor pulse length. Blue colour region; sub saturative film growth..... | 13 |
| Figure 1.7: Plot of growth rate Vs deposition temperature..... | 14 |
| Figure 1.8: Schematic diagram of one cycle of a thermal and a plasma-assisted atomic layer deposition (ALD) process | 16 |
| Figure 1.9: The thermo gravimetric analysis (TGA) of ideal and non-ideal ALD precursors | 20 |
| Figure 1.10: The uniformity and conformality of a) surface-controlled and b) flux-controlled techniques | 27 |

| | |
|--|----|
| Figure 1.11: Overview of materials deposited by ALD..... | 32 |
| Figure 1.12: Zinc precursors. From left to right: MeZn(O ⁱ Pr), Zn(O ⁱ Pr) ₂ , and ZnEt ₂ | 52 |
| Figure 1.13: Germanium precursors a) GeCl ₂ (Dioxane), b) Ge{N(SiMe ₃) ₂ } ₂ , and c) Ge(OCH ₂ CH ₂ NMe ₂) ₂ | 52 |
| Figure 1.14: Co-reactants employed. From left to right: HBpin, PhSiH ₃ , [H ₂ Al(^t BuNCH ₂ CH ₂ NMe ₂)], AlH ₃ (Quinuclidine), BH ₃ (NMe ₃)..... | 53 |
| Figure 2.1: The heterocubane structure of MeZnO ⁱ Pr, a) X-ray crystal structure; Space group: P $\bar{1}$ (2), Cell: a = 7.838 Å, b = 9.468 Å, c = 17.870 Å, α = 77.457°, β = 77.806°, γ = 73.211° b) Chemical diagram | 55 |
| Figure 2.2: ¹ H NMR spectrum of MeZnO ⁱ Pr (Sublimed 65 °C/ 6 mTorr) in d ₆ -benzene . | 58 |
| Figure 2.3: ¹ H NMR spectra of, a) sublimed MeZnO ⁱ Pr, b) MeZnO ⁱ Pr heated at 100 °C /24 h, and c) MeZnO ⁱ Pr heated at 140 °C/24 h in d ₆ -benzene | 59 |
| Figure 2.4: ¹ H NMR spectra of (a) LAIH ₂ , (b) Sublimed MeZnO ⁱ Pr, (c) 1:1 reaction mixture of MeZnO ⁱ Pr with LAIH ₂ in d ₆ -benzene collected at room temperature after 24 hours..... | 64 |
| Figure 2.5: Powder X-ray diffractogram (PXRD) of the grey precipitate collected from the 1:1 reaction mixture of MeZnO ⁱ Pr with LAIH ₂ in d ₆ -benzene, 24 h, RT | 66 |
| Figure 2.6: The proton NMR spectrum of the 1:2 reaction of MeZnO ⁱ Pr with HBpin in d ₆ -benzene collected after 24 hours of mixing the reagents at room temperature..... | 68 |

| | |
|---|----|
| Figure 2.7: The proton NMR spectra of a) HBpin, b) Sublimed MeZnO ⁱ Pr, and the 1:1 reaction of MeZnO ⁱ Pr with HBpin c) 24 h, RT, d) 24 h, 40 °C, e) 24 h, 60 °C and f) 24 h, 80 °C. Solvent; d ₆ -benzene | 70 |
| Figure 2.8: Powder X-ray diffractogram (PXRD) of the grey precipitate collected from the 1:2 reaction of MeZnO ⁱ Pr with HBpin in d ₆ -benzene, 24 h, RT..... | 71 |
| Figure 2.9: The ¹ H NMR spectra of (a) Sublimed MeZnO ⁱ Pr, (b) AlH ₃ (Quinuclidine), (c) 1:1 reaction solution of MeZnO ⁱ Pr with AlH ₃ (Quinuclidine) in d ₆ -benzene collected after heating the reaction mixture for 24 hours at 40 °C..... | 74 |
| Figure 2.10: Powder X-ray diffractogram (PXRD) of the grey precipitate collected from the 1:1 reaction solution of MeZnO ⁱ Pr with AlH ₃ (Quinuclidine) in d ₆ -benzene, 24 h, 40 °C | 75 |
| Figure 2.11: The proton NMR spectrum of the 1:1 reaction of MeZnO ⁱ Pr with BH ₃ (NMe ₃) in d ₆ -benzene, after heating the reaction mixture for 24 hours at 80 °C..... | 76 |
| Figure 2.12: Powder X-ray diffractogram for Zn(O ⁱ Pr) ₂ | 78 |
| Figure 2.13: The proton NMR spectrum of the 1:1 reaction of Zn(O ⁱ Pr) ₂ with LAIH ₂ in d ₆ -benzene collected after 24 hours of mixing the reagents at room temperature..... | 80 |
| Figure 2.14: Powder X-ray diffractogram (PXRD) of the grey precipitate collected from the 1:1 reaction of Zn(O ⁱ Pr) ₂ with LAIH ₂ in d ₆ -benzene, 24 h, RT..... | 81 |
| Figure 2.15: The proton NMR spectrum of the 1:5 reaction of Zn(O ⁱ Pr) ₂ with HBpin in d ₆ -benzne, collected after heating the reaction solution at 40 °C for 24 hours | 83 |

| | |
|--|----|
| Figure 2.16: Powder X-ray diffractogram (PXRD) of the grey precipitate collected from the 1:5 reaction of Zn(O ⁱ Pr) ₂ with HBpin in d ₆ -benzene, 24 h, 40 °C | 84 |
| Figure 2.17: The proton NMR spectrum of the 1:2 reaction of Zn(O ⁱ Pr) ₂ with AlH ₃ (Quinuclidine) in d ₆ -benzene, collected after 24 hours of mixing the reagents at room temperature | 86 |
| Figure 2.18: Powder X-ray diffractogram (PXRD) of the grey precipitate collected from the 1:2 reaction of Zn(O ⁱ Pr) ₂ with AlH ₃ (Quinuclidine) in d ₆ -benzene, 24 h, RT (Black) . | 87 |
| Figure 2.19: The proton NMR spectra of a) BH ₃ (NMe ₃) and b) 1:1 reaction of Zn(O ⁱ Pr) ₂ with BH ₃ (NMe ₃) in d ₆ -benzene, collected after heating the reaction solution for 24 hours at 80 °C | 88 |
| Figure 2.20: The proton NMR spectrum of 1:2 reaction solution of Zn(O ⁱ Pr) ₂ with PhSiH ₃ in d ₆ -benzene, collected after heating the reaction solution for 24 hours at 60 °C..... | 90 |
| Figure 2.21: Powder X-ray diffractogram (PXRD) of the grey precipitate collected from the 1:2 reaction mixture of Zn(O ⁱ Pr) ₂ with PhSiH ₃ in d ₆ -benzene, 24 h, 60 °C..... | 91 |
| Figure 2.22: ¹ H and ¹³ C{ ¹ H} NMR spectra collected for ZnEt ₂ in d ₆ -benzene..... | 93 |
| Figure 2.23: The proton NMR spectrum of the 1:1 reaction of ZnEt ₂ with LAIH ₂ in d ₆ -benzene with enlarged 0- 0.15 ppm region, collected after 24 hours of mixing the reagents at room temperature | 95 |
| Figure 2.24: Powder X-ray diffractogram (PXRD) of the grey precipitate collected from the 1:1 reaction of ZnEt ₂ with LAIH ₂ in d ₆ -benzene, 24 h, RT | 96 |

| | |
|---|-----|
| Figure 2.25: The proton NMR spectrum of the 1:2 reaction of ZnEt ₂ with HBpin in d ₆ -benzene with enlarged 1.05- 1.15 ppm region, collected after 24 hours of mixing the reagents at room temperature..... | 98 |
| Figure 2.26: Powder X-ray diffractogram (PXRD) of the grey precipitate collected from 1:2 reaction of ZnEt ₂ with HBpin in d ₆ -benzene, 24 h, RT | 99 |
| Figure 2.27: The proton NMR spectrum of the 1:1 reaction of ZnEt ₂ with BH ₃ (NMe ₃) in d ₆ -benzene, collected after heating the reaction solution for 24 hours at 80 °C | 100 |
| Figure 2.28: The proton NMR spectrum of the 1:1 reaction between ZnEt ₂ and PhSiH ₃ in d ₆ -benzene collected after heating the reaction solution for 24 hours at 80 °C | 101 |
| Figure 2.29: ¹ H NMR spectra of a) (ⁱ PrO)Bpin, b) MeBpin, and c) 1:2 reaction of MeZnO ⁱ Pr with HBpin (24 h, RT), and d) 1:3 reaction of Zn(O ⁱ Pr) ₂ with HBpin (24 h, 40 °C). Solvent; d ₆ -benzene..... | 103 |
| Figure 2.30: ¹¹ B{ ¹ H} NMR spectra of a) (ⁱ PrO)Bpin, b) MeBpin, and c) 1:2 reaction of MeZnO ⁱ Pr with HBpin (24 h, RT), and d) 1:3 reaction of Zn(O ⁱ Pr) ₂ with HBpin (24 h, 40 °C. Solvent; d ₆ -benzene | 104 |
| Figure 2.31: ¹³ C{ ¹ H} NMR spectra of a) (ⁱ PrO)Bpin, b) MeBpin, and c) 1:2 reaction of MeZnO ⁱ Pr with HBpin (24 h, RT), and d) 1:3 reaction of Zn(O ⁱ Pr) ₂ with HBpin (24 h, 40 °C. Solvent; d ₆ -benzene | 105 |
| Figure 2.32: ¹ H NMR spectra of a) EtBpin, and b) 1:2 reaction of ZnEt ₂ with HBpin (24 h, RT). Solvent; d ₆ -benzene | 106 |

| | |
|--|-----|
| Figure 2.33: $^{13}\text{C}\{^1\text{H}\}$ NMR spectra of a) EtBpin, and b) 1:2 reaction of ZnEt_2 with HBpin (24 h, RT). Solvent; d_6 -benzene..... | 107 |
| Figure 2.34: $^{11}\text{B}\{^1\text{H}\}$ NMR spectra of a) EtBpin, and b) 1:2 reaction of ZnEt_2 with HBpin (24 h, RT). Solvent; d_6 -benzene..... | 108 |
| Figure 2.35: a) ^1H NMR spectrum and b) $^{13}\text{C}\{^1\text{H}\}$ NMR spectrum collected for $\text{LAl}(\text{O}^i\text{Pr})_2$ in d_6 -benzene..... | 110 |
| Figure 2.36: Heteronuclear single quantum correlation (HSQC) NMR spectrum of $\text{LAl}(\text{O}^i\text{Pr})_2$ in d_6 -benzene | 111 |
| Figure 2.37: a) ^1H NMR spectrum and b) $^{13}\text{C}\{^1\text{H}\}$ NMR spectrum collected for LAlEt_2 in d_6 -benzene..... | 113 |
| Figure 2.38: Heteronuclear single quantum correlation (HSQC) NMR spectrum of LAlEt_2 in d_6 -benzene..... | 114 |
| Figure 3.1: Crystal structure of $\text{GeCl}_2(\text{Dioxane})$. a) The chain structure; Space group: $C2/c$, Cell: $a = 7.5811 \text{ \AA}$, $b = 11.6974 \text{ \AA}$, $c = 8.7800 \text{ \AA}$, $\alpha = 90^\circ$, $\beta = 97.129^\circ$, $\gamma = 90^\circ$ and b) Chemical diagram of $\text{GeCl}_2(\text{Dioxane})$ | 121 |
| Figure 3.2: $\text{Ge}\{\text{N}(\text{SiMe}_3)_2\}_2$, a) X-ray structure; Space group: $Pccn$, Cell: $a = 16.632 \text{ \AA}$, $b = 20.323 \text{ \AA}$, $c = 13.148 \text{ \AA}$, $\alpha = \beta = \gamma = 90^\circ$ and b) Chemical diagram | 122 |
| Figure 3.3: $\text{Ge}(\text{OCH}_2\text{CH}_2\text{NMe}_2)_2$, a) X-ray crystal structure; Space group: $P2_12_12_1$, Cell: $a = 10.1606 \text{ \AA}$, $b = 11.2693 \text{ \AA}$, $c = 20.3870 \text{ \AA}$, $\alpha = \beta = \gamma = 90^\circ$ and b) Chemical diagram. | 123 |

| | |
|---|-----|
| Figure 3.4: a) ^1H and b) $^{13}\text{C}\{^1\text{H}\}$ NMR spectra collected for $\text{Ge}(\text{OCH}_2\text{CH}_2\text{NMe}_2)_2$ in d_6 -benzene | 125 |
| Figure 3.5: Proton NMR spectra collected for thermal stress testing of $\text{Ge}(\text{OCH}_2\text{CH}_2\text{NMe}_2)_2$ in d_6 -benzene, a) at RT, b) heated at $100\text{ }^\circ\text{C}/24\text{ h}$ under dynamic argon, and c) heated at $140\text{ }^\circ\text{C}/24\text{ h}$ under dynamic argon | 126 |
| Figure 3.6: The proton NMR spectrum of the 1:1 reaction of $\text{GeCl}_2(\text{Dioxane})$ with LiAlH_2 in d_6 -benzene collected at room temperature after 24 hours..... | 130 |
| Figure 3.7: Powder X-ray diffractogram (PXRD) of the orange precipitate GeH_x formed from the 1:1 reaction of $\text{GeCl}_2(\text{Dioxane})$ and LiAlH_2 in d_6 -benzene, 24 h, RT | 131 |
| Figure 3.8: The proton NMR spectra in d_6 -benzene of a) HBpin and b) 1:2 reaction of $\text{GeCl}_2(\text{Dioxane})$ with HBpin, collected after heating the solution at $60\text{ }^\circ\text{C}$ for 24 hours | 133 |
| Figure 3.9: The proton NMR spectra in d_6 -benzene of a) Quinuclidine, b) $\text{AlH}_3(\text{Quinuclidine})$, and c) 2:1 reaction of $\text{GeCl}_2(\text{Dioxane})$ with $\text{AlH}_3(\text{Quinuclidine})$ collected after 24 hours at $60\text{ }^\circ\text{C}$ | 136 |
| Figure 3.10: The proton NMR spectra in d_6 -benzene of a) $\text{BH}_3(\text{NMe}_3)$ and b) The 3:2 reaction of $\text{GeCl}_2(\text{Dioxane})$ with $\text{BH}_3(\text{NMe}_3)$ collected at room temperature after 24 hours | 139 |
| Figure 3.11: The proton NMR spectrum of the 3:2 reaction of $\text{GeCl}_2(\text{Dioxane})$ and PhSiH_3 in d_6 -benzene collected after 24 hours at $40\text{ }^\circ\text{C}$ | 141 |

| | |
|--|-----|
| Figure 3.12: NMR spectra of $\text{Ge}\{\text{N}(\text{SiMe}_3)_2\}_2$ in d_6 -benzene, a) ^1H NMR and b) $^{13}\text{C}\{^1\text{H}\}$ NMR | 143 |
| Figure 3.13: The proton NMR spectrum of a) the 1:1 reaction of $\text{Ge}\{\text{N}(\text{SiMe}_3)_2\}_2$ and LiAlH_2 in d_6 -benzene collected after heating the reaction at $60\text{ }^\circ\text{C}$ for 24 hours, b) enlarged Ge-H region, and c) enlarged Al-H region | 146 |
| Figure 3.14: The proton NMR spectrum of the 1:4 reaction of $\text{Ge}\{\text{N}(\text{SiMe}_3)_2\}_2$ with HBpin in d_6 -benzene collected after heating the reaction at $60\text{ }^\circ\text{C}$ for 24 hours..... | 148 |
| Figure 3.15: The proton NMR spectrum of the 1:4 reaction of $\text{Ge}\{\text{N}(\text{SiMe}_3)_2\}_2$ and $\text{AlH}_3(\text{Quinuclidine})$ in d_6 -benzene, collected after heating the reaction solution at $80\text{ }^\circ\text{C}$ for 24 hours | 149 |
| Figure 3.16: The proton NMR spectrum of the 1:4 reaction of $\text{Ge}\{\text{N}(\text{SiMe}_3)_2\}_2$ with $\text{BH}_3(\text{NMe}_3)$ in d_6 -benzene, collected after heating the reaction solution at $80\text{ }^\circ\text{C}$ for 24 hours | 150 |
| Figure 3.17: The proton NMR spectrum of the 1:5 reaction of $\text{Ge}\{\text{N}(\text{SiMe}_3)_2\}_2$ with PhSiH_3 in d_6 -benzene, collected after heating the reaction solution at $80\text{ }^\circ\text{C}$ for 24 hours..... | 151 |
| Figure 3.18: The proton NMR spectra in d_6 -benzene of a) $\text{Ge}(\text{OCH}_2\text{CH}_2\text{NMe}_2)_2$, b) LiAlH_2 , and c) the 1:1 reaction of $\text{Ge}(\text{OCH}_2\text{CH}_2\text{NMe}_2)_2$ with LiAlH_2 collected after the reaction had proceeded for 24 hours at room temperature | 152 |
| Figure 3.19: Powder X-ray diffractogram (PXRD) of the orange precipitate GeH_x formed from the 1:1 reaction of $\text{Ge}(\text{OCH}_2\text{CH}_2\text{NMe}_2)_2$ and LiAlH_2 in d_6 -benzene, 24 h, RT..... | 156 |

| | |
|--|-----|
| Figure 3.20: The proton NMR spectrum of the 1:2 reaction of $\text{Ge}(\text{OCH}_2\text{CH}_2\text{NMe}_2)_2$ with HBpin in d_6 -benzene, collected after 24 hours at room temperature | 158 |
| Figure 3.21: Powder X-ray diffractogram (PXRD) of the orange precipitate GeH_x formed from the 1:1 reaction of $\text{Ge}(\text{OCH}_2\text{CH}_2\text{NMe}_2)_2$ and HBpin in d_6 -benzene, 24 h, RT..... | 159 |
| Figure 3.22: The proton NMR spectra in d_6 -benzene of a) Quinuclidine and b) the 1:2 reaction between $\text{Ge}(\text{OCH}_2\text{CH}_2\text{NMe}_2)_2$ and $\text{AlH}_3(\text{Quinuclidine})$ collected after 24 hours at room temperature | 161 |
| Figure 3.23: Powder X-ray diffractogram (PXRD) of the orange precipitate GeH_x formed from the 1:2 reaction of $\text{Ge}(\text{OCH}_2\text{CH}_2\text{NMe}_2)_2$ and $\text{AlH}_3(\text{Quinuclidine})$ in d_6 -benzene, 24 h, RT | 162 |
| Figure 3.24: The proton NMR spectra of the 1:1 reaction solution of $\text{Ge}(\text{OCH}_2\text{CH}_2\text{NMe}_2)_2$ and $\text{BH}_3(\text{NMe}_3)$ in d_6 -benzene, collected at room temperature after 24 hours..... | 164 |
| Figure 3.25: The proton NMR spectrum of the 1:5 reaction of $\text{Ge}(\text{OCH}_2\text{CH}_2\text{NMe}_2)_2$ and PhSiH_3 in d_6 -benzene, collected at room temperature after 24 hours..... | 166 |
| Figure 3.26: Proton NMR spectra collected for reactions between PhSiH_3 and $\text{HOCH}_2\text{CH}_2\text{NMe}_2$ in d_6 -benzene at room temperature, a) 1:3 reaction, b) 1:2 reaction, and c) 1:1 reaction | 168 |
| Figure 3.27: Powder X-ray diffractogram (PXRD) of the orange precipitate GeH_x formed from the 1:5 reaction of $\text{Ge}(\text{OCH}_2\text{CH}_2\text{NMe}_2)_2$ and PhSiH_3 in d_6 -benzene, 24 h, RT..... | 169 |
| Figure 3.28: Powder X-ray diffraction (PXRD) pattern of elemental Germanium | 171 |

| | |
|--|-----|
| Figure 3.29: X-ray diffractogram of the grey-black solid obtained after heating (200 °C, 24 h) the orange GeH _x precipitate from the 1:10 reaction between Ge(OCH ₂ CH ₂ NMe ₂) ₂ and HBpin | 172 |
| Figure 3.30: : X-ray diffractogram of the grey-black solid obtained after heating (200 °C, 48 h) the orange GeH _x precipitate from the 1:10 reaction between Ge(OCH ₂ CH ₂ NMe ₂) ₂ and HBpin | 173 |
| Figure 3.31: X-ray diffractogram of the grey-black solid obtained after heating (230 °C, 48 h) the orange GeH _x precipitate from the 1:10 reaction between Ge(OCH ₂ CH ₂ NMe ₂) ₂ and HBpin | 174 |
| Figure 3.32: X-ray diffractogram of the grey-black solid obtained after heating (200 °C, 24 h) the orange GeH _x precipitate from the 1:10 reaction between Ge(OCH ₂ CH ₂ NMe ₂) ₂ and PhSiH ₃ | 175 |
| Figure 3.33: X-ray diffractogram of the grey-black solid obtained after heating (200 °C, 48 h) the orange GeH _x precipitate from the 1:10 reaction between Ge(OCH ₂ CH ₂ NMe ₂) ₂ and PhSiH ₃ | 176 |
| Figure 3.34: X-ray diffractogram of the grey-black solid obtained after heating (230 °C, 48 h) the orange GeH _x precipitate from the 1:10 reaction between Ge(OCH ₂ CH ₂ NMe ₂) ₂ and PhSiH ₃ | 177 |
| Figure 3.35: ¹ H NMR spectra in d ₆ -benzene collected for, a) The 1:1 solution reaction between GeCl ₂ (Dioxane) and LAIH ₂ (24 h, RT) and b) LAICl ₂ | 179 |

| | |
|--|-----|
| Figure 3.36: $^{13}\text{C}\{^1\text{H}\}$ NMR spectra in d_6 -benzene collected for, a) The 1:1 solution reaction between $\text{GeCl}_2(\text{Dioxane})$ and LiAlH_2 (24 h, RT) and b) LiAlCl_2 | 180 |
| Figure 3.37: Heteronuclear single quantum correlation (HSQC) NMR spectrum in d_6 -benzene collected for the 1:1 solution reaction between $\text{GeCl}_2(\text{Dioxane})$ and LiAlH_2 (24 h, RT) | 181 |
| Figure 3.38: X-ray crystal structure of $(\text{Me}_2\text{NCH}_2\text{CH}_2\text{O})\text{Bpin}$, with ellipsoids drawn at 50% probability | 182 |
| Figure 3.39: a) ^1H , b) $^{13}\text{C}\{^1\text{H}\}$, and c) $^{11}\text{B}\{^1\text{H}\}$ NMR spectra of $(\text{Me}_2\text{NCH}_2\text{CH}_2\text{O})\text{Bpin}$ in d_6 -benzene. | 185 |
| Figure 3.40: Heteronuclear single quantum correlation (HSQC) NMR spectrum collected for $(\text{Me}_2\text{NCH}_2\text{CH}_2\text{O})\text{Bpin}$ in d_6 -benzene | 186 |
| Figure 3.41: Proton NMR spectra collected for thermal stress testing of $(\text{Me}_2\text{NCH}_2\text{CH}_2\text{O})\text{Bpin}$ in d_6 -benzene, a) at RT, b) heated at $100\text{ }^\circ\text{C}/24\text{ h}$ under a dynamic argon flow, and c) heated at $140\text{ }^\circ\text{C}/24\text{ h}$ under a dynamic argon flow | 187 |
| Figure 3.42: a) ^1H , b) $^{13}\text{C}\{^1\text{H}\}$, and c) $^{11}\text{B}\{^1\text{H}\}$ NMR spectra collected for the 1:4 reaction solution of $\text{Ge}\{\text{N}(\text{SiMe}_3)_2\}_2$ and HBpin in d_6 -benzene | 189 |

List of Tables

| | |
|---|-----|
| Table 1.1: Typical thermal ALD materials and selected co-reactants which have been used to generate each material | 24 |
| Table 1.2: Zinc containing precursors used in different CVD/ALD processes | 35 |
| Table 1.3: Germanium containing precursors used in different CVD/ALD processes | 40 |
| Table 1.4: Standard reduction potentials of M^{2+} ions of first row transition metals..... | 46 |
| Table 2.1: Summary of volatility and thermal stability of Zn precursors..... | 56 |
| Table 2.2: Summary of solution reactivity studies of Zn precursors..... | 118 |
| Table 3.1: Selected bond angles ($^{\circ}$) and Bond lengths for $(Me_2NCH_2CH_2O)Bpin$ with estimated standard deviations in parentheses..... | 183 |
| Table 3.2: Summary of solution reactivity studies of Ge(II) precursors | 193 |
| Table 4.1: Amounts of Zn precursors and co-reactants used in solution reactions of $MeZnO^iPr$ and $ZnEt_2$ | 197 |
| Table 4.2: Amounts of $Zn(O^iPr)_2$ and co-reactants used in solution reactions of $Zn(O^iPr)_2$ | 198 |
| Table 4.3: Amounts of $GeCl_2(Dioxane)$ and co-reactants used in solution reactions of $GeCl_2(Dioxane)$ | 199 |
| Table 4.4: Amounts of Ge precursors and co-reactants used in solution reactions of $Ge\{N(SiMe_3)_2\}_2$, and $Ge(OCH_2CH_2NMe_2)_2$ | 201 |

List of Schemes

| | |
|---|----|
| Scheme 1.1: Proposed reaction between AlCl_3 and $[\text{H}_2\text{Al}(\text{tBuNCH}_2\text{CH}_2\text{NMe}_2)]$ leading to Al metal film deposition | 48 |
| Scheme 2.1: Reaction scheme for the synthesis of MeZnO^iPr | 57 |
| Scheme 2.2: General reaction pathways expected for reactions of MeZnO^iPr with hydride reagents to produce elemental zinc | 61 |
| Scheme 2.3: Possible 1:1 reactions between MeZnO^iPr and LiAlH_2 (assuming pathway 2 in the Scheme 2.2)..... | 62 |
| Scheme 2.4: Expected by-products from the 1:2 reaction of MeZnO^iPr with HBpin (assuming pathway 2 in the Scheme 2.2)..... | 66 |
| Scheme 2.5: Possible by-products predicted for the reaction of MeZnO^iPr with $\text{AlH}_3(\text{Quinuclidine})$ (assuming pathway 2 in the Scheme 2.2)..... | 72 |
| Scheme 2.6: Reaction pathway anticipated for reactions of $\text{Zn}(\text{O}^i\text{Pr})_2$ with hydride co-reagents to produce elemental zinc | 77 |
| Scheme 2.7: Expected by-products from the 1:1 reaction of $\text{Zn}(\text{O}^i\text{Pr})_2$ with LiAlH_2 (assuming pathway in the Scheme 2.6)..... | 78 |
| Scheme 2.8: Expected by-products from the 1:2 reaction of $\text{Zn}(\text{O}^i\text{Pr})_2$ with HBpin (assuming pathway in the Scheme 2.6)..... | 81 |

| | |
|--|-----|
| Scheme 2.9: Possible by-products from the reaction of $\text{Zn}(\text{O}^i\text{Pr})_2$ with $\text{AlH}_3(\text{Quinuclidine})$ (assuming pathway in the Scheme 2.6)..... | 85 |
| Scheme 2.10: Possible by-products from the reaction between $\text{Zn}(\text{O}^i\text{Pr})_2$ and PhSiH_3 (assuming pathway in the Scheme 2.6)..... | 89 |
| Scheme 2.11: Reaction pathways anticipated for reactions of ZnEt_2 with hydride co- reagents to produce elemental zinc | 92 |
| Scheme 2.12: By-products anticipated for the 1:1 reaction between ZnEt_2 and LAlH_2 (assuming pathway 02 in the Scheme 2.11)..... | 94 |
| Scheme 2.13: By-product anticipated for the 1:2 reaction between ZnEt_2 and HBpin (assuming pathway 02 in the Scheme 2.11)..... | 97 |
| Scheme 2.14: Reaction scheme for the synthesis of LAlEt_2 | 112 |
| Scheme 3.1: Reaction scheme for the synthesis of $\text{Ge}(\text{OCH}_2\text{CH}_2\text{NMe}_2)_2$ | 124 |
| Scheme 3.2: Proposed reaction pathway for reactions of $\text{GeCl}_2(\text{Dioxane})$ with hydride reagents to produce elemental germanium..... | 128 |
| Scheme 3.3: Expected by-products from the 1:1 reaction between $\text{GeCl}_2(\text{Dioxane})$ with LAlH_2 | 129 |
| Scheme 3.4: Expected by-products from the 1:2 reaction between $\text{GeCl}_2(\text{Dioxane})$ and HBpin | 132 |

| | |
|---|-----|
| Scheme 3.5: Possible by-products predicted for the reaction of $\text{GeCl}_2(\text{Dioxane})$ with $\text{AlH}_3(\text{Quinuclidine})$ | 134 |
| Scheme 3.6: Possible by-products predicted for the reaction of $\text{GeCl}_2(\text{Dioxane})$ with $\text{BH}_3(\text{NMe}_3)$ | 137 |
| Scheme 3.7: Possible by-products predicted for the reaction of $\text{GeCl}_2(\text{Dioxane})$ with PhSiH_3 (Assuming pathway in the Scheme 3.2)..... | 140 |
| Scheme 3.8: Proposed reaction pathway for reactions of $\text{Ge}\{\text{N}(\text{SiMe}_3)_2\}_2$ with hydride reagents to produce elemental germanium..... | 142 |
| Scheme 3.9: Possible by-products predicted for the 1:1 reaction of $\text{Ge}\{\text{N}(\text{SiMe}_3)_2\}_2$ with LiAlH_2 | 144 |
| Scheme 3.10: Expected by-products for the 1:2 reaction between $\text{Ge}\{\text{N}(\text{SiMe}_3)_2\}_2$ and HBpin | 147 |
| Scheme 3.11: Proposed reaction pathway for reactions of $\text{Ge}(\text{OCH}_2\text{CH}_2\text{NMe}_2)_2$ with hydride reagents to produce elemental germanium | 152 |
| Scheme 3.12: Possible by-products predicted for the 1:1 reaction of $\text{Ge}(\text{OCH}_2\text{CH}_2\text{NMe}_2)_2$ and LiAlH_2 | 153 |
| Scheme 3.13: Proposed reaction pathway for the 1:2 reaction between $\text{Ge}(\text{OCH}_2\text{CH}_2\text{NMe}_2)_2$ and HBpin (assuming pathway in the Scheme 3.11) | 157 |

| | |
|--|-----|
| Scheme 3.14: Possible by-products predicted for the reaction of $\text{Ge}(\text{OCH}_2\text{CH}_2\text{NMe}_2)_2$ and $\text{AlH}_3(\text{Quinuclidine})$ | 160 |
| Scheme 3.15: Possible by-products predicted for the reaction of $\text{Ge}(\text{OCH}_2\text{CH}_2\text{NMe}_2)_2$ and $\text{BH}_3(\text{NMe}_3)$ | 163 |
| Scheme 3.16: Possible by-products predicted for the reaction of $\text{Ge}(\text{OCH}_2\text{CH}_2\text{NMe}_2)_2$ and PhSiH_3 | 165 |
| Scheme 3.17: Decomposition of $(\text{GeH})_x$ into its elements..... | 170 |
| Scheme 3.18: Reaction pathway for the synthesis of $(\text{Me}_2\text{NCH}_2\text{CH}_2\text{O})\text{Bpin}$ | 184 |

List of Symbols & Abbreviations

| | |
|-----------|---|
| acac | acetylacetonate |
| Å | Angstrom |
| ALD | atomic layer deposition |
| ALE | atomic layer epitaxy |
| bp | boiling point |
| cm | centimeter |
| CVD | chemical vapor deposition |
| CMOS | complementary metal-oxide semiconductor |
| DMP | dimethylaminopropyl |
| DRAM | dynamic random-access memory |
| δ | symbol for chemical shift |
| eV | Electronvolt |
| EMAG | ethylmethylamido-germane |
| E° | standard reduction potential |
| EtBpin | 2-ethyl-4,4,5,5-tetramethyl-1,3,2-dioxaborolane |
| FRAM | ferroelectric random-access memory |
| GST | Germanium antimony telluride |

| | |
|-------------------------------------|--|
| GPC | growth rates per cycle |
| g | grams |
| Hz | Hertz |
| h | hours |
| HSQC | heteronuclear single quantum correlation |
| HBpin | 4,4,5,5-tetramethyl-1,3,2-dioxaborolane |
| IR | infrared |
| <i>J</i> | symbol for coupling constant |
| LAIH ₂ | [H ₂ Al(^t BuNCH ₂ CH ₂ NMe ₂)] |
| LAi(O ⁱ Pr) ₂ | (^t BuNCH ₂ CH ₂ NMe ₂)Al(O ⁱ Pr) ₂ |
| LAIEt ₂ | (^t BuNCH ₂ CH ₂ NMe ₂)AlEt ₂ |
| LAICl ₂ | (^t BuNCH ₂ CH ₂ NMe ₂)AlCl ₂ |
| MOSFET | metal-oxide-semiconductor field-effect transistor |
| MIM | metal-insulator-metal |
| mp | melting point |
| MHz | mega Hertz |
| min | minute |

| | |
|--|--|
| mg | milligram |
| mL | milliliters |
| mmol | millimoles |
| MeBpin | 2,4,4,5,5-pentamethyl-1,3,2-dioxaborolane |
| M | moles per litre |
| mol | moles |
| nm | nanometer |
| NMR | nuclear magnetic resonance |
| (<i>O</i> ^{<i>i</i>} Pr)Bpin | 2-isopropoxy-4,4,5,5-tetramethyl-1,3,2-dioxaborolane |
| ppm | part per million |
| PVD | physical vapor deposition |
| PEALD | plasma-enhanced atomic layer deposition |
| PXRD | powder X-ray diffraction |
| q | quartet |
| RT | room temperature |
| SEM | scanning electron microscopy |
| sept | septet |

| | |
|-----|------------------------------------|
| s | singlet |
| TMP | tetramethylpiperidino |
| TDA | tetramethyl disilazacyclopentanide |
| THF | tetrahydrofuran |
| TGA | thermo gravimetric analysis |
| TMA | trimethyl aluminum |
| t | triplet |
| V | Volt |

Declaration of Academic Achievement

I, Kasuni Chamini Wedisinghe declare this thesis to be my own work. I am the sole author of this document. No part of this work has been published or submitted for publication or for a higher degree at another institution.

To the best of my knowledge, the content of this document does not infringe on anyone's copyright.

My supervisor, Dr. D. J. H. Emslie and the committee member of my supervisory committee, Dr. I. Vargas-Baca have provided guidance and support at all stages of this project. I completed all of the research work, with the exception of collecting X-ray powder diffraction data which was carried out by Dr. J. Britten, Dr. J. Price, and Declan Dejordy.

CHAPTER 1 - INTRODUCTION

1.1 Microelectronics and their applications in current world

Though the development of the field of electronics began over a century ago, the field of microelectronics only started in late 1960's with the development of integrated circuits (IC).¹ Since then it has been one of the most demanding fields of electronics with increasing demand for smaller and light weight electronic devices with improved device performance. Present day electronic devices such as cellphones, laptops, tablets, digital watches etc. would not have been possible without the evolution of microelectronics.¹

1.2 Miniaturization of device features

Over the past few decades, the trend in the field of microelectronics has been minimisation of device size while enhancing device features. The first transistor was discovered in 1947 at Bell laboratories, which is considered as the landmark in modern electronics.² The transistor was smaller in size and used less power compared to the large vacuum tubes that were used in early electronic devices. Hence, the transistor was adopted as a replacement for the vacuum tubes in electronic devices. In 1965 a simple observation made by Golden E. Moore; the chairman of Intel corporation led to the evolution of the field of microelectronics. This observation, which is called Moore's law, states that the density of components per integrated circuit (IC) would double approximately every 2 years.² The early integrated circuits contained only a few transistors per chip. The number has been

increasing ever since, and current microchips contain billions of transistors per chip (Figure 1.1).³

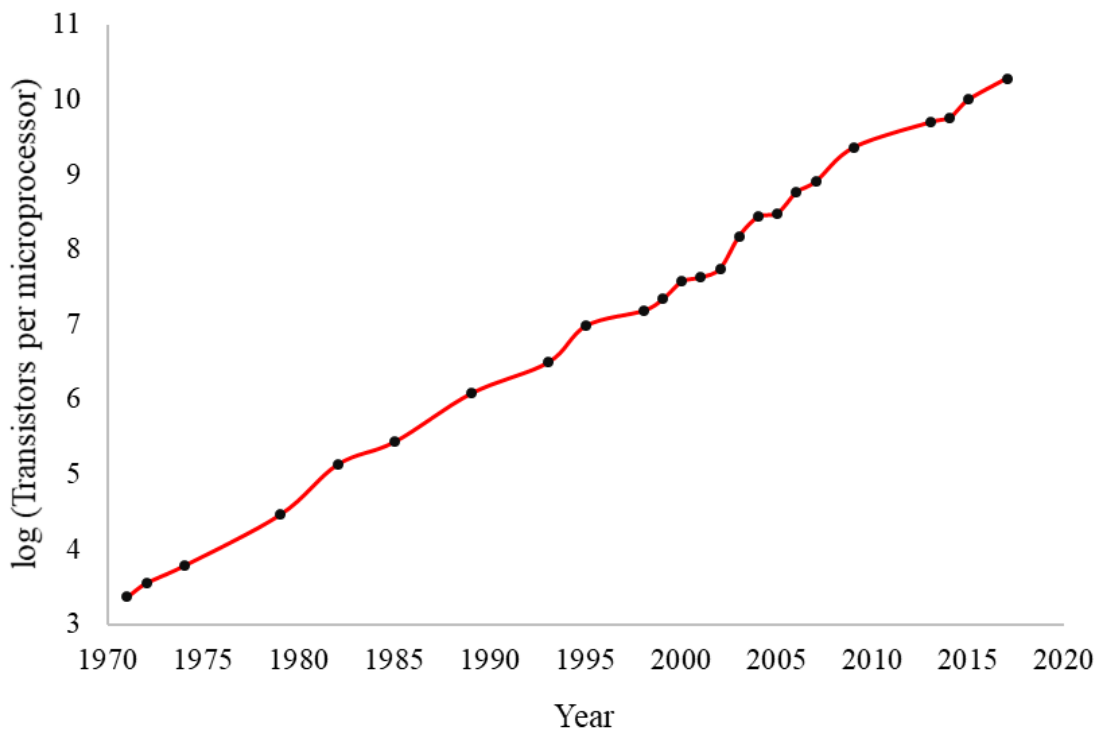


Figure 1.1: Moore’s Law: Number of transistors per microprocessor. Published on the website “Our world in data”.³

The IC complexity is measured by the transistor count which is the number of metal-oxide-semiconductor field-effect transistors (MOSFET) on an IC chip. As of 2019 AMD holds the record for most number of MOSFETS in a single chip with 39.54 billion transistors in its 2nd generation EPYC Rome processor.⁴

The increased density of transistors continuously decreases the transistor technology node, which is dependant on the physical size of the transistor. Technology node is defined as the

length of the silicon channel between source and drain terminals in field effect transistors.⁵ Decreasing the technology node of a transistor enhances device features and power efficiency while decreasing device dimensions. Transistor technology node reached 10 nm in 2016 and 7 nm in 2018.⁶ The 5 nm technology node is currently the most advanced process technology, with mass production started in 2020.⁷ 3 nm node transistors are set to begin fabrication in large scale as early as 2021.⁸

1.3 Thin films and their applications in microelectronics

Development of modern microelectronics would not have been possible without advanced thin film technologies. A thin film is a layer of materials ranging from a few nanometers to micrometers in thickness. Microelectronic devices usually include different types of thin films and their dimensions have been reduced to the nano scale at present. Production of these thin films requires special technologies to obtain films with high accuracy of thickness.⁹ The properties and structures of thin films are highly dependent on the method used for film deposition. Films are deposited on different substrates such as single crystal materials, polymers, organic substrates, etc. depending on their applications. Thin films are used in the microelectronics industry, primarily for microprocessor and memory device applications.¹⁰ Depending on the thin film material, different thin films have unique applications in microelectronics.

1.3.1 Thin film growth techniques

Production of thin films with high conformality, high aspect ratio, and precise control of the film thickness is crucial to continue the current trend of miniaturization of electronic

devices. Vast numbers of deposition methods have been developed over the past few decades for the fabrication of thin films. However, only a limited number of deposition methods can be employed to form thin films which are several nanometers to micrometers in thickness.¹¹

Both physical and chemical vapor deposition methods, including Physical vapor deposition (PVD), Chemical vapor deposition (CVD), and Atomic layer deposition (ALD), have been successful in the production of thin films with <100 nm in thickness.¹² A detailed discussion of all deposition techniques is beyond the scope of this dissertation, hence only the aforementioned three vapor deposition techniques will be discussed in detail.

1.3.2 Physical vapor deposition (PVD)

Physical vapor deposition (PVD) incorporates a range of different thin film deposition techniques such as evaporation, laser-ablation deposition, vacuum-arc based deposition, and different sputter deposition methods.¹³ PVD is an atomistic deposition process where the material is deposited atom by atom.¹⁴ A typical PVD film growth process includes generation of vapors of individual atoms or a cluster of atoms from a solid or liquid substrate and transport of these vapors under a vacuum or low pressure gaseous environment to the substrate, where they condense on the substrate to form the film.¹⁴ Removal of atoms from the original source can be achieved by either thermally heating the source (evaporation) or by bombarding the source with different particles including electrons, atoms, ions, molecules or photons (sputtering).¹³

During vacuum evaporation, atoms generated by thermally heating the source beyond its boiling/sublimation point reach the substrate to form the film (Figure 1.2a). The vacuum environment in the chamber reduces the possibility of contamination and collision of the generated atoms with gas molecules. Gas pressures in the chamber for the vacuum deposition are generally in the range of 10^{-5} to 10^{-9} Torr.¹⁴ The substrate is kept in direct line-of-sight of the source. The distance between the source and the substrate is maintained between 10 and 100 cm to prevent heating of the substrate by optical radiation from the source, and to maximize the deposition area. Vacuum deposition has the ability to deposit material on a large surface area with a rate of approximately 100 nm/min.¹³

Sputter deposition is a deposition method where atoms are ejected from a solid source (target) by bombardment with high energy atomic particles, usually a neutral gas atom.¹⁴ The distance from the source to the substrate is lower compared to vacuum deposition. Incident energy in the range of 50-2000 eV is typically sufficient to overcome the surface binding energy of the target, dislodging surface to near-surface atoms.¹³ These sputtered atoms travel through the chamber and condense on the substrate, forming a thin film of the desired material (Figure 1.2b).

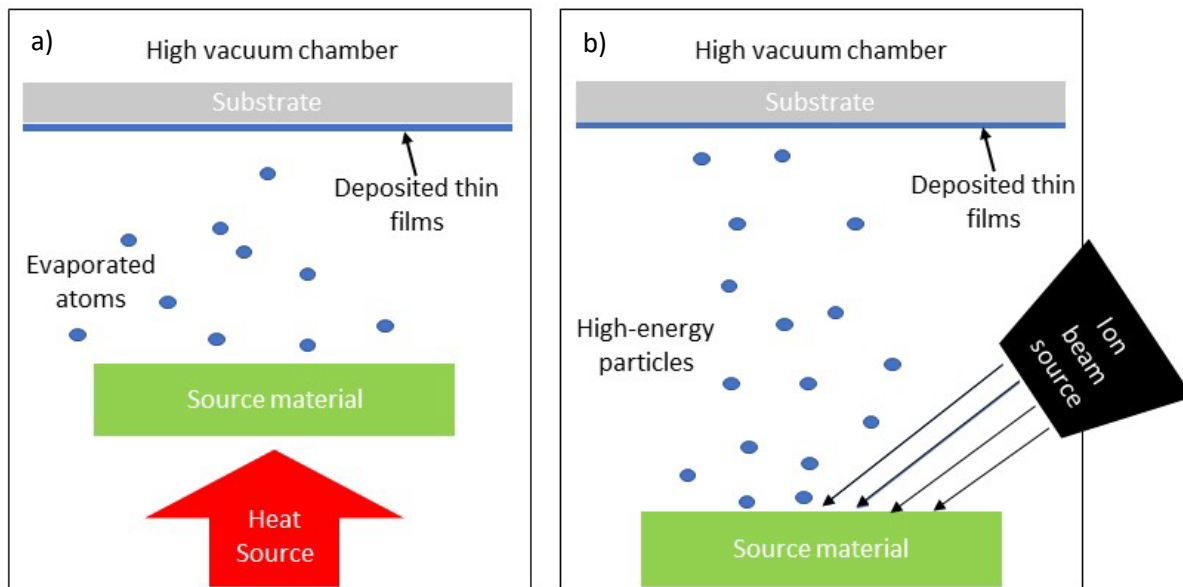


Figure 1.2: Schematic diagram of physical vapor deposition (PVD); a) evaporative PVD, b) sputtering PVD.

Although PVD is able to generate high quality films that are crucial for the microelectronics industry, film growth is highly directional, with both evaporative and the sputtered PVD leading to films with pillar type microstructural features, and limited ability to coat high aspect ratio features.¹⁰

1.3.3 Chemical vapor deposition (CVD)

Chemical vapor deposition (CVD) can be used to produce thin films of most metals, non-metallic elements including carbon and silicon, and many other compounds including nitrides, oxides, and carbides.¹⁵ CVD involves the process of delivering one or more gas phase precursor molecule on to a heated substrate (typically $< 500\text{ }^{\circ}\text{C}$) in a vacuum chamber to form a thin film of the desired product via thermal decomposition of the precursor

material. (Figure 1.3).¹⁶ In a typical CVD process, an inert gas stream is used to introduce gaseous precursor molecules into the reaction chamber, which is maintained under dynamic vacuum. Once these precursor molecules reach the heated area of the reaction chamber, they can be adsorbed onto the substrate, either by physisorption (Van de Waal's attractions with the substrate) or chemisorption (chemical reaction with functional groups on the substrate to form chemical bonds). These adsorbed precursor molecules then undergo thermal decomposition to form the deposited film. In addition to the anticipated surface-based reactions, precursor molecules may thermally decompose or react with each other in the gas phase, producing fine particles that can incorporate into the resulting films.¹⁷ Unreacted precursor molecules along with any gaseous by-products that form during surface reactions are removed from the vacuum chamber with the assistance of an inert gas stream.¹⁶ Precursors for use in CVD must be highly volatile and thermally stable at the delivery temperature, and thermally unstable at the deposition temperature.¹⁷ The desired film thickness in CVD can be controlled by vapor pressure, deposition temperature and the duration of exposure of the substrate to the precursor.¹⁸

Film growth by CVD has many desirable features, including the ability to produce conformal films (especially on surfaces without high aspect ratio nanoscale features) with high purity and relatively high deposition rates.¹⁹ Film deposition in CVD is not limited to line-of-sight from the source as in PVD.¹⁵ However, film growth often requires very high temperatures, and many substrates are not stable at these temperatures. This limitation can be partially eliminated by using plasma CVD (where plasma or plasma-generated radicals are applied to the surface to induce precursor decomposition) or metalorganic CVD (use of

less thermally robust metalorganic precursor molecules).¹⁵ Incorporation of particles into the growing film due to gas phase reactivity, can also lead to defects and non-conformal growth of the film.¹⁶

Additionally, film thickness depends on the amount of precursor reaching each point on the substrate surface, which is difficult to control, especially on large substrates. Furthermore, conformal deposition in high aspect ratio nanoscale features, such as trenches, vias, and overhangs is often not achievable, since precursor molecules decompose before reaching to the bottom of nanoscale features (e.g., 10-20 nm diameter trenches).

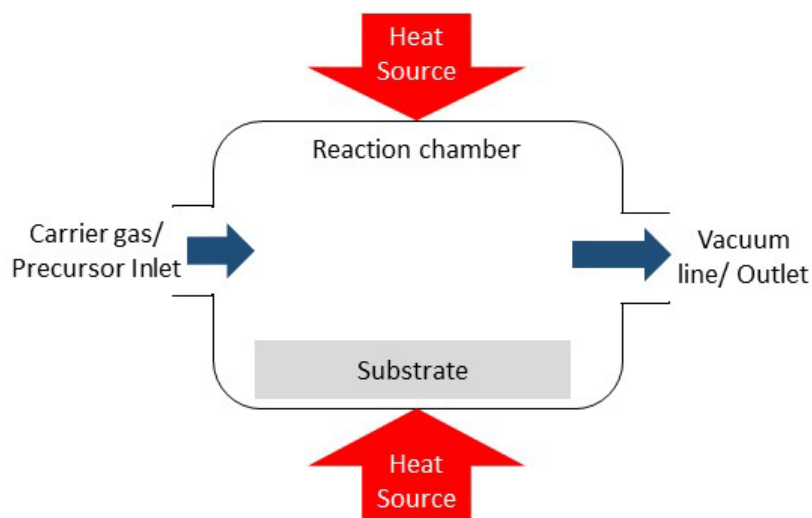


Figure 1.3: Schematic diagram of a chemical vapor deposition (CVD).

1.4 Atomic layer deposition (ALD)

The directional nature of films deposited by both CVD and PVD methods limit their applications in semiconducting devices.¹⁰ However, the continued trend of device minimization in the microelectronics industry has increased the demand for growth of thin films on two and three dimensional substrates. This requires a deposition method that can produce films with high conformality and allows atomic level control of film thickness.²⁰

Atomic layer deposition (ALD) was first discovered in 1977 by Suntola and Antson for the deposition of polycrystalline thin films of ZnS for electroluminescent flat panel display devices.^{12, 21} This process was initially named Atomic Layer Epitaxy (ALE). However, over the past few years, many ALD processes have been developed to deposit a range of materials (e.g., metals, oxides, nitrides, sulphides) and most of these films are not epitaxial, hence the more general name atomic layer deposition (ALD) was adopted.²¹

When considering the deposition principle, ALD is a special modification of CVD, which can overcome most of the limitations that are associated with CVD.²² ALD is a unique technique with the ability to produce thin films with high conformality and atomic level thickness control, due to its sequential self limiting growth pattern.²³ It is the most promising future thin film deposition method for the microelectronics industry, considering the current trend in device miniaturization. Combination of conformal coverage and exceptional control of film thickness allows ALD to deposit on narrow (e.g., width < 22 nm), high aspect ratio trenches, vias, pores and three-dimensional nano scale substrates which wouldn't be achievable using CVD and PVD due to their directional growth.²⁰ This

is illustrated schematically in Figure 1.4, parts a and b; part a shows the typical result of CVD for attempted deposition within narrow high aspect ratio trenches; precursor molecules come in to contact with the substrate surface before reaching the bottom of the trench, filling over the trench rather than producing a conformal coating.²⁰ By contrast, part b shows the result of ALD, where conformal coverage is achieved (the mechanism by which ALD achieves conformal coverage is described below).²⁰ This type of conformal coverage is evident in Figure 1.4 c, which shows a cross-sectional SEM of Al₂O₃ films grown by ALD within nanoscale trenches.

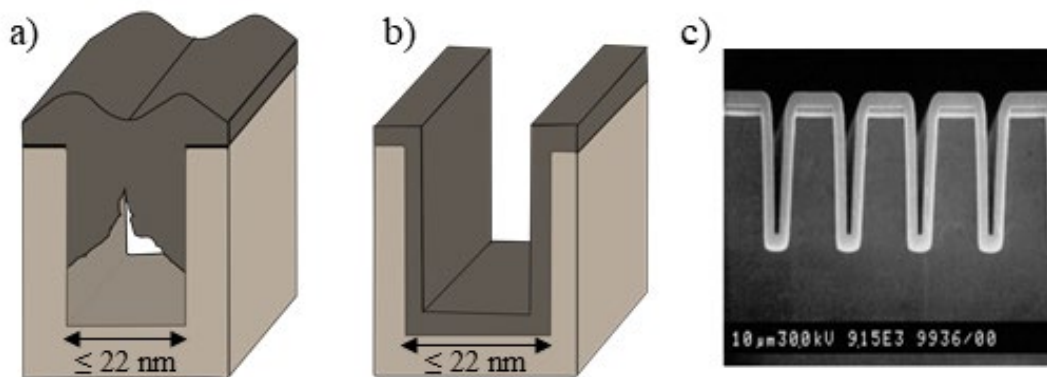


Figure 1.4: Film coverage and conformality illustration of (a) CVD/PVD growth (b) ALD growth on a narrow trench (width < 22 nm), (c) SEM cross sectional image of an ALD grown conformal Al₂O₃ film in trenches. Reprinted with permission from ref. 22. Copyright 2003 John Wiley and Sons.

Film growth in almost all thin film deposition methods is governed by the rate and type of precursor transport and chemical reaction kinetics, with faster film growth only observed

at places where precursor get readily transported, which may lead to uneven film growth.²⁴

By contrast, ALD is divided into two separate self saturating half reactions (vide infra), so film growth in ALD is independent of the precursor transport or exposure time.²⁴

Film deposition in ALD takes place in a cyclic manner.²² A deposition cycle consists of sequential and alternating pulses of two gas phase precursor molecules which react with the substrate or undergo surface-based reactions with one another.²¹ These reactions are known as half reactions.²¹ This process is explained in Figure 1.5 using the deposition of Al_2O_3 on a SiO_2 substrate. First AlMe_3 vapours are pulsed into a vacuum chamber (<1 Torr) with the assistance of an inert gas flow (Typically N_2 or Ar).²¹ These precursor molecules then chemisorb onto the surface of the substrate to form a monolayer. This process is self limiting because adsorption ceases after all accessible surface sites have reacted. At this point, unreacted precursor molecules and reaction by-products (e.g., CH_4) are purged from the reaction chamber with an inert carrier gas.²¹ This is then followed by a pulse of a second gaseous precursor molecule (sometimes referred to as a co-reactant, in this case H_2O), which reacts with the adsorbed monolayer of the first precursor to form a single layer of the desired thin film material. Any excess precursor molecules and reaction by-products are removed from the reaction chamber with the use on an inert carrier gas to complete one growth cycle of ALD.²¹ This process is repeated until the desired film thickness is achieved. Unlike in CVD, gas phase reactions are not observed since the two gaseous precursor molecules are never present in the chamber at the same time.²⁴

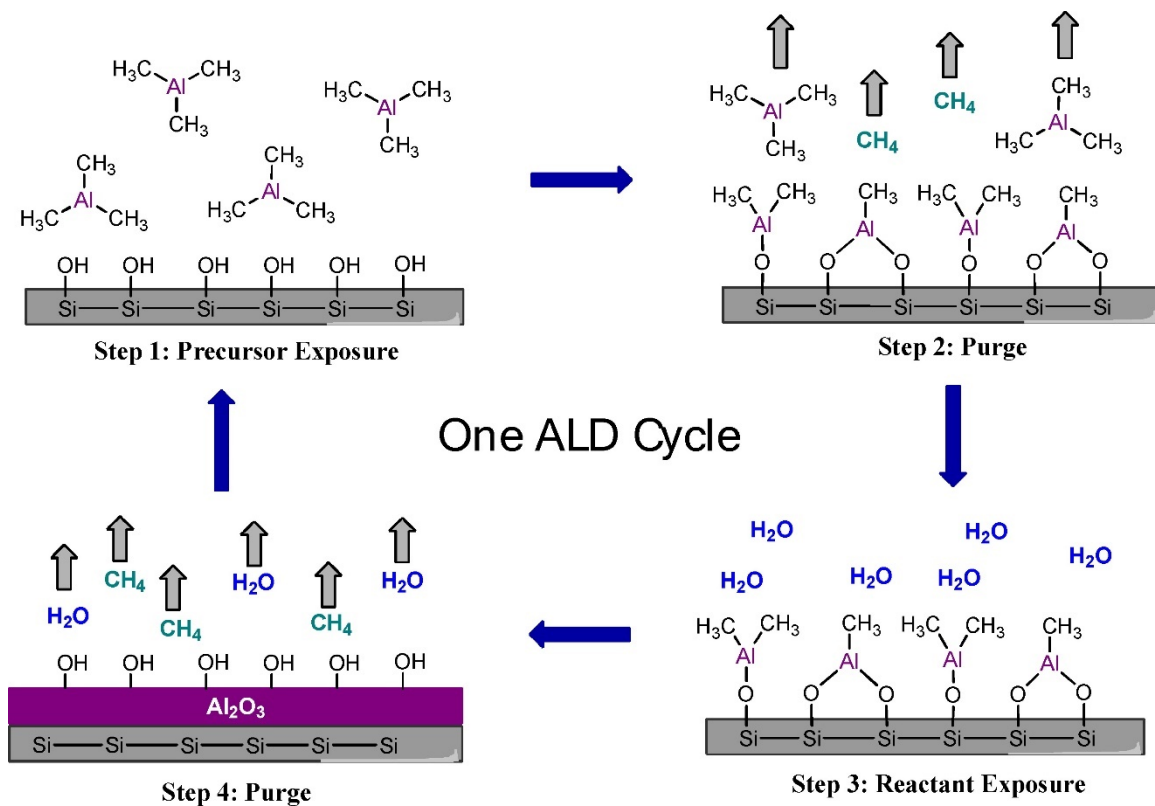


Figure 1.5: Schematic diagram of one ALD cycle of Al_2O_3 film growth using $(\text{CH}_3)_3\text{Al}$ and H_2O . Usually, one growth cycle consists of four steps. 1) exposure to the first precursor 2) purging away excess precursor and by-products 3) exposure to the second precursor 4) purging reaction by-products and excess precursor. Reprinted with permission from ref.20. Copyright 2003 Elsevier.

Figure 1.6 shows a typical saturation curve for ALD, which is one of the hallmark features in ALD film growth.²⁰ When growth rate is plotted against the precursors pulse length it ultimately reaches a plateau region. The growth rate becomes constant after sufficient precursor is delivered to react with all available surface reactive sites on the substrate. The minimum length of the pulse to achieve a constant growth rate is called as the saturative

dose. If the precursor is thermally stable at the deposition temperature used, no film growth can be observed in ALD after the minimum saturative dose of the precursor has been delivered.²⁰ This feature is the reason behind the self-limiting film growth observed in ALD.

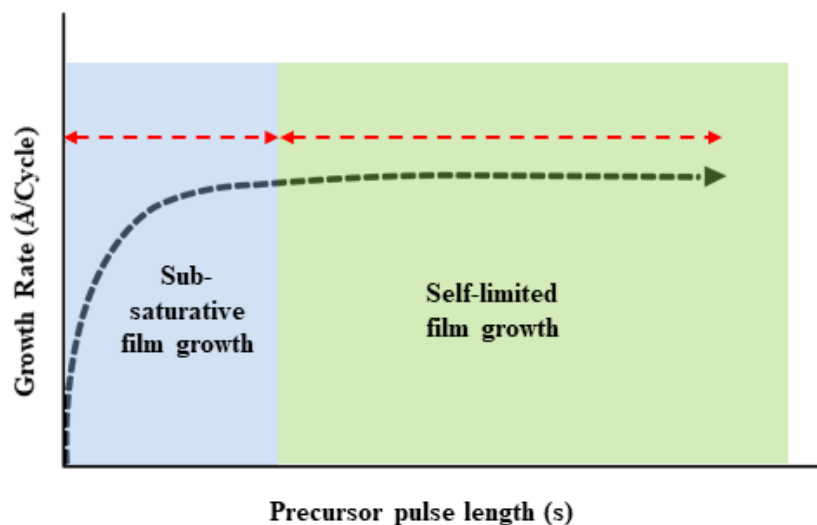


Figure 1.6: Plot of growth rate vs precursor pulse length. Blue colour region; sub saturative film growth. Green colour region; surface reactive sites have become saturated and film growth is self-limiting.²⁰

A plot of growth rate as a function of deposition temperature helps to understand the thermal growth properties of an ideal ALD process (Figure 1.7).²⁰ The plot produces a region where growth rate is constant and shows little or no dependence on the deposition temperature (Figure 1.7 Region B).²⁰ This region is termed the “ALD window” and it can range up to 200 °C, depending on the precursors and materials.²⁰ The ALD window is the ideal deposition temperature range in ALD for film growth. This nearly ideal ALD behaviour lies between two non ideal regions in the plot (Figure 1.7).²⁵

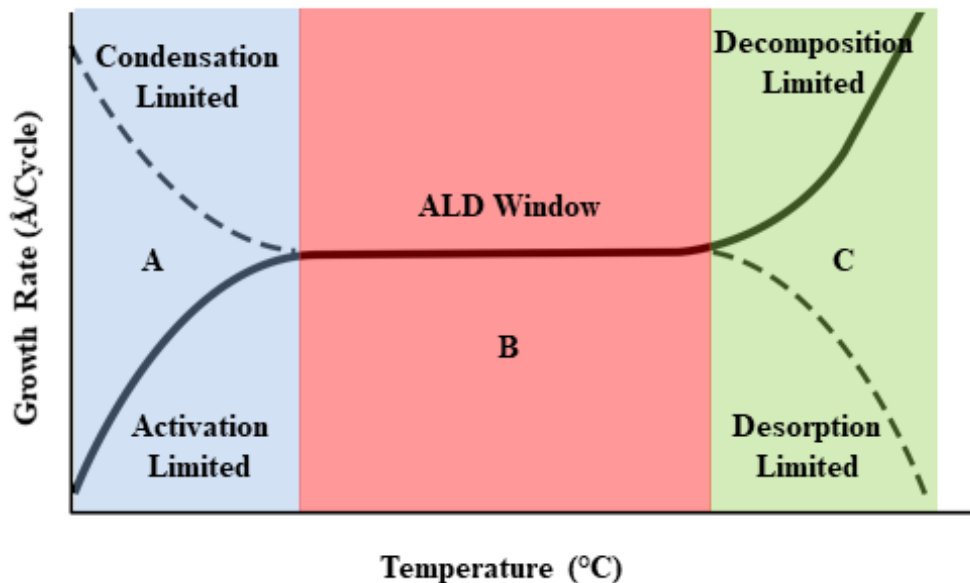


Figure 1.7: Plot of growth rate Vs deposition temperature.²⁰

Within the ALD window, the growth rate should be independent of the deposition temperature. However, this ideal behaviour is not observed in the majority of ALD processes. Outside the ALD window, ALD behaviour is not observed due to disruptions from different chemical and physical processes.¹² Limited available thermal energy at low deposition temperatures, results in inadequate precursor reactivity. This process prevents surface sites from becoming saturated leading to incomplete surface reactions (Figure 1.7 Region A solid line). These reactions will not proceed beyond a certain percentage of completion, decreasing the growth rate at low temperatures. They display a self-limiting behaviour, but films include large amounts of impurities.²⁵ An increase in growth rate at lower temperatures is due to the condensation of reactants on the surface (Figure 1.7 Region A dashed line).²⁵ At higher deposition temperatures, precursor molecules will be unavailable for surface reactions due to their desorption from the substrate. This can result

in a decrease in growth rate at high deposition temperatures (Figure 1.7 Region C dashed line).²⁵ Alternatively, some precursor molecules decompose when the deposition temperature is too high, resulting in a CVD component which affords an increased growth rate (Figure 1.7 Region C solid line).²⁵

There are two main types of ALD processes; thermal ALD and plasma enhanced ALD, which is known as PEALD.²⁶ Both methods are extensively utilized in microelectronic device fabrication. The two processes only differ by how they deliver or produce co-reactant molecules in the second half-reaction. This can be easily described by comparing the process of film deposition for Al_2O_3 (Figure 1.8).²⁷ In the first-half reaction trimethyl aluminum (TMA) molecules react with the surface hydroxyl groups on the substrate and produce CH_4 as a by-product. Excess TMA molecules and CH_4 are purged away from the reactor with a flow of N_2 or Ar gas. During the second half-reaction of the *thermal ALD* process, H_2O vapor is introduced to the reaction chamber (Figure 1.8 top). These H_2O molecules then react with Al and CH_3 groups on the surface to produce a single layer of Al_2O_3 . CH_4 is produced as a by-product during the reaction. By contrast, during the second half-reaction of the *PEALD* process for Al_2O_3 deposition, oxygen radicals are generated by igniting oxygen plasma above the substrate (Figure 1.8 bottom). These highly reactive oxygen radicals react with surface Al- CH_3 groups and produce a single layer of Al_2O_3 . The reaction produce CO_2 and H_2O as by-products.²⁷

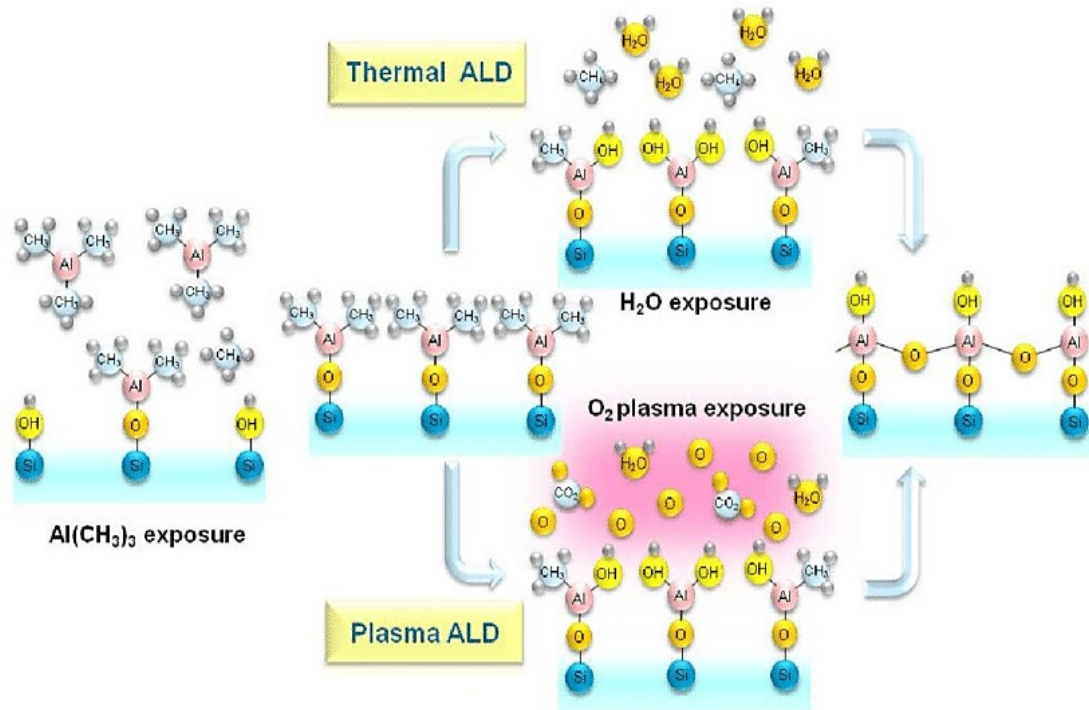


Figure 1.8: Schematic diagram of one cycle of a thermal and a plasma-assisted atomic layer deposition (ALD) process. Each cycle consists of two half-reactions: first, the trimethylaluminum (TMA) molecules react with the hydroxyl groups attached to the silicon surface; second, the molecules are reacted with H₂O (thermal ALD) or an O₂ plasma (plasma ALD). Reprinted with permission from ref. 27. Copyright 2010 IEEE.

1.4.1 Plasma enhanced ALD (PEALD)

In Plasma enhanced ALD (PEALD), a plasma source is used to generate high energy plasma species. These plasma species are usually radicals with high energy and high reactivity that can readily react with surface bound precursor molecules. H₂, N₂, NH₃ and O₂ are most frequently used plasmas in PEALD.²⁶ PEALD is extensively used to deposit thin films of single elements where hydrogen radicals are used as the reducing agent to

reduce the metal precursor.²⁵ Film deposition by PEALD offers several advantages including lower processing temperatures due to the high reactivity of plasma species, and higher growth rates relative to thermal ALD.²⁶ However, poor film conformality is often observed in PEALD due to recombination of plasma species on the substrate.²⁰ This radical recombination process limits the utility of PEALD to deposit film within high aspect ratio structures.²⁵ In addition, reactor design and reaction chemistries involved in PEALD are more complex than those in conventional thermal ALD.²⁸

1.4.2 Thermal ALD

Thermal ALD utilizes thermal energy to drive film growth. In thermal ALD the energy requirement for surface reactions are completely provided as thermal energy by heating the substrate.²⁹ In thermal ALD co-reactant molecules react with the chemisorbed precursor molecules on the surface of a heated substrate. Deposition temperatures can range from as low as room temperature to about 350 °C, depending on the thermal stability and reactivity of the precursor and co-reactant.²⁸ Unlike many PEALD processes, thermal ALD allows for conformal deposition on high aspect ratio nanoscale features.

1.4.3 Substrate Selection

ALD is a process that is strongly dependent on the properties of substrate surface, as chemisorption of precursor on the substrate depends on the number and type of reactive surface sites that are available. In the initial stage of ALD growth (where deposition occurs on the initial substrate surface, rather than the deposited film), the nature and concentration of reactive sites on a substrate is dictated by the substrate material, pre-treatment method,

and crystallographic orientation. Some surfaces resist any ALD growth, while some have longer initial nucleation times.³⁰

Depending on the application, different substrates are used in ALD, including H-terminated silicon, SiO₂, Al₂O₃, glass, Si₃N₄, GaAs, ceramics, metals, polymers, and fibres.³¹ Deposition temperature also has to be taken into consideration when considering certain substrates, as some substrates (e.g., polymers) cannot withstand high temperatures.³¹

1.4.4 Precursor properties and reactivity

Precursor properties and reactivity are critical in a typical ALD process. Precursors in ALD might be gasses, volatile liquids or solids, depending on the ALD process.²² Most solid and some liquid precursors must be heated to generate a sufficient vapor pressure for effective mass transport of the precursor.²² Many ALD precursors have also been used for CVD, or have structures related to those of CVD precursors.³² A suitable precursor for ALD should have following chemical and physical properties.

1. A precursor must be sufficiently volatile (minimum value of approximately 0.1 Torr equilibrium vapor pressure at the delivery temperature).³³ Non ideal ALD behaviour resulting from precursor condensation on the substrate can be prevented if the precursor can be delivered to the reaction chamber at a temperature below the substrate temperature.¹⁰ Also, precursor pulse durations will be impractically long if the precursor doesn't have adequate vapor pressure at temperatures below its decomposition temperature.³⁴

2. High thermal stability. The precursor must be thermally stable (on a long time scale) at the delivery bubbler temperature and (on a short time scale) at the growth temperature.²¹ Thermal decomposition of a precursor will lead to non self-limiting chemical vapor deposition (CVD) like growth.²⁰ However, somewhat thermally unstable precursors with a low decomposition rate, can still be utilized in certain applications, including protective coating applications, as it only has a small effect on the overall film growth.²²
3. Reactivity: Precursor molecules should react rapidly and irreversibly with surface functional groups of the substrate, and with co-reactant molecules.³⁵ High reactivity enables lower ALD deposition temperatures, and faster surface saturation leading to shorter cycle times.³³ Reactions must only give rise to unreactive, volatile by-products. After completion of the reaction, neither the precursor nor its by-products should react with, etch, adsorb or dissolve in the growing film.^{12,21} Excessive adsorption results in non self-limiting CVD like film growth while etching can decrease the growth rate and uniformity of the film.¹²

In addition to these main properties, it is also beneficial to have a low melting point for the precursor since liquid precursors can help to reduce the particle incorporation into the film, unlike solid precursors. However, because film thickness in ALD is only dependent on the number of cycles, use of liquid precursors is not as critical as in CVD.¹⁰ Though its not crucial for an ALD process, there are several other useful properties of a precursor including low toxicity, ease of handling, ease of synthesis and scale up, and low cost.³⁶

High purity precursors are desirable in ALD, especially for the applications of microelectronics.³⁴

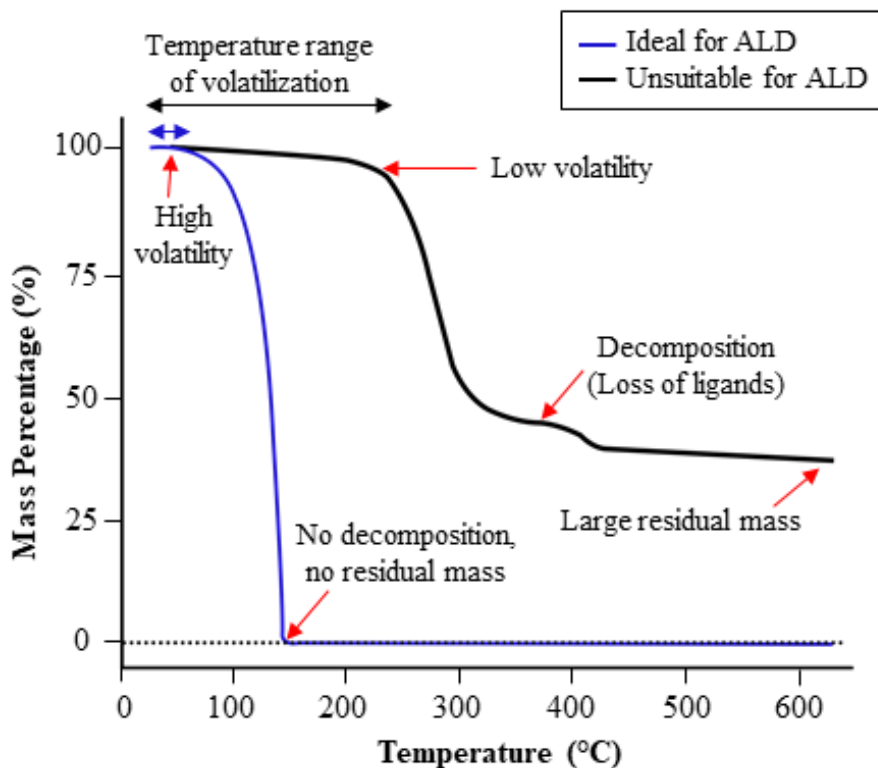


Figure 1.9: The thermo gravimetric analysis (TGA) of ideal and non-ideal ALD precursors. Reprinted/adapted with permission from ref.12. Copyright 2015 Elsevier.

An ideal ALD precursor must be volatile at low temperature and thermally stable with no decomposition at lower temperatures. High volatility is indicated by mass percentage reaching 0 over a small temperature window, and thermal stability is indicated by zero residual mass (Blue curve). There are many compounds that undergo a slow volatilization over a large temperature window (Black curve). The mass loss in this curve is possibly due

to a decomposition. Large residual mass and loss of ligands due to decomposition is indicated by numerous plateau regions and mass loss along the TG curve.¹²

A precursor with the greater volatility is almost always preferred in ALD (Figure 1.9). Volatility of a compound is affected mainly by intermolecular interactions (e.g., H bonding or π stacking). Volatility also depends on the molecular weight and shape of the molecule.¹² Volatility and thermal stability is typically studied using thermo gravimetric analysis (TGA), which shows the weight loss of a compound as a function of the temperature. Generally heavy molecules with a high symmetry show low volatility compared to the light molecules with low symmetry. However, there are many exceptions to this general rule.¹² Highly volatile precursors are usually monomers with low molecular weight ligands. Intermolecular forces as well as the shape of the precursor molecule is also influenced by ligands.¹² Unfortunately, it is challenging to find an ideal ALD precursor, and selecting a precursor is always a compromise between volatility, reactivity, stability and cost.²¹

There are few incidences where elements have been employed as ALD precursors instead of compounds. These elements include Zn, Cd and Hg, but most other metals don't have sufficient vapor pressure to be utilized as precursors in ALD.³⁴ Frequently used ligands in metal precursors are halides, alkyls, cyclopentadienyls, alkoxides, alkyl amides, amidinates, β -diketonates, guanidates, etc.³⁶ Whenever possible, the ligands in precursors are modified to attain the desired chemical and physical properties. These modifications usually focus on changing the size of the ligand, fluorination and/or adding additional donor groups (e.g., amines) to the ligand.³⁶ New approaches, like use of heteroleptic complexes,

where a metal center is connected to two or more different ligands, can be used to further tune the properties of precursor molecules.

Highly reactive, stable, inexpensive halide-based precursors are widely used in industrial applications, although, they have a high tendency to contaminate the film at lower temperatures, and the possibility to produce corrosive by-products during the reaction (e.g., HCl).¹² The aforementioned issues can be eliminated by using organometallic compounds like metal alkyl or metal carbonyl complexes, while maintaining high vapor pressure and reactivity. However, a challenge with these compounds is the reactively weak metal-carbon bond, which can result in low thermal stability and shelf-life. A stronger metal-carbon bond is present in cyclopentadienyl complexes (e.g., FeCp₂ or CoCp₂), where the cyclopentadienyl ligands can saturate the metal center both electronically and coordinately.¹² However, the strength of metal-cyclopentadienyl bonds can hinder reactivity, preventing complete ligand removal and resulting in films with low purity. As an alternative, many ALD precursors contain metal-alkoxide or metal-alkylamide linkages. However, for some metals, the oligomerization ability of homoleptic alkoxide and alkylamide complexes reduces their volatility. Thermal stability can also be a concern with alkylamide precursors, especially if held in a heated bubbler over a long period of time. By contrast, alkoxide complexes tend to be more thermally stable and to have a better shelf life.¹²

1.4.5 Co-reactant chemistry

Selecting a suitable co-reactant is equally important for a successful ALD process. Co-reactants in ALD are most of the time nonmetal, volatile, small molecules. These can be elements such as H₂ or O₂, small molecules like NH₃ and H₂O, or alkyl compounds such as ZnEt₂. Alternatively, higher energy species like plasma and plasma-enhanced radicals are also used as co-reactants in PEALD.¹²

Co-reactants are subject to the same chemical and physical requirements as precursors. The main objective of the co-reactant is to efficiently react with adsorbed precursor molecules, leading to the desired product and volatile by-products.¹² The effectiveness of this reactivity depends primarily on the volatility, reactivity, and stability of the co-reactant molecules.

Table 1.1: Typical thermal ALD materials and selected co-reactants which have been used to generate each material.³⁷

| Material | Common co-reactants |
|------------------|---|
| Metal oxides | H ₂ O, H ₂ O ₂ , O ₃ , CH ₃ OH, CH ₃ COOH |
| Metal nitrides | NH ₃ , N ₂ H ₄ , ^t BuNH ₂ , Me ₂ NNH ₂ , |
| Metal carbides | C ₂ H ₄ , C ₂ H ₂ |
| Metal phosphides | PH ₃ , P(NMe ₂) ₃ , |
| Metal arsenides | AsH ₃ , As(NMe ₂) ₃ |
| Metal sulfides | H ₂ S, Et ₂ S ₂ |
| Metal selenides | H ₂ Se, Se(SiEt ₃) ₂ |
| Metal tellurides | H ₂ Te, Te(SiEt ₃) ₂ |
| Metal fluorides | HF, TiF ₄ , TaF ₅ |
| Pure element | H ₂ , Si ₂ H ₆ , SiH ₂ Et ₂ , HCHO, NH ₃ , O ₂ |

Table 1.1 summarizes the most common ALD materials with common non-metallic co-reactants used. The most studied ALD materials are metal oxides and metal nitrides, with a large number of non-metal co-reactants available to deposit them. Among all co-reactants, H₂O is one of the most studied co-reactants for metal oxide deposition, though the use of H₂O as a co-reactant comes with many challenges, like relatively low volatility, and

difficulties in purging due to strong adsorption to surfaces.¹² NH_3 is the most widely used co-reactant for metal nitride ALD, although substituted amines and hydrazines also have been effectively employed.¹²

1.5 Characteristics and advantages of thin films deposited by ALD

Surface saturated and self-limiting growth behaviour provide ALD with many advantages over other thin film deposition methods.³⁸ These advantages are outlined in detail below.

1.5.1 Atomic scale deposition

Due to presence of finite number of adsorption sites on a substrate, once the surface is saturated, reactions stop in ALD, leading to a monolayer deposition during each cycle. As a result, the film thickness in ALD is only proportional to the number of deposition cycles employed for the reaction.³⁹ The thickness of the film produced in ALD is independent from the amount of precursor or co-reactant used for the reaction. The desired thickness can therefore be precisely controlled by simply adjusting the number of deposition cycles of an ALD reaction.

1.5.2 Low temperature deposition

Compared to many other film deposition methods including CVD and PVD, ALD typically employs lower temperatures (<350 °C) for film deposition. If appropriate precursor, co-reactant, and reaction conditions are met, ALD processes produce high purity, pinhole free, and conformal films at temperatures as low as room temperature. Film deposition at low temperature is crucial for flexible electronics involving thermally fragile substrates such as

polymers or organic materials.¹² Most of these substrate materials require deposition temperatures below 200 °C, which is challenging to accomplish using other thin film deposition methods such as CVD and PVD.¹² However, relatively high temperatures are desired in some ALD processes to access certain crystalline phases. For example, rutile TiO₂ is deposited only at elevated substrate temperatures by ALD.¹²

1.5.3 High uniformity and conformality

When it comes to the fabrication of microelectronic device components, self-limiting growth behaviour in ALD poses many advantages. Since the film deposition in ALD only happens due to surface reactions, changes in precursor flux will not affect the film thickness. If a sufficient flux reaches all areas, ALD can produce films with the same thickness, regardless of the differences in the flux of precursor, either in different areas on a substrate or in a three-dimensional structure.¹²

When comparing with flux-controlled deposition methods, surface-controlled methods have the capacity to produce uniform films in a large area. Since ALD is a surface-controlled method, an ideal ALD process can produce a perfectly uniform film (Figure 1.10 a). However, to obtain a uniform film in flux-controlled methods (e.g., CVD or PVD), a constant precursor flux must be applied over the whole area of the substrate; a condition that is difficult to achieve in real-life. When a sufficient precursor flux is given, ALD can perfectly cover a three-dimensional structure, which is known as conformality (Figure 1.10 c). A uniform coverage throughout a three-dimensional structure is referred to as high conformality. A low conformality, with variations in thickness over a three-dimensional

structure is observed in flux-controlled methods. Though it is possible to enhance uniformity with reactor engineering, it is challenging and cannot be 100% effective. This makes conformality a unique and very desirable characteristic of films deposited using ALD.¹²

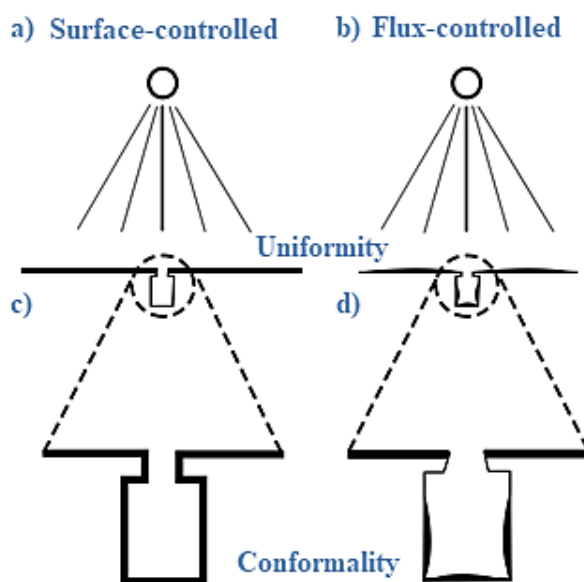


Figure 1.10: The uniformity and conformality of a) surface-controlled and b) flux-controlled techniques. The magnified area indicates film deposition on a three-dimensional feature; c) surface-controlled processes result in a constant film thickness throughout the structure d) film thickness depends on the line-of-sight for flux-controlled processes, resulting in uneven film thickness throughout the structure. Reprinted/adapted with permission from ref. 12. Copy right 2015 Elsevier.

Reproducibility and scalability are other advantages of the surface controlled and self-limiting growth behaviour of ALD. Also, ALD can produce pinhole-free thin films which is vital for barrier and passivation applications.³⁸

1.6 Applications of ALD in microelectronics

The major industrial application of ALD is production of semiconductor devices including both microprocessors and memory devices.³⁸ High permittivity (high k) devices are critical in current microelectronic devices. ALD is the most promising thin film fabrication method that could produce high k devices including, gate oxides, memory capacity dielectrics, and ferroelectrics.²² Current transistor fabrication processes focus on ALD to produce pinhole free, conformal films with well controlled thickness and a high dielectric constant.²¹ In addition to these, metals and nitrides for electrodes and interconnects are also deposited using ALD.²²

1. High k gate dielectrics

High k-dielectrics are mainly used for transistor gate stacks in microelectronic devices.²¹ The most common gate oxide used in electronic devices is the SiO₂ metal-oxide semiconductor field effect transistor (MOSFET). However down scaling of SiO₂ MOSFETs to a 1.0 nm thickness or below is associated with high gate leakage currents due to tunneling effects.⁴⁰ In order to overcome the above issue, highly uniform and pinhole free high-k gate materials deposition has been vastly researched using ALD. Commonly used ALD high-k dielectrics include; Al₂O₃, HfO₂, AlN, BeO.⁴⁰ Al₂O₃ deposited by ALD, is one of the earliest high k gate oxides that was used to replace

SiO₂ as the gate dielectric. Due to its higher dielectric constant, HfO₂ was used to replace Al₂O₃.⁴⁰ However, both Al₂O₃ and HfO₂ have large band gaps, hence they play a vital role as high-k dielectrics in three-dimensional memory and energy storage devices.⁴⁰

2. DRAM capacitors

Capacitors play a major role in evolution of dynamic random-access memory (DRAM) devices.⁴¹ Current microelectronic devices require (DRAM) units containing metal-insulator-metal (MIM) capacitors having a high capacitance density and a low leakage current.⁴² Multiphase materials such as BaTiO₃ and SrTiO₃ can also be used as high-k materials. However, obtaining a low leakage current is challenging due to the small band gap of these oxides.⁴² Doped-dielectrics have been identified as a potential solution to address the above issues associated with undoped high-k dielectric materials.⁴¹ For example, Y doped ZrO₂ films deposited by ALD were found to possess a higher capacitance density (30.2 compared to 19.1 for undoped ZrO₂) and a lower leakage current (60 times lower compared to undoped ZrO₂).⁴²

3. Transition metal nitrides

Transition-metal nitrides are usually used as metallization barriers and as gate metals in microelectronic devices.²² For example, dielectric breakdown caused by Cu ion diffusion into the surrounding dielectrics can be prevented using TaN and TiN barrier layers.^{43,44} Metal gates are required to eliminate the film thickness increasing effect of

the depletion layer capacitance in polysilicon gate electrodes.²² Owing to its excellent thermal stability, and low resistivity, TiN is an ideal candidate for metal gates.⁴⁴

4. Metal films

Metal films have numerous uses in microelectronics including, noble metals in ferroelectric random-access memory (FRAM), and high and low workfunction metals for dual-gate MOSFETs.²² Cu films deposited using ALD are employed as the primary interconnect material in integrated circuits.⁴⁵ Ni films deposited by ALD have applications in magnetic random-access memory devices, Ni-Si contact materials, and metal insulators.⁴⁵ However, synthesis of metal films using ALD has been quite challenging due to lack of an appropriate mechanism to adsorb metal precursor onto the metal surface without any surface functional groups.²²

1.7 Limitations and disadvantages of ALD

Though film deposition with ALD offers many advantages, there are also some disadvantages associated with the process. One of the major issues with ALD is its low rate of film deposition, with growth rates in the range of 1-100 nm h⁻¹. This is mainly due to long cycle times required to pulse the precursor and co-reactant and to purge volatile by-products, combined with growth rates per cycle (GPCs) between 0.01 and 0.5 nm/cycle.²¹ Reactor design and the aspect ratio of the substrate also affect the growth rate per hour.²¹ Based on the preceding discussion, ALD is not useful for deposition of films that are micrometers in thickness, considering the time consumption. Processing large batches of substrates in one ALD process is one of the ways to overcome the slow growth rate

associated with ALD. However, single wafer processing is preferred for microelectronics applications.²²

Another drawback of ALD, relative to PVD, is that incomplete reactions can leave impurities on the deposited film. For example, 0.1-1 atom % impurity levels are found in oxide films deposited by ALD using either metal halides or metal alkyls with water as the co-reactant. The carrier gas also can act as a source of impurity in some instances, for example oxygen sensitive AlN films. Because the amount and nature of impurities depend on the exact details of the film deposition method used, films must be thoroughly studied before use. Post deposition treatments such as high temperature annealing under a different environment (e.g., vacuum, H₂ or O₂) might also affect the purity and the microstructure of the film.²²

1.8 Overview of materials deposited by ALD

A wide range of materials have been successfully deposited by ALD. These compounds range from pure elements to metal oxides, metal nitrides etc. Though it is challenging, compounds with three or more elements also have been deposited by ALD.²¹ Figure 1.11 provides an overview of materials that have been deposited by ALD processes. Not all materials can be deposited by ALD due to limited availability of reaction pathways and appropriate precursors.

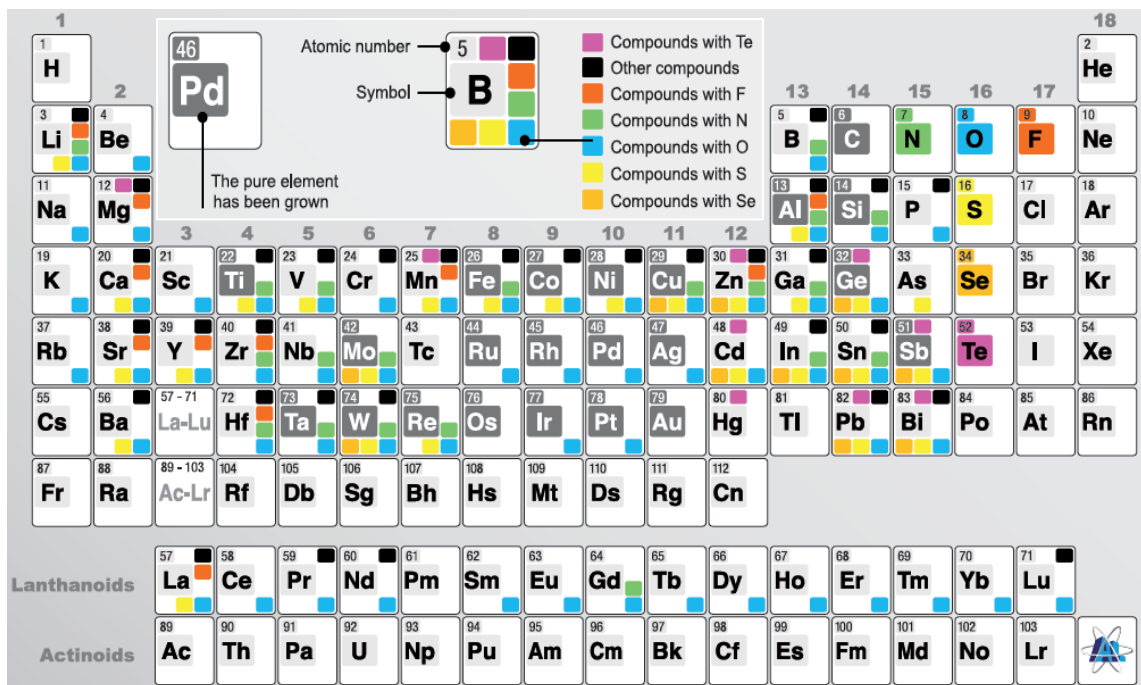


Figure 1.11: Overview of materials deposited by ALD. Published on the website “Overview of all materials prepared by atomic layer deposition (ALD)”⁴⁶

Metal oxides are currently the most developed area of compounds that can be deposited by ALD. Al_2O_3 is the most studied oxide deposited by ALD, typically using trimethylaluminum (TMA) with H_2O , and was first discovered by Higashi et al.⁴⁷ A wide variety of precursors are available for metal oxide ALD processes including metal halides, alkylamides, alkoxides, and cyclopentadienyl complexes.⁴⁸ Metal oxide deposition by ALD has gained more attention as it has the ability to produce high-k dielectric oxide thin film layers, which has a high demand in microelectronics due to their wide range of applications.⁴⁸ ZrO_2 , HfO_2 and Al_2O_3 are the most studied high-k oxides by ALD which have a high permittivity.⁴⁹ TiO_2 is another oxide of interest owing to its wide range of applications including corrosion resistive coatings, self cleaning surfaces, and solar cells.⁴⁹

To avoid metal corroding cracks, pinhole-free conformal thin film layers are essential to prevent contact between the metal and the corroding media, which can be only obtained by ALD.⁵⁰ Another class of oxides that is of current technological interest is binary and ternary rare earth metal oxides.⁴⁹ These oxides are ideal candidates for gate oxides, corrosion resistant coatings and protective film coatings due to their high thermodynamic stability. La_2O_3 , Gd_2O_3 , Y_2O_3 , and Pr_2O_3 , are among the most studied rare earth metal oxide processes by ALD.⁵¹ In addition to these oxides, other oxides such as MgO , ZnO , and Fe_2O_3 are also of importance as antireflective coatings owing to their high refractive index values.⁴⁹

Metal nitrides are another class of compounds that have a wide range of applications in microelectronics. The main use of metal nitrides is as barriers in integrated circuits to prevent interdiffusion and reaction of metals with silicon or insulators.⁵² Appropriate candidates should be highly pure, conformal and thin, conductive and have good adhesion towards metal and insulators, and deposition temperatures below 400 °C.⁵² TiN and TaN are the extensively studied nitrides for this purpose. For most ALD nitride processes NH_3 is used as the nitrogen source. The major problem with early transition metal nitride processes is the requirement to reduce the metal to the +3 oxidation state. Sometimes this needs the use of very strong reducing agents.⁵² For example, Zn is used as a reducing agent for the TaN deposition process using TaCl_5 and NH_3 . Ta_3N_5 is formed in the absence of Zn .⁵³

Most of the ALD nitride processes use a transition metal chloride as the precursor with NH_3 as the co-reactant. Growth of TiN from TiCl_4 and NH_3 is by far the most studied metal

nitride process by ALD, though the process still has some limitations, such as a low deposition rate due to the modest reactivity of NH_3 , and incorporation of chlorine into the growing film.⁴⁸ Recent research has focused on finding more reactive reducing agents, or more effective nitrogen precursors, in order to overcome these issues. For example, studies done by Juppo et al. have successfully employed trimethylaluminum (TMA) and 1,1-dimethylhydrazine as a reducing agent and a nitrogen source respectively, for the ALD process of TiN.^{54,55} TiCl_4 , NbCl_5 , and MoCl_5 are some of the metal halides that can be reduced easily using 1,1-dimethylhydrazine.⁵⁵

1.9 Zn precursors used in CVD/ALD processes

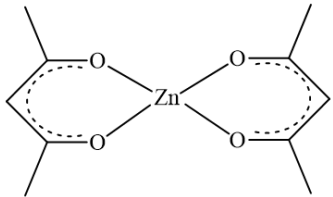
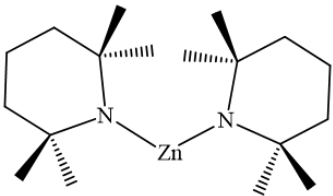
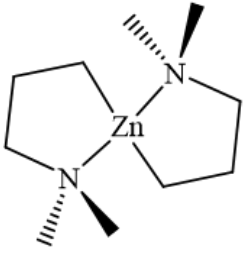
A wide range of zinc containing precursors have been developed for CVD and ALD processes of different materials. A detailed discussion on all available precursors is beyond the scope of this study. Hence, some of the extensively used precursors, their structures and properties are summarized in Table 1.2.

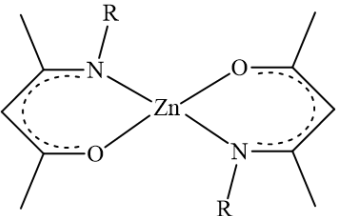
ZnEt_2 ,⁵⁶⁻⁶⁷ ZnMe_2 ,⁵⁷ $\text{MeZn}(\text{O}^i\text{Pr})$,^{68,69} and bis(dimethylaminopropyl) zinc ($[\text{Zn}(\text{DMP})_2]$)⁷⁰ have already been used in ALD processes as zinc precursors and indicate sufficient volatility to be employed as a zinc precursor for elemental Zn ALD process. However, zinc containing precursors; $\text{Zn}\{\text{N}(\text{SiMe}_3)_2\}_2$, $\text{MeZn}(\text{O}^i\text{Bu})$, zinc acetylacetonate ($\text{Zn}(\text{acac})_2$), bis(tetramethylpiperidino) zinc ($\text{Zn}(\text{TMP})_2$), and zinc bis(ketoiminates) have not been previously used in ALD processes. These zinc precursors indicate sufficient volatility and thermal stability, and might be viable (in combination with a suitable co-reactant) as zinc precursors for elemental zinc deposition by thermal ALD.

Table 1.2: Zinc containing precursors used in different CVD/ALD processes.

| Precursor | Structure | Volatility | CVD/ALD process | Remarks |
|-------------------|-----------|---|--|--|
| ZnEt ₂ | Et—Zn—Et | Volatile at 20 °C B.P. 117 °C Decomposes above 300 °C ⁷¹ | ALD of Cu ⁵⁶ ALD of ZnO ⁵⁷⁻⁶⁶ ALD of ZnS ⁶⁷ | Usually delivered between 5-25 °C ⁵⁶⁻⁶⁷ |
| ZnMe ₂ | Me—Zn—Me | Very volatile at 20 °C B.P. 46 °C Decomposes at 170 ⁷² | ALD of ZnO ⁵⁷ ALD of ZnS ⁷³ | Delivered between -25 to -8 °C ⁵⁷ |
| ZnCl ₂ | Cl—Zn—Cl | | ALD of ZnO ^{74,75} | Delivered between 390-400 °C ^{74,75} M.P. 293 °C |
| ZnI ₂ | I—Zn—I | | ALD of ZnO ⁷⁶ | Delivered at 240 °C ⁷⁶ Melting point: 446 °C |

| Precursor | Structure | Volatility | CVD/ALD process | Remarks |
|--|--|---|--|--|
| Zn(OAc) ₂ | $\begin{array}{c} \text{O} \quad \quad \quad \text{O} \\ \parallel \quad \quad \parallel \\ \text{CH}_3\text{CO} - \text{Zn} - \text{OCCH}_3 \end{array}$ | Decomposes above 250 °C ⁷⁷ | ALD of ZnO ^{57,78} ALD of ZnS ⁷⁹ ALD of ZnF ₂ ⁸⁰ | Delivered between 230-250 °C ^{57,78-80} TGA available ⁷⁷ M.P. 242 °C ⁷⁷ |
| MeZn(O ⁱ Pr) | Me — Zn — O ⁱ Pr | Sublimes at 65 °C/6 mTorr. Decomposes above 300 °C ⁸¹ | ALD of ZnO ⁶⁸ CVD of ZnO ⁶⁹ | Delivered between 70-80 °C ^{68,69} |
| MeZn(O ^t Bu) | Me — Zn — O ^t Bu | Sublimes above 80 °C/ 0.1 Torr ⁶⁹ Decomposes above 150 °C ⁶⁹ | CVD of ZnO ⁶⁹ | Delivered at 80 °C ⁶⁹ |
| Zn{N(SiMe ₃) ₂ } ₂ | $\begin{array}{c} \text{Me}_3\text{Si} \quad \quad \quad \text{SiMe}_3 \\ \diagdown \quad \quad \diagup \\ \text{N} - \text{Zn} - \text{N} \\ \diagup \quad \quad \diagdown \\ \text{Me}_3\text{Si} \quad \quad \quad \text{SiMe}_3 \end{array}$ | Melting point: 12.5 °C Decomposes above 200 °C ⁸² | CVD of ZnSe ⁸² | Delivered at 80 °C ⁸² TGA not available |

| Precursor | Structure | Volatility | CVD/ALD process | Remarks |
|--|---|--|--------------------------|---|
| Zn(C ₅ H ₇ O ₂) ₂ (Zn(acac) ₂) |  | Sublimes at 110 °C/0.1 Torr ⁸³ Decomposes below 200 °C ⁸⁴ | CVD of ZnO ⁸⁵ | Delivered at 60-85 °C ⁸⁵ TGA available ⁸⁴ Melting point: 126.5 °C ⁸⁴ |
| Zn(TMP) ₂ (TMP = tetramethylpiperidino) |  | Sublimes 75-80 °C/10 mTorr ⁸⁶ | CVD of ZnO ⁸⁶ | Delivered between 70-90 °C ⁸⁶ Melting point: 59 °C ⁸⁷ |
| [Zn(DMP) ₂] (DMP = dimethylaminopropyl) |  | Decompose above 150 ⁷⁰ | ALD of ZnO ⁷⁰ | Delivered at 55 °C ⁷⁰ TGA available ⁷⁰ Melting point: 45 °C ⁷⁰ |

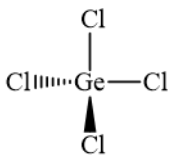
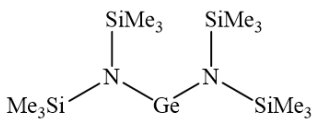
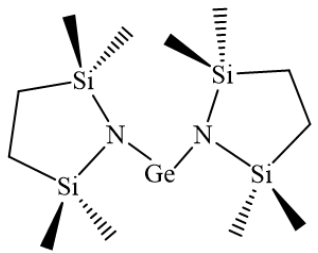
| Precursor | Structure | Volatility | CVD/ALD process | Remarks |
|-----------------------|---|--|--------------------------|---|
| Zincbis(ketoiminates) |  <p> 1: R = O(CH₂)₂CH₃ 2: R = O(CH₂)₃CH₃ </p> | Decomposition over 200 ⁸⁸ Vaporize at (1) 110 °C/5 mbar and (2) 115 °C /5 mbar ⁸⁸ | CVD of ZnO ⁸⁸ | Delivered at 120 °C ⁸⁸ TGA available ⁸⁸ Melting point: (1) 57 °C, (2) 60 °C ⁸⁸ |

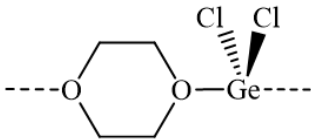
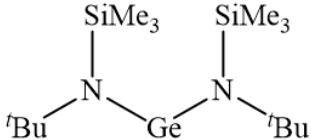
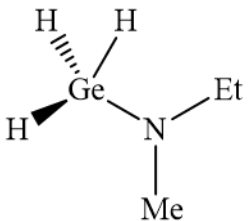
1.10 Ge precursors used in CVD/ALD processes

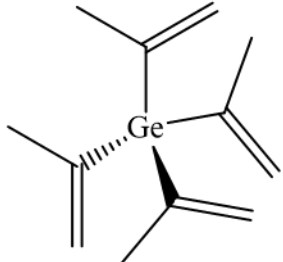
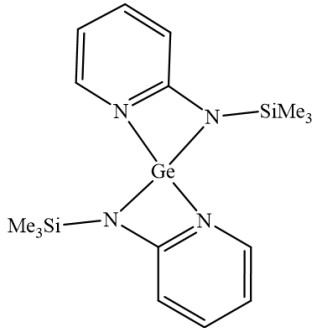
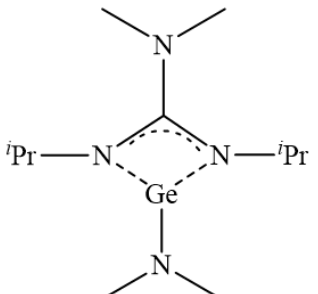
Table 1.3 illustrates the germanium containing precursors, that have been used for different CVD and ALD processes. Though, both CVD and ALD processes utilize tetravalent germanium precursors, Ge(II) precursors are considered as most suitable precursor molecules for low temperature CVD/ALD processes.⁸⁹ However, to date only a few Ge(II) precursors have been successfully used in CVD and ALD processes.⁸⁹

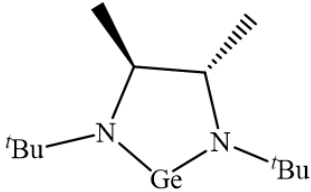
GeCl₂(Dioxane),^{90,91} Ge(guan)(NMe₂),⁹² and N-heterocyclic germanium(II) ([Ge(II)(κ²-(N^tBu)CH(CH₃)CH(CH₃)(N^tBu))])⁹³ complexes are some of the Ge(II) complexes that have been used in ALD. These complexes indicate adequate volatility and thermal stability for use as germanium precursors for ALD processes. Some Ge(II) complexes, that have only been used for CVD processes also demonstrate high volatility and thermal stability and would be potential candidates as germanium precursors for elemental Ge ALD processes. Examples include, Ge{N(SiMe₃)₂}₂, tetramethyl disilazacyclopentane germanium (Ge(TDA)₂), and Ge{N(^tBu)(SiMe₃)}₂.

Table 1.3: Germanium containing precursors used in different CVD/ALD processes.

| Precursor | Structure | Volatility | CVD/ALD process | Remarks |
|---|--|---|---|---|
| GeCl ₄ |  | B. P. 83 °C | CVD of Nb ₃ Ge ⁹⁴ | Delivered at 0 °C ⁹⁴ |
| Ge{N(SiMe ₃) ₂ } ₂ |  | B. P. 60 °C/ 0.4 Torr ⁹⁵ | CVD of Ge ⁹⁶ | Delivered at 80 °C ⁹⁶ TGA available ⁹⁶ M. P. 32-33 °C |
| Ge(TDA) ₂ TDA = Tetramethyl disilazacyclopentane |  | Yellow/orange liquid at RT ⁹⁷ Volatile above 150 °C ⁹⁷ | CVD of GST (Ge-Sb-Te) films ⁹⁷ | Delivered at 90-110 °C ⁹⁷ TGA available ⁹⁷ |

| Precursor | Structure | Volatility | CVD/ALD process | Remarks |
|--|--|---|--|--|
| GeCl ₂ (Dioxane) |  | | ALD of GST (Ge-Sb-Te) films ^{90,91} | Delivered at 70 °C ^{90,91} Melting point 176-178 °C ⁹⁸ |
| Ge{N(^t Bu)(SiMe ₃)} ₂ |  | Yellow/orange liquid at RT ⁹⁷ Melting point: 21-22 °C Volatile above 150 °C ⁹⁷ | CVD of GST (Ge-Sb-Te) films ⁹⁷ | Delivered at 90-110 ⁹⁷ TGA available ⁹⁷ |
| Ethylmethyamido- germane (EMAG) H ₃ GeN(CH ₃)(C ₂ H ₅) |  | | CVD of Ge ⁹⁹ | Delivered at 60 °C ⁹⁹ TGA available ⁹⁹ High thermal stability (up to 500 °C ⁹⁹) |

| Precursor | Structure | Volatility | CVD/ALD process | Remarks |
|---|---|--|--|--|
| $\text{Ge}(\text{C}_3\text{H}_5)_4$ |  | Decomposes around 243 °C ¹⁰⁰ Vapour pressure 1.45 Torr/50 °C ¹⁰⁰ | CVD of GST (Ge-Sb-Te) films ¹⁰⁰ | Delivered at 50 °C ¹⁰⁰ |
| Aminopyridinato Ge |  | Volatile above 140 °C ⁸⁹ | CVD of Ge ⁸⁹ | Delivered at 140 °C ⁸⁹ TGA available ⁸⁹ M. P. 106-108 °C ⁸⁹ |
| Ge(II)guanidinate $\text{Ge}(\text{guan})\text{NMe}_2$ |  | Thermally stable up to 180 °C ⁹² Vapour pressure 0.079 Torr/ 65 °C ⁹² | ALD of GeTe ⁹² | Delivered at 65 °C ⁹² DSC available ⁹² |

| Precursor | Structure | Volatility | CVD/ALD process | Remarks |
|--|---|--|-----------------------------|---|
| N-heterocyclic germylene [Ge(II)(κ^2 - (<i>N</i> 'Bu)CH(CH ₃)CH(CH ₃)(<i>N</i> 'Bu))] |  | Vapour pressure 0.71 Torr/40 °C ⁹³ Distilled at 60 °C/1 torr ⁹³ | ALD of GeS ⁹³ | Delivered at 40 °C ⁹³ TGA available ⁹³ |

1.11 Overview of pure elements deposited by ALD

Though many ALD processes exist for the deposition of many metal-containing materials (oxides, nitrides, sulphides, etc.) only a few pure elements have been deposited by ALD. Over the years different reaction chemistries have been developed for metal ALD processes by utilizing different co-reactants including air and O₃, H₂, amines and hydrazines and main group hydrides etc.¹⁰

ALD of pure elements are important in microelectronics due to their broad range of applications.²² Transition metal films are usually employed as contact plugs in ferroelectric and dynamic random access memories (FRAMs and DRAMs), dual-gate metal-oxide semiconductor field effect transistors (MOSFETs), diffusion barriers, and interconnects.⁴⁸

Investigation of the reaction mechanisms involved in ALD is challenging, as reaction by-products are mixed with large amounts of unreacted precursor in each deposition cycle.¹⁰¹ Usually in situ characterization methods (e.g., mass spectrometric, gas analysis, and quartz crystal microbalance measurement) in combination with several other characterization methods are used to probe the mechanisms involved in film deposition.¹⁰¹ Different reaction mechanisms have been proposed for the film deposition of main group elements via ALD processes.

Owing to the positive reduction potential of Cu²⁺ and the availability of suitable reducing agents, Cu deposition is among the most studied elemental deposition process by ALD with a variety of well developed precursors and co-reactants available for the deposition.^{20 101} Cu deposition using CuCl and H₂ was the first studied ALD Cu deposition process.¹⁰² It

was also the first studied ALD process that involves metal reduction using hydrogen molecules.¹⁰²

Another well developed metal ALD process involves tungsten.⁵² Smooth, highly pure tungsten films have been deposited using WF_6 and Si_2H_6 below 325 °C.¹⁰³ Among the first row transition metals, both Co and Ni have also been deposited by ALD, though it is a less active area of research compared to Cu ALD.²⁰

Table 1.4 summarises standard reduction potentials of the +2 ion of first row transition metals. Compared to Cu, Ni, and Co, other elements have highly negative reduction values. Hence, the reduction of these elements is difficult, and only a few successful ALD processes have been reported over the years.²⁰

Table 1.4: Standard reduction potentials of M^{2+} ions of first row transition metals.

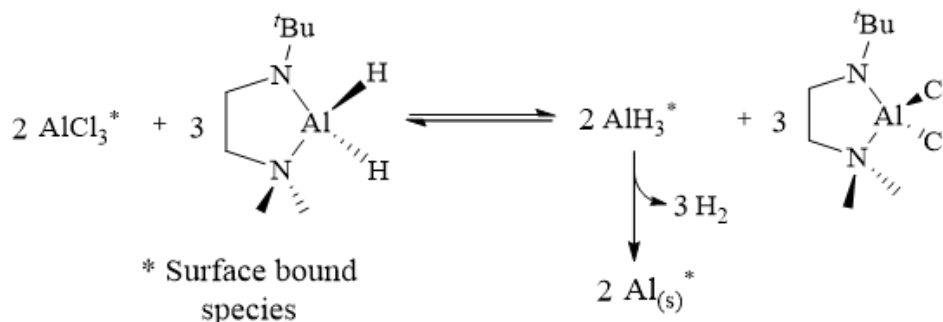
| $M^{2+} + 2e \rightarrow M^0$ | E^0 (V) |
|-------------------------------|-----------|
| Cu | 0.3419 |
| Ni | -0.257 |
| Co | -0.280 |
| Fe | -0.447 |
| Mn | -1.185 |
| Cr | -0.913 |
| V | -1.175 |
| Ti | -1.630 |

Only a handful of main group elements including Al, Si, C, Ge, and Sb have been deposited by ALD to date. ALD of group IV elements utilizing radical reactions (C, Si, and Ge) was first achieved in 1993 using halogenated radical precursors along with atomic hydrogen.¹⁰⁴ Carbon in the form of diamond has been deposited using gas phase radicals of CCl_3 with atomic hydrogen under high vacuum conditions (above substrate 0.1 Torr and background < 0.01 Torr).¹⁰⁴ A similar ALD process deposited diamond films on Mo substrates using CF_3 radicals with atomic hydrogen under high vacuum conditions.¹⁰⁵ These ALD processes make use of hydrogen abstraction processes to deposit the pure element.¹⁰⁴ For example, in carbon PEALD using CCl_3 radicals and atomic hydrogen, a surface hydrogen atom is abstracted by a CCl_3 radical, forming $CHCl_3$ and creating a vacant site on the surface. A

CCl_3 radical then immediately occupies the vacant site. This process continues until surface is completely covered with CCl_3 groups. This reaction is self terminating as the abstraction rate of a halogen is insignificant compared to abstraction of a hydrogen atom. In the process of reactivation of the surface, hydrogen atoms abstract chlorine atoms to form HCl, regenerating a monolayer of carbon.¹⁰⁴

Elemental Si has been deposited using various precursors by PEALD; for instance, SiCl_2H_2 with atomic hydrogen,¹⁰⁶ Si_2Cl_6 with Si_2H_6 ,¹⁰⁷ and Si_2Cl_6 with atomic hydrogen.¹⁰⁸ However, only few thermal ALD processes available for Si deposition. A thermal ALD process for Si film deposition was reported using SiCl_4 with Si_2H_6 . In this process, smooth films of Si were obtained on SiO_2 substrate at temperatures between 355 and 385 °C.¹⁰⁹ However, impractically long pulse times of 2-4 minutes were required.¹⁰⁹ SiCl_4 is pulsed into the chamber at 375 °C until the surface has become saturated. This is followed by an Si_2H_6 pulse. The reaction is assumed to proceed as follows: (1) HCl is formed from the reaction between a chlorine atom in SiCl_4 and a surface Si-H group, and (2) Si_2H_6 reacts with the resulting surface Si-Cl groups to release HCl.¹⁰⁹

Aluminum is the most electropositive element ($\text{Al}^{3+} \rightarrow \text{Al}^0$, $E^\circ = -1.676$) deposited by a thermal ALD process to date.¹¹⁰ Winter et al. in 2018 synthesized a highly volatile (mp: 31-32 °C; sublimation temperature: 40 °C/50 mTorr), thermally stable aluminum hydride complex, $\text{H}_2\text{Al}(\text{tBuNCH}_2\text{CH}_2\text{NMe}_2)$, which in combination with AlCl_3 was used to deposit aluminum films at around 140 °C by thermal ALD.¹¹⁰



Scheme 1.1: Proposed reaction between AlCl_3 and $[\text{H}_2\text{Al}(\text{tBuNCH}_2\text{CH}_2\text{NMe}_2)]$ leading to Al metal film deposition.¹¹⁰

The Scheme 1.1 illustrates the reaction pathway between AlCl_3 and $\text{H}_2\text{Al}(\text{tBuNCH}_2\text{CH}_2\text{NMe}_2)$ leading to the deposition of Al.¹¹⁰ First, AlCl_3 is introduced into the reaction chamber where it is chemisorbed on to the surface. Introduction of $\text{H}_2\text{Al}(\text{tBuNCH}_2\text{CH}_2\text{NMe}_2)$ produces surface bound AlH_3 species along with $\text{Cl}_2\text{Al}(\text{tBuNCH}_2\text{CH}_2\text{NMe}_2)$ from the hydride-halide ligand exchange between two reactants. This highly unstable surface bound AlH_3 would then decompose to Al and H_2 gas.¹¹⁰ The process produces high quality Al films with a purity higher than 94% at 100 °C.¹¹⁰ The authors used Si, SiO_2 , Pt, Cu, and TiN substrates, and although Al deposition was observed on all substrates, bright silver-coloured films were only observed on Cu and TiN substrates.¹¹⁰ The strongly reducing nature of $\text{H}_2\text{Al}(\text{tBuNCH}_2\text{CH}_2\text{NMe}_2)$ could potentially be used to deposit other metals that have more positive redox potentials compared to Al^{3+} .¹¹⁰

1.11.1 Zinc

Alkyl zinc precursors have been widely used for CVD of metallic zinc. However, they tend to incorporate high amounts of carbon impurities into the growing film, which can be decreased to some degree by using hydrogen as a carrier gas.¹¹¹ Dimethyl zinc decomposes in the vapor phase to produce zinc metal at 270-370 °C. The resulting films were found to contain carbon impurities, and the major volatile by-product was methane, along with minor amounts of ethane, ethylene, propane, and propene.¹¹¹ Diethylzinc is a more frequently used zinc CVD precursor as it tends to give purer films compared to dimethylzinc.¹¹² Diethylzinc is decomposed in the vapor phase at 175-225 °C, affording zinc films. These films contain fewer carbon impurities, and the major volatile by-products were ethane and n-butane.¹¹¹

Allyl compounds of zinc such as bis(allyl)zinc ((C₃H₅)₂Zn) and bis(2-methylallyl)zinc ((C₄H₇)₂Zn) have also been used as Zn precursors in CVD processes.¹¹¹ Allyl compounds react with hydrogen and form propene, and also generate hexadiene by reductive elimination at relatively low temperatures, so they are particularly well suited to form clean metallic zinc films.¹¹¹ Both (C₃H₅)₂Zn and (C₄H₇)₂Zn produce pure metallic Zn films at temperatures as low as 150 °C.¹¹¹ Analysis of gaseous by products revealed over 75% of 1,5-hexadiene for the (C₃H₅)₂Zn process, and 2,5-dimethyl-1,5-hexadiene for the (C₄H₇)₂Zn process.¹¹¹ Though there are numerous zinc precursors available for the deposition of pure Zn by CVD, no thermal ALD processes are available for the deposition of Zn metal.

1.11.2 Germanium

Use of Ge in electronic devices dates back to 1947, when the first transistor was created using Ge bulk crystals.¹¹³ Ge possesses some highly advantageous properties for electronic devices, such as a carrier mobility which is the highest among all common semiconductor materials.¹¹⁴ However, Si replaced Ge in early electronic devices, as Si was more available, lower cost, and easier to grow and process.¹¹⁴ However, owing to its high carrier mobility, demand for Ge in microelectronic devices is rapidly increasing. With device minimization in effect, Si devices rapidly reach their limits, since down scaling of devices requires reduced transistor dimensions, in which speed of transistors are dominated by the injection velocity of carriers, which is directly proportional to mobility of the material.¹¹⁴ Furthermore, the high and near symmetrical carrier mobilities of Ge have made it one of the most intensively studied channel materials for MOSFET devices, and one of the most promising materials for high transport channel devices.^{114 115} Moreover, Ge thin films are also considered as a promising replacement for Si in complementary metal-oxide semiconductor (CMOS) devices.

Many vapor phase methods including CVD and PEALD have been developed to deposit Ge thin films for different applications.¹¹⁴ Though it is expensive, highly toxic, and difficult to obtain with high purity, GeH₄ is the most used precursor for Ge deposition. Other precursors including Ge₂H₆, GeCl₄ and some organometallic complexes of Ge such as trimethyl germane, tetraethyl germane and diethyl germane have also been effectively employed for high temperature Ge deposition by various deposition methods.¹¹⁴

GeH₄ rapidly decomposes at relatively low temperatures to deposit Ge, and has been used in CVD to produce Ge thin films at around 300 °C.¹¹⁶ However, GeH₄ is not suitable for high temperature applications as it readily decomposes in the gas phase at high temperatures.¹¹⁴ GeCl₄ is the commonly used Ge precursor in high temperature applications. GeCl₄ with H₂ gas have been used to obtain high quality Ge films at 565 °C by CVD.¹¹⁷ In this process a surface adsorbed GeCl₂ molecule that derives directly from GeCl₄ reacts with surface adsorbed hydrogen atoms to produce elemental Ge.¹¹⁷

Iso-butylgermane is the first CVD organogermanium precursor which was used to grow high purity Ge films at 500 °C.¹¹⁸ Another organogermanium precursor used in elemental Ge CVD is Ge(N(SiMe₃)₂)₂, where high purity Ge thin films were deposited on Si substrates at 325 °C.⁹⁶ Analysis of the volatile products of this reaction revealed large amounts of Me₆Si₂ along with minor amounts of Me₃SiNH₂, (Me₃Si)₂NH, and Me₃SiH.⁹⁶

The only ALD process for Ge employs dimethylgermane (GeMe₂H₂) in an atomic hydrogen assisted process at 480 °C (atomic hydrogen was generated using a tungsten filament heated to 1700 °C).¹¹⁹ To date there are no known thermal ALD processes (those which do not involve radicals) available for the deposition of Ge thin films.

1.11.3 Thesis objective

The current study focuses on investigation and development of precursor molecules to obtain germanium and zinc films by thermal ALD. Neither of these elements have been deposited by a thermal ALD process. This work is focused on ligand-exchange reactions with co-reactants to produce unstable zinc or germanium hydride species, which will then reductively eliminate to produce the pure element. We investigated the reactivity of three zinc precursors and three germanium precursors. Zinc precursors used in the study include; $\text{MeZn}(\text{O}^i\text{Pr})$, $\text{Zn}(\text{O}^i\text{Pr})_2$, and ZnEt_2 , (Figure 1.12).

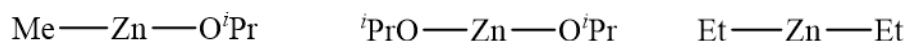


Figure 1.12: Zinc precursors. From left to right: $\text{MeZn}(\text{O}^i\text{Pr})$, $\text{Zn}(\text{O}^i\text{Pr})_2$, and ZnEt_2 .

Germanium precursors used in the study include; $\text{GeCl}_2(\text{Dioxane})$, $\text{Ge}\{\text{N}(\text{SiMe}_3)_2\}_2$ and $\text{Ge}(\text{OCH}_2\text{CH}_2\text{NMe}_2)_2$ (Figure 1.13).

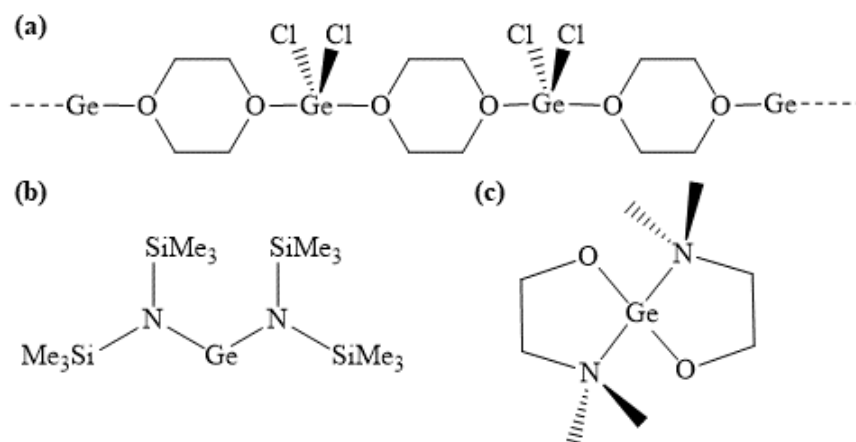


Figure 1.13: Germanium precursors a) $\text{GeCl}_2(\text{Dioxane})$, b) $\text{Ge}\{\text{N}(\text{SiMe}_3)_2\}_2$, and c) $\text{Ge}(\text{OCH}_2\text{CH}_2\text{NMe}_2)_2$.

Several co-reactants with different reducing capacities were employed in this work, such as 4,4,5,5-tetramethyl-1,3,2-dioxaborolane (HBpin), PhSiH₃, [H₂Al(^tBuNCH₂CH₂NMe₂)] (LAlH₂)¹¹⁰, BH₃(NMe₃), and AlH₃(Quinuclidine)¹²⁰ (Figure 1.14).

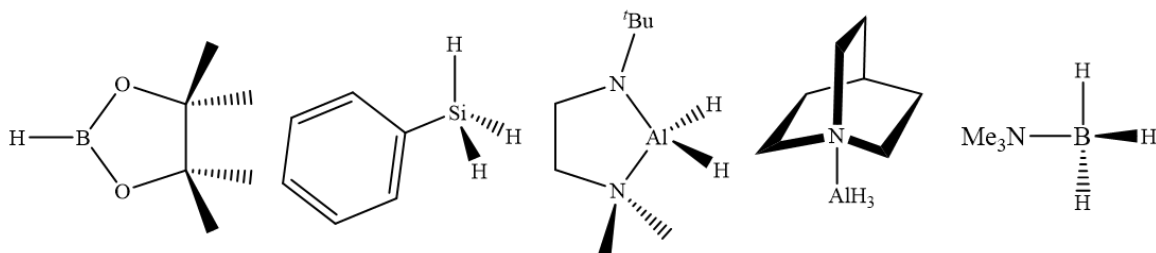


Figure 1.14: Co-reactants employed. From left to right: HBpin, PhSiH₃, [H₂Al(^tBuNCH₂CH₂NMe₂)]¹¹⁰, AlH₃(Quinuclidine), BH₃(NMe₃).

Solution reactivity studies between the precursors and co-reactants were used to evaluate the reactivity of potential precursors. The thermal stability and volatility of potential precursors were also studied, to investigate their suitability for ALD.

CHAPTER 2 – SOLUTION REACTIVITY STUDIES OF ZINC (Zn)

PRECURSORS

2.1 Selection of Precursors - Stability and Volatility

The goal of this research is to investigate potential precursors/co-reactant pairs to obtain elemental zinc films by thermal ALD. This investigation requires careful selection of appropriate precursors in order to maximize the possibility of producing elemental zinc with the co-reactants employed in the study. Elemental ALD processes are less common compared to other ALD processes, due to limited availability of appropriate co-reactants and ideal precursors to react with these co-reactants.¹²¹

Two homoleptic zinc precursors of the form $[Zn^{II}L_2]$ where, L is either isopropoxide ($OCH(CH_3)_2$) or Ethyl (CH_2CH_3), and one alkylzinc alkoxide of the form of $[RZn^{II}L]$ where, R is methyl (CH_3), and L is isopropoxide ($OCH(CH_3)_2$) were investigated as zinc precursors in the current study.

$MeZnO^iPr$ is a white crystalline solid, which stays as a tetramer of the form of $[MeZnO^iPr]_4$ (heterocubane) in solid state with a central Zn_4O_4 framework (Figure 2.1).⁸¹ It has a sublimation temperature of 65 °C/ 6 mTorr and thermally decomposes above 300 °C into ZnO under inert atmosphere.⁸¹ $MeZnO^iPr$ is a promising ALD precursor as it can be delivered to the reactor at relatively low temperatures and is easily accessible even on multigram scale.⁸¹ It has been used as the zinc precursor for ZnO deposition in several CVD and ALD processes.^{81,69,68}

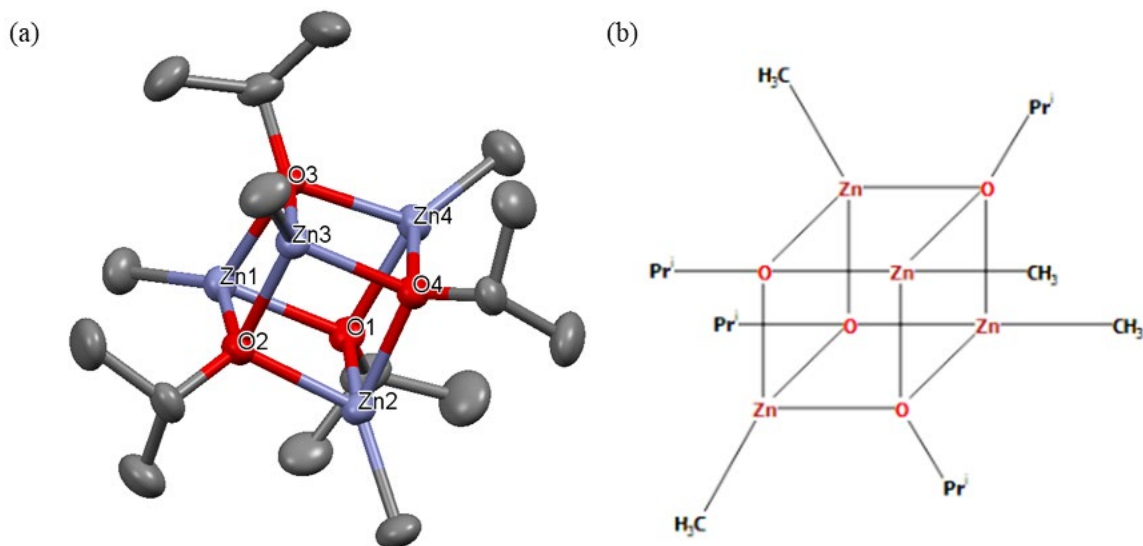


Figure 2.1: The heterocubane structure of MeZnO^iPr , a) X-ray crystal structure; Space group: $P\bar{1}(2)$, Cell: $a = 7.838 \text{ \AA}$, $b = 9.468 \text{ \AA}$, $c = 17.870 \text{ \AA}$, $\alpha = 77.457^\circ$, $\beta = 77.806^\circ$, $\gamma = 73.211^\circ$ b) Chemical diagram.⁸¹

$\text{Zn}(\text{O}^i\text{Pr})_2$ is a moisture sensitive, polymeric white solid which is insoluble in common organic solvents.¹²² It decomposes before it reaches its melting point.¹²² Thermogravimetric analysis (TGA) of $\text{Zn}(\text{O}^i\text{Pr})_2$ indicates that it decomposes in two different steps and ZnO is produced as a result of decomposition.¹²³ $\text{Zn}(\text{O}^i\text{Pr})_2$ sublimes at $80 \text{ }^\circ\text{C}/ 6 \text{ mTorr}$ and it is reported to decompose above $300 \text{ }^\circ\text{C}$.¹²²

Diethylzinc (ZnEt_2) is a highly pyrophoric, colourless liquid with a boiling point of $117 \text{ }^\circ\text{C}$. Owing to its high vapor pressure and reactivity with many reagents, ZnEt_2 is a more frequently utilized precursor in many CVD and ALD processes.¹²⁴ ZnEt_2 is the most widely used precursor for ALD deposition of ZnO .¹²⁵ Several processes have been developed to use ZnEt_2 with H_2O ⁶² and ZnEt_2 with O_2 ⁶⁶ for the deposition of ZnO films. Other than for

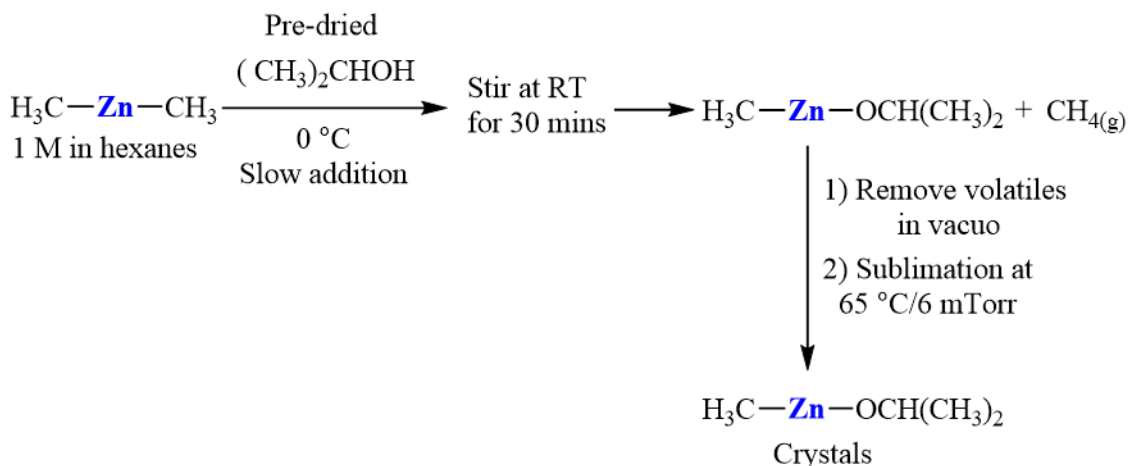
the deposition of ZnO, ZnEt₂ has also been used as a precursor in the deposition of ZnS films by ALD.^{124 126} In addition to its function as a zinc precursor in ALD processes for zinc containing compounds, studies have been conducted using ZnEt₂ as a co-reactant, mostly for elemental copper ALD.⁵⁶ ZnEt₂ is an inexpensive, thermally stable, volatile liquid which can be readily delivered to the ALD reactor at room temperature, hence making it a promising precursor candidate.

Table 2.1: Summary of volatility and thermal stability of Zn precursors.

| Precursor | Sublimation T or Boiling point | Decomposition T |
|------------------------------------|--------------------------------|-----------------------------|
| MeZnO ⁱ Pr | 65 °C/ 6 mTorr | Above 300 °C ⁸¹ |
| Zn(O ⁱ Pr) ₂ | 80 °C/ 6 mTorr | Above 300 °C ¹²² |
| ZnEt ₂ | Boiling point 117 °C | Above 300 °C ⁷¹ |

2.2 Precursor synthesis

From the three zinc precursors that were employed for this study, only MeZnOⁱPr was synthesized in the lab. The other two zinc precursors; Zn(OⁱPr)₂ and ZnEt₂ are commercially available. It has been established in literature, that reactions of R₂Zn compounds with alcohols (R¹OH) only give rise to alkylzinc alkoxides of the type of RZn(OR¹), without displacing the second alkyl group on the zinc, even in the presence of excess alcohol in the reaction mixture.^{69,127} Using a slightly modified literature procedure, which had previously used in the Emslie lab, MeZnOⁱPr can be prepared as a white solid with a yield of 90% (Scheme 2.1).⁶⁹



Scheme 2.1: Reaction scheme for the synthesis of MeZnOⁱPr.

The synthesis of MeZnOⁱPr involves reaction of Dimethylzinc (1.00 M solution in hexanes) with pre-dried isopropanol. Isopropanol is added dropwise to a dimethylzinc solution at 0 °C which then slowly allowed to reach to room temperature. In order to isolate the crude product of MeZnOⁱPr, residual volatiles were removed in vacuo. The crude product was

sublimed at 65 °C/ 6 mTorr to obtain the white crystalline solid of MeZnOⁱPr. The proton NMR spectrum of the sublimed MeZnOⁱPr was collected (Figure 2.2) which produced matching data with published values in literature.¹²⁸ In the ¹H NMR spectrum, the methyl group on zinc produces a singlet at -0.23 ppm and a doublet at 1.19 ppm was observed for the two methyl groups on isopropoxide group. A septet at 3.96 ppm corresponds to the proton on the isopropoxide group.

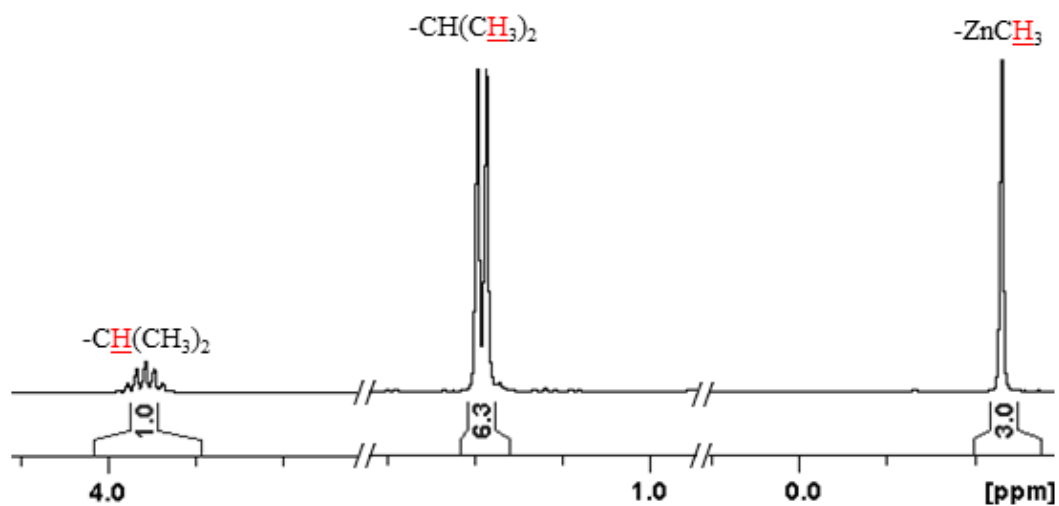


Figure 2.2: ¹H NMR spectrum of MeZnOⁱPr (Sublimed 65 °C/ 6 mTorr) in d₆-benzene.

Thermal stress testing of MeZnOⁱPr was done to evaluate its thermal stability. A solid sample of MeZnOⁱPr was heated at 100 °C and 140 °C for 24 hours under an argon flow. Comparison of proton NMR spectra collected for sublimed MeZnOⁱPr (Figure 2.3 a) and MeZnOⁱPr heated at 100 °C (Figure 2.3 b) and 140 °C (Figure 2.3 c) indicates no decomposition up to 140 °C.

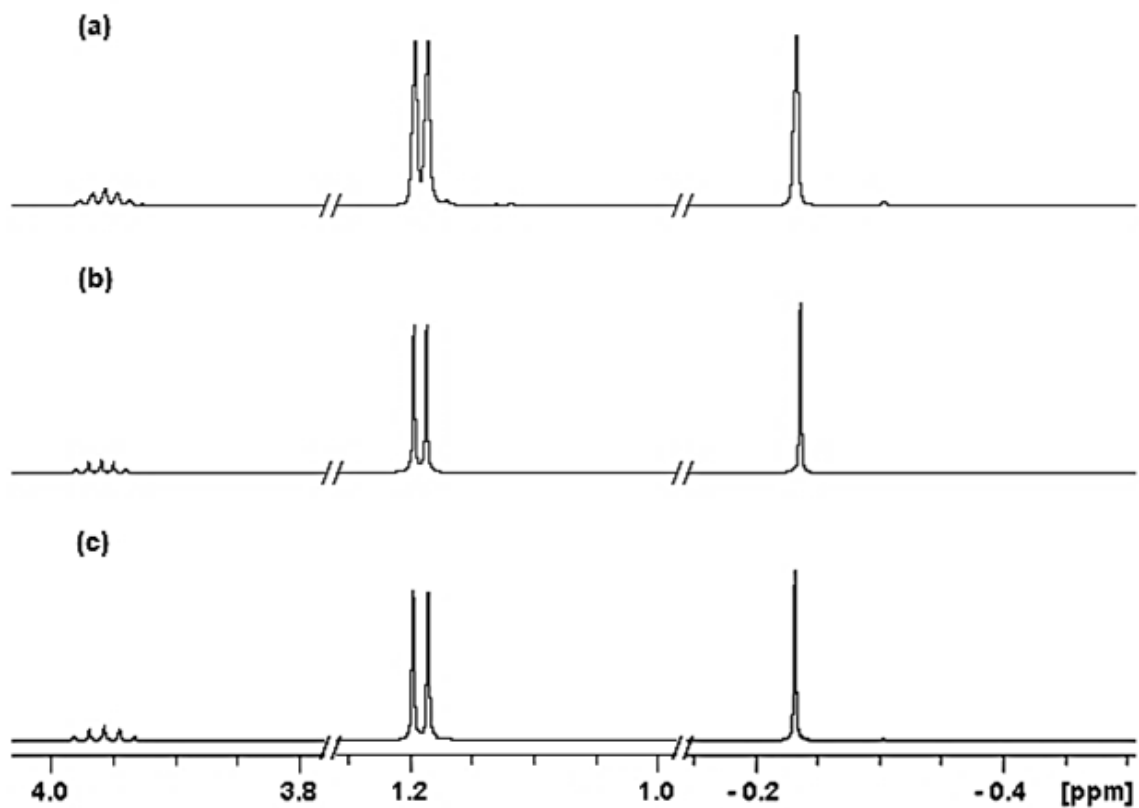
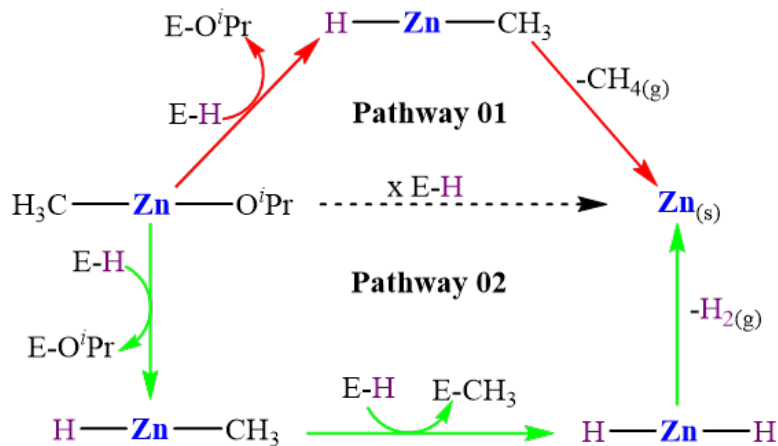


Figure 2.3: ^1H NMR spectra of, a) sublimed MeZnO^iPr , b) MeZnO^iPr heated at 100 °C /24 h, and c) MeZnO^iPr heated at 140 °C/24 h in d_6 -benzene.

2.3 Solution reactivity studies

Solution screening reactions were carried out as preliminary studies to investigate reactivity in solution between potential ALD precursors and co-reactants. Results of the solution reactivity studies can be used to identify particularly promising precursor/co-reactant combinations for zinc metal deposition by ALD. Furthermore, solution reactivity studies also provide insight into reaction mechanisms and by-products formed in the reactions. Solutions of the reactants were mixed together at room temperature and were then maintained at several different temperatures from 20 to 80 °C for 24 hours at each temperature, as a method of examining reactivity at elevated temperatures. Several different stoichiometries between reagents were employed to study the product distribution. Some reactions indicated no change regardless of the stoichiometric ratios between reagents. Hence, only reactions that indicated a difference based on the stoichiometric ratios have been described in detail. All solution reactions were carried out on an NMR scale, where each reagent was mixed on a scale of a few milligrams (10-25 mg). NMR spectra were collected to study the reaction pathways and to identify the soluble by-products formed in the reactions. Any precipitate or other by-products formed in the reactions were isolated and characterized where applicable. Powder X-ray diffraction (PXRD) was used as the main method to characterize precipitates formed in reactions.

2.3.1 Solution reactivity studies of MeZnOⁱPr

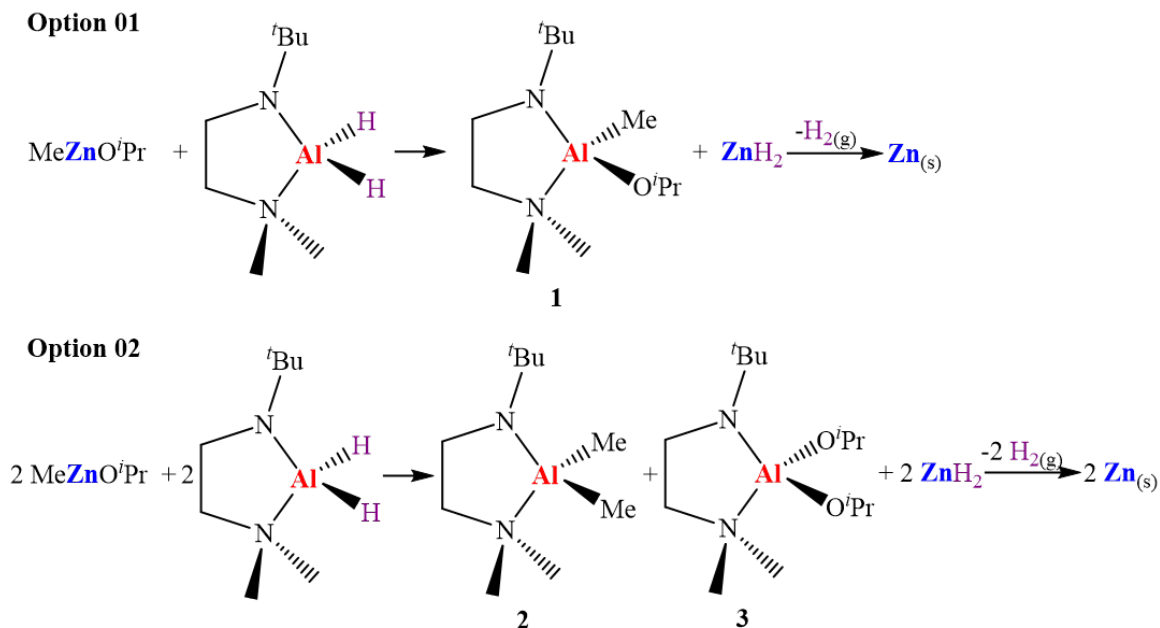


Scheme 2.2: General reaction pathways expected for reactions of MeZnOⁱPr with hydride reagents to produce elemental zinc. E = Bpin, LAIH (L = ^tBuNCH₂CH₂NMe₂), AlH₂(Quinuclidine), BH₂(NMe₃), or PhSiH₂.

The general reaction pathways anticipated for solution reactions between MeZnOⁱPr and hydride co-reagents are shown in Scheme 2.2. The isopropoxide group on MeZnOⁱPr is expected to be more reactive compared to the methyl group. Hence, both pathways start with a ligand exchange reaction between the co-reactant and the isopropoxide group on MeZnOⁱPr to produce HZnCH₃ as the first intermediate. In the first reaction pathway, HZnCH₃ then reductively eliminates CH₄ gas as a by-product to produce elemental zinc. The second reaction pathway predicts that once HZnCH₃ is produced, it will react with another co-reactant molecule to produce ZnH₂, a pyrophoric, unstable zinc hydride which slowly decomposes at room temperature to elemental zinc and H₂ gas.¹²⁹ Hence, according to the predicted reaction pathways, all reactions that show a reactivity must either produce

CH₄ gas which is detected by a peak at 0.16 ppm in d₆-benzene or H₂ gas with a peak at 4.47 ppm in d₆-benzene in the proton NMR spectrum of the respective reaction.

2.3.1.1 Reaction of MeZnOⁱPr with LAIH₂



Scheme 2.3: Possible 1:1 reactions between MeZnOⁱPr and LAIH₂ (assuming pathway 2 in the Scheme 2.2).

Solutions of MeZnOⁱPr and LAIH₂ in d₆-benzene were mixed together in a 1:1 ratio at room temperature. Vigorous formation of a white cloudy suspension and release of a gas were immediately observed after mixing the reagents. The white suspension gradually started to turn in to a grey precipitate within 3-4 hours, and had completely turned in to a grey precipitate after leaving the reaction solution overnight at room temperature. Winter et al, in their studies of the reactivity of LAIH₂ with AlCl₃ observed that both hydride groups on LAIH₂ get exchanged with chloride groups to produce LAICl₂.¹¹⁰ Hence, similar reactivity

was anticipated for the reaction of MeZnO^iPr with LiAlH_2 as shown in Scheme 2.3 Option 01, forming $\text{LiAlMe(O}^i\text{Pr)}$ as the major by-product of the reaction.

In the presence of equimolar amounts of MeZnO^iPr and LiAlH_2 in the reaction mixture, it is also possible to produce by-products 2 and 3 as shown in Scheme 2.3 option 02. Production of these by-products will still lead to the formation of unstable ZnH_2 , but identifying individual by-products by NMR spectroscopy will be more difficult.

Figure 2.4 shows NMR spectra for (a) LiAlH_2 , (b) Sublimed MeZnO^iPr , and (c) The 1:1 reaction between MeZnO^iPr and LiAlH_2 in d_6 -benzene at room temperature after 24 hours. Spectrum c shows that the reaction is complete after 24 hours, as unreacted MeZnO^iPr or LiAlH_2 is not present in the reaction mixture (Figure 2.4).

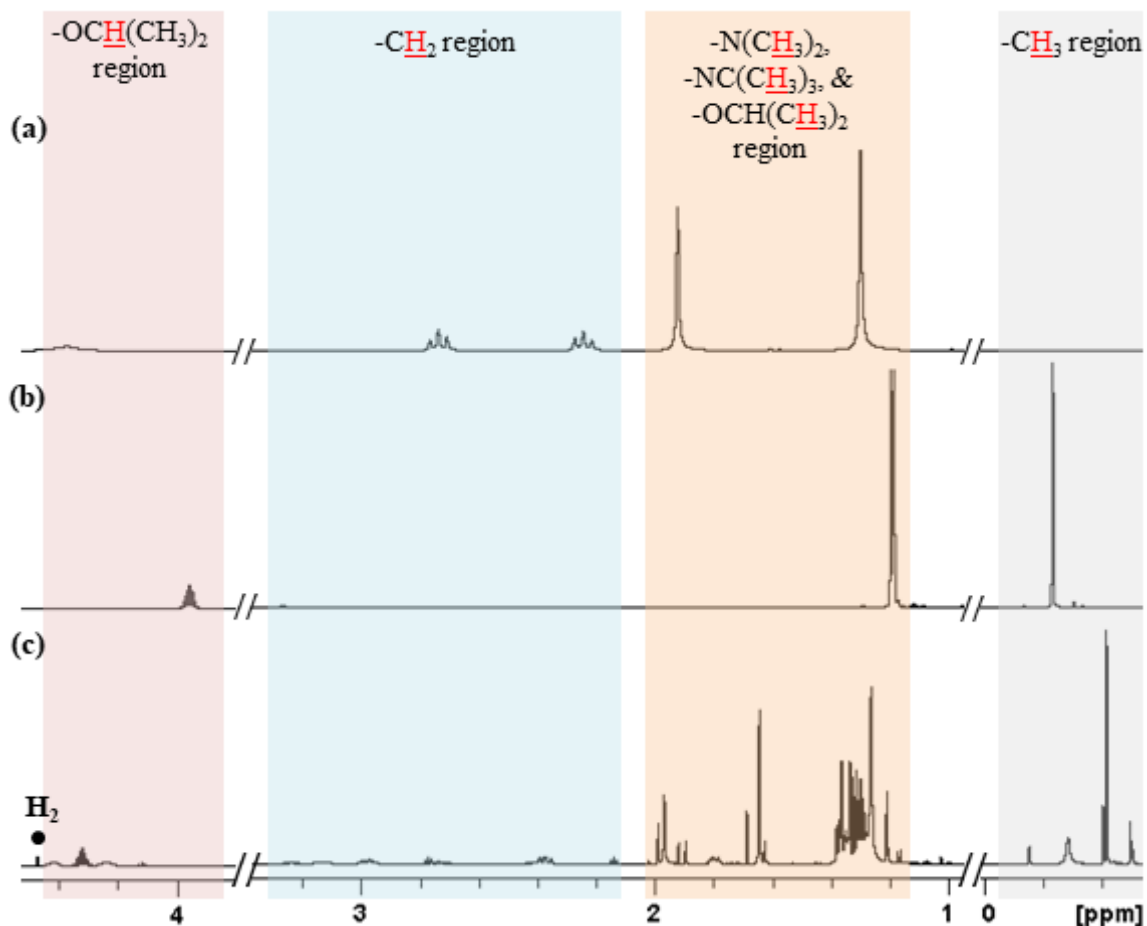


Figure 2.4: ^1H NMR spectra of (a) LAIH_2 , (b) Sublimed MeZnO^iPr , (c) 1:1 reaction mixture of MeZnO^iPr with LAIH_2 in d_6 -benzene collected at room temperature after 24 hours. H_2 is labelled with a circle.

The anticipated major by-product 01 (by-product 01 in Scheme 2.3) was not distinguishable from the proton NMR spectrum (Figure 2.4 c), due to the formation of multiple by-products. The spectrum reveals formation of hydrogen ($\delta = 4.47$ ppm in d_6 -benzene; indicated in Figure 2.4 with a circle), consistent with the formation of ZnH_2 (Scheme 2.2 reaction pathway 02) which reductively eliminates hydrogen gas to produce elemental zinc.

Apart from the hydrogen peak, identification of other peaks was challenging due to complexity of the spectrum. Comparison of NMR spectra collected after heating the reaction mixture at different temperatures up to 80 °C, did not reveal any significant difference. Another reaction between MeZnO^iPr and LiAlH_2 was attempted with 2 equivalents of LiAlH_2 to see if the reaction would produce a clean NMR spectrum. However, the proton NMR spectrum collected indicated multiple by-product formation and was similar to the proton NMR spectrum of the 1:1 reaction of MeZnO^iPr and LiAlH_2 . Since the proton NMR spectra from both reactions reveal a mixture of products, further studies were not carried out to isolate or to identify by-products of the reaction.

The grey precipitate produced in the reaction was separated by centrifugation and rinsed with toluene followed by hexanes to remove any soluble by-products. A powder X-ray diffractogram (PXRD) of the precipitate was collected (Figure 2.5) and aligned well with the diffraction pattern of hexagonal zinc.

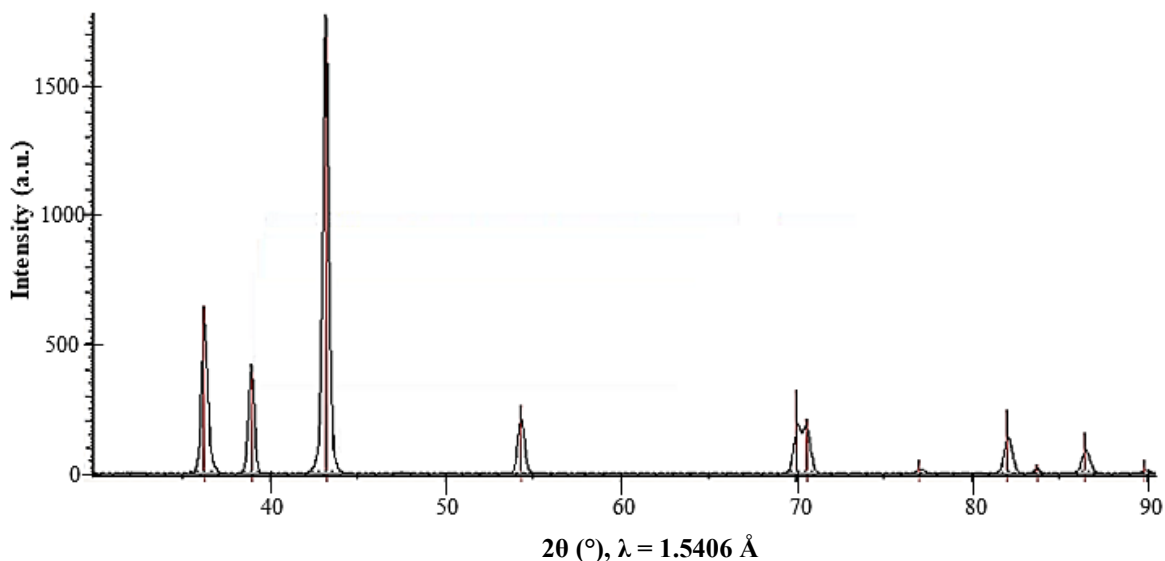
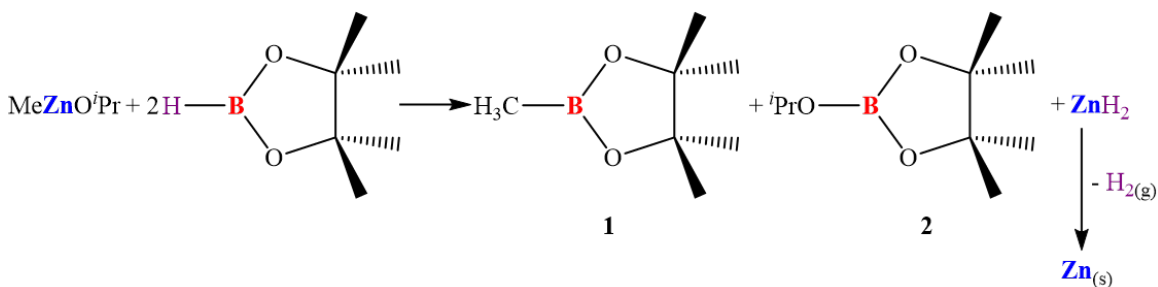


Figure 2.5: Powder X-ray diffractogram (PXRD) of the grey precipitate collected from the 1:1 reaction mixture of MeZnO^iPr with LAH_2 in d_6 -benzene, 24 h, RT. Red lines indicate the diffraction pattern corresponding to hexagonal zinc.

2.3.1.2 Reaction of MeZnO^iPr with HBpin



Scheme 2.4: Expected by-products from the 1:2 reaction of MeZnO^iPr with HBpin (assuming pathway 2 in the Scheme 2.2).

The reaction between MeZnO^iPr and HBpin is expected to produce MeBpin (Product 01) and $(^i\text{PrO})\text{Bpin}$ (Product 02) as indicated in Scheme 2.4. Given the reactivity of the

isopropoxide group, (*i*PrO)Bpin (Product 02) was expected to form at first, followed by formation of MeBpin (Product 01). In order to investigate the reactivity in solution, two equivalents of HBpin reagent were added to a one equivalent of MeZnO*i*Pr solution in d_6 -benzene at room temperature. A white cloudy suspension started to form soon after mixing the reagents at room temperature and remained unchanged after 12 hours. The reaction took about 24 hours to complete at room temperature, at which point the white suspension had turned in to a grey precipitate.

The proton NMR spectrum of the 1:2 reaction of MeZnO*i*Pr with HBpin in d_6 -benzene collected 24 hours after mixing reagents at room temperature was used to identify reaction by-products (Figure 2.6). The spectrum reveals formation of a 1:1 mixture of MeBpin (Figure 2.6 Triangles) and (*i*PrO)Bpin (Figure 2.6 Squares) as predicted. The peak corresponding to hydrogen gas is overlapped with the septet of methine proton in the isopropyl group of (*i*PrO)Bpin hence, a small hump is observed on the middle peak of the septet ((Figure 2.6: Enlarged region; Labelled with a circle). A little amount of excess HBpin remained after the reaction, and is indicated with an asterisk (Figure 2.6). Further characterization of (*i*PrO)Bpin and MeBpin is discussed in section 2.4.

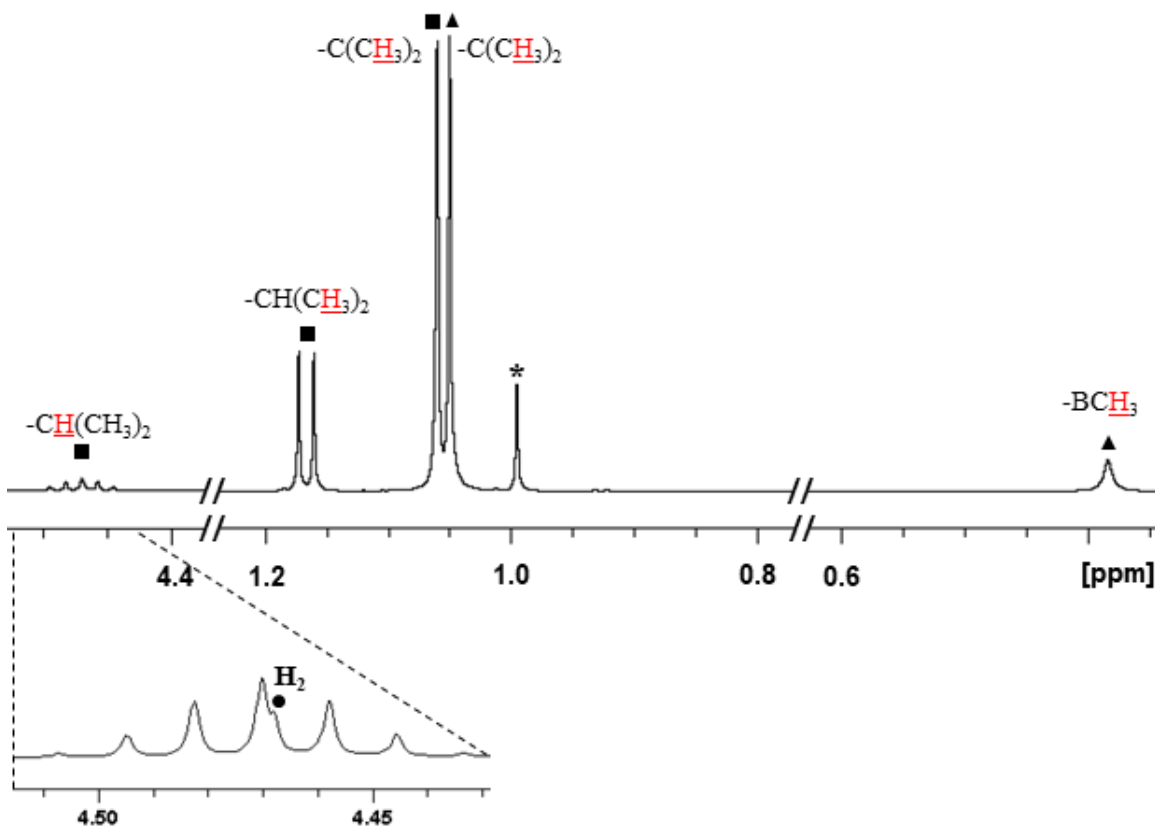


Figure 2.6: The proton NMR spectrum of the 1:2 reaction of MeZnO^iPr with HBpin in d_6 -benzene collected after 24 hours of mixing the reagents at room temperature. Squares indicate peaks related to $(^i\text{PrO})\text{Bpin}$ and triangles indicate peaks related to MeBpin . Excess HBpin is marked with an asterisk.

Exciting information on the reactivity of Me group and O^iPr group was able to be obtained from the 1:1 reaction between MeZnO^iPr and HBpin in d_6 -benzene. The proton NMR spectra collected for the 1:1 reaction of MeZnO^iPr with HBpin at RT in d_6 -benzene, after heating at 40 °C, 60 °C, and 80 °C are shown in Figure 2.7.

As evident from the proton NMR spectra collected, soon after mixing reagents at room temperature $(^i\text{PrO})\text{Bpin}$ starts to form (Labelled with squares) with only a little amount of

MeBpin. Formation of (*i*PrO)Bpin gives rise to the formation of MeZnH as the intermediate, which was assumed to produce ZnMe₂ and ZnH₂. The singlet at -0.67 ppm might be from ZnMe₂ as it is closer to the chemical shift (-0.62 ppm) reported for ZnMe₂ in d₅-chlorobenzene.¹³⁰ The reaction did not go to completion as not enough HBpin was available to replace both the Me and O^{*i*}Pr groups on Zn. Heating the reaction solution from 40-80 °C indicated that with increasing temperature, the amount of MeBpin (Labelled with triangles) increases. This is evident by the increase in peak height of the methyl singlet (CH₃-B) at 0.4 ppm and peak height of the singlet of four methyl groups on Bpin at 1.05 ppm. It seems that Me and O^{*i*}Pr groups exchange between ZnMe₂ and (*i*PrO)Bpin to reproduce MeZnO^{*i*}Pr with MeBpin under conditions where no more HBpin is available to react with ZnMe₂. This is evident from the increase of peaks intensities corresponding to MeZnO^{*i*}Pr.

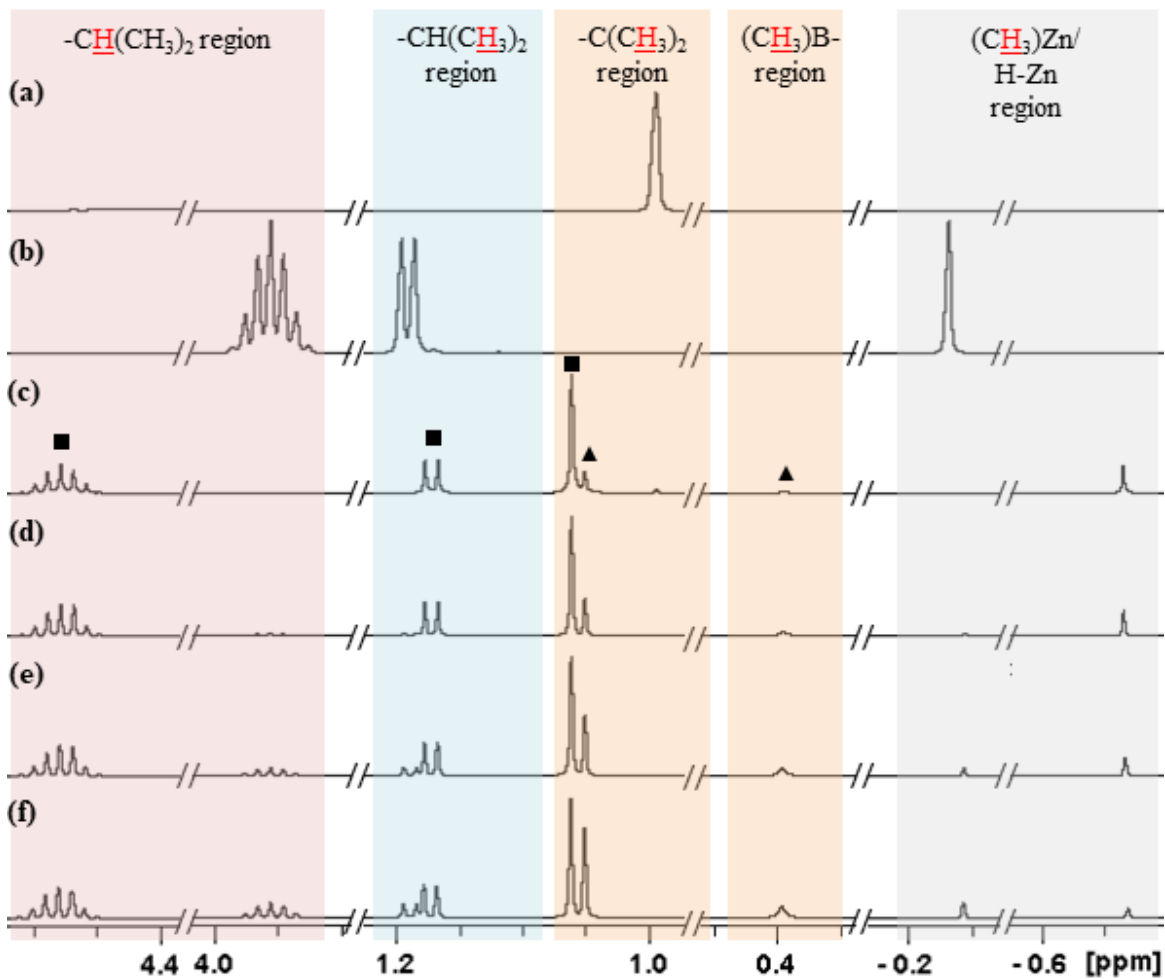


Figure 2.7: The proton NMR spectra of a) HBpin, b) Sublimed MeZnOⁱPr, and the 1:1 reaction of MeZnOⁱPr with HBpin after c) 24 h at RT, d) 24 h at 40 °C, e) 24 h at 60 °C and f) 24 h at 80 °C. Solvent; d₆-benzene. Squares indicate (iPrO)Bpin and triangles indicate MeBpin.

In order to collect the grey precipitate formed in the 1:2 reaction, reaction by-products and solvents were removed by centrifugation and the precipitate was washed with toluene and then with hexanes. A powder X-ray diffractogram of the precipitate is shown in Figure 2.8, which confirms the formation of elemental zinc during the reaction.

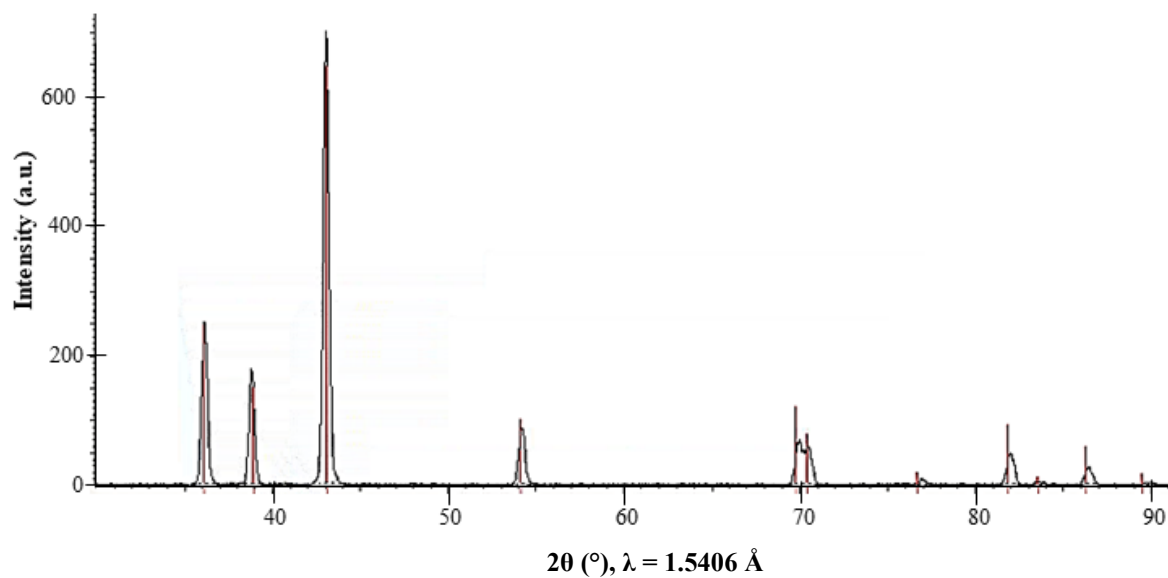
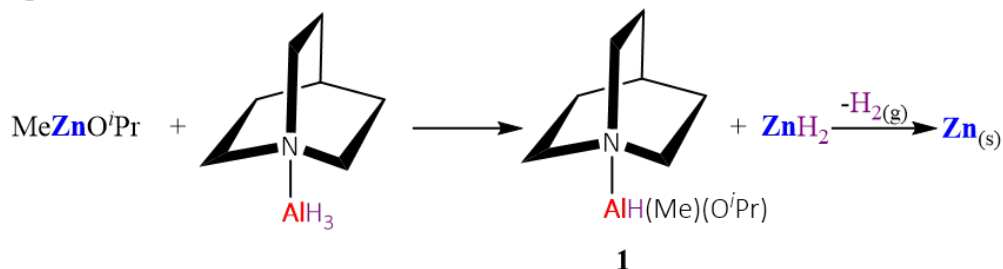


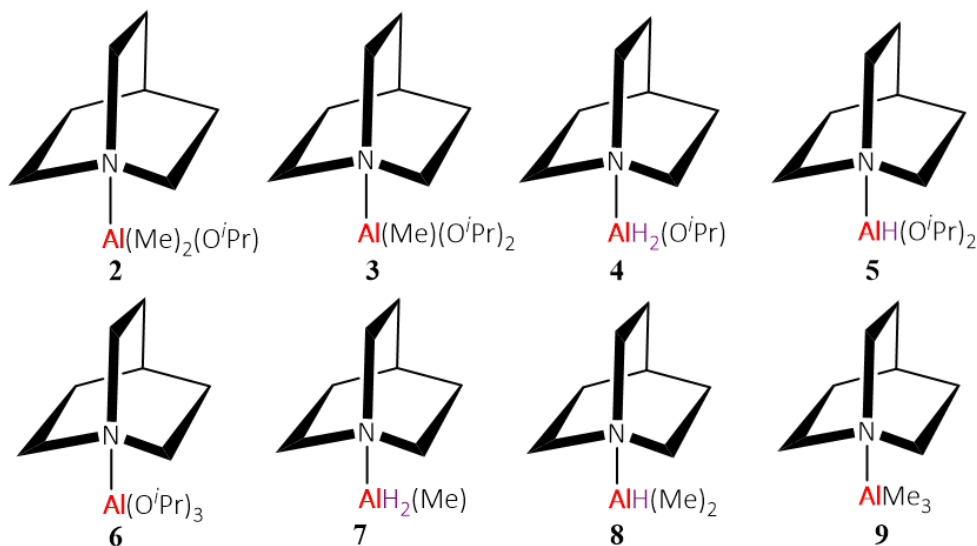
Figure 2.8: Powder X-ray diffractogram (PXRD) of the grey precipitate collected from the 1:2 reaction of MeZnO^{*i*}Pr with HBpin in d₆-benzene, 24 h, RT. Red lines indicate the diffraction pattern corresponding to hexagonal zinc.

2.3.1.3 Reaction of MeZnOⁱPr with AlH₃(Quinuclidine)

Option 01



All other possible products



Scheme 2.5: Possible by-products predicted for the reaction of MeZnOⁱPr with AlH₃(Quinuclidine) (assuming pathway 2 in the Scheme 2.2).

Solutions of MeZnOⁱPr and AlH₃(Quinuclidine) were prepared in d₆-benzene and they were mixed together in a 1:1 ratio at room temperature. Gradual formation of a white cloudy suspension was observed after few hours at room temperature and the suspension remained unchanged after 24 hours. Heating the reaction mixture for 24 hours at 40 °C transformed the white suspension into a grey precipitate. Scheme 2.5 illustrates possible by-products with the potential to form during the reaction. Product 01 (Scheme 2.5) was the major by-

product expected from the reaction, where two hydride groups on aluminum of $\text{AlH}_3(\text{Quinuclidine})$ are replaced with methyl and isopropoxide groups from MeZnO^iPr . However, the reaction has the ability to produce several other by-products (Product 02-Product 09) depending on the stoichiometric ratio in which MeZnO^iPr and $\text{AlH}_3(\text{Quinuclidine})$ react with each other (Scheme 2.5).

The proton NMR spectrum of the reaction solution in d_6 -benzene collected after heating the reaction mixture for 24 hours at 40°C is shown in Figure 2.9 (c). The NMR spectrum indicates the formation of hydrogen gas ($\delta = 4.47$ ppm). However, it is difficult to identify other peaks in the spectrum due to the formation of multiple ^iPr and Me-containing by-products. Comparison of proton NMR spectra of sublimed MeZnO^iPr (Figure 2.9 a) and $\text{AlH}_3(\text{Quinuclidine})$ (Figure 2.9 b) with the reaction mixture of MeZnO^iPr with $\text{AlH}_3(\text{Quinuclidine})$ (Figure 2.9 c) indicates the complete consumption of both $\text{AlH}_3(\text{Quinuclidine})$ and MeZnO^iPr during the reaction. Further investigation into identification of the products formed in the reaction was not continued as it might be challenging to isolate by-products from the reaction mixture.

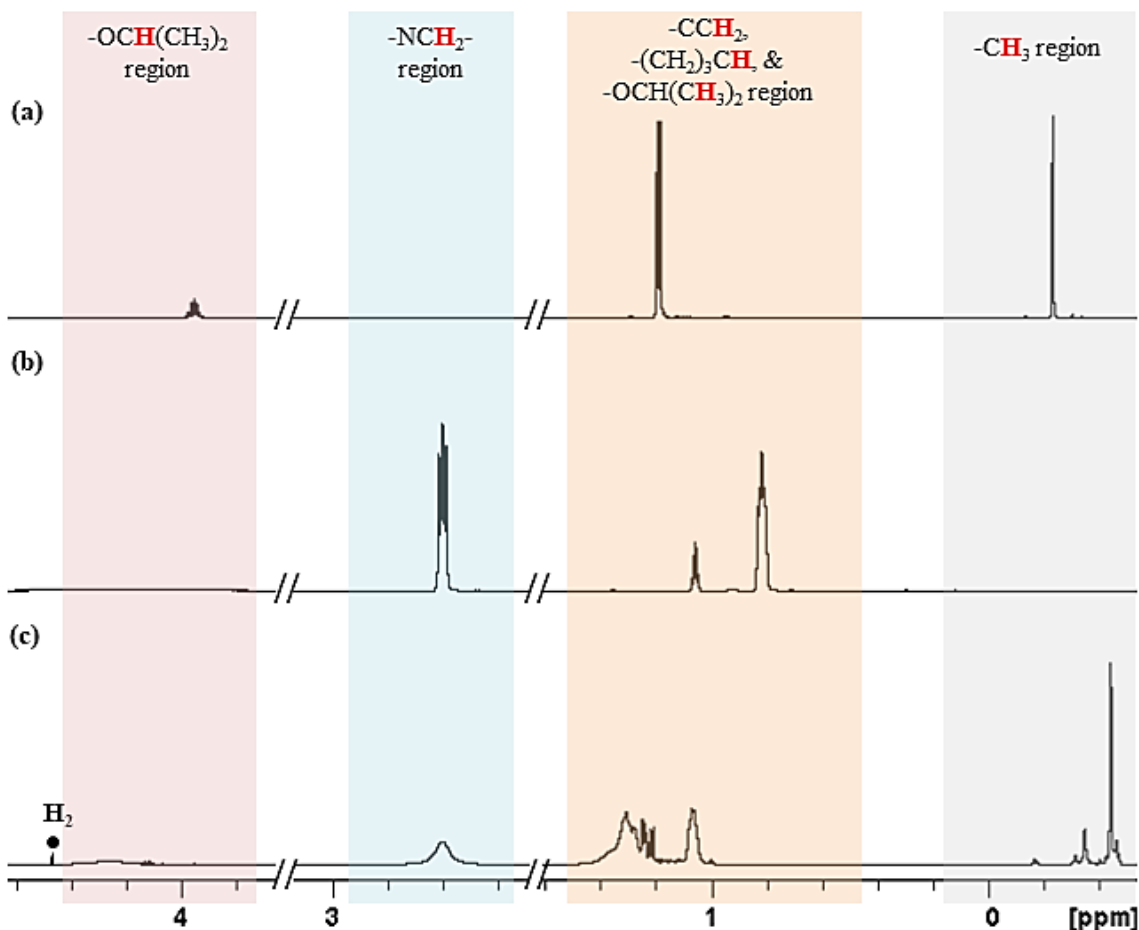


Figure 2.9: The ^1H NMR spectra of (a) Sublimed MeZnO'Pr, (b) $\text{AlH}_3(\text{Quinuclidine})$, (c) 1:1 reaction solution of MeZnO'Pr with $\text{AlH}_3(\text{Quinuclidine})$ in d_6 -benzene collected after heating the reaction mixture for 24 hours at 40°C .

The grey precipitate collected from the reaction was separated and washed with hexanes which produced a sticky precipitate which was difficult to characterize. The reaction was repeated again, and the precipitate was collected, followed by washing with toluene followed by hexanes. A powder X-ray diffractogram of the collected precipitate is shown in Figure 2.10. As illustrated by the diffractogram, the diffraction pattern of the collected

precipitate aligns well with the diffraction pattern of hexagonal zinc, verifying the formation of elemental zinc during the reaction.

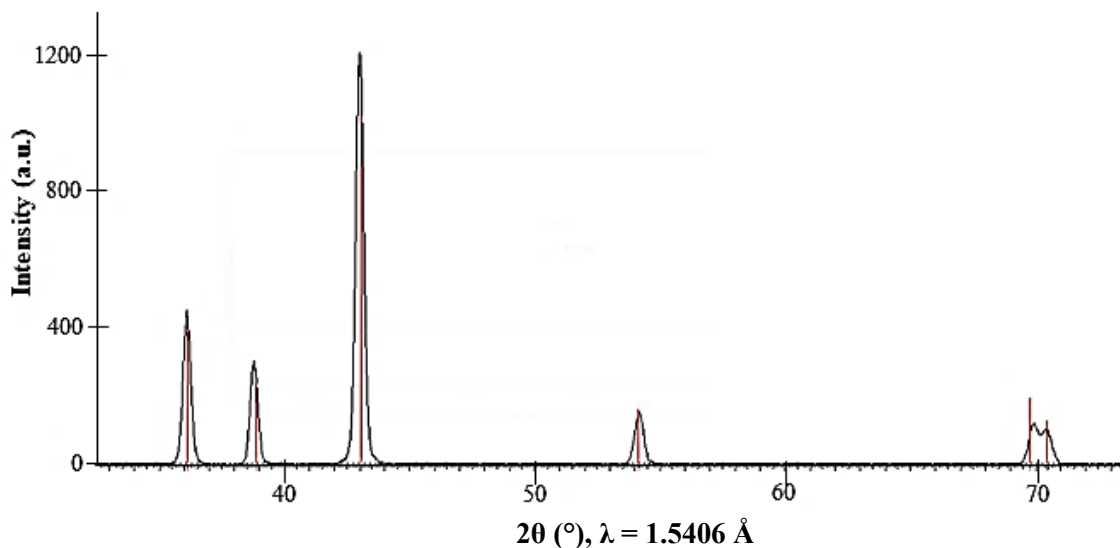


Figure 2.10: Powder X-ray diffractogram (PXRD) of the grey precipitate collected from the 1:1 reaction solution of MeZnOⁱPr with AlH₃(Quinuclidine) in d₆-benzene, 24 h, 40 °C. Red lines indicate the diffraction pattern corresponding to hexagonal zinc.

2.3.1.4 Reaction of MeZnOⁱPr with BH₃(NMe₃)

Solutions of MeZnOⁱPr and BH₃(NMe₃) were prepared in d₆-benzene and were mixed together in a 1:1 ratio at room temperature. No visual change was observed upon mixing the reagents. To investigate if the reactivity between the two reagents is affected by increasing the reaction temperature, the reaction mixture was heated for 24 hours at different temperatures up to 80 °C. The ¹H NMR spectrum collected after heating the reaction mixture for 24 hours at 80 °C is shown in Figure 2.11 and indicates no reactivity between the two reagents.

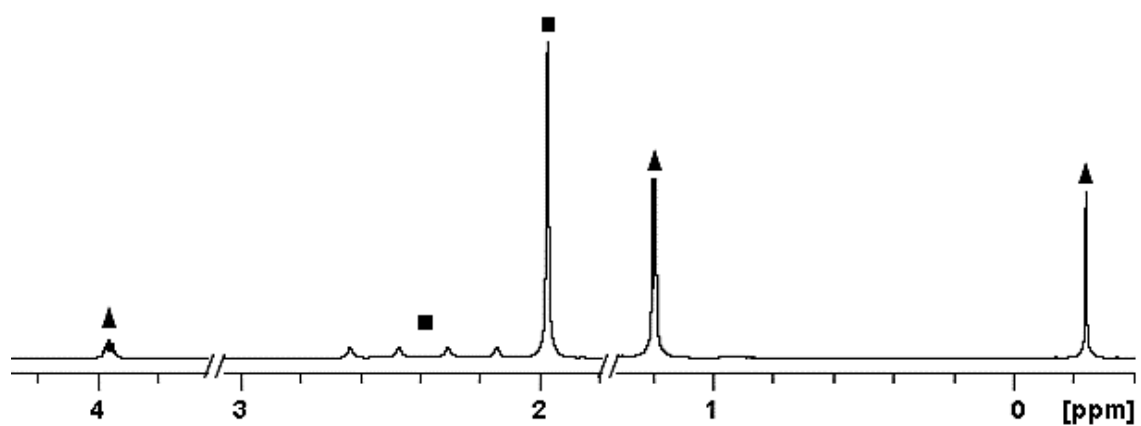
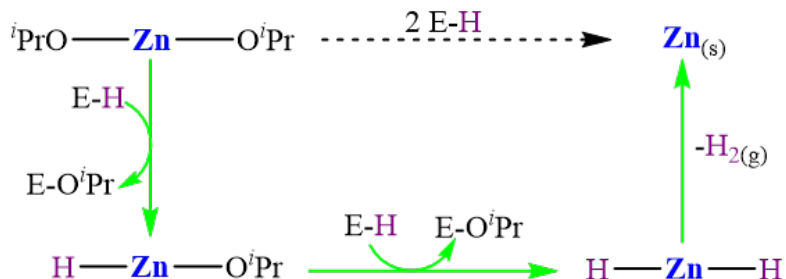


Figure 2.11: The proton NMR spectrum of the 1:1 reaction of MeZnO'Pr with BH₃(NMe₃) in d₆-benzene, after heating the reaction mixture for 24 hours at 80 °C. Squares indicate peaks corresponding to free BH₃(NMe₃) and triangles indicate peaks corresponding to free MeZnO'Pr.

2.3.2 Solution reactivity studies of $\text{Zn}(\text{O}^i\text{Pr})_2$



Scheme 2.6: Reaction pathway anticipated for reactions of $\text{Zn}(\text{O}^i\text{Pr})_2$ with hydride co-reagents to produce elemental zinc. E = Bpin, LAIH (L = $t\text{BuNCH}_2\text{CH}_2\text{NMe}_2$), $\text{AlH}_2(\text{Quinuclidine})$, $\text{BH}_2(\text{NMe}_3)$, or PhSiH_2 .

The reaction pathway anticipated for solution reactions between $\text{Zn}(\text{O}^i\text{Pr})_2$ with hydride-reducing co-reagents is shown in Scheme 2.6. This pathway involves two separate ligand exchange reactions between a hydride group of the co-reactant and an isopropoxide group on zinc to produce ZnH_2 , a pyrophoric, unstable zinc hydride which slowly decomposes at room temperature to elemental zinc and H_2 gas.¹²⁹ Hence, according to the predicted reaction pathway, all reactions must produce H_2 gas.

For solution studies, the ^1H NMR spectra of $\text{Zn}(\text{O}^i\text{Pr})_2$ could not be collected due to insolubility of $\text{Zn}(\text{O}^i\text{Pr})_2$ in common organic solvents. For comparison purposes, a powder X-ray diffractogram of $\text{Zn}(\text{O}^i\text{Pr})_2$ was collected (Figure 2.12).

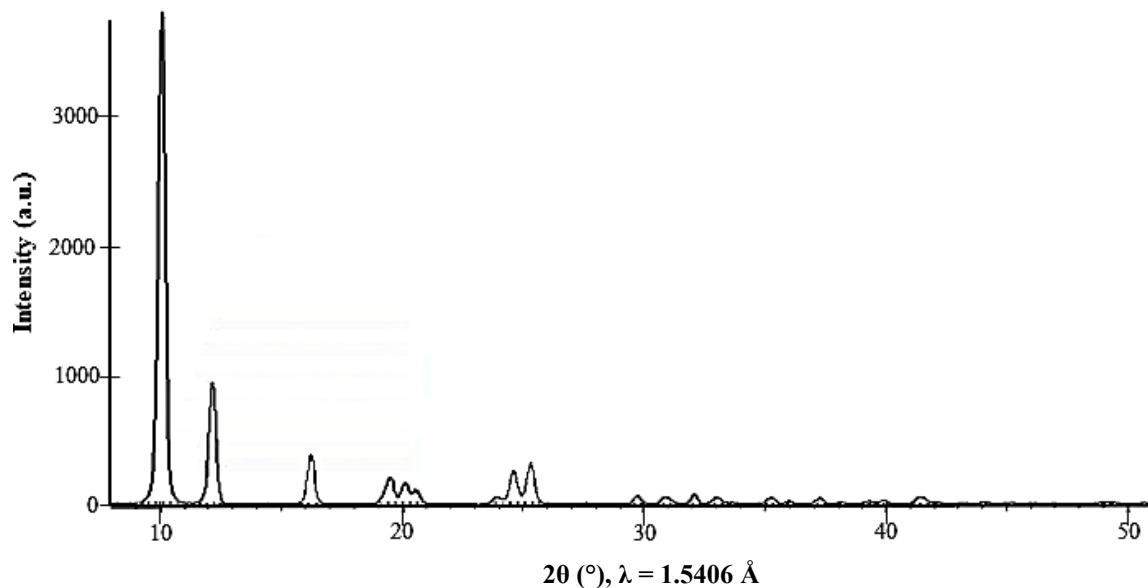
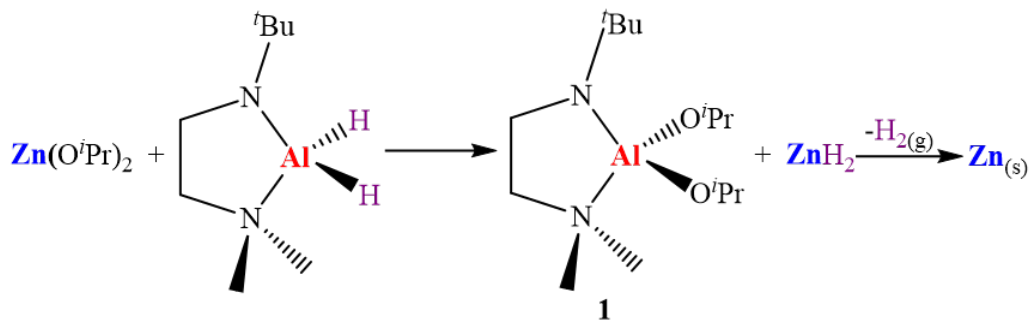


Figure 2.12: Powder X-ray diffractogram for $\text{Zn}(\text{O}^i\text{Pr})_2$.

2.3.2.1 Reaction of $\text{Zn}(\text{O}^i\text{Pr})_2$ with LiAlH_2



Scheme 2.7: Expected by-products from the 1:1 reaction of $\text{Zn}(\text{O}^i\text{Pr})_2$ with LiAlH_2 (assuming pathway in the Scheme 2.6).

To investigate the reactivity between $\text{Zn}(\text{O}^i\text{Pr})_2$ and LiAlH_2 , $\text{Zn}(\text{O}^i\text{Pr})_2$ was added to a solution of LiAlH_2 in d_6 -benzene in a 1:1 ratio at room temperature. Initially no reaction was observed, which might be due to the low solubility of $\text{Zn}(\text{O}^i\text{Pr})_2$ in d_6 -benzene. A white

suspension started to form after 3-4 hours at room temperature and slowly started to turn grey after about 6 hours. After 24 hours at room temperature, a grey precipitate was observed at the bottom of the J-young tube. Product 01 was expected as the only by-product of the reaction (Scheme 2.7), and is produced by replacing both hydride groups on LiAlH_2 with isopropoxide groups from $\text{Zn}(\text{O}^i\text{Pr})_2$.

As is evident from the proton NMR spectrum (Figure 2.13), the major by-product produced in the reaction is $\text{LiAl}(\text{O}^i\text{Pr})_2$ (Product 01) as anticipated (Scheme 2.7). Two methyl groups on nitrogen of the ligand backbone gave rise to a single peak suggesting a symmetric molecule, as expected for $\text{LiAl}(\text{O}^i\text{Pr})_2$ (Figure 2.13). The chemical shift values are nearly identical for the tertiary butyl group on the ligand and the two diastereotopic CHMe_2 signals. Hence, they appear as a one multiplet which integrated to close to the expected 21 protons (Figure 2.13). Further characterization of $\text{LiAl}(\text{O}^i\text{Pr})_2$ is discussed in Section 2.4. The appearance of hydrogen (Figure 2.13: Labelled with a circle) and formation of $\text{LiAl}(\text{O}^i\text{Pr})_2$ indicates that both iso-propoxide groups on Zn undergo ligand exchange reaction with LiAlH_2 to produce unstable ZnH_2 .

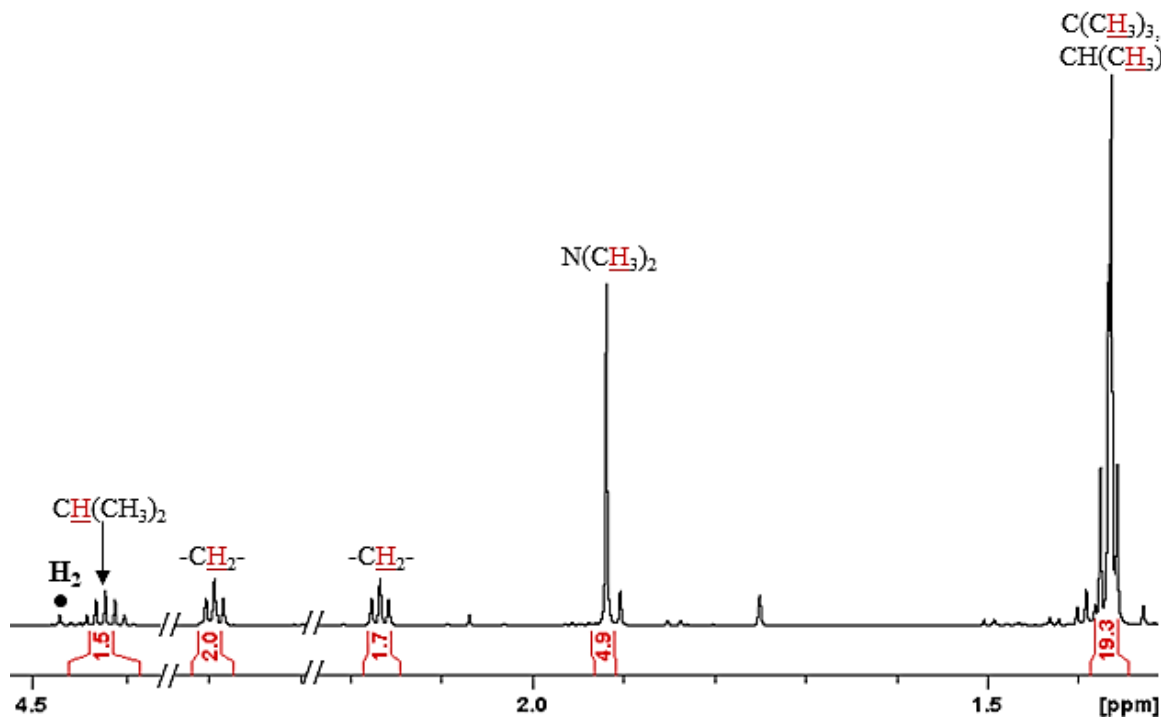


Figure 2.13: The proton NMR spectrum of the 1:1 reaction of $\text{Zn}(\text{O}^i\text{Pr})_2$ with LAiH_2 in d_6 -benzene collected after 24 hours of mixing the reagents at room temperature. Hydrogen peak at 4.47 ppm is labelled with a circle.

The grey precipitate formed in the reaction was separated by centrifugation and washed with toluene followed by hexanes. An X-ray diffractogram of the precipitate (Figure 2.14) confirms the formation of elemental zinc during the reaction. In addition to all the peaks in the diffractogram corresponding to hexagonal Zn, one extra peak can be seen at 2-theta 39° which might be due to an insoluble impurity left in the reaction.

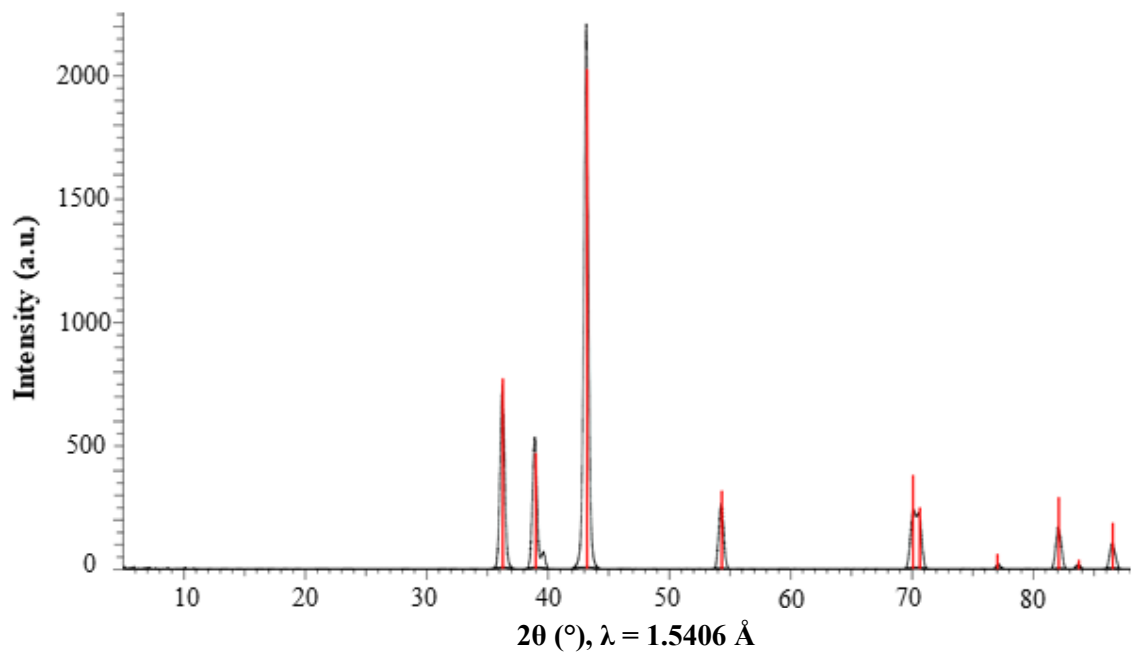
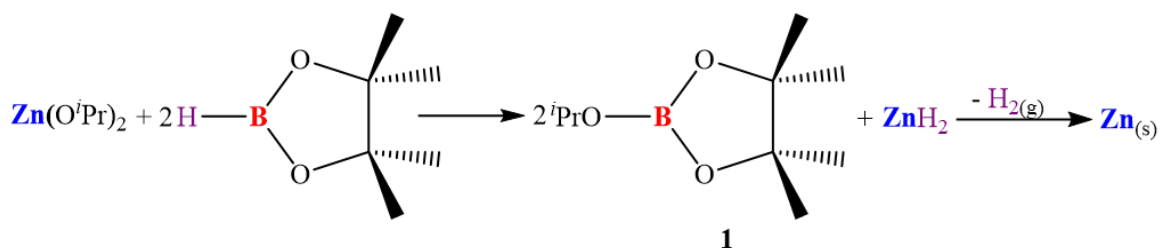


Figure 2.14: Powder X-ray diffractogram (PXRD) of the grey precipitate collected from the 1:1 reaction of $\text{Zn}(\text{O}^i\text{Pr})_2$ with LiAlH_2 in d_6 -benzene, 24 h, RT. Red lines indicate the diffraction pattern corresponding to hexagonal zinc.

2.3.2.2 Reaction of $\text{Zn}(\text{O}^i\text{Pr})_2$ with HBpin



Scheme 2.8: Expected by-products from the 1:2 reaction of $\text{Zn}(\text{O}^i\text{Pr})_2$ with HBpin (assuming pathway in the Scheme 2.6).

Scheme 2.8 represents the expected reaction pathway for the reaction between $\text{Zn}(\text{O}^i\text{Pr})_2$ and HBpin. According to the Scheme 2.8, the only by-product expected to be formed during the reaction is $(^i\text{PrO})\text{Bpin}$ (Product 01). To study the solution reactivity between two reagents, $\text{Zn}(\text{O}^i\text{Pr})_2$ was mixed with a solution of HBpin in d_6 -benzene in a 1:2 ratio at room temperature. Visual observations and NMR data collected suggested a slow reaction between two reagents and the reaction could not reach completion even after heating the reaction solution at 80 °C for 24 hours, which might be due to the very low solubility of $\text{Zn}(\text{O}^i\text{Pr})_2$. To overcome the above issue another reaction was carried out with an excess amount of HBpin. A gradual formation of a white cloudy suspension was observed at room temperature which remained unchanged after 24 hours. Heating the reaction solution at 40 °C for 24 hours resulted in a grey precipitate.

The proton NMR spectrum of the reaction solution collected after heating the reaction mixture at 40 °C for 24 hours is shown in Figure 2.15. As evident from the NMR spectrum, the formation of the anticipated by-product $(^i\text{PrO})\text{Bpin}$ was confirmed (Figure 2.15). However, as both methine protons of the isopropyl group of $(^i\text{PrO})\text{Bpin}$ and the hydrogen gas show up on the spectrum at the same position, one peak in the septet appears larger than expected (Figure 2.15: Enlarged region, H_2 is labelled with a circle). The NMR spectrum of $(^i\text{PrO})\text{Bpin}$ was shown to be identical to that of a commercial sample of $(^i\text{PrO})\text{Bpin}$ and further characterization of $(^i\text{PrO})\text{Bpin}$ is discussed in Section 2.4.

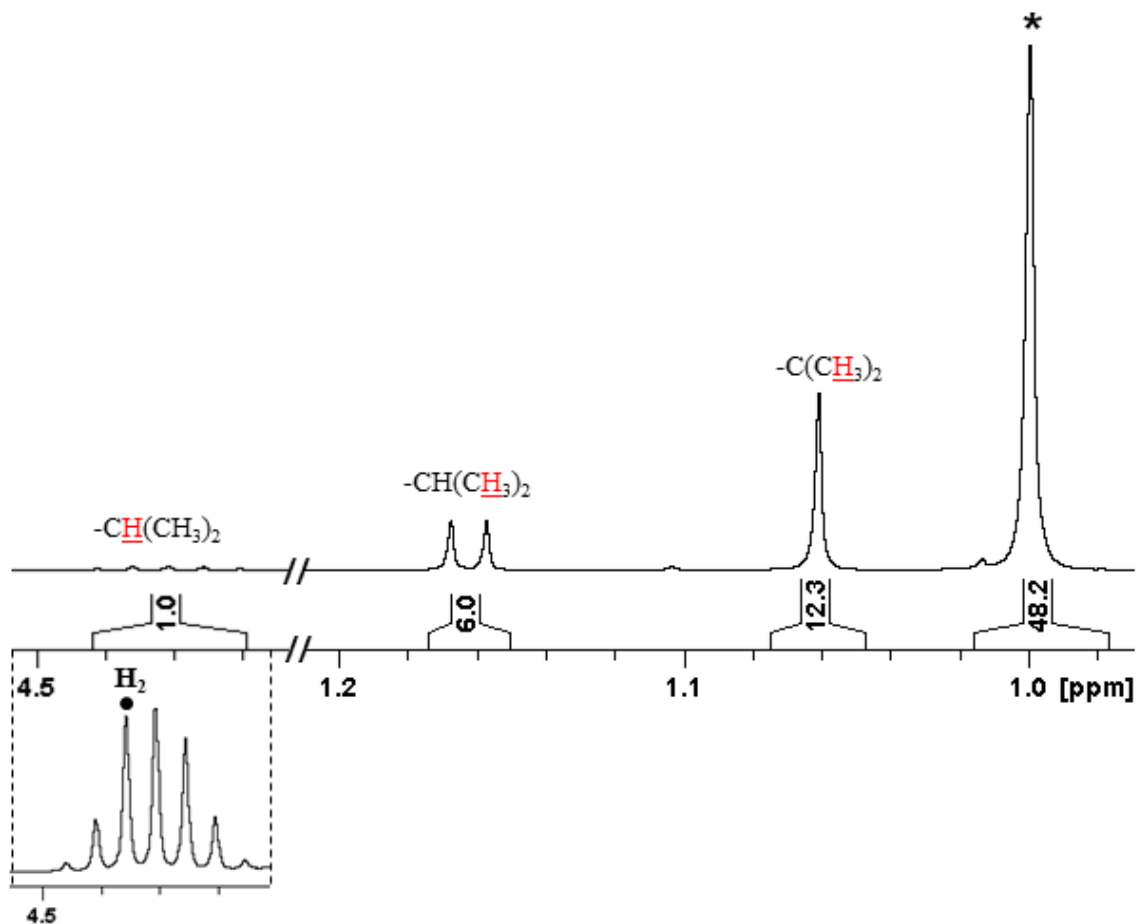


Figure 2.15: The proton NMR spectrum of the 1:5 reaction of $\text{Zn}(\text{O}^i\text{Pr})_2$ with HBpin in d_6 -benzene, collected after heating the reaction solution at 40 °C for 24 hours. Excess HBpin is labelled with an asterisk and H_2 is labelled with a circle. All other peaks in the spectrum are identical with those for commercially purchased (^iPrO)Bpin.

The grey precipitate formed in the reaction was isolated and washed with toluene and hexanes to remove any soluble contaminants. An X-ray diffractogram of the precipitate (Figure 2.16). confirmed the formation of elemental zinc during the reaction.

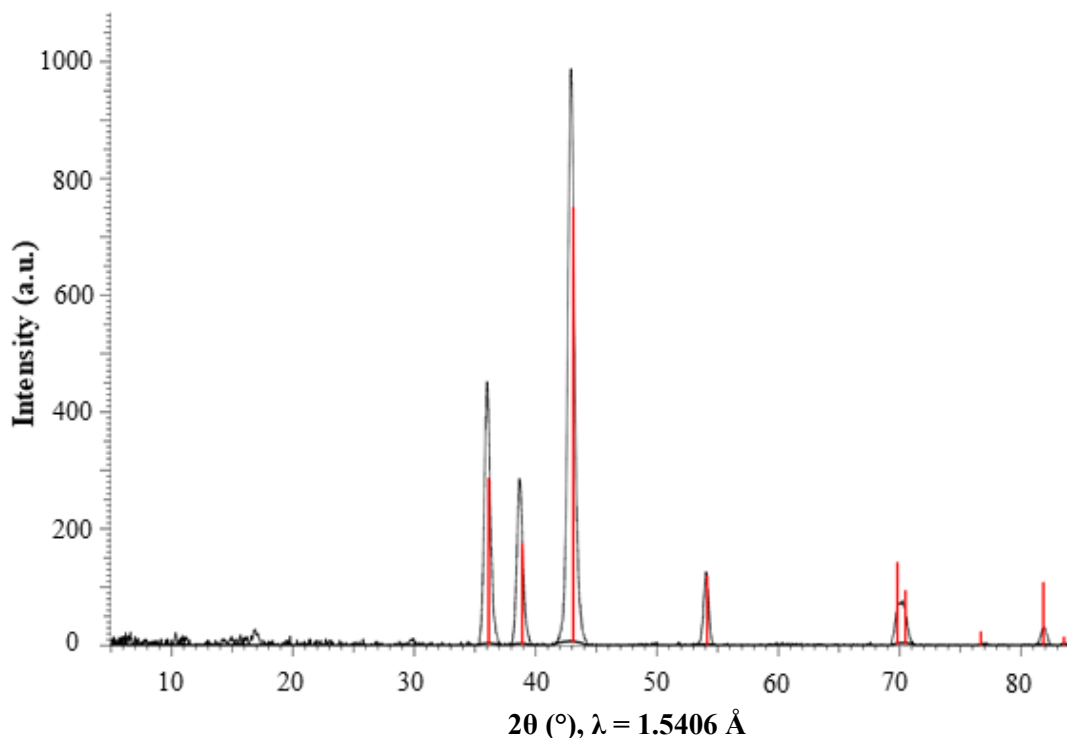


Figure 2.16: Powder X-ray diffractogram (PXRD) of the grey precipitate collected from the 1:5 reaction of $\text{Zn}(\text{O}^i\text{Pr})_2$ with HBpin in d_6 -benzene, 24 h, 40 °C. Red lines indicate the diffraction pattern corresponding to hexagonal zinc.

2.3.2.3 Reaction of $\text{Zn}(\text{O}^i\text{Pr})_2$ with $\text{AlH}_3(\text{Quinuclidine})$

$\text{Zn}(\text{O}^i\text{Pr})_2$ was mixed with a solution of $\text{AlH}_3(\text{Quinuclidine})$ in d_6 -benzene in a 1: 2 ratio at room temperature. No visual change was observed immediately after mixing reagents and a white cloudy suspension gradually started to form after about 6 hours which remained unchanged after 12 hours. The white suspension turned in to a grey precipitate after leaving the reaction solution for 24 hours at room temperature. Scheme 2.9 predicts Product 01 as the major by-product of the reaction which is produced by replacing two hydride groups on $\text{AlH}_3(\text{Quinuclidine})$ with isopropoxide groups on $\text{Zn}(\text{O}^i\text{Pr})_2$. However, depending on how

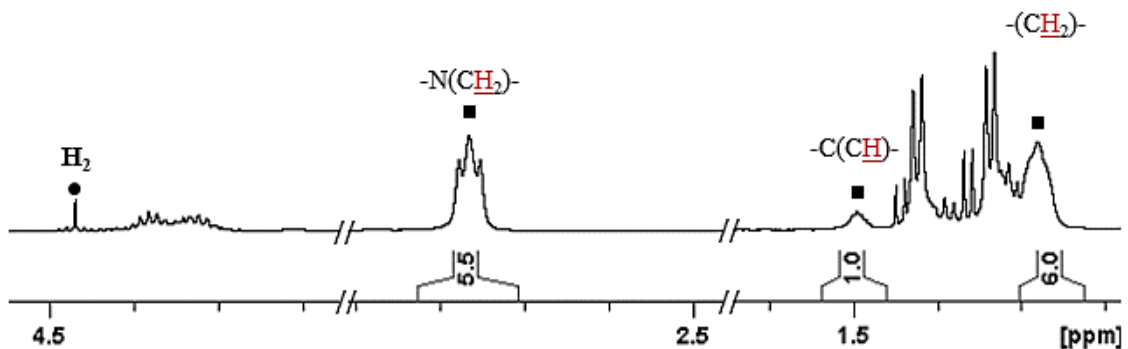


Figure 2.17: The proton NMR spectrum of the 1:2 reaction of $\text{Zn}(\text{O}^i\text{Pr})_2$ with $\text{AlH}_3(\text{Quinuclidine})$ in d_6 -benzene, collected after 24 hours of mixing the reagents at room temperature. Squares indicate free quinuclidine.

A sticky grey precipitate was obtained after rinsing the precipitate with hexanes. Hence, another series of washings were done with toluene followed by hexanes to collect a dry precipitate for PXRD analysis. The collected powder X-ray diffractogram of the precipitate is indicated in Figure 2.18. This diffractogram confirms the formation of elemental zinc during the reaction. However, large amounts of unreacted $\text{Zn}(\text{O}^i\text{Pr})_2$ also remain in the precipitate (Figure 2.18).

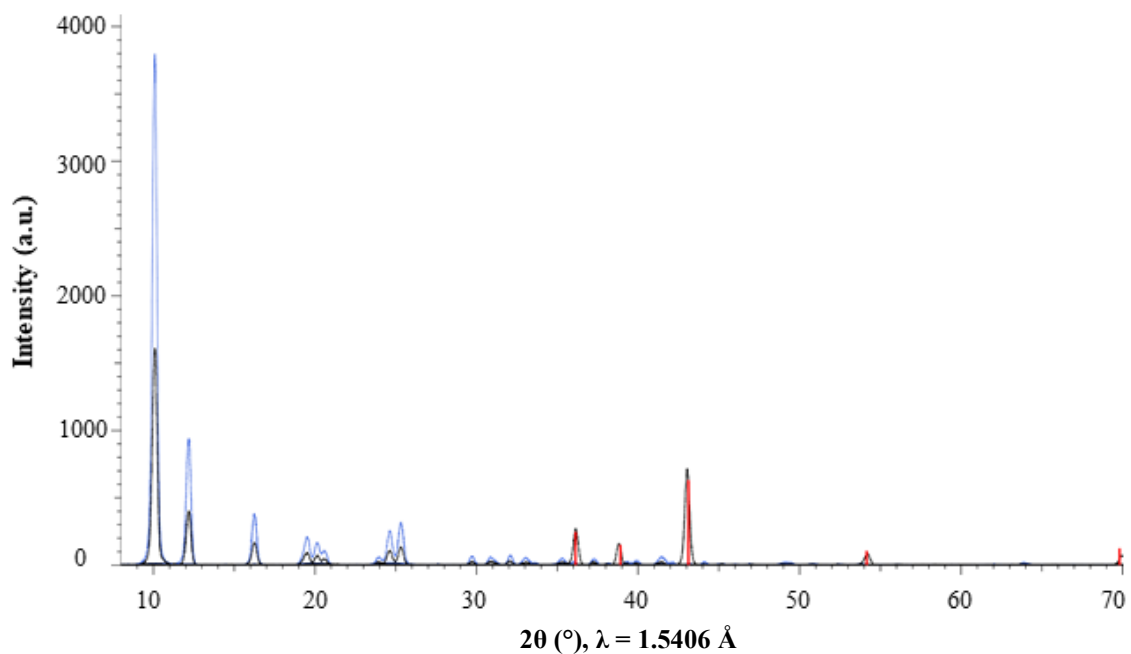


Figure 2.18: Powder X-ray diffractogram (PXRD) of the grey precipitate collected from the 1:2 reaction of $\text{Zn}(\text{O}^i\text{Pr})_2$ with AlH_3 (Quinuclidine) in d_6 -benzene, 24 h, RT (Black). Red lines indicate the diffraction pattern corresponding to hexagonal zinc. Diffractogram showed in blue colour corresponds to $\text{Zn}(\text{O}^i\text{Pr})_2$ and indicates the remaining unreacted $\text{Zn}(\text{O}^i\text{Pr})_2$ in the precipitate.

2.3.2.4 Reaction of $\text{Zn}(\text{O}^i\text{Pr})_2$ with $\text{BH}_3(\text{NMe}_3)$

In an attempt to examine the reactivity of $\text{Zn}(\text{O}^i\text{Pr})_2$ towards $\text{BH}_3(\text{NMe}_3)$, solutions of the reagents in d_6 -benzene were mixed in a 1:1 ratio at room temperature.

The proton NMR spectrum of the reaction mixture collected after heating at 80 °C for 24 hours, is illustrated in Figure 2.19 (b) along with the proton NMR spectrum of $\text{BH}_3(\text{NMe}_3)$ (Figure 2.19 a), and indicates that no reaction took place.

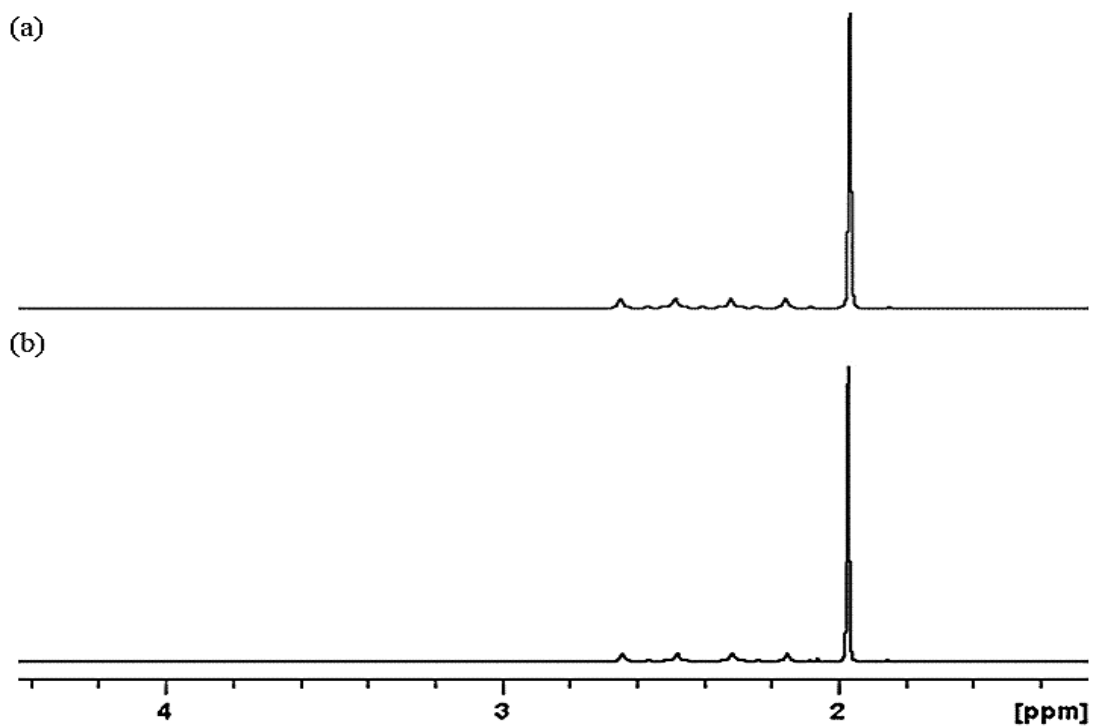
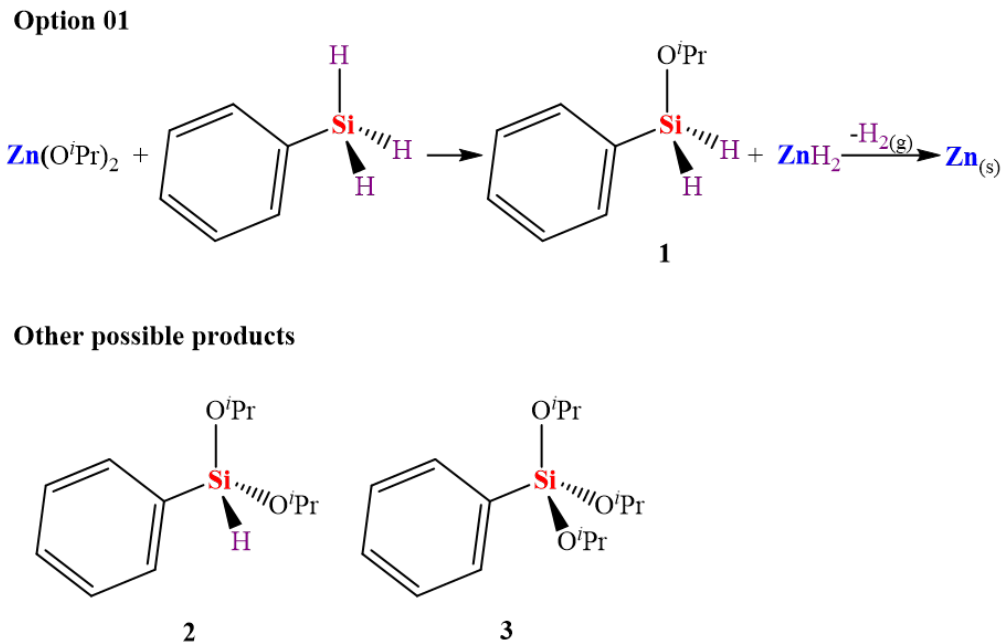


Figure 2.19: The proton NMR spectra of a) $\text{BH}_3(\text{NMe}_3)$ and b) 1:1 reaction of $\text{Zn}(\text{O}^i\text{Pr})_2$ with $\text{BH}_3(\text{NMe}_3)$ in d_6 -benzene, collected after heating the reaction solution for 24 hours at 80 °C.

2.3.2.5 Reaction of $\text{Zn}(\text{O}^i\text{Pr})_2$ with PhSiH_3



Scheme 2.10: Possible by-products from the reaction between $\text{Zn}(\text{O}^i\text{Pr})_2$ and PhSiH_3 (assuming pathway in the Scheme 2.6).

A solution of PhSiH_3 in d_6 -benzene was mixed with $\text{Zn}(\text{O}^i\text{Pr})_2$ in a 1:2 ratio at room temperature. The reaction solution remained unchanged even after heating the reaction solution for 24 hours at 40 °C. However, gradual formation of a grey precipitate was observed after heating the reaction solution at 60 °C/ 24 hours. Scheme 2.10 illustrates different by-products that can be expected during the reaction based on the number of hydride ligands replaced in PhSiH_3 .

The proton NMR spectrum of the reaction mixture was collected after heating the 1:2 reaction solution of $\text{Zn}(\text{O}^i\text{Pr})_2$ and PhSiH_3 in d_6 -benzene for 24 hours at 60 °C (Figure 2.20).

A delay time of 15s was used while collecting the proton NMR to ensure proper integration

of the SiH signals. The spectrum clearly indicates the formation of hydrogen gas (Figure 2.20 labelled with a circle). Formation of $\text{PhSiH}(\text{O}^i\text{Pr})_2$ (Product 02) was observed as the major by-product of the reaction (Figure 2.20: Indicated with squares) while $\text{PhSiH}_2(\text{O}^i\text{Pr})$ was also observed as a minor product (Figure 2.20: Indicated with triangles), judged by the proton NMR spectrum. Unreacted excess PhSiH_3 is also seen in the spectrum (Figure 2.20) which is labelled with an asterisk. Further isolation or characterization were not attempted on the reaction by-products.

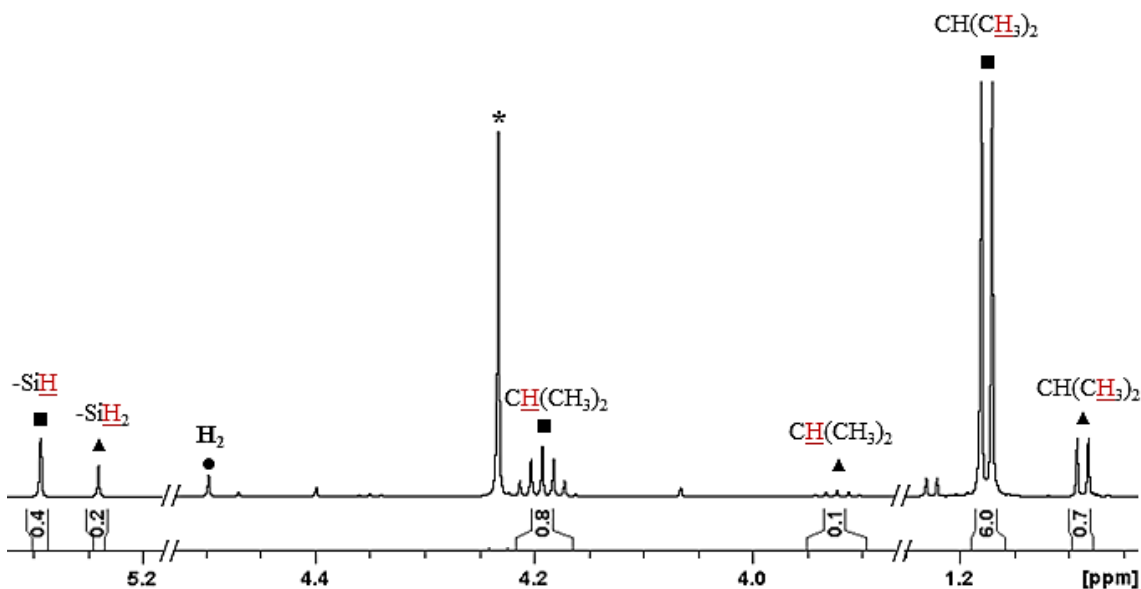


Figure 2.20: The proton NMR spectrum of 1:2 reaction solution of $\text{Zn}(\text{O}^i\text{Pr})_2$ with PhSiH_3 in d_6 -benzene, collected after heating the reaction solution for 24 hours at $60\text{ }^\circ\text{C}$. A delay time of 15s was used to ensure proper integration of SiH signals. Squares indicate the peaks corresponding to $\text{PhSiH}(\text{O}^i\text{Pr})_2$, triangles indicate $\text{PhSiH}_2(\text{O}^i\text{Pr})$, and the asterisk indicates the unreacted excess PhSiH_3 .

The grey precipitate was separated and washed with toluene followed by hexanes prior to collecting the X-ray diffractogram (Figure 2.21), which confirms the formation of elemental zinc. However, 2 extra peaks can be seen in the diffractogram with 2θ values of approximately 10° and 12° (Figure 2.21 labelled with red asterisks) due to a small amount of unreacted $\text{Zn}(\text{O}^i\text{Pr})_2$ present in the precipitate.

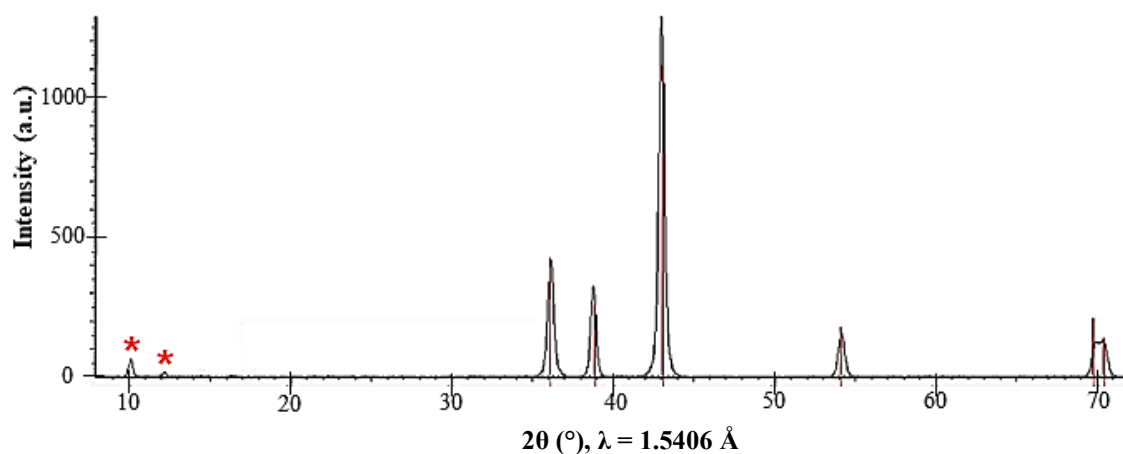
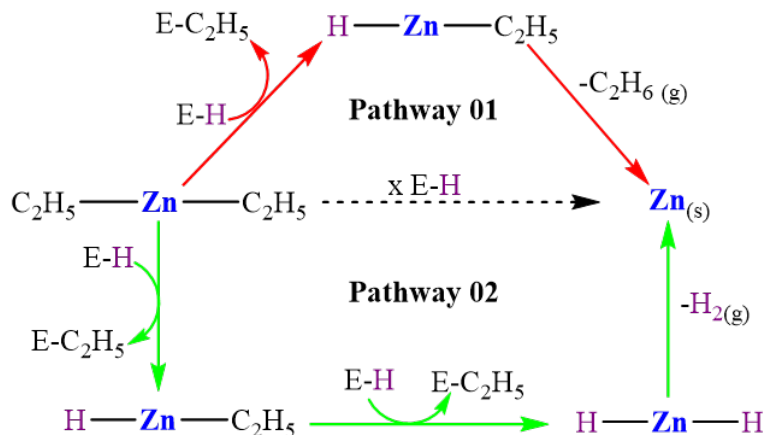


Figure 2.21: Powder X-ray diffractogram (PXRD) of the grey precipitate collected from the 1:2 reaction mixture of $\text{Zn}(\text{O}^i\text{Pr})_2$ with PhSiH_3 in d_6 -benzene, 24 h, 60°C . Red asterisks indicate the unreacted $\text{Zn}(\text{O}^i\text{Pr})_2$ present in the precipitate.

2.3.3 Solution reactivity studies of ZnEt₂



Scheme 2.11: Reaction pathways anticipated for reactions of ZnEt₂ with hydride-reducing reagents to produce elemental zinc. E = Bpin, LAIH (L = ^tBuNCH₂CH₂NMe₂), AlH₂(Quinuclidine), BH₂(NMe₃), or PhSiH₂.

The general reaction pathways anticipated for solution reactions between ZnEt₂ with hydride co-reagents are shown in Scheme 2.11. Both pathways start with a ligand exchange reaction between a hydride group of the co-reactant and an ethyl group on ZnEt₂ as the first step to produce HZnC₂H₅ as the intermediate. As illustrated by Scheme 2.11 in reaction pathway 01, HZnC₂H₅ then reductively eliminates ethane gas (C₂H₆) as a by-product to produce elemental zinc. The second reaction pathway predicts that once HZnC₂H₅ is produced, it subsequently undergoes another ligand exchange reaction with a hydride group of the co-reactant molecule to produce ZnH₂, which then slowly decomposes at room temperature to elemental zinc and H₂ gas.¹²⁹ Hence, according to the predicted reaction pathways, all reactions that show a reactivity must either produce C₂H₆ (Scheme 2.11 Reaction pathway 01) or H₂ gas (Scheme 2.11 Reaction pathway 02).

^1H and $^{13}\text{C}\{^1\text{H}\}$ NMR spectra of ZnEt_2 were collected in d_6 -benzene for comparison in solution studies (Figure 2.22).

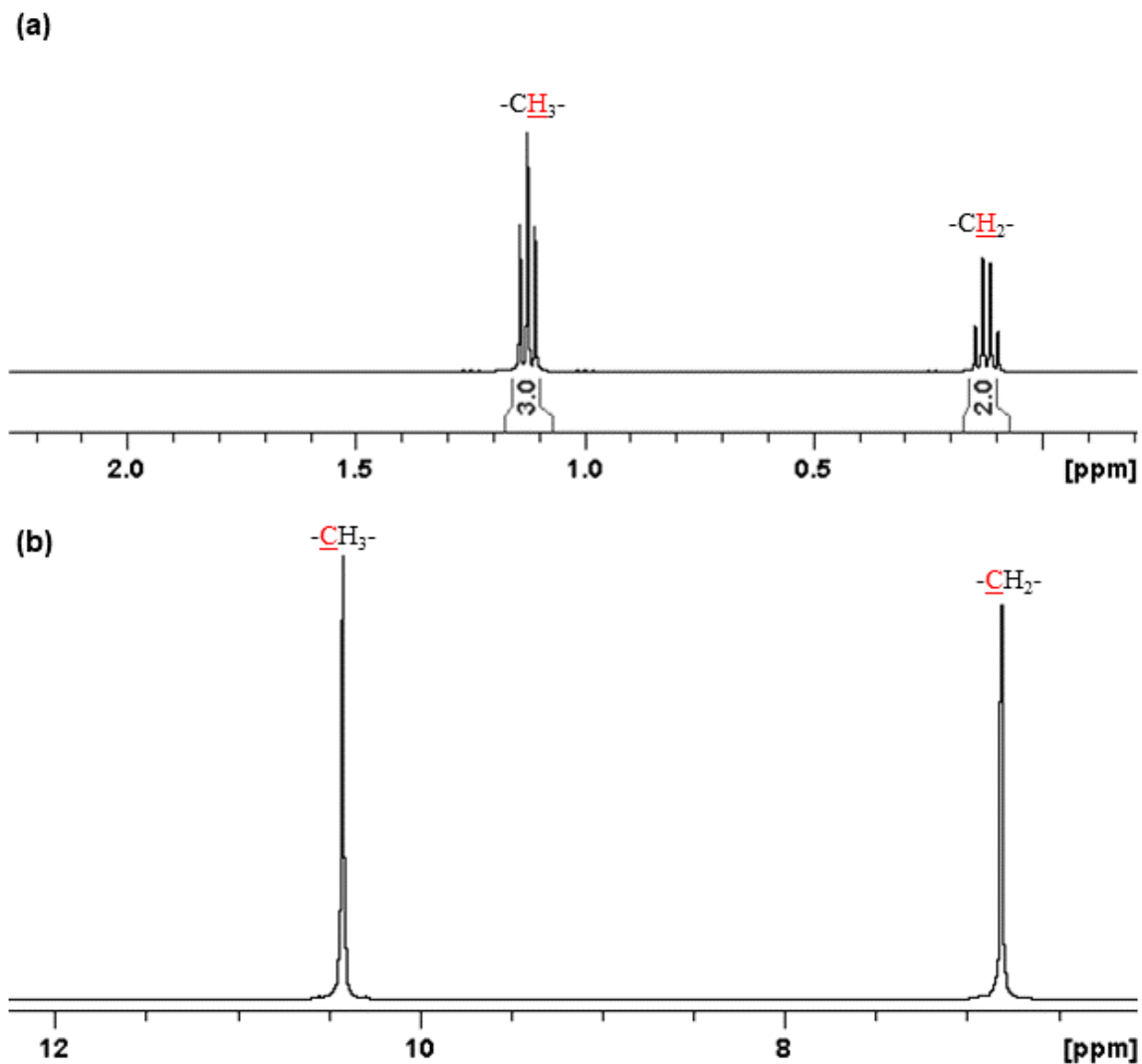
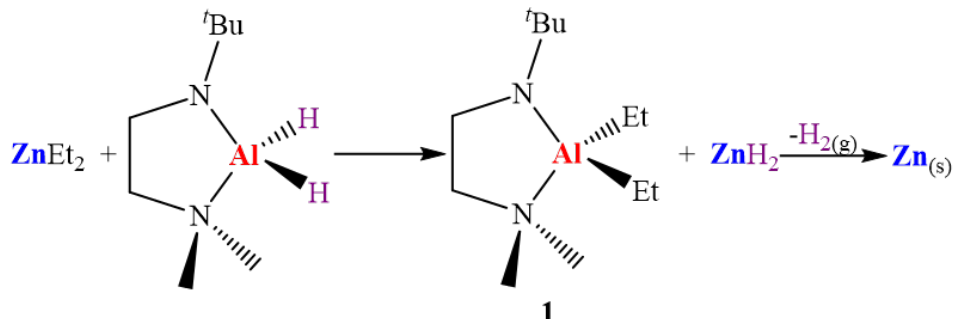


Figure 2.22: ^1H and $^{13}\text{C}\{^1\text{H}\}$ NMR spectra collected for ZnEt_2 in d_6 -benzene.

2.3.3.1 Reaction of ZnEt₂ with LAIH₂



Scheme 2.12: By-products anticipated for the 1:1 reaction between ZnEt₂ and LAIH₂ (assuming pathway 02 in the Scheme 2.11).

Solutions of ZnEt₂ and LAIH₂ were prepared in d₆-benzene and were mixed together in a 1:1 ratio at room temperature. Formation of a white cloudy suspension and a gas evolution were observed immediately after mixing the two reagents. The white suspension turned into a grey precipitate within 10 minutes. After leaving the reaction mixture overnight at room temperature, the precipitate had settled down to the bottom of the J-young tube, leaving a clear supernatant. Scheme 2.12 predicts Product 01 as the only by-product of the reaction which is formed as the result of both hydride groups on LAIH₂ being exchanged with two ethyl groups on ZnEt₂.

The proton NMR spectrum (Figure 2.23) collected after 24 hours of mixing reagents at room temperature, clearly indicates the formation of hydrogen gas at 4.47 ppm (Figure 2.23: Labelled with a circle). Analysing the spectrum suggests the formation of LAIEt₂ as the only by-product of the reaction. To further confirm the identity of the by-product, LAIEt₂ was isolated from a separate reaction between ZnEt₂ and LAIH₂ with a 50% yield

and $^{13}\text{C}\{^1\text{H}\}$, HSQC NMR spectra for LAIEt_2 were collected. Further characterization of LAIEt_2 is discussed in Section 2.4. Analysing these spectra confirms the by-product as LAIEt_2 .

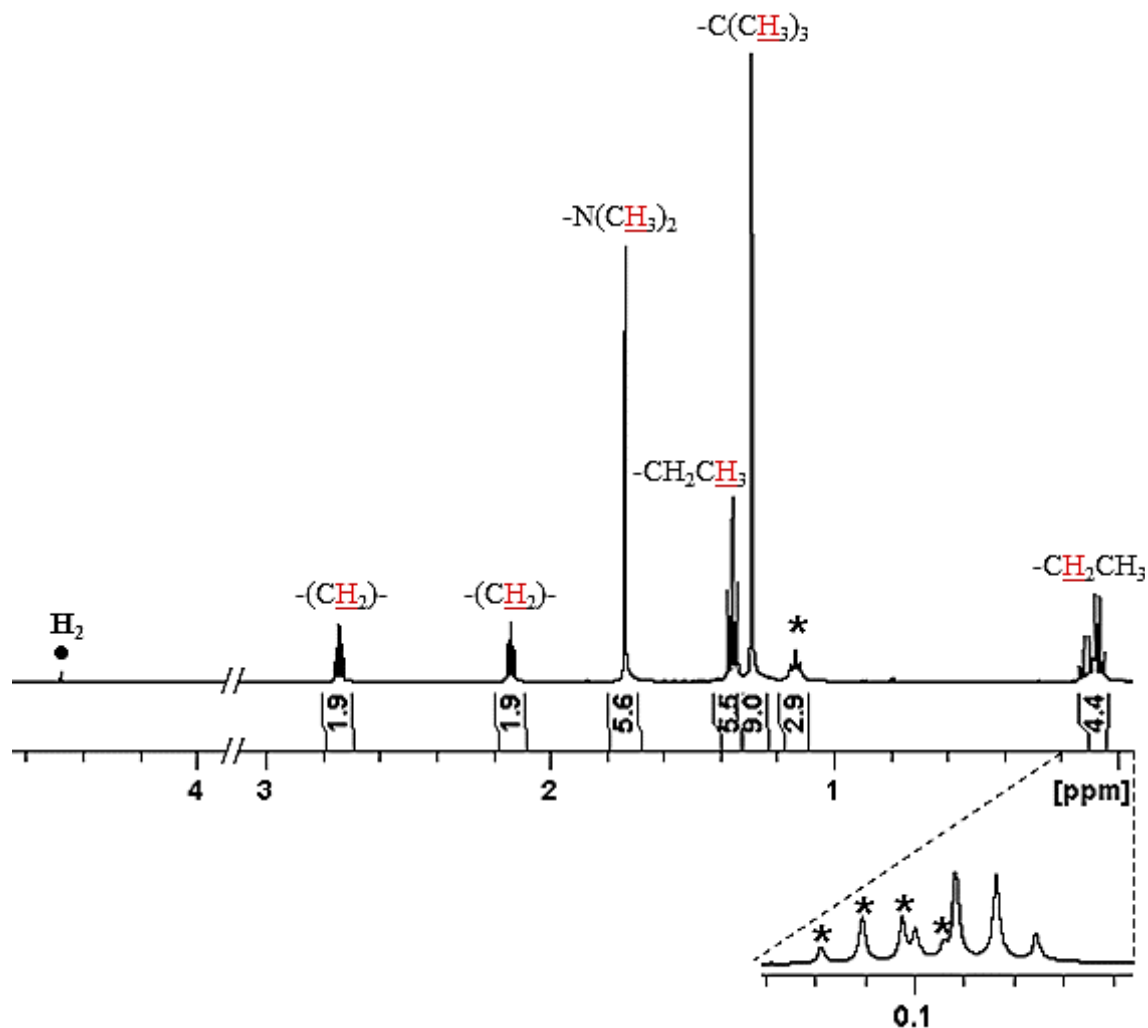


Figure 2.23: The proton NMR spectrum of the 1:1 reaction of ZnEt_2 with LAIH_2 in d_6 -benzene with enlarged 0- 0.15 ppm region, collected after 24 hours of mixing the reagents at room temperature. The asterisks indicate peaks for unreacted, excess ZnEt_2 .

The grey precipitate produced in the reaction was isolated by centrifugation and washed with toluene followed by hexanes. The X-ray diffractogram of the precipitate is shown in Figure 2.24, and indicates that the precipitate is elemental zinc.

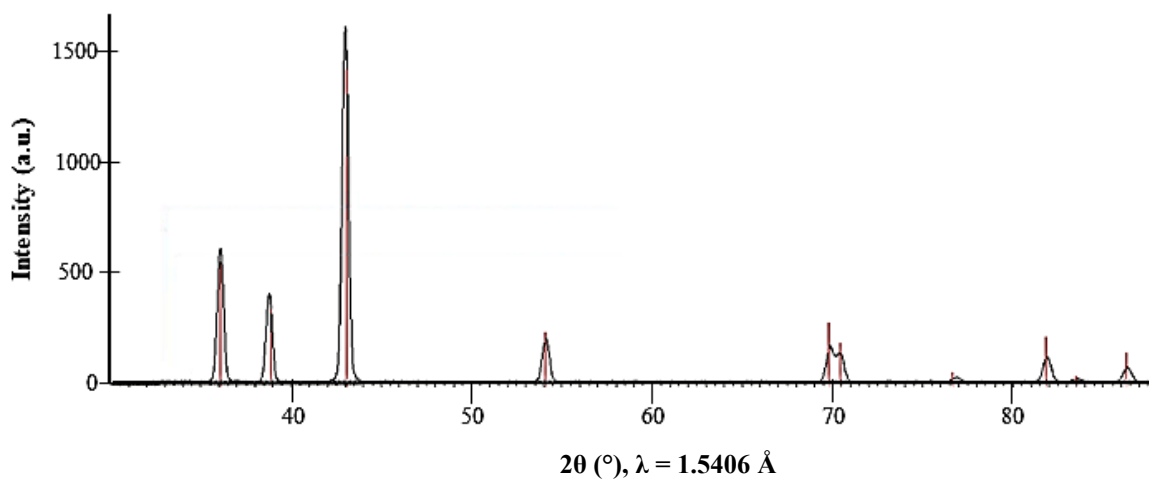
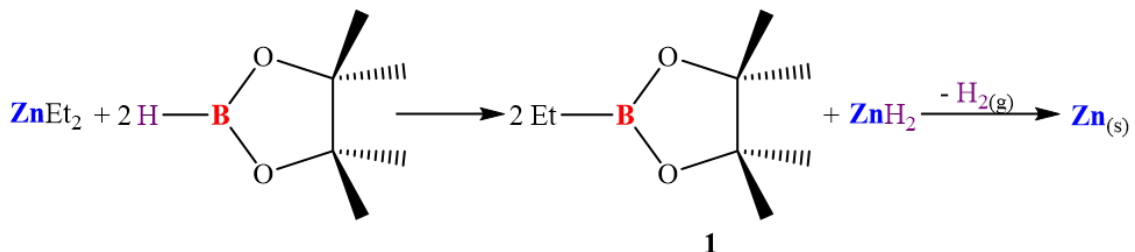


Figure 2.24: Powder X-ray diffractogram (PXRD) of the grey precipitate collected from the 1:1 reaction of ZnEt_2 with LiAlH_2 in d_6 -benzene, 24 h, RT. Red lines indicate the diffraction pattern corresponding to hexagonal zinc.

2.3.3.2 Reaction of ZnEt₂ with HBpin



Scheme 2.13: By-product anticipated for the 1:2 reaction between ZnEt₂ and HBpin (assuming pathway 02 in the Scheme 2.11).

Solutions of ZnEt₂ and HBpin in d₆-benzene were mixed together in a 1:2 ratio at room temperature. A white cloudy suspension started to form slowly after mixing the reagents which gradually started to turn in to a grey precipitate after 6 hours. A clear supernatant and a grey precipitate were observed after 24 hours. Product 01, where the hydride group on HBpin has been replaced with an ethyl group from ZnEt₂ was predicted as the only by-product of the reaction (Scheme 2.13).

A proton NMR spectrum of the reaction solution was collected at room temperature 24 hours after mixing the reagents (Figure 2.25). The spectrum indicates the formation of hydrogen gas with a peak at 4.47 ppm (Figure 2.25: Labelled with a circle). The only by-product observed from the reaction was EtBpin along with some unreacted ZnEt₂. The formation of EtBpin was confirmed by comparison of ¹H, ¹³C{¹H}, and ¹¹B{¹H} NMR spectra with that of commercial sample of EtBpin. Further characterization of EtBpin is discussed in the section 2.4.

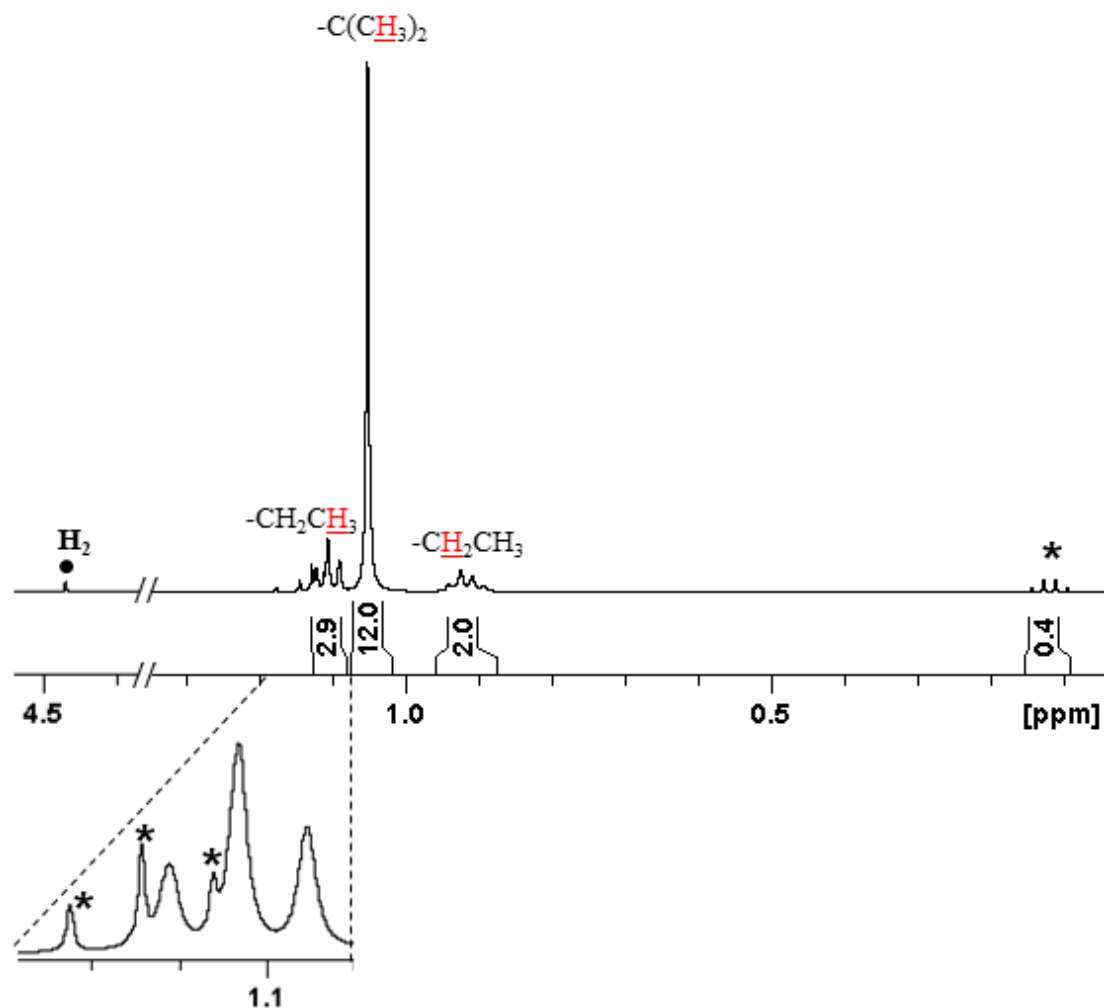


Figure 2.25: The proton NMR spectrum of the 1:2 reaction of ZnEt₂ with HBpin in d₆-benzene with enlarged 1.05- 1.15 ppm region, collected after 24 hours of mixing the reagents at room temperature. Asterisks indicate unreacted, excess ZnEt₂.

The grey precipitate from the reaction was isolated by centrifugation and the precipitate was washed with toluene followed by hexanes to remove any soluble contaminants. Figure 2.26 shows the X-ray diffractogram, which confirms the formation of elemental zinc.

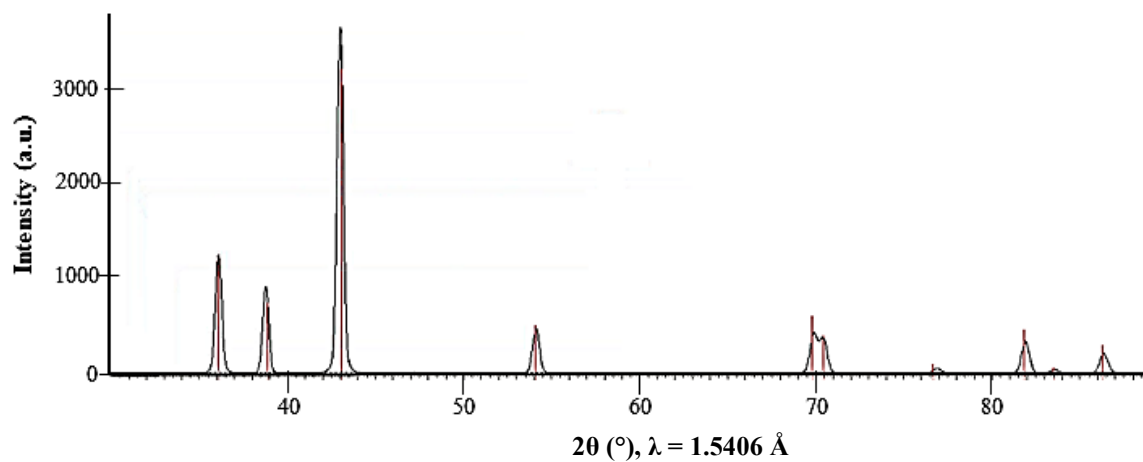


Figure 2.26: Powder X-ray diffractogram (PXRD) of the grey precipitate collected from 1:2 reaction of ZnEt_2 with HBpin in d_6 -benzene, 24 h, RT. Red lines indicate the diffraction pattern corresponding to hexagonal zinc.

2.3.3.3 Reaction of ZnEt₂ with BH₃NMe₃

Solutions of ZnEt₂ and BH₃(NMe₃) in d₆-benzene were mixed in a 1:1 ratio at room temperature. The resulting solution was colourless, and no visual change was observed upon heating the reaction solution up to 80 °C for 24 hours. The proton NMR spectrum (Figure 2.27) confirmed that no reaction had taken place.

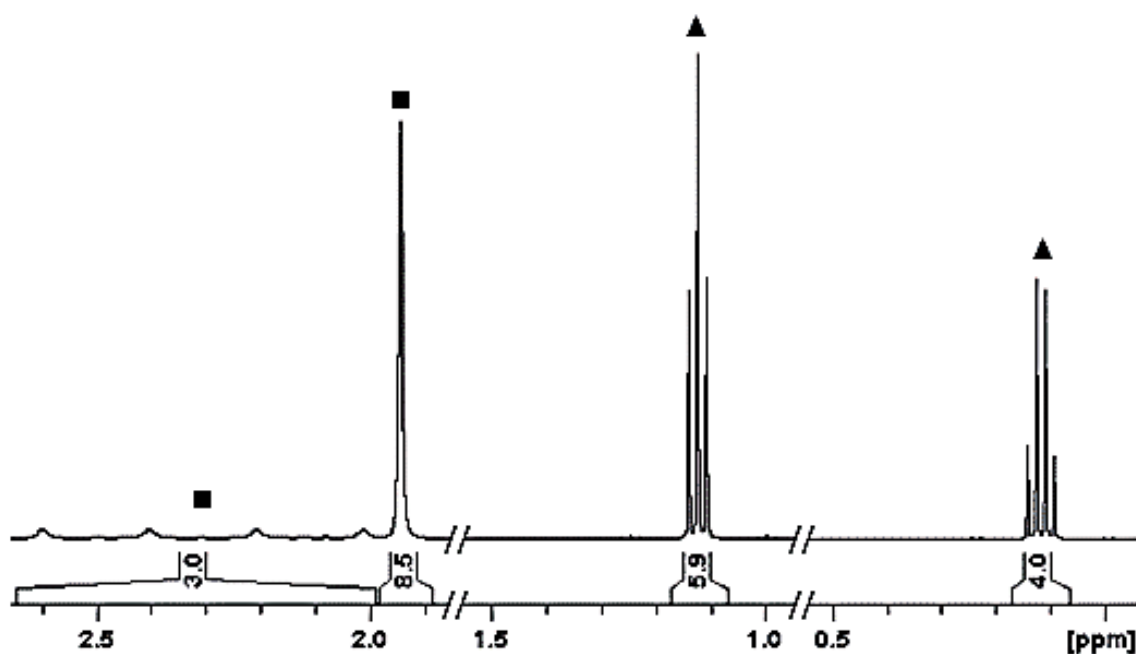


Figure: 2.27: The proton NMR spectrum of the 1:1 reaction of ZnEt₂ with BH₃(NMe₃) in d₆-benzene, collected after heating the reaction solution for 24 hours at 80 °C. Squares indicate free BH₃(NMe₃) and triangles indicate free ZnEt₂.

2.3.3.4 Reaction of ZnEt_2 with PhSiH_3

An equimolar amount of PhSiH_3 was added to a solution of ZnEt_2 in d_6 -benzene at room temperature. A colourless, clear solution was observed after mixing the reagents. The reaction solution indicated no change after heating at $80\text{ }^\circ\text{C}$ for 24 hours and the proton NMR spectrum (Figure 2.28) confirmed that no reaction had taken place.

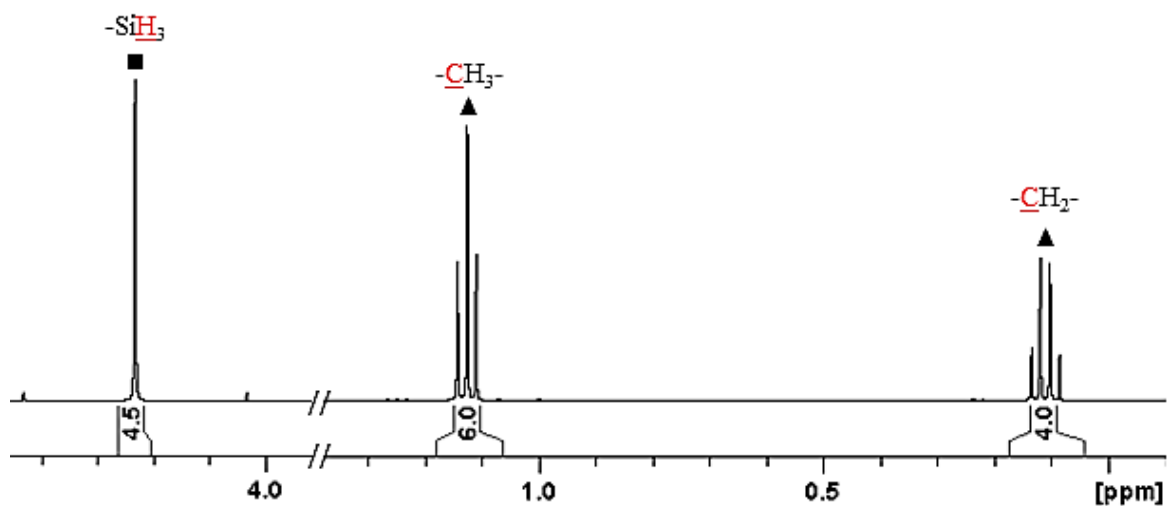


Figure 2.28: The proton NMR spectrum of the 1:1 reaction between ZnEt_2 and PhSiH_3 in d_6 -benzene collected after heating the reaction solution for 24 hours at $80\text{ }^\circ\text{C}$. The square indicates free PhSiH_3 and the triangles indicate free ZnEt_2 .

2.4 Further characterization of by-products formed in solution reactions with HBpin and LAIH₂

Solution reactions with HBpin or LAIH₂ proceeded cleanly (forming just one or two reaction by-products), so attempts were taken to further characterize those products.

2.4.1 MeBpin, (*i*PrO)Bpin, and EtBpin

All zinc precursors examined in the current study successfully produced elemental zinc upon reaction with HBpin, along with MeBpin, (*i*PrO)Bpin and/or EtBpin. From the 1:2 reaction of MeZnO^{*i*}Pr with HBpin in d₆-benzene, MeBpin and (*i*PrO)Bpin were produced. Both of these reagents are commercially available. ¹H, ¹³C{¹H} and ¹¹B{¹H} NMR spectra were collected for commercial samples of MeBpin and (*i*PrO)Bpin in d₆-benzene and compared against the NMR spectra of the 1:2 reaction between MeZnO^{*i*}Pr with HBpin in d₆-benzene. Figure 2.29 a, b, and c indicate the ¹H NMR spectra collected for (*i*PrO)Bpin, MeBpin, and the 1:2 reaction of MeZnO^{*i*}Pr with HBpin. Except for the excess HBpin remaining in the reaction, all other peaks align with MeBpin and (*i*PrO)Bpin, confirming the formation of MeBpin and (*i*PrO)Bpin during the reaction.

¹¹B{¹H} NMR spectra (Figure 2.30) and ¹³C{¹H} NMR spectra (Figure 2.31) were also collected in the same manner, and except for peaks corresponding to unreacted HBpin, all other peaks align with MeBpin and (*i*PrO)Bpin. These NMR spectra provide further support for the formation of MeBpin and (*i*PrO)Bpin during the reaction between MeZnO^{*i*}Pr and HBpin.

The 1:3 reaction of $\text{Zn}(\text{O}^i\text{Pr})_2$ with HBpin in d_6 -benzene (40 °C, 24 h) produced (i PrO)Bpin as the only by-product. This product was conclusively identified by comparison of the ^1H , $^{13}\text{C}\{^1\text{H}\}$, and $^{11}\text{B}\{^1\text{H}\}$ NMR spectra for the reaction mixture (Figure 2.29, Figure 2.30, and Figure 2.31 respectively) with those for a commercial sample of (i PrO)Bpin.

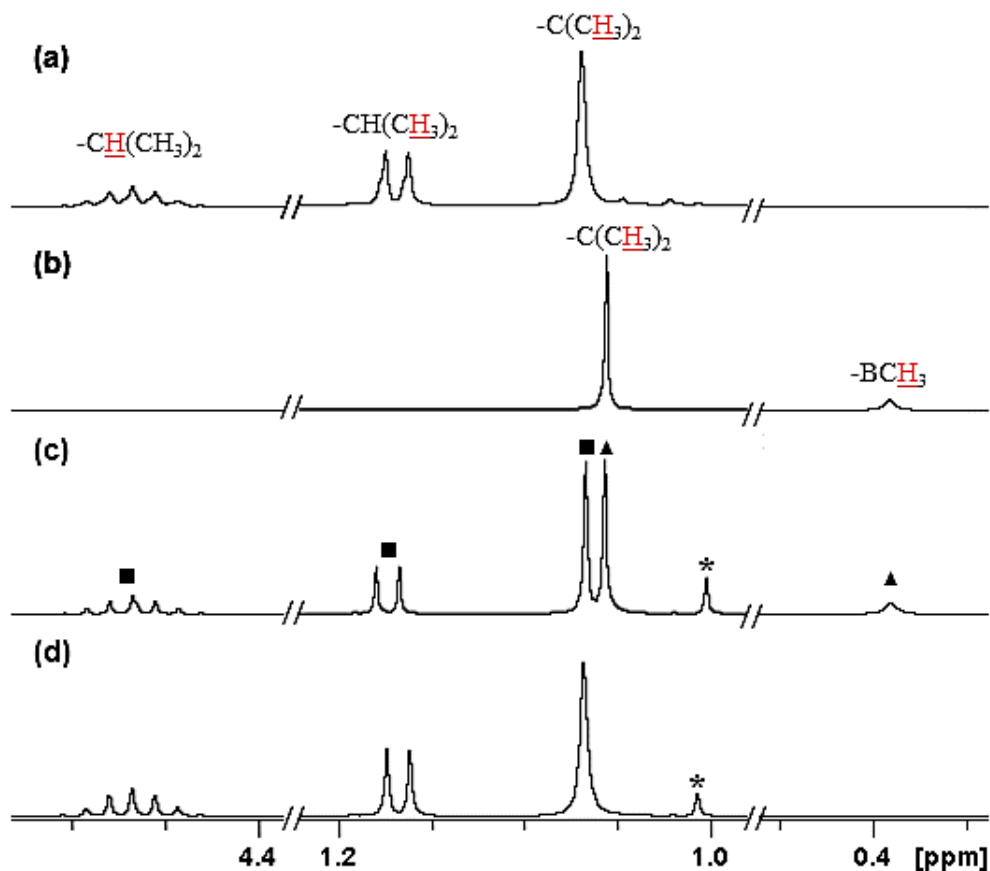


Figure 2.29: ^1H NMR spectra of a) (i PrO)Bpin, b) MeBpin, and c) 1:2 reaction of MeZnO^iPr with HBpin (24 h, RT), and d) 1:3 reaction of $\text{Zn}(\text{O}^i\text{Pr})_2$ with HBpin (24 h, 40 °C). Solvent; d_6 -benzene. Squares indicate peaks related to (i PrO)Bpin and triangles indicate peaks related to MeBpin. Excess HBpin is marked with an asterisk.

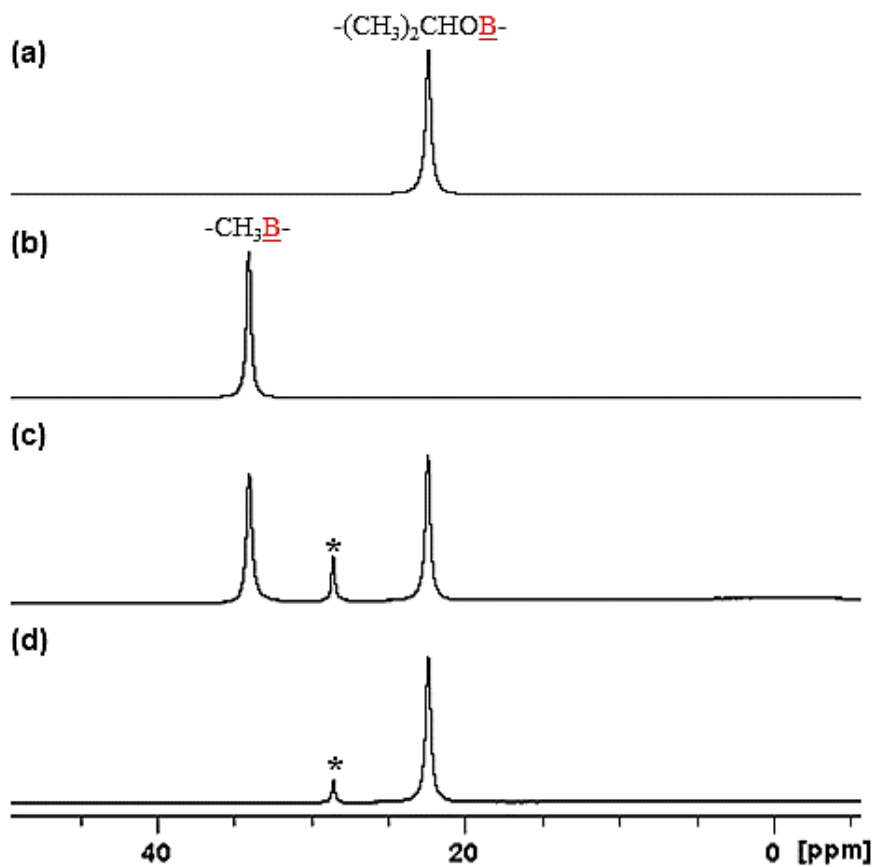


Figure 2.30: $^{11}\text{B}\{^1\text{H}\}$ NMR spectra of a) $(i\text{PrO})\text{Bpin}$, b) MeBpin , and c) 1:2 reaction of $\text{MeZnO}i\text{Pr}$ with HBpin (24 h, RT), and d) 1:3 reaction of $\text{Zn}(\text{O}i\text{Pr})_2$ with HBpin (24 h, 40 $^\circ\text{C}$). Solvent; d_6 -benzene. The asterisk indicates unreacted HBpin .

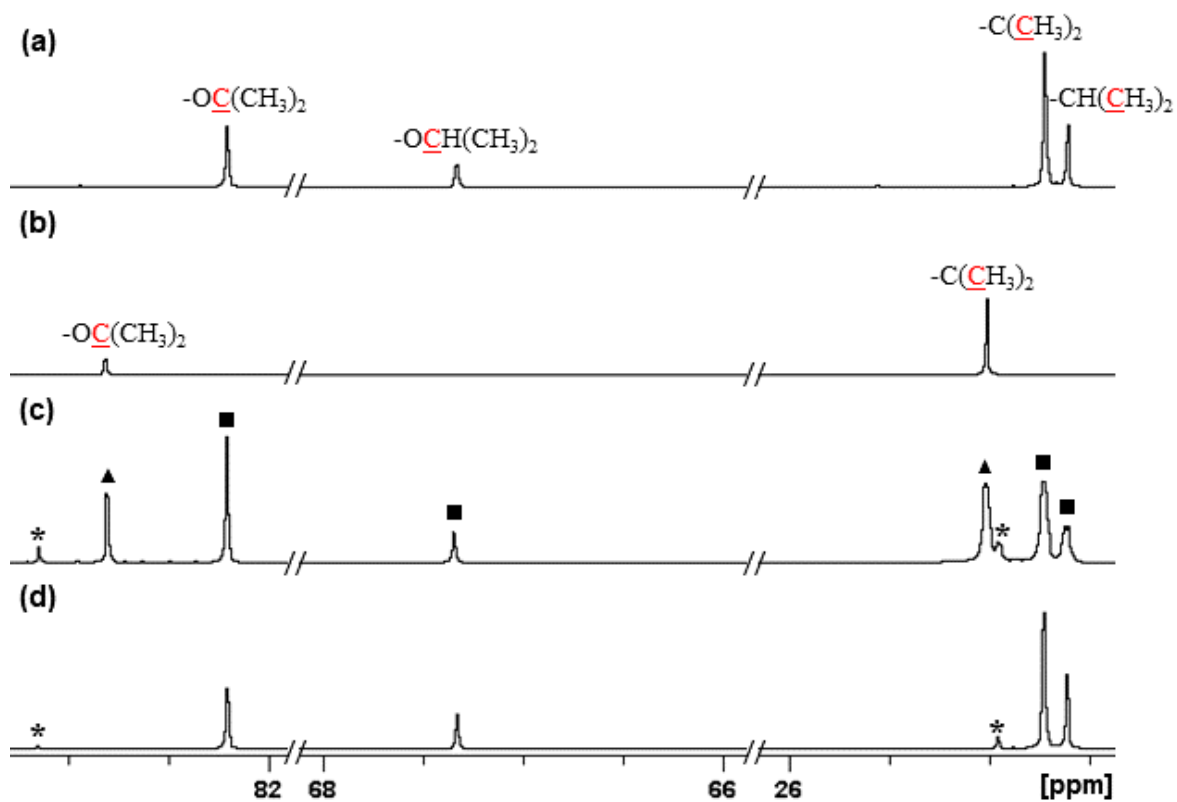


Figure 2.31: $^{13}\text{C}\{^1\text{H}\}$ NMR spectra of a) (*i*PrO)Bpin, b) MeBpin, and c) 1:2 reaction of MeZnO*i*Pr with HBpin (24 h, RT), and d) 1:3 reaction of Zn(O*i*Pr)₂ with HBpin (24 h, 40 °C). Solvent; *d*₆-benzene. Squares indicate peaks related to (*i*PrO)Bpin and triangles indicate peaks related to MeBpin. Excess HBpin is marked with an asterisk.

EtBpin was the only by-product produced in the 1:2 reaction between ZnEt_2 and HBpin (24 h, RT, d_6 -benzene). Comparison of the ^1H , $^{13}\text{C}\{^1\text{H}\}$, and $^{11}\text{B}\{^1\text{H}\}$ NMR spectra for the reaction mixture (Figure 2.32, Figure 2.33, Figure 2.34 respectively) with those for a commercial sample of EtBpin allowed conclusive identification of this by-product.

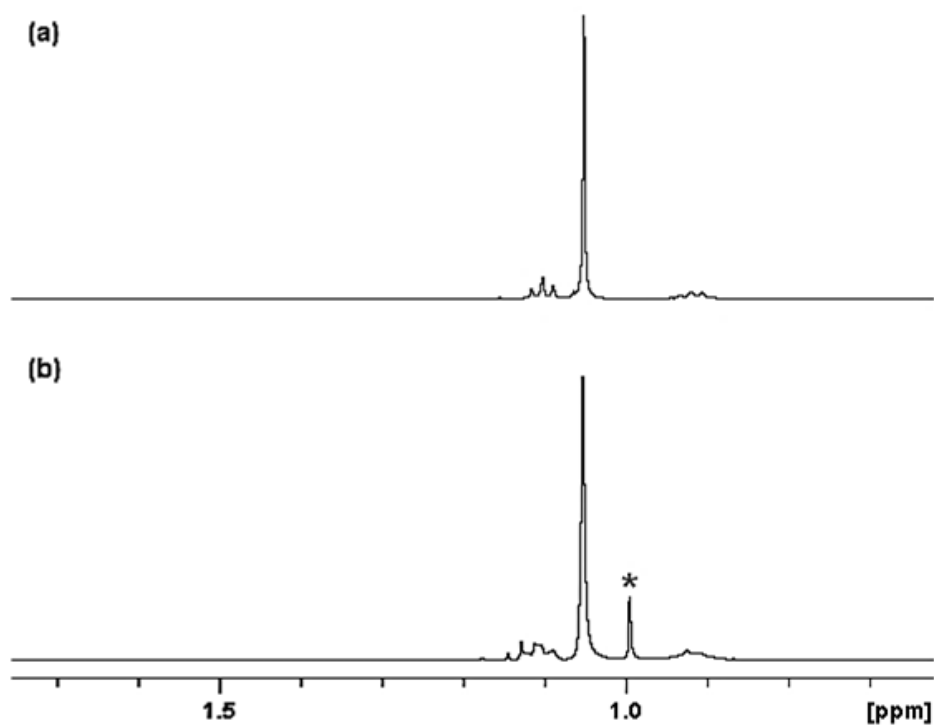


Figure 2.32: ^1H NMR spectra of a) EtBpin, and b) 1:2 reaction of ZnEt_2 with HBpin (24 h, RT). Solvent; d_6 -benzene. The asterisk indicates unreacted HBpin.

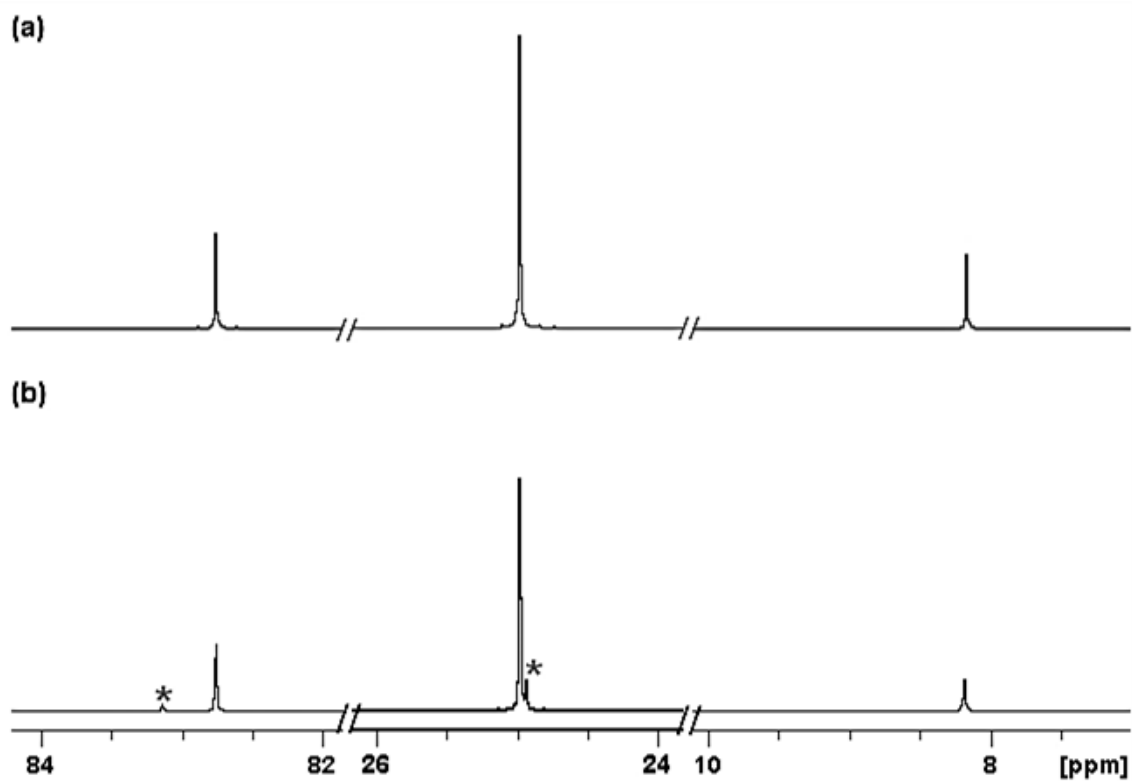


Figure 2.33: $^{13}\text{C}\{^1\text{H}\}$ NMR spectra of a) EtBpin, and b) 1:2 reaction of ZnEt_2 with HBpin (24 h, RT). Solvent; d_6 -benzene. The asterisks indicate unreacted HBpin.

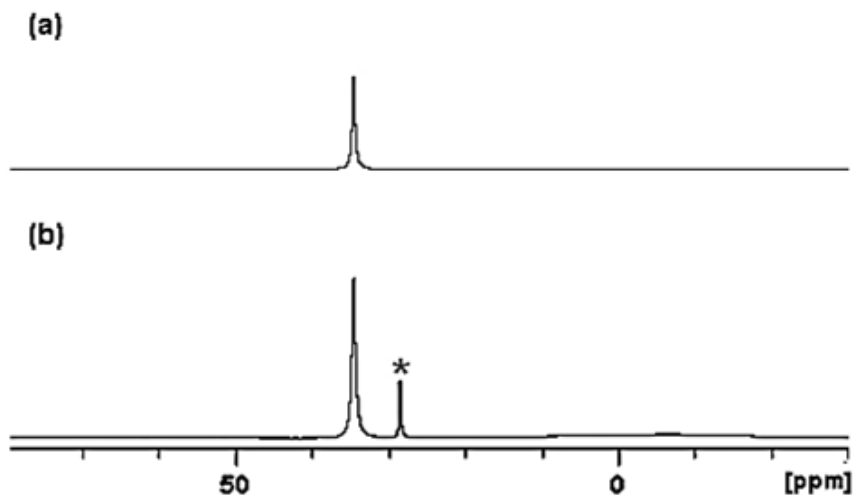


Figure 2.34: $^{11}\text{B}\{^1\text{H}\}$ NMR spectra of a) EtBpin, and b) 1:2 reaction of ZnEt_2 with HBpin (24 h, RT). Solvent; d_6 -benzene. The asterisk indicates unreacted HBpin.

2.4.2 (*t*-BuNCH₂CH₂NMe₂)Al(O^{*i*}Pr)₂ (LAl(O^{*i*}Pr)₂)

The 1:1 reaction of Zn(O^{*i*}Pr)₂ with LAlH₂ in d₆-benzene seemed to produce LAl(O^{*i*}Pr)₂ as identified by the proton NMR spectrum. In order to further characterize the by-product, excess Zn(O^{*i*}Pr)₂ was reacted with a solution of LAlH₂ in d₆-benzene at room temperature to completely convert LAlH₂ into LAl(O^{*i*}Pr)₂. Excess, unreacted Zn(O^{*i*}Pr)₂ was removed along with elemental zinc precipitates to collect LAl(O^{*i*}Pr)₂ in d₆-benzene and the solution was concentrated. Further characterizations of LAl(O^{*i*}Pr)₂ were done by collecting ¹H, ¹³C{¹H}, and HSQC NMR spectra of the compound. Comparison of ¹H NMR spectrum (Figure 2.35 a), ¹³C{¹H} NMR spectrum (Figure 2.35 b), and the HSQC NMR spectrum (Figure 2.36) evidently confirms the formation of LAl(O^{*i*}Pr)₂ without any significant impurities.

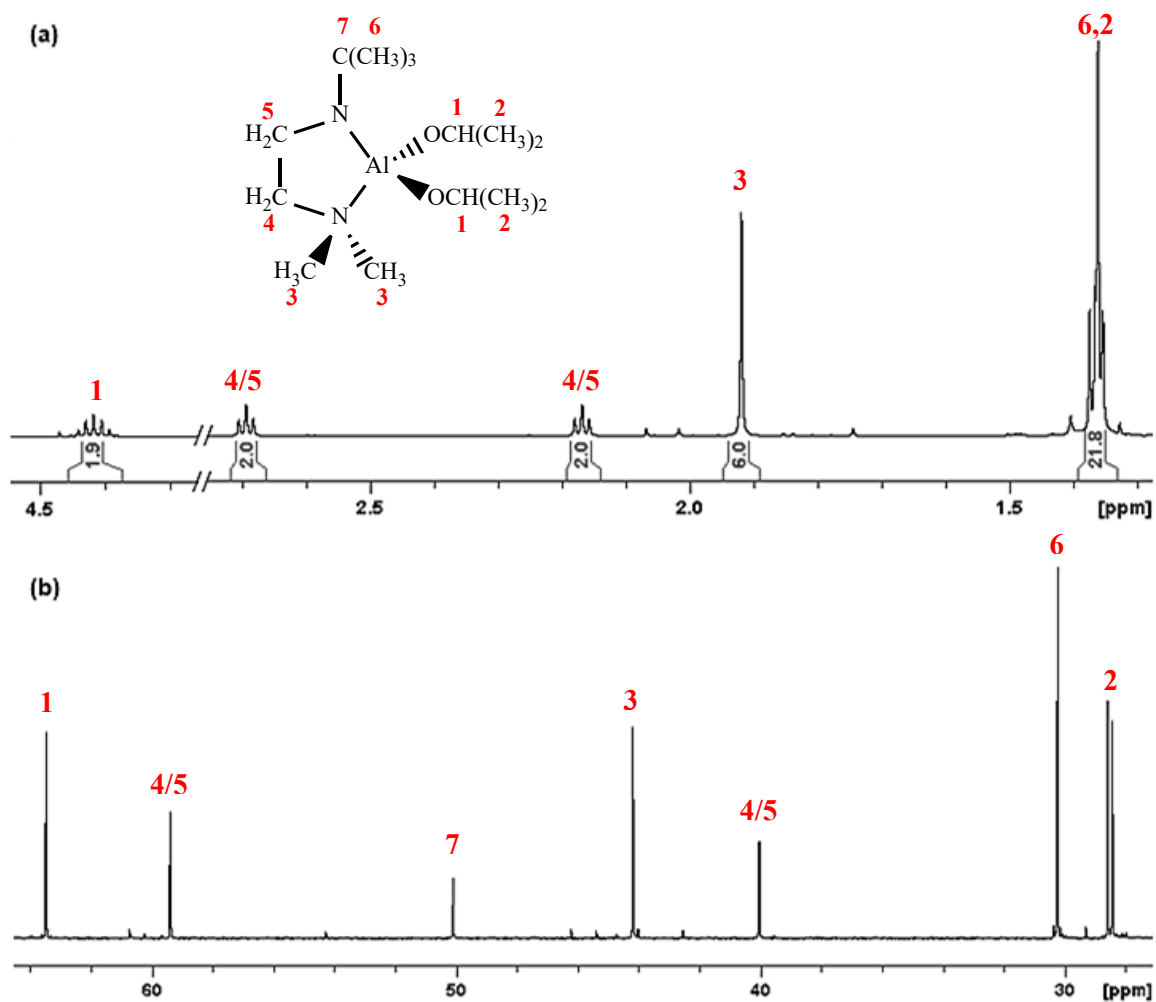


Figure 2.35: a) ^1H NMR spectrum and b) $^{13}\text{C}\{^1\text{H}\}$ NMR spectrum collected for $\text{LAl}(\text{O}^i\text{Pr})_2$ in d_6 -benzene.

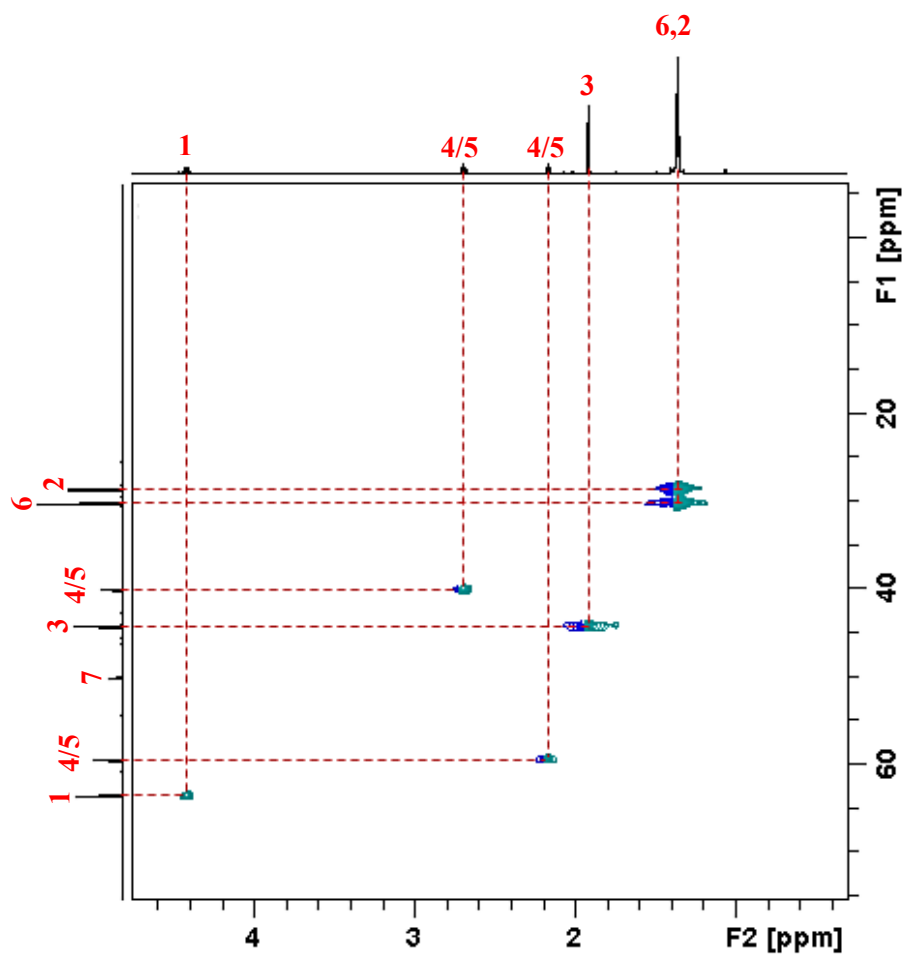
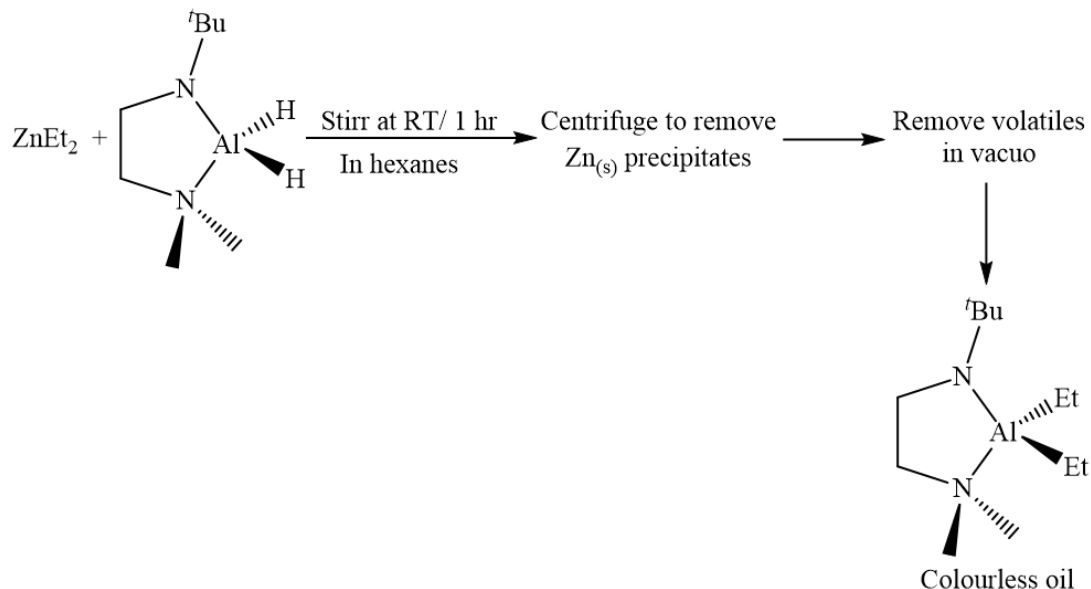


Figure 2.36: Heteronuclear single quantum correlation (HSQC) NMR spectrum of LAI(O^{*i*}Pr)₂ in d₆-benzene.

2.4.3 (^tBuNCH₂CH₂NMe₂)AlEt₂ (LAlEt₂)



Scheme 2.14: Reaction scheme for the synthesis of LAlEt₂.

LAlEt₂ was synthesized by the reaction between ZnEt₂ and LAlH₂. Solutions of these reagents in benzene were mixed in a 1:1 ratio at room temperature and stirred for few hours. The resulting reaction mixture was centrifuged to remove elemental zinc precipitates. Volatiles were removed in vacuo to obtain a colourless oil with a yield of 50%. In order to characterize LAlEt₂, NMR spectra of the compound were collected (Figure 2.37). Both ¹H and ¹³C{¹H} spectra indicate the formation of LAlEt₂ without any impurities. An HSQC-NMR spectrum collected for LAlEt₂ (Figure 2.38) provides the direct C-H connectivity.

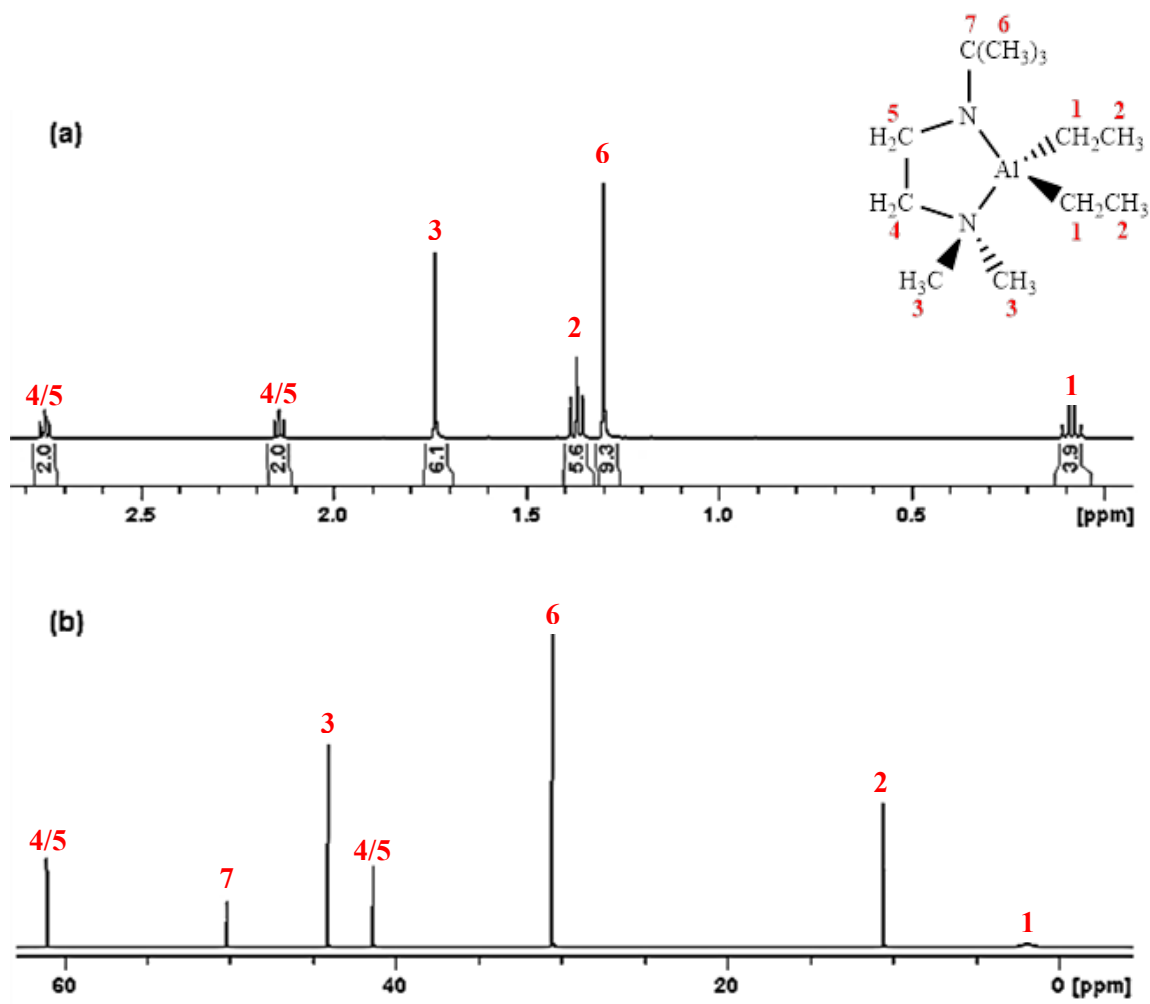


Figure 2.37: a) ^1H NMR spectrum and b) $^{13}\text{C}\{^1\text{H}\}$ NMR spectrum collected for LAIEt_2 in d_6 -benzene.

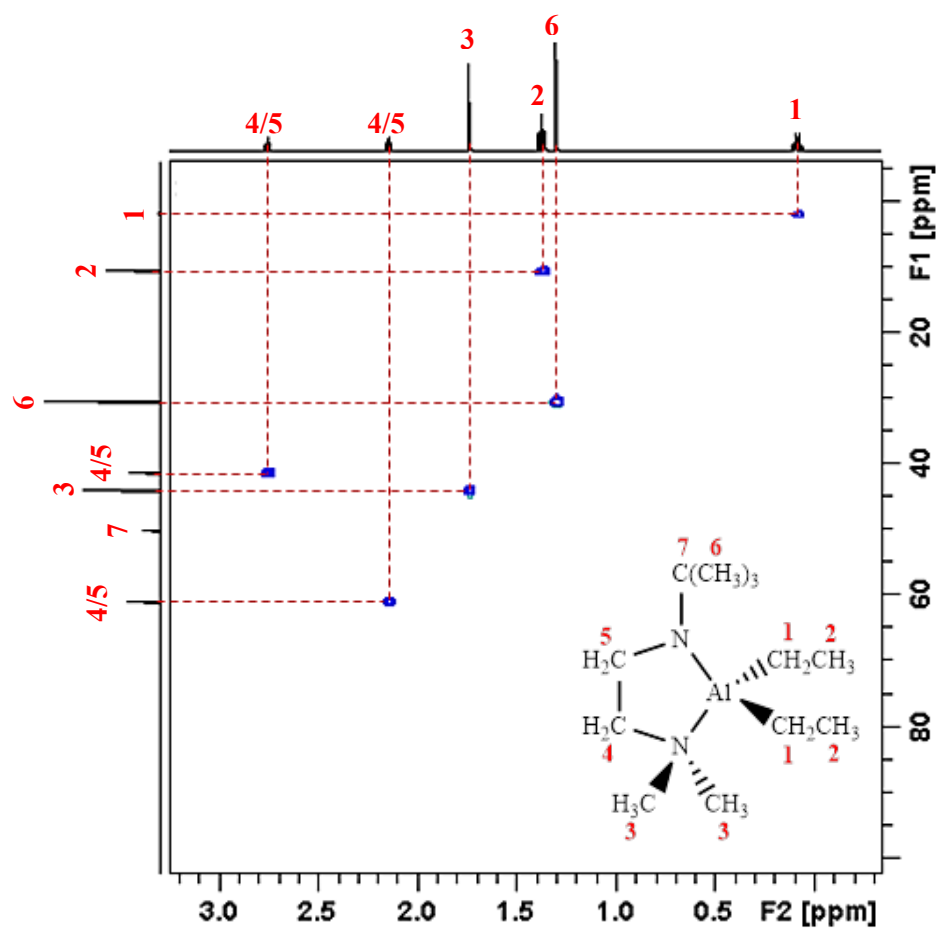


Figure 2.38: Heteronuclear single quantum correlation (HSQC) NMR spectrum of LAIEt_2 in d_6 -benzene.

2.5 Summary, conclusions, and future work

Solution reactions of $\text{MeZn}(\text{O}^i\text{Pr})$ and ZnEt_2 with hydride co-reagents were expected to follow two different pathways (Scheme 2.2 and Scheme 2.11 respectively). According to Scheme 2.2, solution reactions of $\text{MeZn}(\text{O}^i\text{Pr})$ should produce either CH_4 or H_2 gas while Scheme 2.11 predicts ZnEt_2 to produce either C_2H_6 or H_2 gas. However, analyzing the ^1H NMR spectra collected for reactions of both $\text{MeZn}(\text{O}^i\text{Pr})$ and ZnEt_2 with the various co-reactants (those that reacted) confirmed the formation of H_2 gas. No indication of formation of CH_4 or C_2H_6 was observed in solution screening studies. This confirms that solution reactions of both $\text{MeZn}(\text{O}^i\text{Pr})$ and ZnEt_2 follow the reaction pathway 02, which replaces both ligands on Zn with hydride groups to produce ZnH_2 . This ZnH_2 then undergoes reductive elimination to produce elemental Zn and H_2 gas. Similar reactivity was observed for solution reactions of $\text{Zn}(\text{O}^i\text{Pr})_2$, where formation of H_2 gas was detected in ^1H NMR spectra collected for reaction solutions. Formation of H_2 gas was confirmed as follows; the J-young tube was left open for few hours in the glovebox and the ^1H NMR spectrum was collected again, which revealed the disappearance of the H_2 peak at 4.47 ppm in d_6 -benzene.

Table 2.2 indicates a summary of results obtained from solution reactivity studies for all three zinc precursors with hydride co-reactants. None of the precursors indicated a reactivity with $\text{BH}_3(\text{NMe}_3)$ even after heating the reaction solutions at $80\text{ }^\circ\text{C}$ for 24 hours. Hence, $\text{BH}_3(\text{NMe}_3)$ appears to be the least reactive co-reactant in solution with the precursors studied. With $\text{AlH}_3(\text{Quinuclidine})$ (previous studies by an Emslie group member), LAH_2 , and HBpin , ZnEt_2 indicated the highest reactivity by forming elemental

Zn within hours after mixing reagents. However, it did not indicate any reactivity with either PhSiH_3 or $\text{BH}_3(\text{NMe}_3)$, even at temperatures up to $80\text{ }^\circ\text{C}$. From the two co-reactants that ZnEt_2 reacted with, the highest reactivity was observed with LAlH_2 compared to the reactivity with HBpin.

$\text{MeZn}(\text{O}^i\text{Pr})$ reacted with all co-reactants except $\text{BH}_3(\text{NMe}_3)$. The reactivity of $\text{MeZn}(\text{O}^i\text{Pr})$ with co-reactants can be arranged as follows from highest reactivity to lowest reactivity; $\text{LAlH}_2 > \text{HBpin} > \text{AlH}_3(\text{Quinuclidine}) > \text{PhSiH}_3 > \text{BH}_3(\text{NMe}_3)$ (no reaction). Elemental Zn was formed at room temperature from reactions with both LAlH_2 and HBpin.

Solution screening reactions of $\text{Zn}(\text{O}^i\text{Pr})_2$ indicated that $\text{Zn}(\text{O}^i\text{Pr})_2$ reacts with every co-reactant except $\text{BH}_3(\text{NMe}_3)$. However, comparing the reactivity of $\text{Zn}(\text{O}^i\text{Pr})_2$ against that of $\text{MeZn}(\text{O}^i\text{Pr})$ suggests a low reactivity for $\text{Zn}(\text{O}^i\text{Pr})_2$ which might be due to its insolubility in organic solvents. As a result, most solution reactions of $\text{Zn}(\text{O}^i\text{Pr})_2$ either required more time, heat or a large excess of the co-reactant to complete the reaction. In situations where co-reactant was not in large excess, traces of unreacted $\text{Zn}(\text{O}^i\text{Pr})_2$ were found in the precipitate with elemental zinc. Washing the precipitate with different organic solvents did not remove $\text{Zn}(\text{O}^i\text{Pr})_2$ as it is insoluble. However, this might not be an issue for ALD reactor studies since only gas phase reactions are considered, not reactions in solution. $\text{Zn}(\text{O}^i\text{Pr})_2$ reacted fastest with LAlH_2 and the reaction with $\text{AlH}_3(\text{Quinuclidine})$ was quicker (elemental Zn at RT, 24 h) than the reaction with HBpin, which required heating to complete the reaction (elemental Zn at $40\text{ }^\circ\text{C}$). The order of reactivity of $\text{Zn}(\text{O}^i\text{Pr})_2$ with co-reactants is as follows; $\text{LAlH}_2 > \text{AlH}_3(\text{Quinuclidine}) > \text{HBpin} > \text{PhSiH}_3 > \text{BH}_3(\text{NMe}_3)$ (no reaction).

LAlH_2 , HBpin, and $\text{AlH}_3(\text{Quinuclidine})$ are the only co-reactants to react with all three Zn precursors. LAlH_2 indicated the highest reactivity with all three Zn precursors and produced elemental Zn at room temperature. HBpin indicated a high reactivity with both $\text{MeZn}(\text{O}^i\text{Pr})$ and ZnEt_2 , and managed to produce elemental Zn at room temperature, but the reaction with $\text{Zn}(\text{O}^i\text{Pr})_2$ required heating the reaction solution at $40\text{ }^\circ\text{C}$ to complete the reaction.

Considering the overall reactivity shown by the precursors and their volatility, ZnEt_2 would be a good candidate to start reactor studies as it is a liquid and can be delivered to the reactor at room temperature. $\text{MeZn}(\text{O}^i\text{Pr})$ also indicates a decent reactivity and volatility which might be useful for reactor studies. Out of all co-reactants studied, reactions with LAlH_2 and HBpin could be employed as they indicated the highest reactivity with precursors.

Future studies would focus on reactor studies from the promising reactions of Zn precursors. For example, reactions of ZnEt_2 and $\text{MeZn}(\text{O}^i\text{Pr})$ with LAlH_2 and HBpin. This would require identifying the volatility and thermal stability of by-products formed during the reaction of ZnEt_2 with LAlH_2 and $\text{MeZn}(\text{O}^i\text{Pr})$ with LAlH_2 . Also identifying and characterizing the reaction by-products formed in the reaction between $\text{MeZn}(\text{O}^i\text{Pr})$ and LAlH_2 would be required to understand the appropriateness of the reaction for ALD reactor studies. Given that the availability and low cost of PhSiH_3 , reactions of PhSiH_3 with both $\text{MeZn}(\text{O}^i\text{Pr})$ and $\text{Zn}(\text{O}^i\text{Pr})_2$ would also be of interest as future ALD reactor studies.

Table 2.2: Summary of solution reactivity studies of Zn precursors. (* Indicates results from previous solution studies carried out by Dr. J. Price from Emslie lab).

| Precursors | Co-reactants | | | | |
|--|--|---|---|---|-------------------------------------|
| | LAIH ₂ | AlH ₃ (Quinuclidine) | HBpin | PhSiH ₃ | BH ₃ (NMe ₃) |
| Precursor: Co-reactant ratio | 1:1 | 1:1 | 1:2 | 1:1* | 1:1 |
| MeZn(OⁱPr) | White suspension forms immediately. Zn _(s) starts to form after 3-4 hours, RT. | White suspension remains after 24 h, RT. Zn _(s) starts to form at 40 °C. | White suspension forms immediately & remained unchanged after 12 hours. Zn _(s) at RT after 24 h | Zn _(s) at 90 °C | No reaction |
| Precursor: Co-reactant ratio | 1:1 | 1:2 | 1:5 | 1:2 | 1:1 |
| Zn(OⁱPr)₂ | White suspension starts to form in 3-4 hours. Zn _(s) starts to form after 6 hours, RT. | White suspension starts to form after 6 hours & unchanged after 12 hours. Zn _(s) at RT after 24 h | White suspension forms slowly & remained unchanged after 24 h Zn _(s) at 40 °C | Clear solution at 40 °C Zn _(s) at 60 °C | No reaction |

| Precursors | Co-reactants | | | | |
|------------------------------|--|--|---|------------------|-----------------------------|
| | LAIH_2 | $\text{AlH}_3(\text{Quinuclidine})$ | HBpin | PhSiH_3 | $\text{BH}_3(\text{NMe}_3)$ |
| Precursor: Co-reactant ratio | 1:1 | 1:1* | 1:2 | 1:1 | 1:1 |
| ZnEt₂ | Immediately starts to form $\text{Zn}_{(s)}$ within 10 minutes at RT | $\text{Zn}_{(s)}$ starts to form immediately after mixing the reagents. No film deposition on ALD reactor | White suspension forms immediately. $\text{Zn}_{(s)}$ starts to form after 6 hours, RT | No reaction | No reaction |

CHAPTER 3 – SOLUTION REACTIVITY STUDIES OF GERMANIUM (Ge) PRECURSORS

3.1 Selection of precursors - Stability and Volatility

Thermal ALD processes to deposit elemental Ge films have not been achieved before. Hence, one of the two goals of this research is to investigate potential precursor/co-reactant pairs with the intension of obtaining elemental germanium films by a thermal ALD process. Judicious selection of appropriate precursors is required to maximize the possibility of producing elemental germanium with co-reactants employed in this study.

Three homoleptic germanium precursors of the form $[\text{Ge}^{\text{II}}\text{L}_2]$ where, L is either Chloride, Bis(trimethylsilyl)amide ($\text{N}(\text{SiMe}_3)_2$), or Dimethylamino ethoxide ($\text{OCH}_2\text{CH}_2\text{NMe}_2$), were investigated as Ge precursors in the current study.

$\text{GeCl}_2(\text{Dioxane})$ is a moisture sensitive, white solid with a melting point of 176-178 °C.⁹⁸ It is insoluble in most organic solvents but slightly soluble in Et_2O and soluble in THF.⁹⁸ By comparison, dioxane-free GeCl_2 is less stable and disproportionates rapidly into GeCl_4 and elemental Ge at 70 °C. Dioxane has the ability to prevent this process by stabilizing GeCl_2 , in which it acts as a Lewis base and donates to vacant p orbital of the Ge atom in GeCl_2 .¹³¹ $\text{GeCl}_2(\text{Dioxane})$ has widely been used as the Ge precursor for ALD of Germanium antimony telluride (GST) materials, where it was delivered to the reactor at temperatures as low as 70 °C.^{91,90} $\text{GeCl}_2(\text{Dioxane})$ crystallizes in space group C 2/c with the structure containing infinite chains of alternating GeCl_2 and dioxane molecules with a

Ge-O distance of 2.399 Å.¹³² Figure 3.1 indicates the X-ray crystal structure and chemical diagram of GeCl₂(Dioxane).

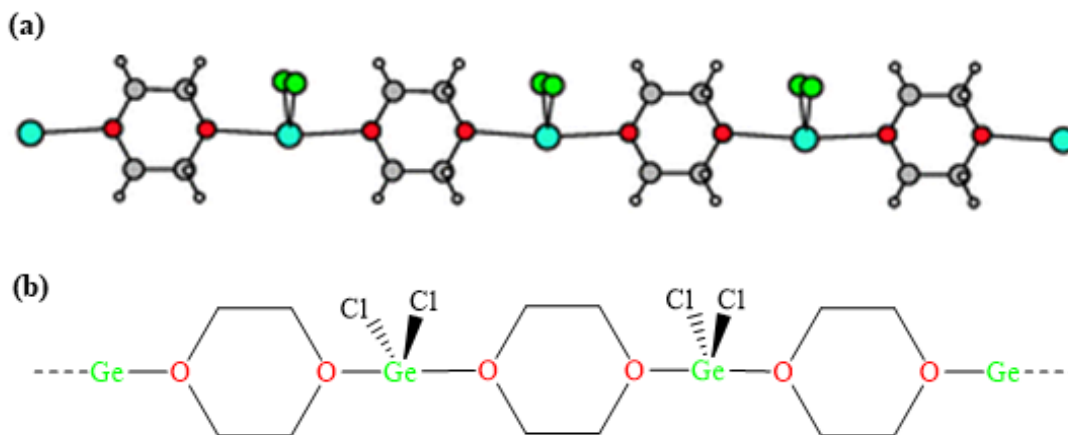


Figure 3.1: Crystal structure of GeCl₂(Dioxane). a) The chain structure; Space group: C 2/c, Cell: a = 7.5811 Å, b = 11.6974 Å, c = 8.7800 Å, $\alpha = 90^\circ$, $\beta = 97.129^\circ$, $\gamma = 90^\circ$ and b) Chemical diagram of GeCl₂(Dioxane).^{132,133} Reprinted with permission from ref. 6. Copyright 2010 Royal Society of Chemistry.

Ge{N(SiMe₃)₂}₂ is a volatile yellow solid with a melting point of 32-33 °C and a boiling point of 60 °C/ 0.4 Torr.⁹⁵ This two coordinate Ge compound is diamagnetic and a monomer in solid state.¹³⁴ Also, it exhibits a V-shaped geometry around Ge in which the central atom possesses a stereochemically active lone pair of electrons. This allows the central atom to have a singlet electronic ground state and hence, these molecules are described as carbene analogs.¹³⁴ The high reactivity and the high vapor pressure of Ge{N(SiMe₃)₂}₂ makes it an ideal candidate for CVD/ALD processes. It has been previously employed as a precursor in CVD processes to obtain elemental Ge at the deposition temperature of 325 °C.⁹⁶ Ge{N(SiMe₃)₂}₂ crystalizes in space group Pccn and

the X-ray crystal structure and the chemical diagram of $\text{Ge}\{\text{N}(\text{SiMe}_3)_2\}_2$ are indicated in Figure 3.2.¹³⁴

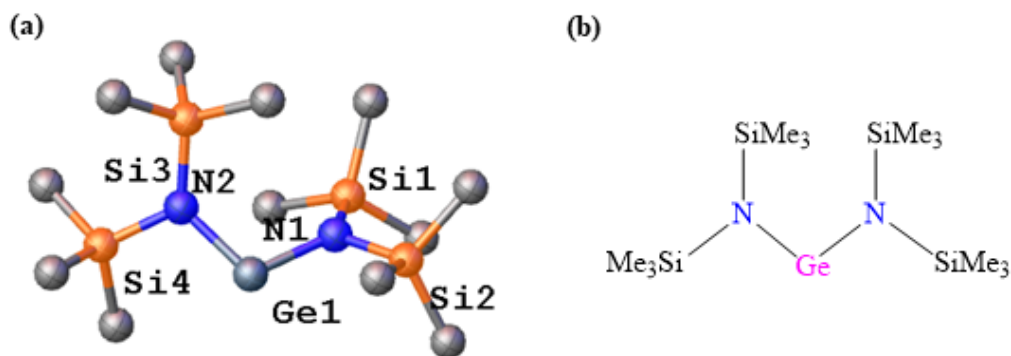


Figure 3.2: $\text{Ge}\{\text{N}(\text{SiMe}_3)_2\}_2$, a) X-ray structure; Space group: *Pccn*, Cell: $a = 16.632 \text{ \AA}$, $b = 20.323 \text{ \AA}$, $c = 13.148 \text{ \AA}$, $\alpha = \beta = \gamma = 90^\circ$ and b) Chemical diagram.¹³⁴

$\text{Ge}(\text{OCH}_2\text{CH}_2\text{NMe}_2)_2$ is a volatile, white crystalline solid, which is only stable under anaerobic conditions and is soluble in standard organic solvents.¹³⁵ $\text{Ge}(\text{OCH}_2\text{CH}_2\text{NMe}_2)_2$ is a sterically non-hindered monomeric compound with intramolecular $\text{Ge} \leftarrow \text{N}$ coordination bonds.¹³⁵ $\text{Ge}(\text{OCH}_2\text{CH}_2\text{NMe}_2)_2$ can be synthesized from rapid alcoholysis of $\text{Ge}\{\text{N}(\text{SiMe}_3)_2\}_2$ by 2-dimethylamino ethanol.¹³⁵ $\text{Ge}(\text{OCH}_2\text{CH}_2\text{NMe}_2)_2$ sublimes at $70^\circ\text{C}/1 \text{ mTorr}$ and its melting point is $67\text{-}68^\circ\text{C}$.¹³⁵ Thermal stability studies of $\text{Ge}(\text{OCH}_2\text{CH}_2\text{NMe}_2)_2$ revealed that it is stable up to 140°C . $\text{Ge}(\text{OCH}_2\text{CH}_2\text{NMe}_2)_2$ is a promising Ge precursor for ALD processes, as it can be delivered to the reactor at relatively low temperatures due to its volatility, it can be easily synthesized in large scale, and it possesses adequate thermal stability. However, it has not been previously employed in CVD or ALD processes. $\text{Ge}(\text{OCH}_2\text{CH}_2\text{NMe}_2)_2$ crystallizes in the space group $\text{P}2_12_12_1$ and

Ge(II) atom adopts a distorted trigonal bipyramidal configuration with a lone pair electron in the equatorial position.¹³⁵ Figure 3.3 indicates the X-ray crystal structure and chemical diagram of $\text{Ge}(\text{OCH}_2\text{CH}_2\text{NMe}_2)_2$.

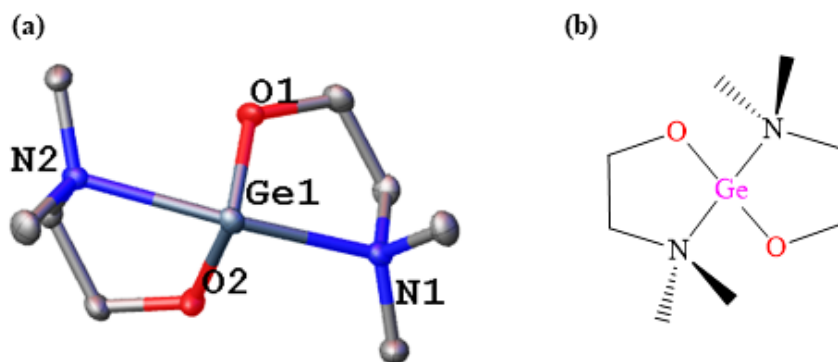
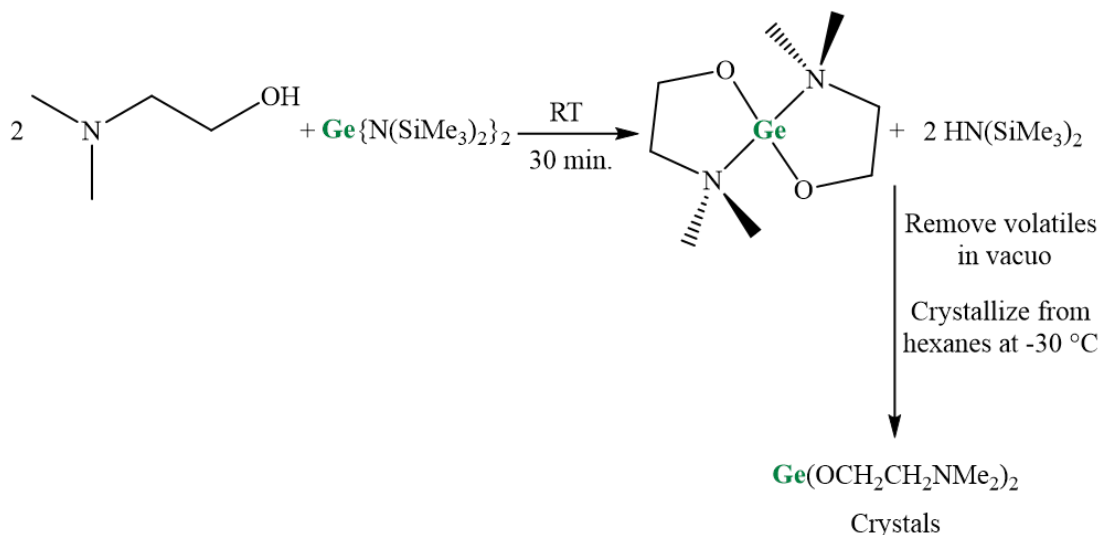


Figure 3.3: $\text{Ge}(\text{OCH}_2\text{CH}_2\text{NMe}_2)_2$, a) X-ray crystal structure; Space group: $P2_12_12_1$, Cell: $a = 10.1606 \text{ \AA}$, $b = 11.2693 \text{ \AA}$, $c = 20.3870 \text{ \AA}$, $\alpha = \beta = \gamma = 90^\circ$ and b) Chemical diagram.¹³⁵

3.2 Precursor synthesis

From the three germanium precursors that were employed in the current study, only $\text{Ge}(\text{OCH}_2\text{CH}_2\text{NMe}_2)_2$ was synthesized in the lab. The other two germanium precursors, $\text{GeCl}_2(\text{Dioxane})$ and $\text{Ge}\{\text{N}(\text{SiMe}_3)_2\}_2$, are commercially available.



Scheme 3.1: Reaction scheme for the synthesis of $\text{Ge}(\text{OCH}_2\text{CH}_2\text{NMe}_2)_2$.¹³⁵

$\text{Ge}(\text{OCH}_2\text{CH}_2\text{NMe}_2)_2$ was synthesized via the reaction of $\text{Ge}\{\text{N}(\text{SiMe}_3)_2\}_2$ with pre-dried $\text{Me}_2\text{NCH}_2\text{CH}_2\text{OH}$, following the literature procedure, as shown in the Scheme 3.1.¹³⁵ The exothermic reaction was complete in several minutes and the only by-product of the reaction, hexamethyldisilazane was removed in vacuo. The crude product was collected and recrystallized from hexanes at $-30\text{ }^\circ\text{C}$ to obtain a white crystalline solid with a yield of 73%. The ^1H and $^{13}\text{C}\{^1\text{H}\}$ NMR spectra of $\text{Ge}(\text{OCH}_2\text{CH}_2\text{NMe}_2)_2$ were collected (Figure 3.4) and compared against spectral data mentioned in literature to evaluate the purity of the

product and effectiveness of the reaction.¹³⁵ Comparison of spectral data confirmed the formation of pure $\text{Ge}(\text{OCH}_2\text{CH}_2\text{NMe}_2)_2$.

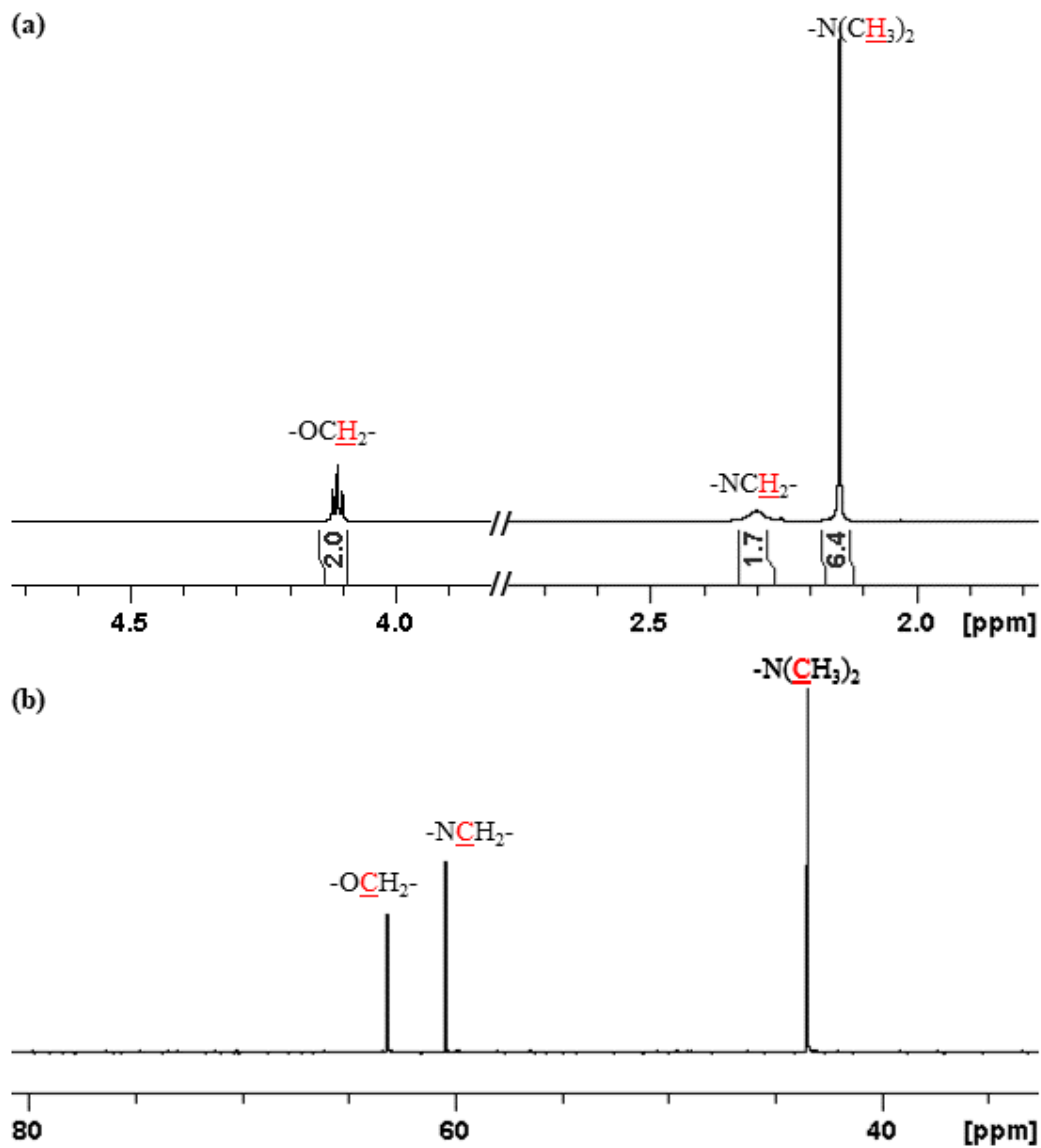


Figure 3.4: a) ^1H and b) $^{13}\text{C}\{^1\text{H}\}$ NMR spectra collected for $\text{Ge}(\text{OCH}_2\text{CH}_2\text{NMe}_2)_2$ in d_6 -benzene.

An ideal ALD precursor should have a good thermal stability to prevent its decomposition at deposition temperatures. Thermal stability of $\text{Ge}(\text{OCH}_2\text{CH}_2\text{NMe}_2)_2$ was investigated by heating a solid sample of $\text{Ge}(\text{OCH}_2\text{CH}_2\text{NMe}_2)_2$ under dynamic argon for 24 hours at 100 °C and 140 °C, and the proton NMR spectrum after heating at each temperature was collected (Figure 3.5). No visual change was observed for $\text{Ge}(\text{OCH}_2\text{CH}_2\text{NMe}_2)_2$ at these temperatures. Comparison of NMR spectra collected after heating at 100 °C and 140 °C with the pure $\text{Ge}(\text{OCH}_2\text{CH}_2\text{NMe}_2)_2$ sample shows that $\text{Ge}(\text{OCH}_2\text{CH}_2\text{NMe}_2)_2$ is stable up to 140 °C.

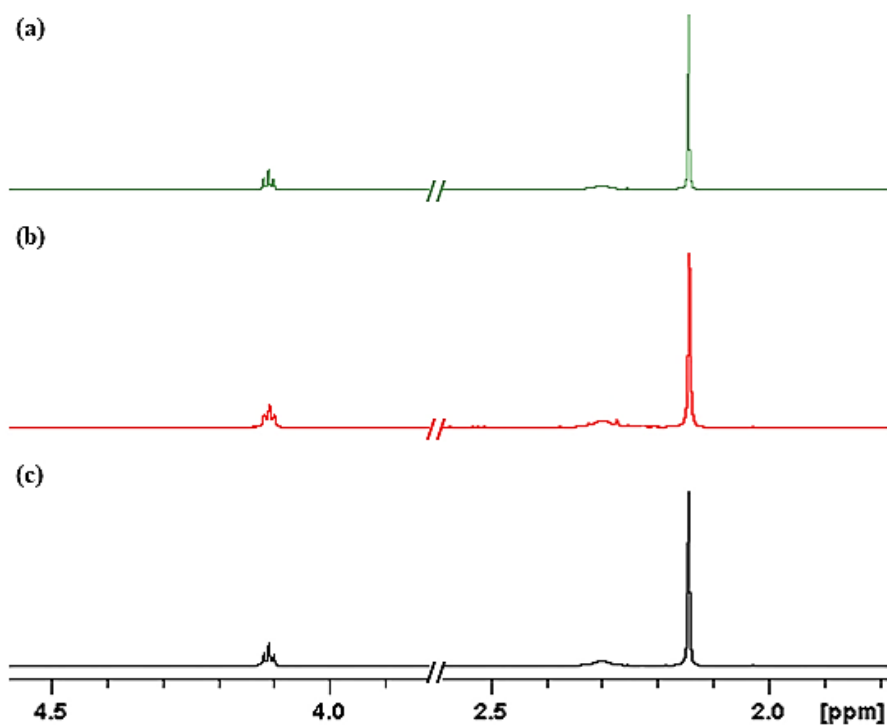


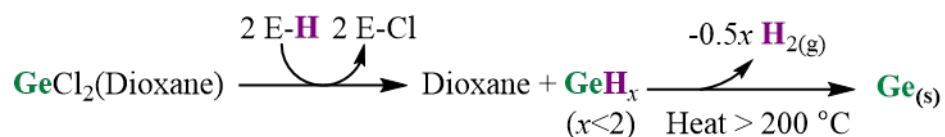
Figure 3.5: Proton NMR spectra collected for thermal stress testing of $\text{Ge}(\text{OCH}_2\text{CH}_2\text{NMe}_2)_2$ in d_6 -benzene, a) at RT, b) heated at 100 °C/24 h under dynamic argon, and c) heated at 140 °C/24 h under dynamic argon.

3.3 Solution reactivity studies

To explore reactivity between potential Ge precursors and reducing reagents, solution screening reactions were carried out. Analyzing information obtained from solution reactivity studies helps to identify particularly promising precursors/co-reactant combinations for elemental germanium deposition by ALD. Furthermore, solution reactivity studies can also provide insight into reaction mechanisms and by-products formed in the reactions. Solutions of the reactants prepared in d_6 -benzene and were mixed together at room temperature. These reaction solutions then maintained at several different temperatures from 20 to 80 °C for 24 hours at each temperature, as a method of examining reactivity at elevated temperatures. Several different stoichiometries between reagents were used to study the product distribution. Some solution reactions indicated no change in reactivity upon changing stoichiometric ratios between reagents. Reactions that indicated a difference in reactivity based on the stoichiometric ratios have been described in detail. NMR scale reactions, where reagents were mixed in few milligrams (10-25 mg) were employed for solution screening studies. Reaction pathways and the by-products formed in the reactions were identified using NMR spectra collected for each reaction. Any precipitates formed in the reactions were isolated and characterized where applicable; powder X-ray diffraction (PXRD) was used as the main method to characterize precipitates formed in reactions.

3.3.1 Solution reactivity studies of GeCl₂(Dioxane)

Reactivity of GeCl₂(Dioxane) in solution towards all hydride co-reactants (Figure 1.17) was investigated. GeCl₂(Dioxane) is nearly insoluble in most common organic solvents and only soluble in THF. However, d₈-THF is an expensive solvent compared to d₆-benzene and residual THF peak in ¹H NMR spectrum overlaps with the 1,4-dioxane peak. Hence reactions were carried out in d₆-benzene, despite the low solubility of GeCl₂(Dioxane) in this solvent.

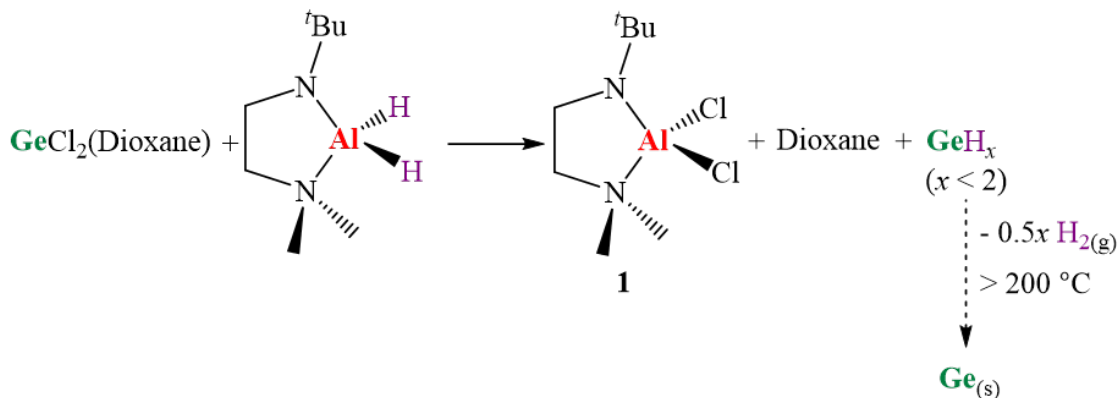


Scheme 3.2: Proposed reaction pathway for reactions of GeCl₂(Dioxane) with hydride reagents to produce elemental germanium. E = Bpin, LAIH (L = ^tBuNCH₂CH₂NMe₂), AlH₂(Quinuclidine), BH₂(NMe₃), or PhSiH₂.

The general reaction pathways anticipated for solution reactions between GeCl₂(Dioxane) and hydride co-reagents are shown in Scheme 3.2. During the first step of the reaction, a ligand exchange reaction replaces both chloride groups on GeCl₂(Dioxane) to produce a polymeric germanium hydride (GeH_x, x < 2) as the first intermediate, along with 1,4-dioxane.^{136,137} GeH_x is then expected to reductively eliminate hydrogen gas to produce elemental germanium at temperatures around 200 °C.^{136,137} Synthesis and thermal stability of GeH_x is discussed in detail in Section 3.4. Since x is less than 2 in GeH_x, reactions that

produce GeH_x are expected to produce hydrogen gas, which will give rise to a peak in the proton NMR spectrum at 4.47 ppm in d_6 -benzene.

3.3.1.1 Reaction of $\text{GeCl}_2(\text{Dioxane})$ with LAIH_2



Scheme 3.3: Expected by-products from the 1:1 reaction between $\text{GeCl}_2(\text{Dioxane})$ with LAIH_2 .

Scheme 3.3 suggests that the reaction between $\text{GeCl}_2(\text{Dioxane})$ and LAIH_2 would produce AlCl_2 as the only by-product. AlCl_2 is produced as a result of both hydride groups on LAIH_2 being replaced with chloride groups on $\text{GeCl}_2(\text{Dioxane})$. Dioxane will be released as a result of the reaction. AlCl_2 is a known compound and has been fully characterized by Blakeny et al, during their study on elemental Al deposition using ALD.¹¹⁰

The solution reactivity between $\text{GeCl}_2(\text{Dioxane})$ and LAIH_2 were investigated by mixing $\text{GeCl}_2(\text{Dioxane})$ with a solution of LAIH_2 in d_6 -benzene in a 1:1 ratio at room temperature. The reaction solution immediately formed an orange-coloured precipitate which gradually turned dark orange/brown at room temperature. Gas evolution was also observed, and it was identified as hydrogen gas by proton NMR spectroscopy (Figure 3.6). The proton NMR

spectrum of the reaction mixture collected 24 hours after mixing the reagents at room temperature is shown in Figure 3.6. Formation of LAiCl_2 during the reaction was confirmed by comparing NMR spectra collected for LAiCl_2 against NMR spectra of LAiCl_2 available in literature.¹¹⁰ Further characterization of LAiCl_2 is discussed in the Section 3.5. Free dioxane released in the reaction can be seen in the spectrum at 3.35 ppm.

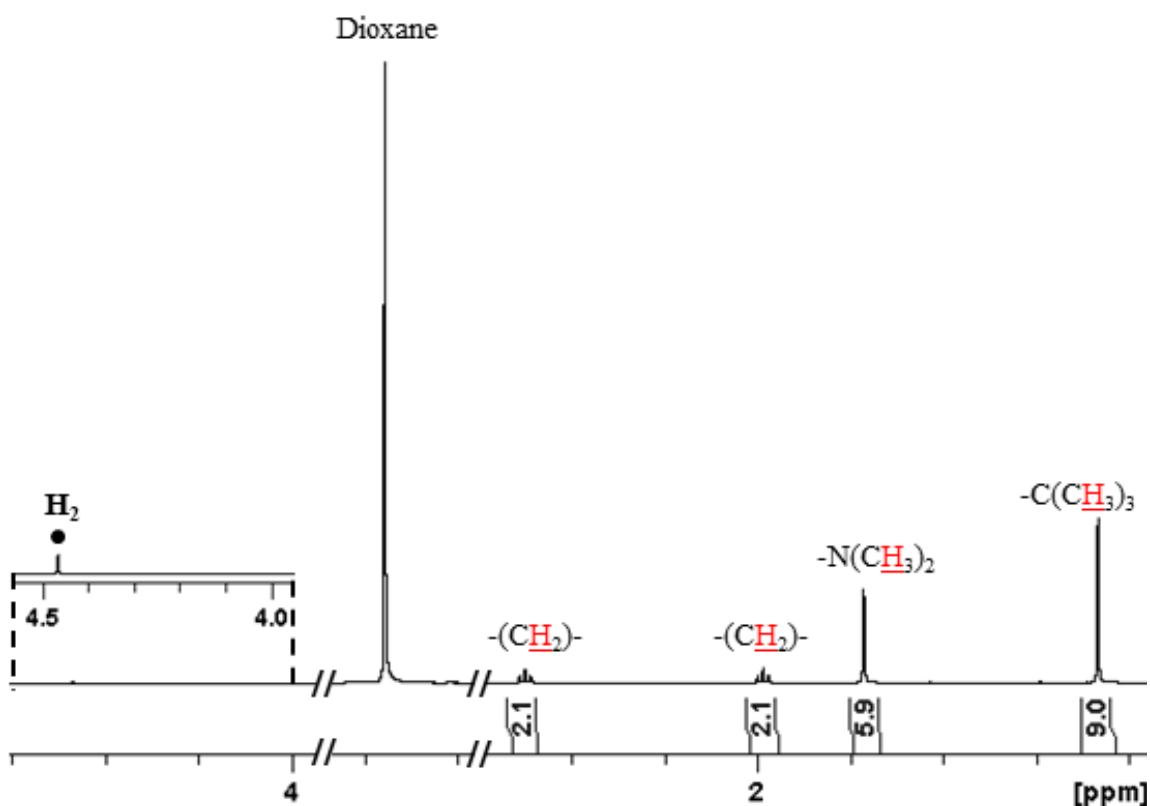


Figure 3.6: The proton NMR spectrum of the 1:1 reaction of $\text{GeCl}_2(\text{Dioxane})$ with LAiH_2 in d_6 -benzene collected at room temperature after 24 hours. The hydrogen peak is labelled with a circle.

The orange precipitate formed in the reaction was separated using centrifugation and soluble contaminants were removed by washing with toluene followed by hexanes. Figure

3.7 shows the X-ray diffractogram collected for the precipitate. Based on the diffractogram, the precipitate is amorphous.

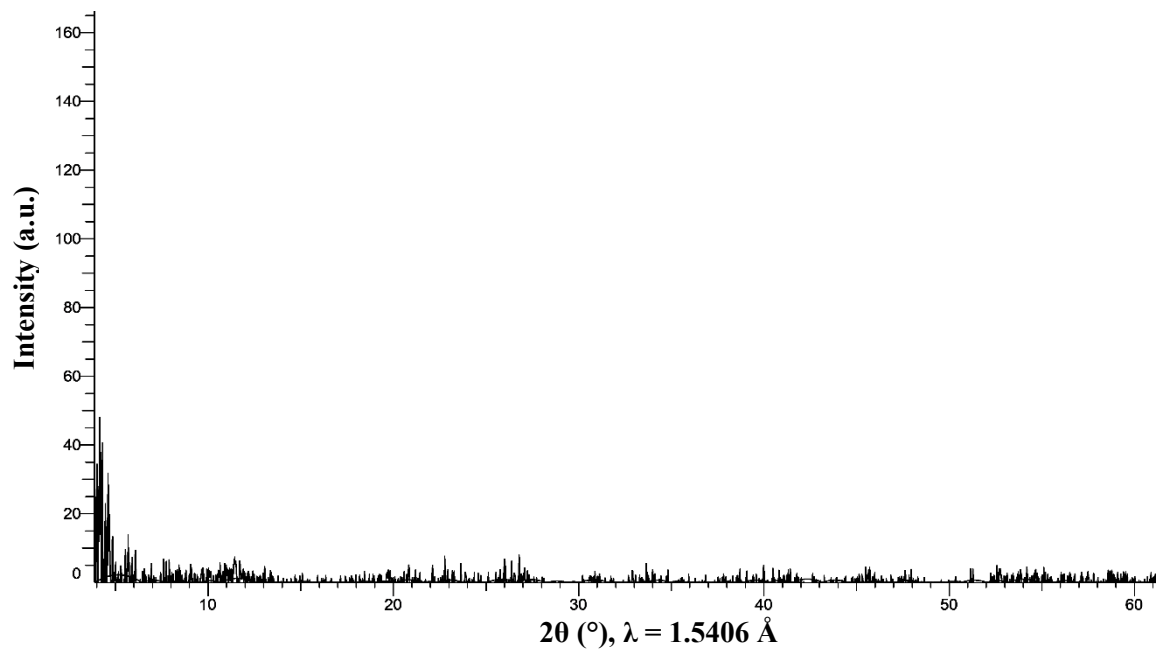
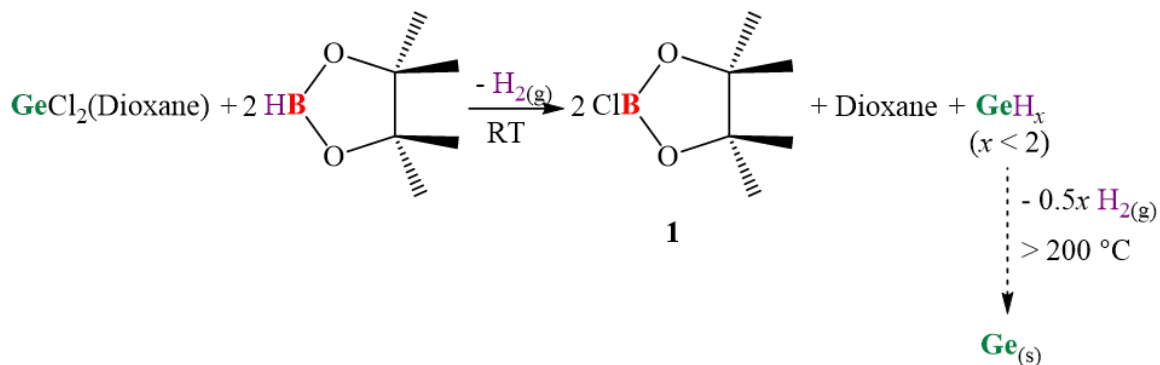


Figure 3.7: Powder X-ray diffractogram (PXRD) of the orange precipitate GeH_x formed from the 1:1 reaction of GeCl_2 (Dioxane) and LiAlH_2 in d_6 -benzene, 24 h, RT.

3.3.1.2 Reaction of GeCl₂(Dioxane) with HBpin



Scheme 3.4: Expected by-products from the 1:2 reaction between GeCl₂(Dioxane) and HBpin.

A 1:2 reaction between GeCl₂(Dioxane) and HBpin was expected to produce ClBpin as the only by-product along with 1,4-dioxane (Scheme 3.4). ClBpin is produced as the result of the exchange of hydride on HBpin with chloride on GeCl₂(Dioxane). To explore the reactivity, GeCl₂(Dioxane) was added to a solution of HBpin in *d*₆-benzene in a 1:2 ratio at room temperature. A gradual development of a yellow colour was observed after mixing reagents and no further change in the colour was observed between 20 to 80 °C. No precipitate was observed from the reaction.

The proton NMR spectrum collected for the reaction mixture after heating the solution at 60 °C for 24 hours is shown in Figure 2.8b along with the proton NMR spectrum of HBpin (Figure 2.8a). Except for the 1,4-dioxane peak at 3.35 ppm and the unreacted HBpin remains in the reaction solution (marked with an asterisk), it was difficult to identify other peaks due to the complexity of the spectrum. The reactivity of this precursor/co-reactant

pair was not considered to be promising for ALD of elemental germanium, so was not studied further.

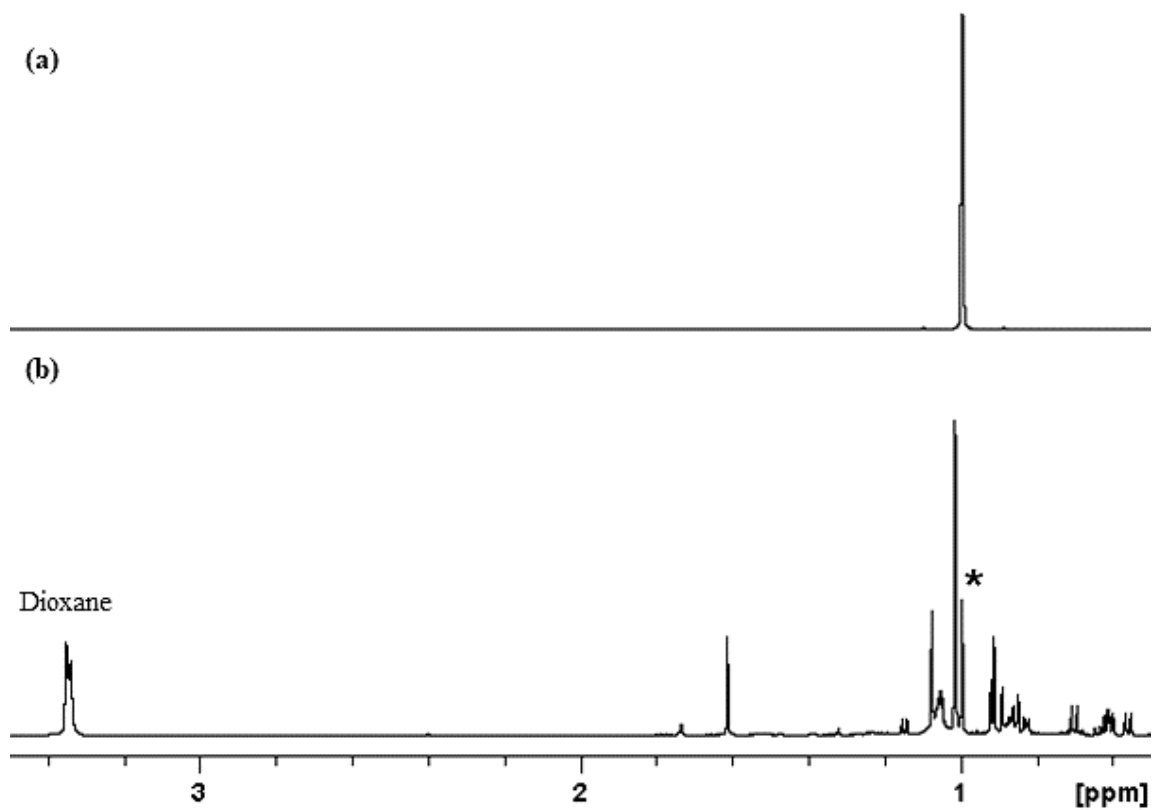
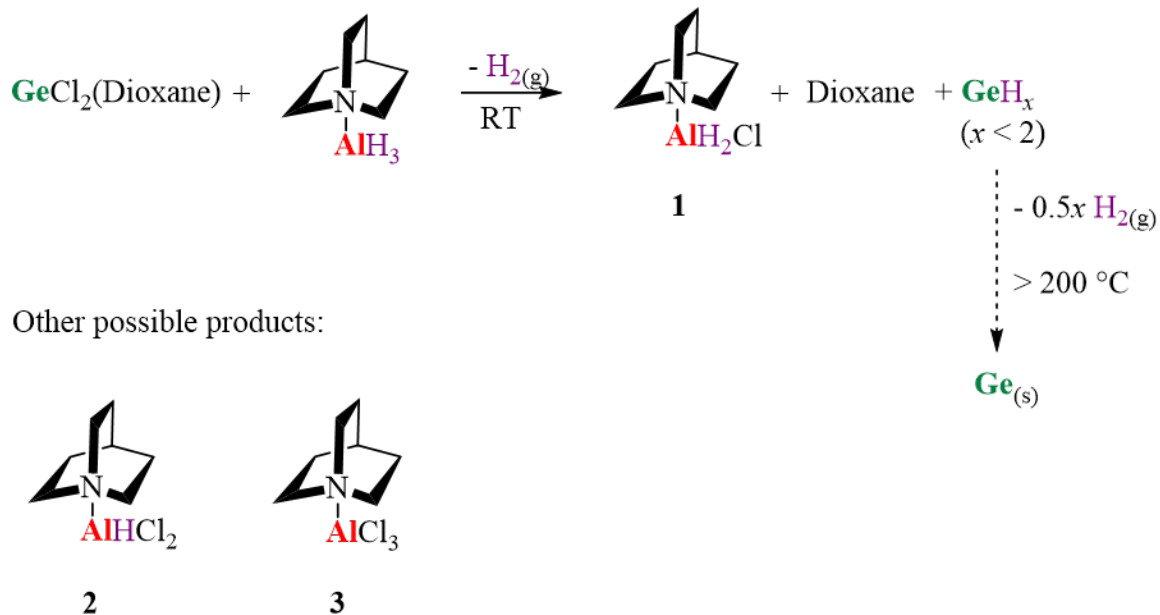


Figure 3.8: The proton NMR spectra in d_6 -benzene of a) HBpin and b) 1:2 reaction of $\text{GeCl}_2(\text{Dioxane})$ with HBpin, collected after heating the solution at 60°C for 24 hours. The asterisk indicates unreacted HBpin.

3.3.1.3 Reaction of GeCl₂(Dioxane) with AlH₃(Quinuclidine)

Scheme 3.5: Possible by-products predicted for the reaction of GeCl₂(Dioxane) with AlH₃(Quinuclidine).

The ligand exchange reaction between GeCl₂(Dioxane) and AlH₃(Quinuclidine) has the ability to form three different products (Scheme 3.5). Exchange of one hydride group with a chloride group on GeCl₂(Dioxane) will produce AlH₂Cl(Quinuclidine) (Product 01) as the by-product whereas exchange of 2 and 3 hydride groups will produce AlHCl₂(Quinuclidine) (Product 02) and AlCl₃(Quinuclidine) (Product 03) respectively.

GeCl₂(Dioxane) was mixed together with a solution of AlH₃(Quinuclidine) in d₆-benzene in a 2:1 ratio at room temperature which resulted in a yellow solution initially and an orange-coloured precipitate within 30 minutes. A Proton NMR spectrum of the reaction solution indicated the presence of unreacted AlH₃(Quinuclidine), which only disappeared

after heating the reaction mixture at 60 °C for 24 hours. Figure 3.9 c) indicates the proton NMR spectrum of the reaction solution (60 °C, 24 h), along with proton NMR spectra of quinuclidine and $\text{AlH}_3(\text{Quinuclidine})$ for comparison (Figure 3.9 a and Figure 3.9 b respectively). The spectrum of the reaction solution confirms the H_2 gas evolution (Figure 3.9- Labelled with a circle). The proton NMR spectrum of the reaction suggests the formation of three different types of quinuclidine adducts. Comparison of NMR spectra revealed that none of these products are quinuclidine or $\text{AlH}_3(\text{Quinuclidine})$. Quinuclidine produces three different peaks in the proton NMR spectrum with the ratio 6:6:1. The proton NMR spectrum of the reaction indicates formation of three different sets of peaks, each with the ratio 6:6:1 (each set of peaks is labelled with a different symbol; squares, stars, and triangles), which suggests the formation of quinuclidine in three different chemical environments. The quadrupolar Al center produces a broad Al-H resonance in 3.5-4.5 ppm range for $\text{AlH}_3(\text{Quinuclidine})$, and a comparable peak was not observed in the NMR spectrum of the reaction solution. However, full characterization of each quinuclidine-containing product was difficult with only the information obtained from proton NMR spectrum.

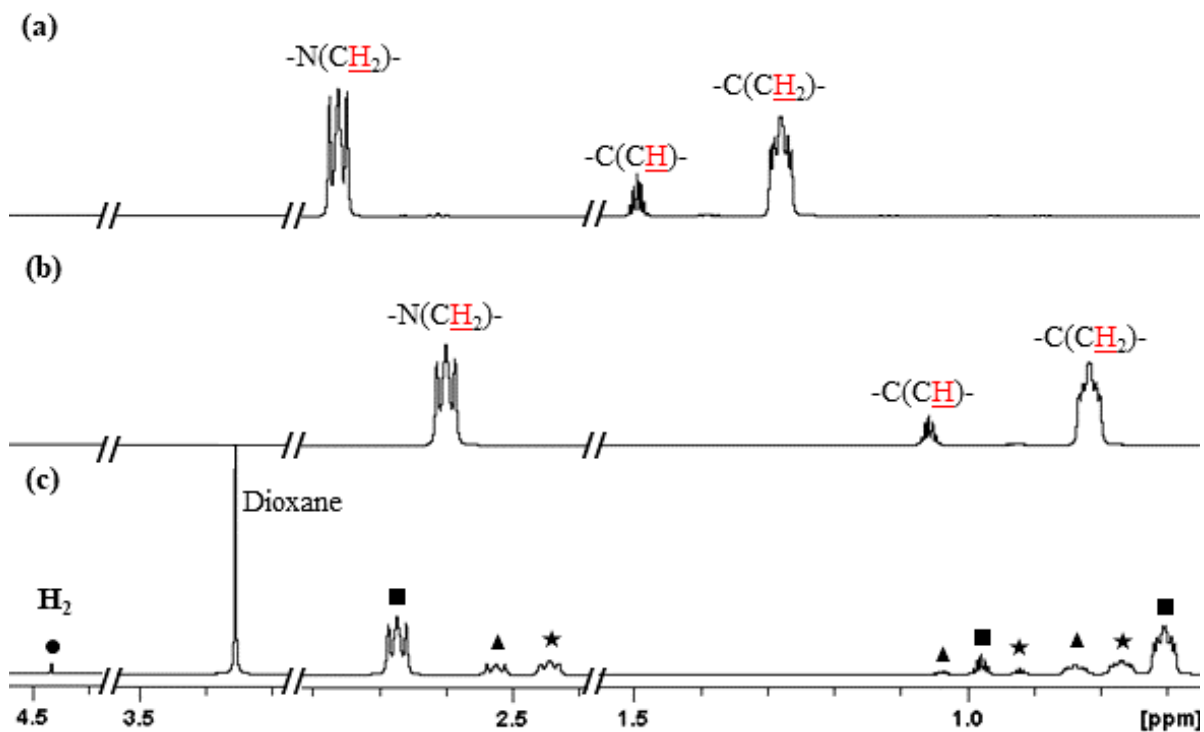
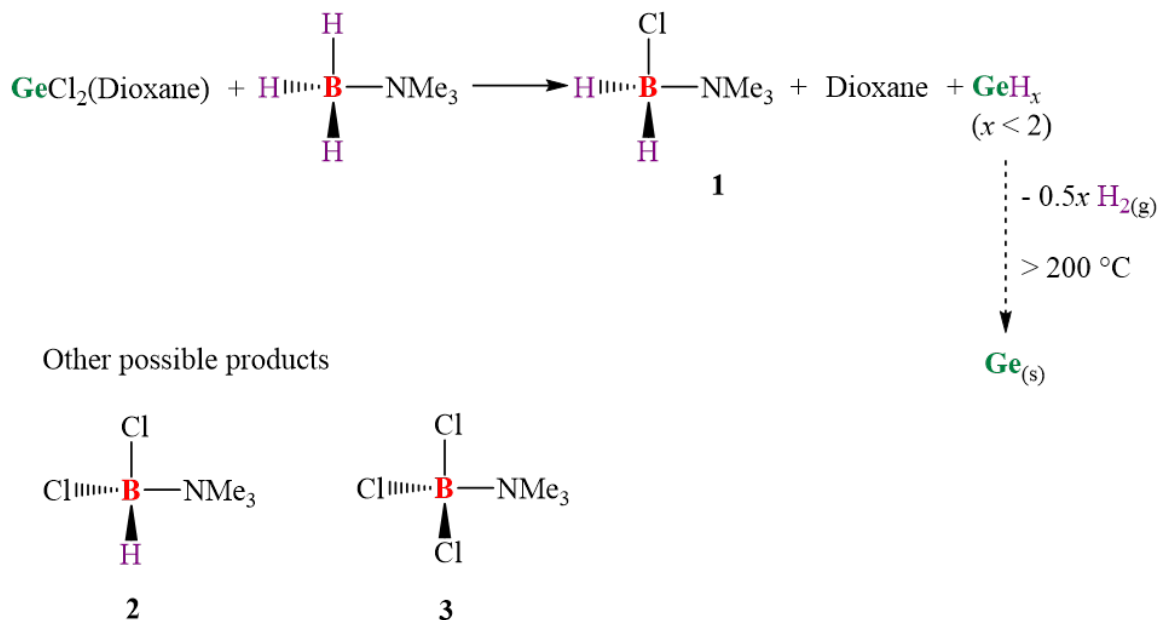


Figure 3.9: The proton NMR spectra in d_6 -benzene of a) Quinuclidine, b) $AlH_3(Quinuclidine)$, and c) 2:1 reaction of $GeCl_2(Dioxane)$ with $AlH_3(Quinuclidine)$ collected after 24 hours at 60 °C. Hydrogen peak is labelled with a circle. Different quinuclidines products are labelled with three different symbols: squares, triangles, and stars.

3.3.1.4 Reaction of GeCl_2 (Dioxane) with $\text{BH}_3(\text{NMe}_3)$ 

Scheme 3.6: Possible by-products predicted for the reaction of $\text{GeCl}_2(\text{Dioxane})$ with $\text{BH}_3(\text{NMe}_3)$.

Ligand exchange reactions between $\text{GeCl}_2(\text{Dioxane})$ and $\text{BH}_3(\text{NMe}_3)$ could result in three different by-products depending on how many hydride groups on $\text{BH}_3(\text{NMe}_3)$ are replaced with chloride groups (Scheme 3.6). $\text{BH}_2\text{Cl}(\text{NMe}_3)$ (Product 01) was expected as the major by-product from the reaction, which is formed as a result of one hydride group exchange with chloride group. Exchange of two hydride groups will produce $\text{BHCl}_2(\text{NMe}_3)$ (Product 02) and exchange of all three hydride groups will produce $\text{BCl}_3(\text{NMe}_3)$ (Product 03) respectively.

In order to study $\text{GeCl}_2(\text{Dioxane})$ reactivity in solution with $\text{BH}_3(\text{NMe}_3)$, $\text{GeCl}_2(\text{Dioxane})$ was added to a solution of $\text{BH}_3(\text{NMe}_3)$ in d_6 -benzene in a 3:2 ratio at room temperature.

The resulting solution instantly turned a yellow colour, and a gas evolution was observed. The yellow solution gradually produced an orange-coloured precipitate after 24 hours at room temperature. The proton NMR spectrum of the reaction solution collected 24 hours after mixing reagents to analyze the soluble reaction products is shown in Figure 3.10 b along with the proton NMR spectrum of $\text{BH}_3(\text{NMe}_3)$ (Figure 3.10 a). The proton NMR spectrum confirms the evolution of hydrogen gas (Figure 3.10-Labelled with a circle). The proton NMR spectrum indicates two different types of B-H peaks (Labelled with a square and a star in 2.1-3.2 ppm range). H atom bound to boron are expected to produce a quartet with a 1:1:1:1 ratio in the proton NMR spectrum. However, B-H peaks observed in the spectrum appear as two sets of triplets due to overlap of the fourth peak in the quartet with other peaks. Relative integrations of the NMe_3 peak and B-H peak of, $\sim 9:2$ and $\sim 9:1$ suggest the formation of $\text{BH}_2\text{Cl}(\text{NMe}_3)$ (Product 01) (labelled with squares), and $\text{BHCl}_2(\text{NMe}_3)$ (Product 02) (labelled with stars), respectively. No unreacted BH_3NMe_3 was observed in the spectrum. Similar to the other reactions of $\text{GeCl}_2(\text{Dioxane})$, a 1,4-dioxane peak was observed at 3.35 ppm in the spectrum.

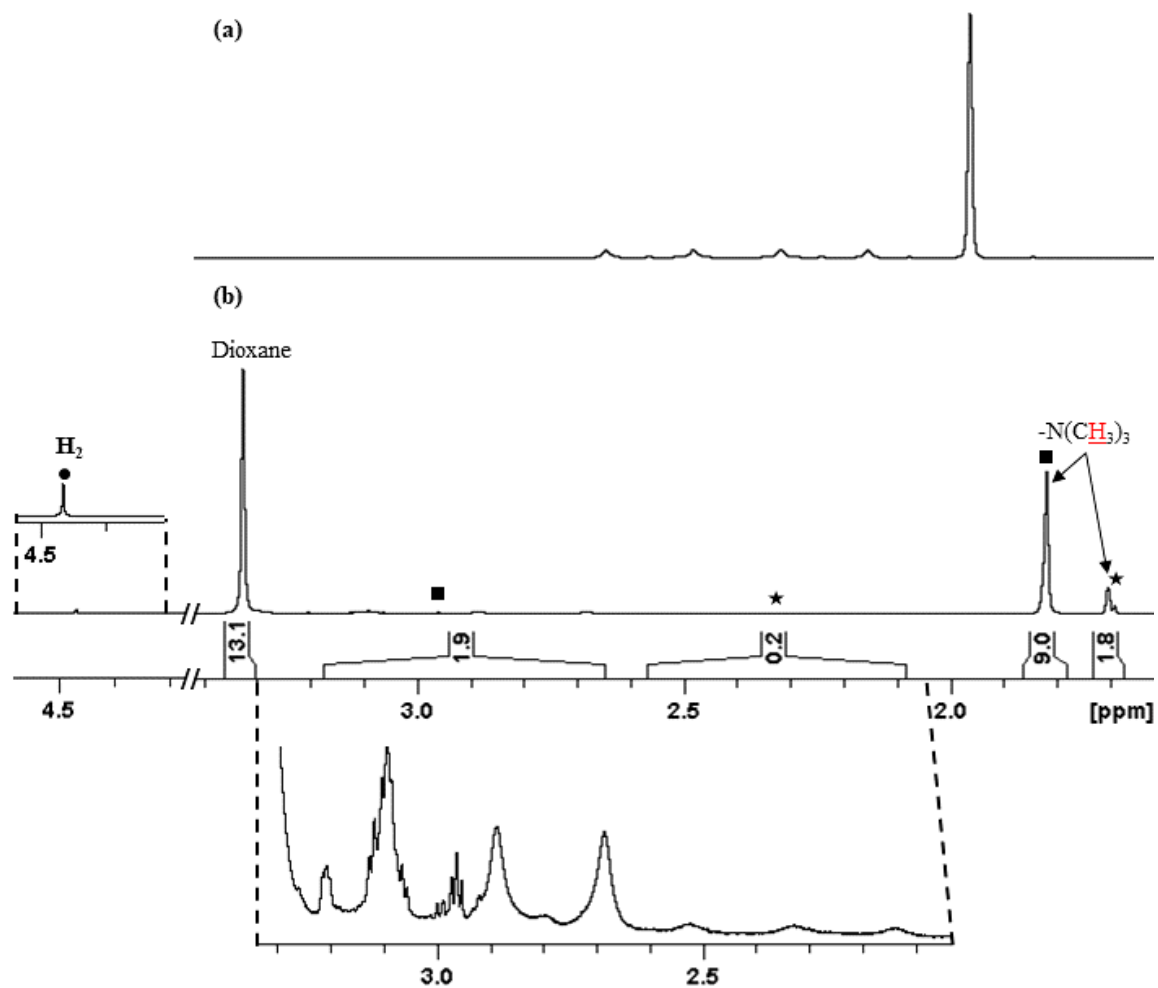
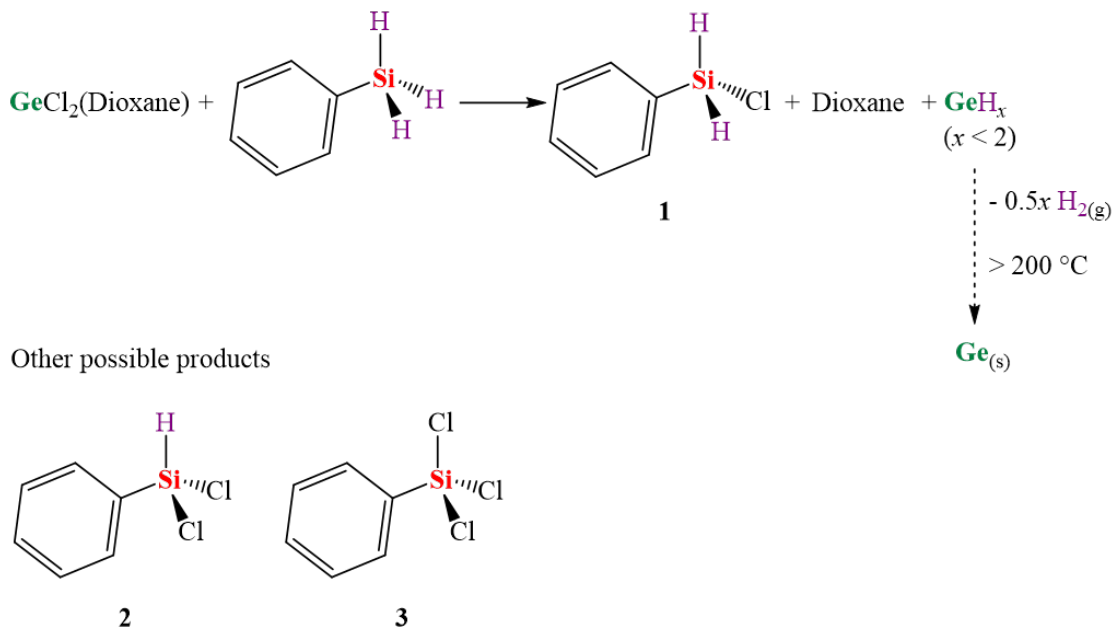


Figure 3.10: The proton NMR spectra in d_6 -benzene of a) $BH_3(NMe_3)$ and b) The 3:2 reaction of $GeCl_2(Dioxane)$ with $BH_3(NMe_3)$ collected at room temperature after 24 hours. Circle indicates the peak for hydrogen gas. $BH_2Cl(NMe_3)$ is labelled with squares and $BHCl_2(NMe_3)$ is labelled with stars.

3.3.1.5 Reaction of $\text{GeCl}_2(\text{Dioxane})$ with PhSiH_3



Scheme 3.7: Possible by-products predicted for the reaction of $\text{GeCl}_2(\text{Dioxane})$ with PhSiH_3 (Assuming pathway in the Scheme 3.2).

According to the Scheme 3.7, three by-products can be formed from the reaction of $\text{GeCl}_2(\text{Dioxane})$ with PhSiH_3 . Formation of these by-products is dependent on how many hydride groups get replaced with chloride groups.

Solution reactivity of $\text{GeCl}_2(\text{Dioxane})$ with PhSiH_3 was studied by mixing $\text{GeCl}_2(\text{Dioxane})$ with a solution of PhSiH_3 in d_6 -benzene in a 3:2 ratio. The reaction immediately produced a yellow colour solution, and a yellow precipitate was only observed after heating the reaction solution at $40\text{ }^\circ\text{C}$ for 24 hours. The proton NMR spectrum of the reaction solution collected after heating for 24 hours at $40\text{ }^\circ\text{C}$ is shown in Figure 3.11. As evident from the proton NMR spectrum formation of PhSiH_2Cl (Product 01) can be confirmed by a peak at

5.06 ppm.¹³⁸ Formation of PhSiHCl_2 (Product 02) would result in a peak at 5.74 ppm and was not detected in the reaction.¹³⁸ Formation of PhSiCl_3 (Product 03) would not be detectable from the region shown in the spectrum as it lacks any Si-H bonds. The region that indicates peaks corresponding to phenyl rings overlaps considerably, hence it was not possible to identify all of the peaks separately. Formation of hydrogen gas was observed in the spectrum (labelled with a circle) along with 1,4-dioxane peak at 3.35 ppm.

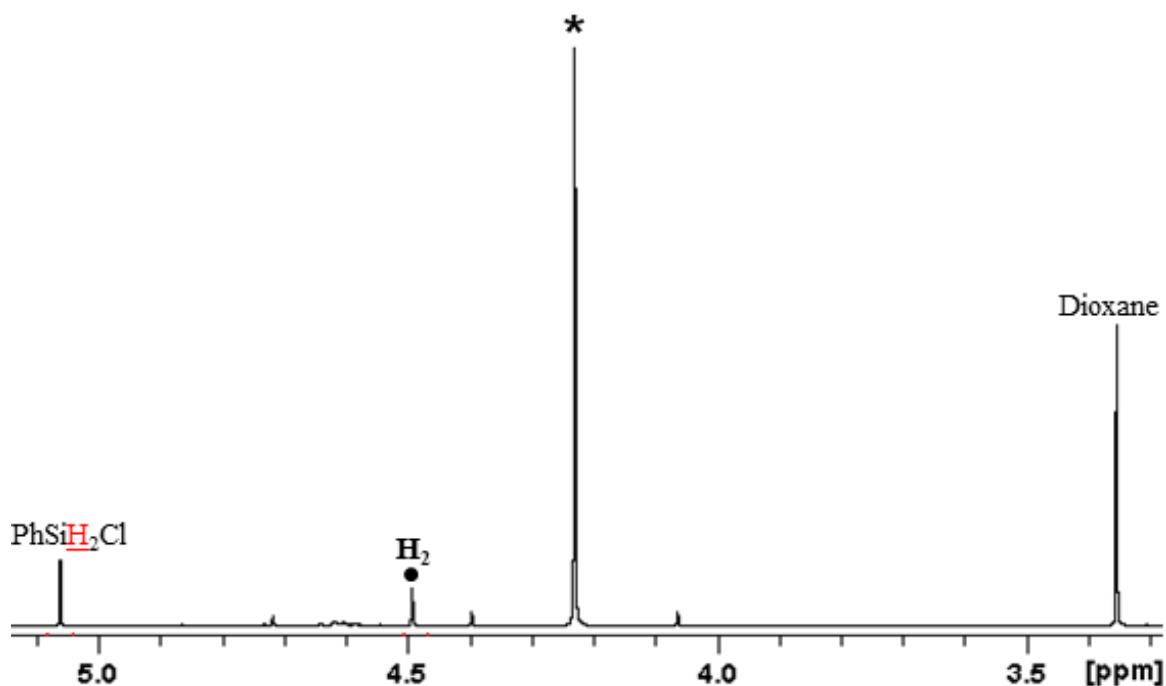
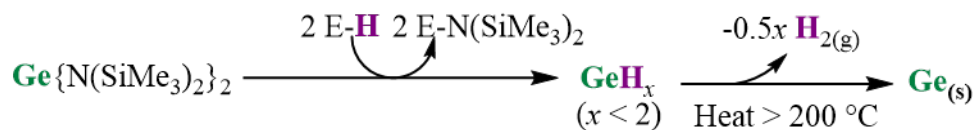


Figure 3.11: The proton NMR spectrum of the 3:2 reaction of $\text{GeCl}_2(\text{Dioxane})$ and PhSiH_3 in d_6 -benzene collected after 24 hours at 40 °C. Unreacted excess PhSiH_3 is marked with an asterisk and H_2 is labelled with a circle.

3.3.2 Solution reactivity studies of $\text{Ge}\{\text{N}(\text{SiMe}_3)_2\}_2$



Scheme 3.8: Proposed reaction pathway for reactions of $\text{Ge}\{\text{N}(\text{SiMe}_3)_2\}_2$ with hydride reagents to produce elemental germanium. E = Bpin, LAIH (L= $t\text{BuNCH}_2\text{CH}_2\text{NMe}_2$), $\text{AlH}_2(\text{Quinuclidine})$, $\text{BH}_2(\text{NMe}_3)$, or PhSiH_2 .

The general reaction pathways anticipated for solution reactions between $\text{Ge}\{\text{N}(\text{SiMe}_3)_2\}_2$ with hydride co-reagents are shown in Scheme 3.8. A ligand exchange reaction between $\text{Ge}\{\text{N}(\text{SiMe}_3)_2\}_2$ and hydride co-reactants could replace both $\text{N}(\text{SiMe}_3)_2$ groups on $\text{Ge}\{\text{N}(\text{SiMe}_3)_2\}_2$ giving rise to a polymeric germanium hydride (GeH_x , $x < 2$) as the first intermediate, which will produce elemental Ge and hydrogen gas upon heating around 200 $^\circ\text{C}$.^{136,137} A positive reaction would indicate the formation of hydrogen gas during the solution reaction, which could be detected in the proton NMR spectrum with a peak at 4.47 ppm in d_6 -benzene.

For comparison purposes ^1H and $^{13}\text{C}\{^1\text{H}\}$ NMR spectra of $\text{Ge}\{\text{N}(\text{SiMe}_3)_2\}_2$ were collected and shown in Figure 3.12.

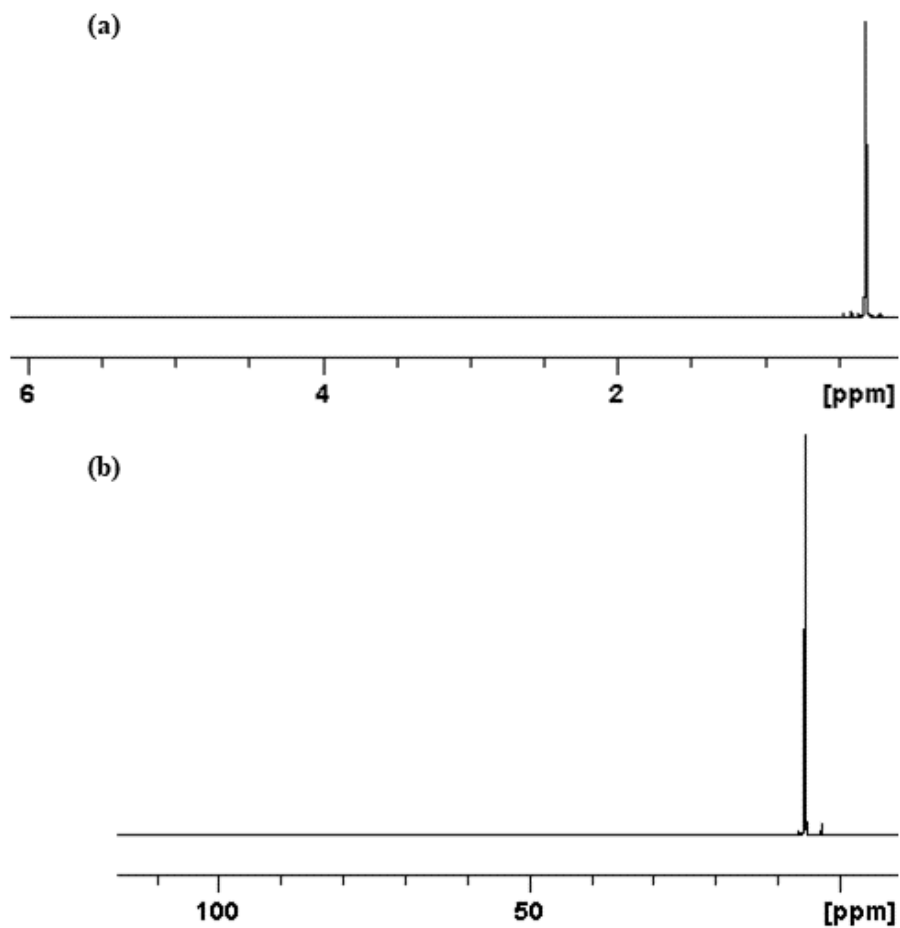
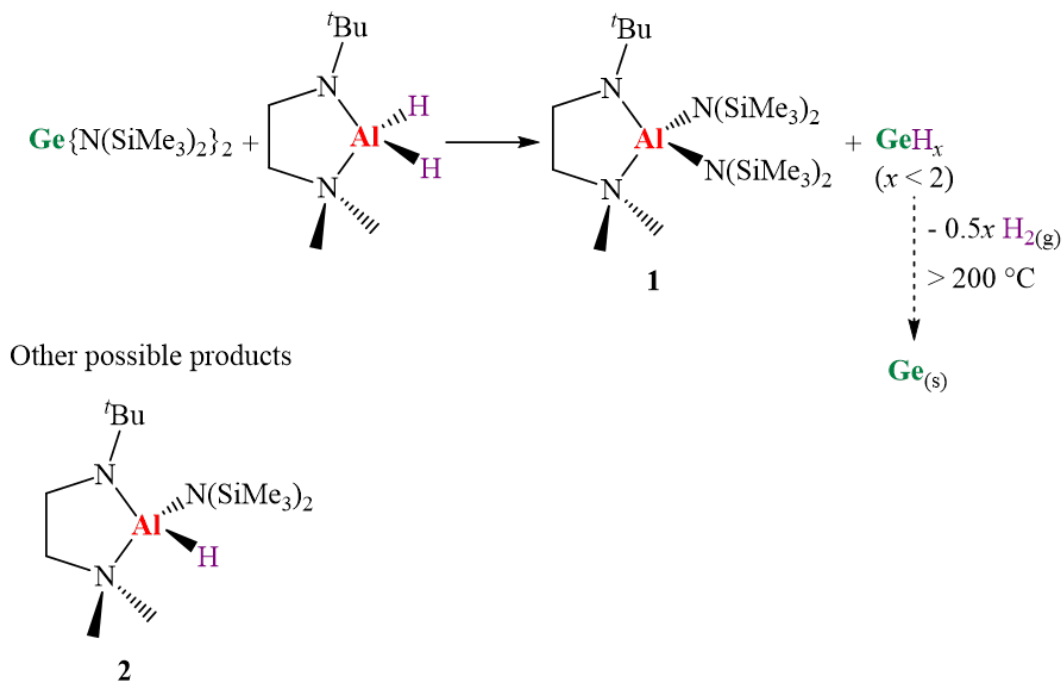


Figure 3.12: NMR spectra of $\text{Ge}\{\text{N}(\text{SiMe}_3)_2\}_2$ in d_6 -benzene, a) ^1H NMR and b) $^{13}\text{C}\{^1\text{H}\}$ NMR.

3.3.2.1 Reaction of $\text{Ge}\{\text{N}(\text{SiMe}_3)_2\}_2$ with LAIH_2



Scheme 3.9: Possible by-products predicted for the 1:1 reaction of $\text{Ge}\{\text{N}(\text{SiMe}_3)_2\}_2$ with LAIH_2 .

The ligand exchange reaction between $\text{Ge}\{\text{N}(\text{SiMe}_3)_2\}_2$ and LAIH_2 could produce two different by-products as indicated in the Scheme 3.9. Replacing both hydride groups on LAIH_2 will produce $\text{LA}\{\text{N}(\text{SiMe}_3)_2\}_2$ (Product 01) whereas replacing only one hydride group will produce $\text{LAH}\text{N}(\text{SiMe}_3)_2$ (Product 02) along with $\text{GeHN}(\text{SiMe}_3)_2$. To investigate the reactivity between the reagents, solutions of $\text{Ge}\{\text{N}(\text{SiMe}_3)_2\}_2$ and LAIH_2 were prepared in d_6 -benzene and were mixed together in a 1:1 ratio at room temperature. The resulting solution was clear and pale yellow in colour and no further change in the colour was observed between 20 to 80 °C.

The proton NMR spectrum of the reaction solution collected after heating the reaction solution at 60 °C for 24 hours is shown in Figure 3.13. The spectrum agrees with the formation of $\text{LAlH}\{\text{N}(\text{SiMe}_3)_2\}$ (Product 02) and $\text{GeH}_x\{\text{N}(\text{SiMe}_3)_2\}_y$ ($x \geq 0$; $y < 2$) (Figure 3.13-labelled with a square). The two methyl groups attached to nitrogen in product 02, are in different chemical environments, hence they produce two singlets at 1.74 and 1.91 ppm, each with the expected integration of 3H. Similarly, for the $\text{N}(\text{SiMe}_3)_2$ group, the methyl substituents on the two Si atoms are different from each other and produce two different singlets at 0.38 and 0.45 ppm, each with the expected integration of 9H. The CH_2 region of the ligand is complex and the four CH_2 signals (1H each) could not be identified separately. The proton bound to Al gave rise to a broad peak in the 4.88-3.54 ppm region. A singlet for an $\text{N}(\text{SiMe}_3)_2$ group in $\text{GeH}_x\{\text{N}(\text{SiMe}_3)_2\}_y$ was observed at 0.09 ppm, and the 1:1 integration ratio of the peak to the $\text{LAlH}\{\text{N}(\text{SiMe}_3)_2\}$ peaks (together) is consistent with the formation of a $\text{GeH}_x\{\text{N}(\text{SiMe}_3)_2\}_y$ product with one $\text{N}(\text{SiMe}_3)_2$ group per germanium. A peak at 6.02 ppm may also correspond to a GeH resonance. However, it integrates to ~10% of the expected value for $\text{GeH}\{\text{N}(\text{SiMe}_3)_2\}$. Consequently, the exact nature of the germanium containing product in the reaction is unclear.

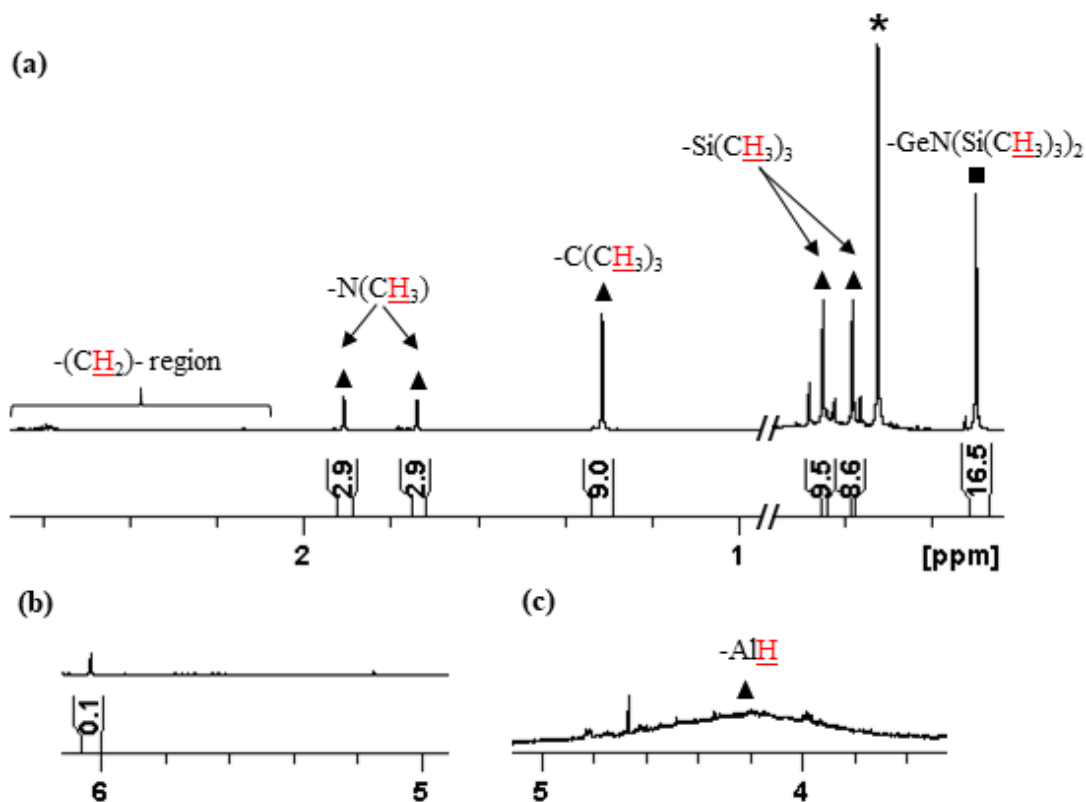
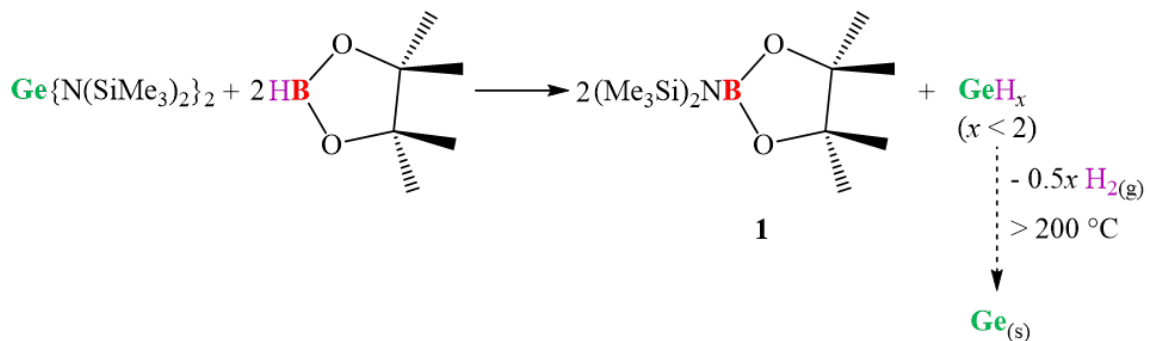


Figure 3.13: The proton NMR spectrum of a) the 1:1 reaction of $\text{Ge}\{\text{N}(\text{SiMe}_3)_2\}_2$ and LAiH_2 in d_6 -benzene collected after heating the reaction at 60°C for 24 hours, b) enlarged Ge-H region, and c) enlarged Al-H region. Unreacted $\text{Ge}\{\text{N}(\text{SiMe}_3)_2\}_2$ remaining in the reaction is labelled with an asterisk. $\text{LAiHN}(\text{SiMe}_3)_2$ is labelled with triangles and $\text{GeH}_x\{\text{N}(\text{SiMe}_3)_2\}_y$ ($x \geq 0$; $y < 2$) is labelled with a square.

3.3.2.2 Reaction of $\text{Ge}\{\text{N}(\text{SiMe}_3)_2\}_2$ with HBpin

Scheme 3.10: Expected by-products for the 1:2 reaction between $\text{Ge}\{\text{N}(\text{SiMe}_3)_2\}_2$ and HBpin.

As illustrated in the reaction scheme 3.10, a 1:2 reaction between $\text{Ge}\{\text{N}(\text{SiMe}_3)_2\}_2$ and HBpin is expected to produce $\{(\text{Me}_3\text{Si})_2\text{N}\}\text{Bpin}$ (Product 01) as the only by-product, by replacing hydride group on HBpin with an $\text{N}(\text{SiMe}_3)_2$ group. To investigate this reactivity, a solution of $\text{Ge}\{\text{N}(\text{SiMe}_3)_2\}_2$ in d_6 -benzene was mixed with a solution of HBpin in a 1:4 ratio at room temperature. The reaction solution was initially colourless and gradually developed a yellow colour upon heating at 60°C for 24 hours. No precipitate formation was observed in this reaction.

The proton NMR spectrum of the reaction solution collected after heating the reaction at 60°C for 24 hours is shown in Figure 3.14. Information obtained from the proton NMR spectrum suggests the formation of $\{(\text{Me}_3\text{Si})_2\text{N}\}\text{Bpin}$ (Product 01) during the reaction as the only by-product. A peak due to the methyl groups on Si appears at 0.33 ppm with the expected integration of 18H and a peak due to the methyl groups on Bpin can be seen at 1.03 ppm with the expected integration of 12H. Some unreacted HBpin can also be seen in the spectrum (Figure 3.14-labelled with an asterisk). As with the reaction between

$\text{Ge}\{\text{N}(\text{SiMe}_3)_2\}_2$ and LiAlH_2 , a singlet was observed at 0.09 ppm, presumably due to the remaining $\text{N}(\text{SiMe}_3)_2$ group on germanium. However, integration of this peak relative to that of the $\{(\text{Me}_3\text{Si})_2\text{N}\}$ Bpin by-product is 1:3, rather than the expected 1:1 ratio based on the reaction stoichiometry. A possible GeH signal was also located at 6.02 ppm, and integrates to approximately 1H relative to the $\text{N}(\text{SiMe}_3)_2$ signal (18H). However, this ratio contrasts that observed in the reaction of $\text{Ge}\{\text{N}(\text{SiMe}_3)_2\}_2$ with LiAlH_2 , indicating that the signals at 0.09 and 6.02 ppm do not arise from the same compound. The exact nature of the $\text{GeH}_x\{\text{N}(\text{SiMe}_3)_2\}_y$ ($x \geq 0$; $y < 2$) product in this reaction is unclear. Further characterization of $\{(\text{Me}_3\text{Si})_2\text{N}\}$ Bpin is discussed in Section 3.5.

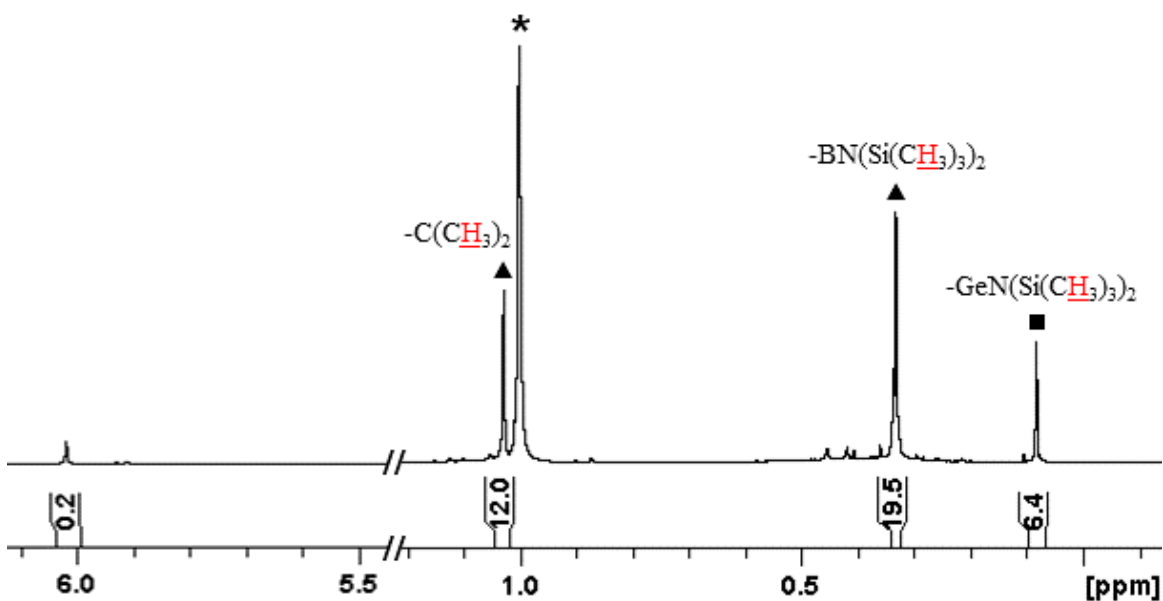


Figure 3.14: The proton NMR spectrum of the 1:4 reaction of $\text{Ge}\{\text{N}(\text{SiMe}_3)_2\}_2$ with HBpin in d_6 -benzene collected after heating the reaction at 60 °C for 24 hours. The asterisk indicates unreacted HBpin. Triangle indicate peaks correspond to $\{(\text{Me}_3\text{Si})_2\text{N}\}$ Bpin and $\text{GeH}_x\{\text{N}(\text{SiMe}_3)_2\}_y$ ($x \geq 0$; $y < 2$) is labelled with a square.

3.3.2.3 Reaction of $\text{Ge}\{\text{N}(\text{SiMe}_3)_2\}_2$ with $\text{AlH}_3(\text{Quinuclidine})$

To investigate the reactivity between $\text{Ge}\{\text{N}(\text{SiMe}_3)_2\}_2$ and $\text{AlH}_3(\text{Quinuclidine})$, solutions of both reagents in d_6 -benzene were mixed together in a 1:4 ratio at room temperature. The resulting solution was colourless and heating the reaction solution up to $80\text{ }^\circ\text{C}$ for 24 hours did not indicate any visible changes. The proton NMR spectrum collected for the reaction mixture after heating at $80\text{ }^\circ\text{C}$ for 24 hours, is shown in Figure 3.15 and indicates that the two reagents did not react with each other.

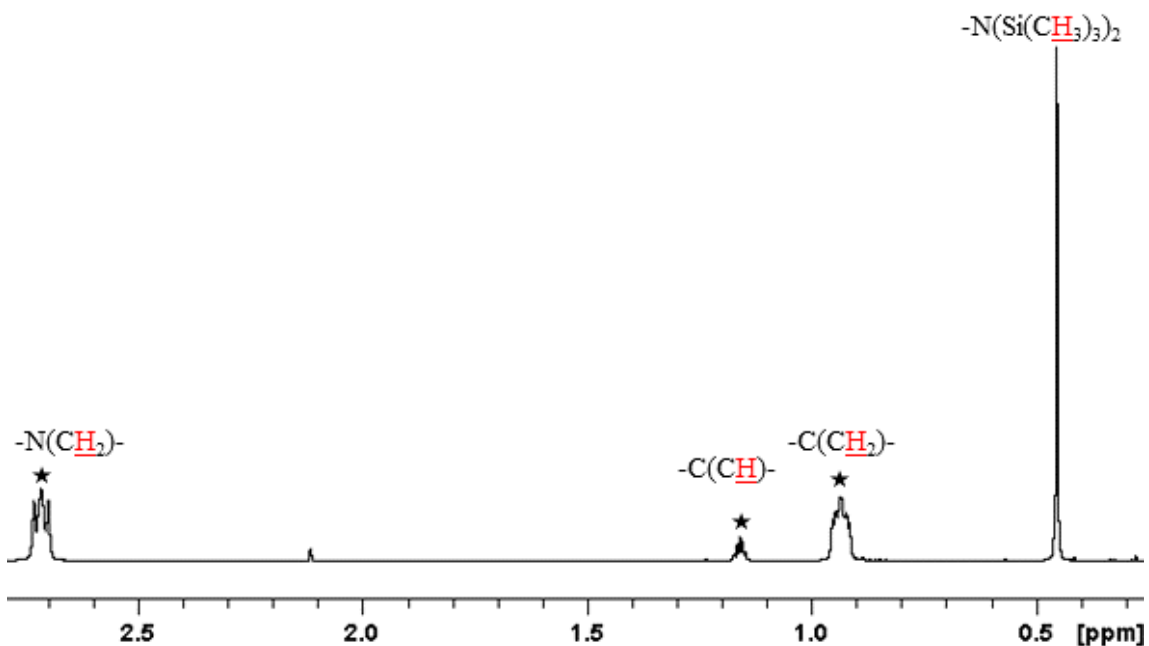


Figure 3.15: The proton NMR spectrum of the 1:4 reaction of $\text{Ge}\{\text{N}(\text{SiMe}_3)_2\}_2$ and $\text{AlH}_3(\text{Quinuclidine})$ in d_6 -benzene, collected after heating the reaction solution at $80\text{ }^\circ\text{C}$ for 24 hours. Stars indicate the peaks of $\text{AlH}_3(\text{Quinuclidine})$.

3.3.2.4 Reaction of $\text{Ge}\{\text{N}(\text{SiMe}_3)_2\}_2$ with $\text{BH}_3(\text{NMe}_3)$

A solution of $\text{Ge}\{\text{N}(\text{SiMe}_3)_2\}_2$ in d_6 -benzene was mixed together with a solution of $\text{BH}_3(\text{NMe}_3)$ in a 1:4 ratio at room temperature to investigate the solution reactivity between the two reagents. A colourless solution was formed after mixing reagents at room temperature and did not change colour upon heating up to $80\text{ }^\circ\text{C}$ for 24 hours. The proton NMR spectrum of the reaction solution collected after heating the reaction mixture for 24 hours at $80\text{ }^\circ\text{C}$ is shown in Figure 3.16 and indicates that the two reagents did not react with each other.

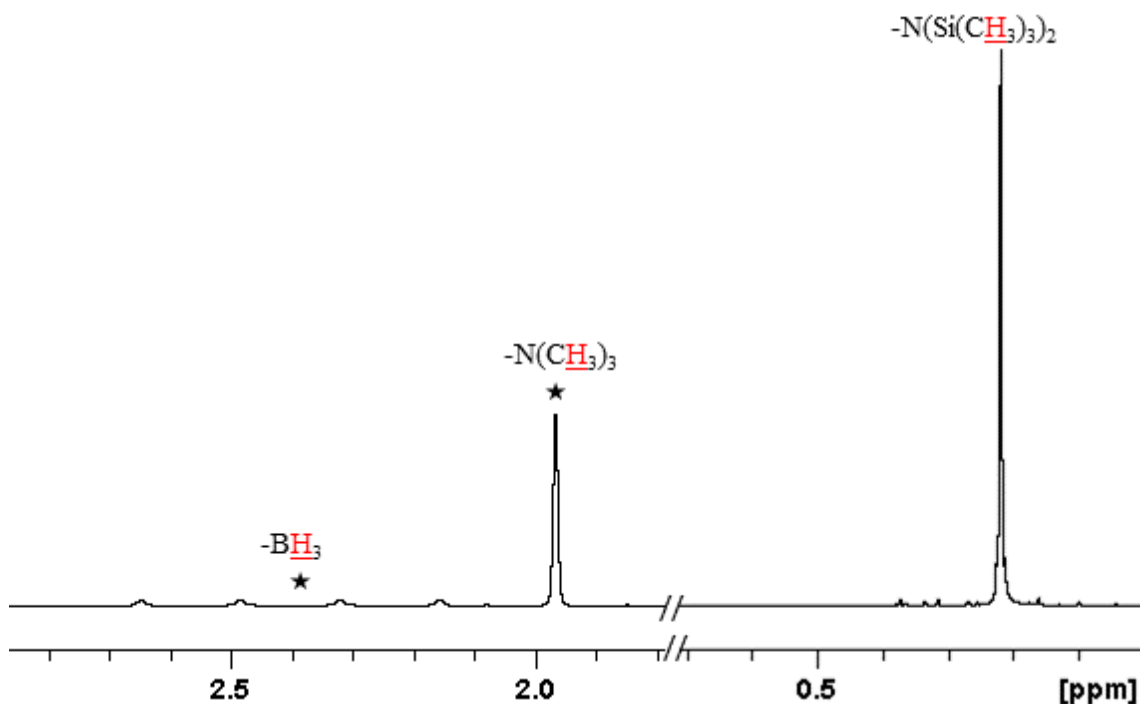


Figure 3.16: The proton NMR spectrum of the 1:4 reaction of $\text{Ge}\{\text{N}(\text{SiMe}_3)_2\}_2$ with $\text{BH}_3(\text{NMe}_3)$ in d_6 -benzene, collected after heating the reaction solution at $80\text{ }^\circ\text{C}$ for 24 hours. Stars indicate the peaks of $\text{BH}_3(\text{NMe}_3)$.

3.3.2.5 Reaction of $\text{Ge}\{\text{N}(\text{SiMe}_3)_2\}_2$ with PhSiH_3

A solution of $\text{Ge}\{\text{N}(\text{SiMe}_3)_2\}_2$ in d_6 -benzene was mixed with a solution of PhSiH_3 in a 1:5 ratio at room temperature to investigate the solution reactivity of $\text{Ge}\{\text{N}(\text{SiMe}_3)_2\}_2$ with PhSiH_3 . A clear colourless solution was formed upon mixing the reagents and did not change colour upon heating the reaction solution to $80\text{ }^\circ\text{C}$ for 24 hours. The proton NMR spectrum of the reaction solution was collected after heating at $80\text{ }^\circ\text{C}$ for 24 hours (Figure 3.17) and indicates that two reactants did not react.

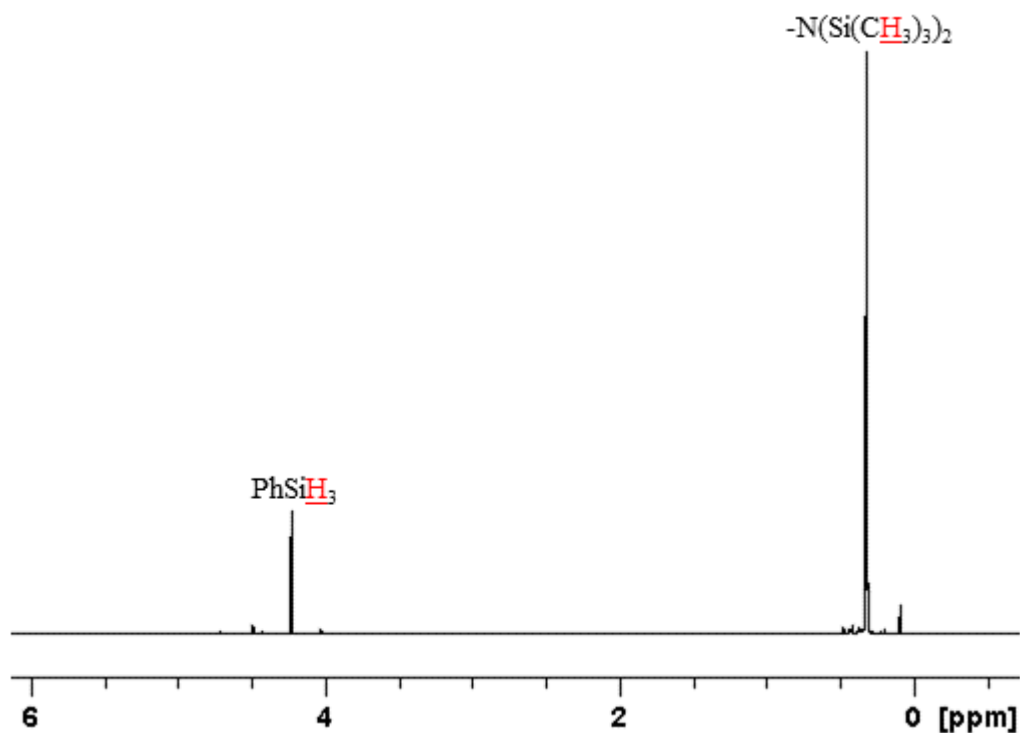
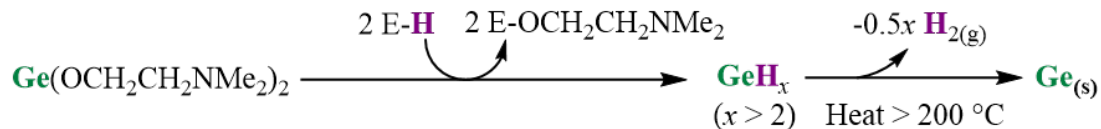


Figure 3.17: The proton NMR spectrum of the 1:5 reaction of $\text{Ge}\{\text{N}(\text{SiMe}_3)_2\}_2$ with PhSiH_3 in d_6 -benzene, collected after heating the reaction solution at $80\text{ }^\circ\text{C}$ for 24 hours.

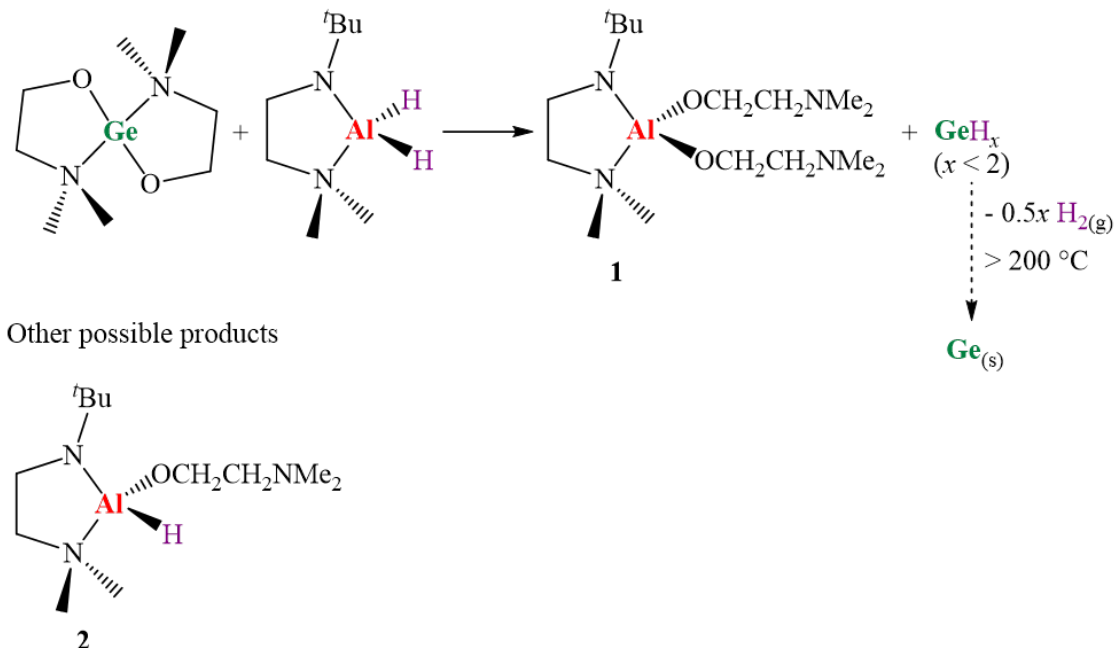
3.3.3 Solution reactivity studies of $\text{Ge}(\text{OCH}_2\text{CH}_2\text{NMe}_2)_2$



Scheme 3.11: Proposed reaction pathway for reactions of $\text{Ge}(\text{OCH}_2\text{CH}_2\text{NMe}_2)_2$ with hydride reagents to produce elemental germanium. E = Bpin, LAIH (L= ${}^t\text{BuNCH}_2\text{CH}_2\text{NMe}_2$), AlH_2 (Quinuclidine), BH_2 (NMe_3), or PhSiH_2 .

Scheme 3.11 illustrates the general reaction pathway anticipated for solution reactions between $\text{Ge}(\text{OCH}_2\text{CH}_2\text{NMe}_2)_2$ with hydride-reducing co-reagents. A ligand exchange reaction is expected to replace both $\text{OCH}_2\text{CH}_2\text{NMe}_2$ groups on $\text{Ge}(\text{OCH}_2\text{CH}_2\text{NMe}_2)_2$ and would produce a polymeric germanium hydride (GeH_x , $x < 2$) with hydrogen gas which can be detected in proton NMR spectrum at 4.47 ppm in d_6 -benzene.^{136,137} The polymeric GeH_x is expected to produce elemental Ge upon heating around 200 °C.^{136,137}

3.3.3.1 Reaction of $\text{Ge}(\text{OCH}_2\text{CH}_2\text{NMe}_2)_2$ with LAIH_2



Scheme 3.12: Possible by-products predicted for the 1:1 reaction of $\text{Ge}(\text{OCH}_2\text{CH}_2\text{NMe}_2)_2$ and LAIH_2 .

A ligand exchange reaction between $\text{Ge}(\text{OCH}_2\text{CH}_2\text{NMe}_2)_2$ and LAIH_2 reagents is predicted to produce $\text{LA}(\text{OCH}_2\text{CH}_2\text{NMe}_2)_2$ (Product 01) by replacing both hydride groups on LAIH_2 , or $\text{LAH}(\text{OCH}_2\text{CH}_2\text{NMe}_2)$ (Product 02) by replacing only one hydride group on LAIH_2 (Scheme 3.12).

Solutions of $\text{Ge}(\text{OCH}_2\text{CH}_2\text{NMe}_2)_2$ and LAIH_2 were prepared in d_6 -benzene and were mixed together in a 1:1 ratio at room temperature. Upon mixing reagents, formation of a dark orange precipitate was observed along with gas formation. A Proton NMR spectrum of the reaction mixture was collected 24 hours after mixing reagents, and is shown in Figure 3.18

c along with the proton NMR spectra of $\text{Ge}(\text{OCH}_2\text{CH}_2\text{NMe}_2)_2$ and LiAlH_2 (Figure 3.18 a and Figure 3.18 b respectively). The proton NMR spectrum of the reaction solution contains a set of broad peaks and identification of by-products of the reaction was difficult. The NMR spectrum indicates that no unreacted $\text{Ge}(\text{OCH}_2\text{CH}_2\text{NMe}_2)_2$ or LiAlH_2 remains in the solution. The reaction was expected to produce $\text{LiAl}(\text{OCH}_2\text{CH}_2\text{NMe}_2)_2$ (Product 01) as the major by-product. Formation of hydrogen gas during the reaction was confirmed by the proton NMR spectrum (Figure 3.18 – Enlarged region; labelled with a circle). Except for the hydrogen peak, other peaks in the proton NMR spectrum were not identified. Another reaction between the two reagents was carried out as mentioned above, with a 1:2 ratio between $\text{Ge}(\text{OCH}_2\text{CH}_2\text{NMe}_2)_2$ and LiAlH_2 . However, the resulting proton NMR spectrum appeared similar to the proton NMR spectrum of the 1:1 reaction.

After the reaction was complete, solvents were removed by centrifugation to collect the dark orange precipitate. This precipitate was washed with toluene followed by hexanes. The dry powder of the precipitate was used to collect the X-ray diffractogram (Figure 3.19) and indicates an amorphous solid.

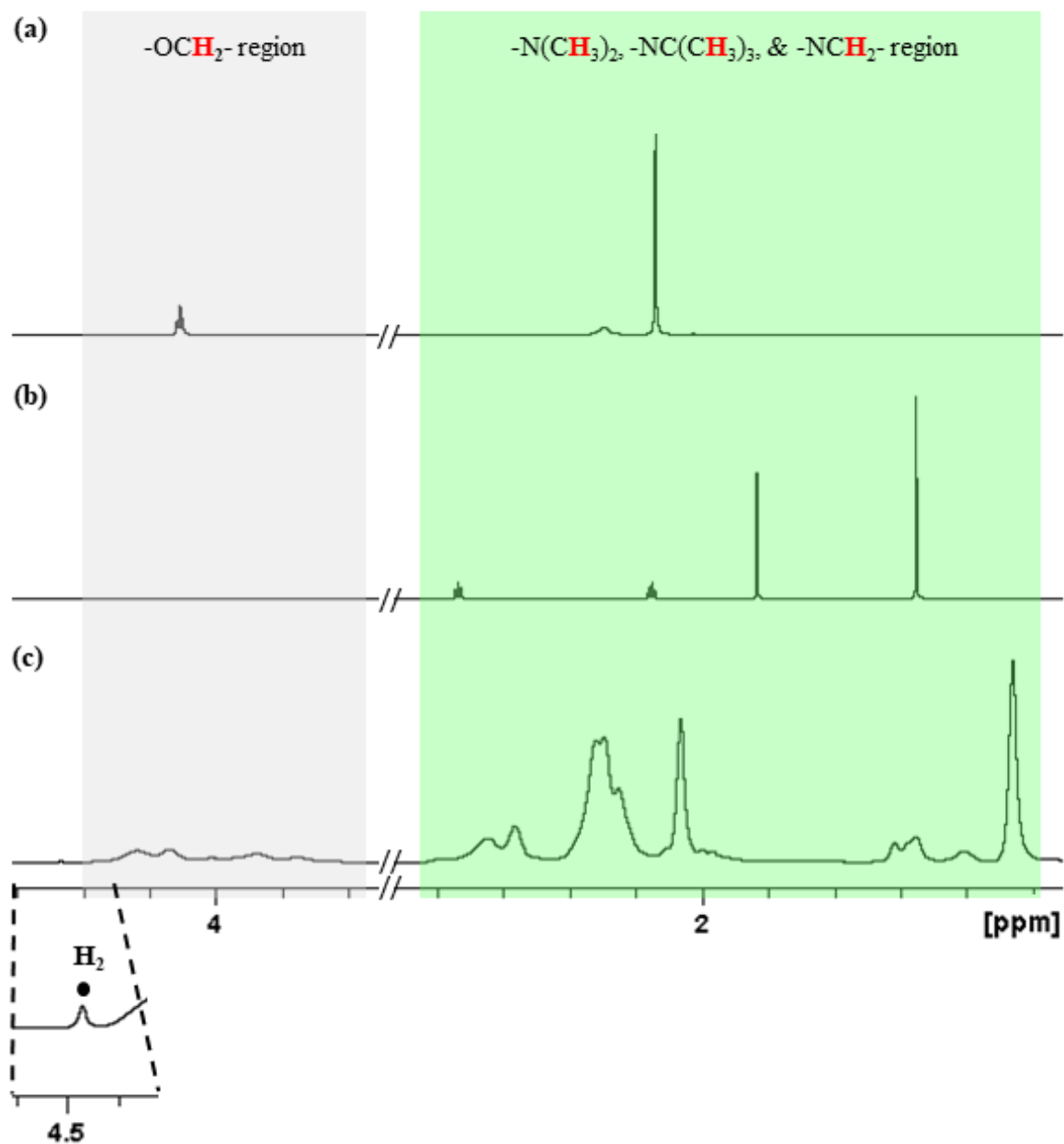


Figure 3.18: The proton NMR spectra in d_6 -benzene of a) $\text{Ge}(\text{OCH}_2\text{CH}_2\text{NMe}_2)_2$, b) LAIH_2 , and c) the 1:1 reaction of $\text{Ge}(\text{OCH}_2\text{CH}_2\text{NMe}_2)_2$ with LAIH_2 collected after the reaction had proceeded for 24 hours at room temperature. The circle indicates the hydrogen gas.

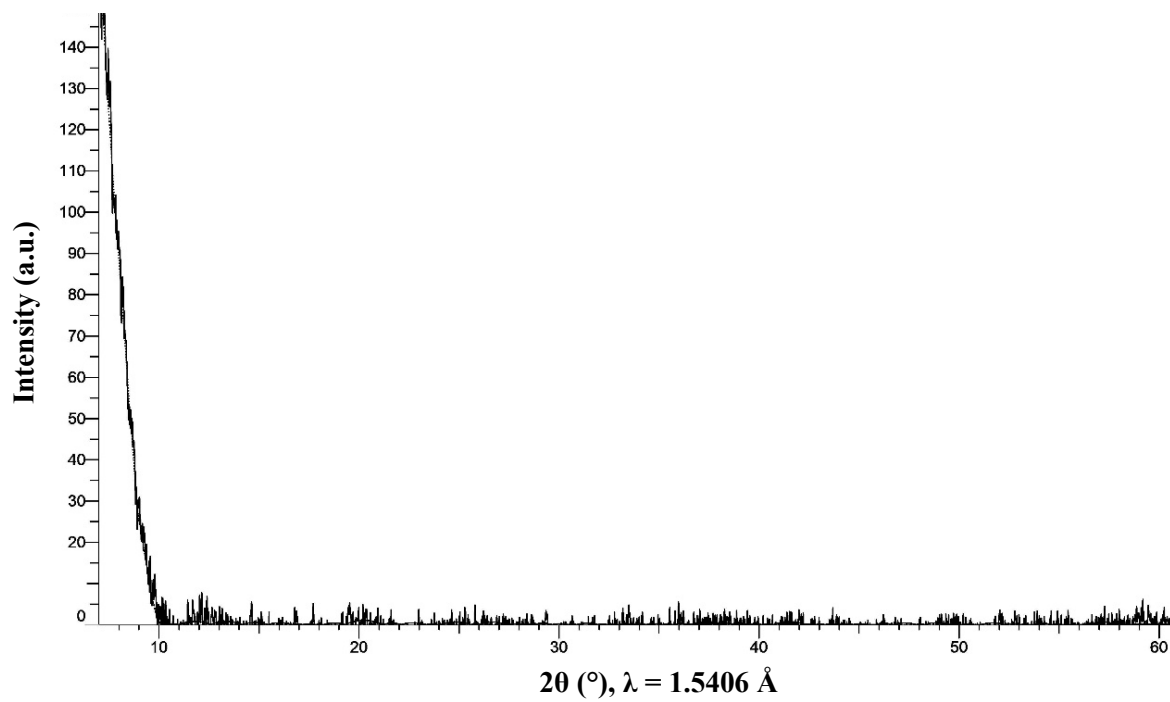
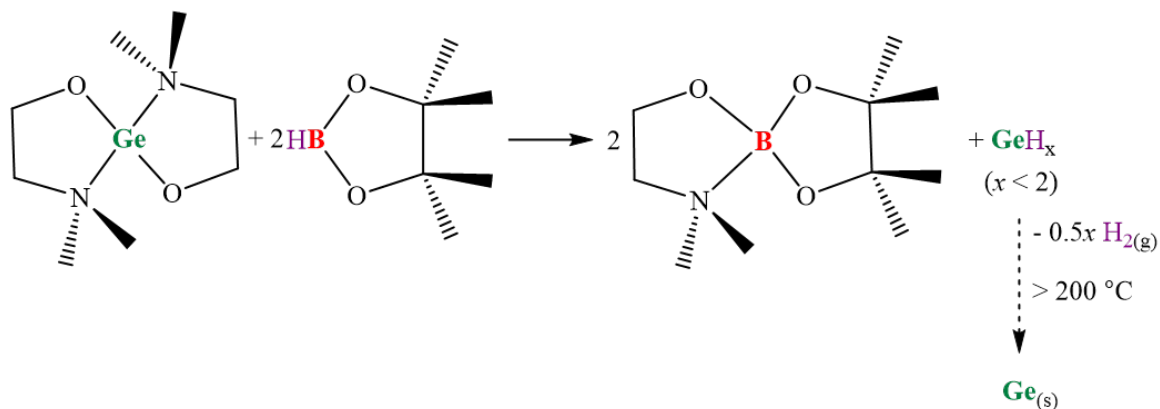


Figure 3.19: Powder X-ray diffractogram (PXRD) of the orange precipitate GeH_x formed from the 1:1 reaction of $\text{Ge}(\text{OCH}_2\text{CH}_2\text{NMe}_2)_2$ and LiAlH_2 in d_6 -benzene, 24 h, RT.

3.3.3.2 Reaction of $\text{Ge}(\text{OCH}_2\text{CH}_2\text{NMe}_2)_2$ with HBpin



Scheme 3.13: Proposed reaction pathway for the 1:2 reaction between $\text{Ge}(\text{OCH}_2\text{CH}_2\text{NMe}_2)_2$ and HBpin (assuming pathway in the Scheme 3.11).

A 1:2 reaction between $\text{Ge}(\text{OCH}_2\text{CH}_2\text{NMe}_2)_2$ and HBpin was expected to produce $(\text{Me}_2\text{NCH}_2\text{CH}_2\text{O})\text{Bpin}$ (Product 01) as the only by-product as illustrated in Scheme 3.13.

A solution of $\text{Ge}(\text{OCH}_2\text{CH}_2\text{NMe}_2)_2$ prepared in d_6 -benzene was added to a solution of HBpin at room temperature in a 1:2 ratio. A vigorous reaction was observed after mixing reagents which soon formed an orange-coloured precipitate. The proton NMR spectrum of the solution was collected after the reaction had proceeded for 24 hours at room temperature and indicated the completion of the reaction (Figure 3.20). The only by-product observed in the spectrum appeared to be $(\text{Me}_2\text{NCH}_2\text{CH}_2\text{O})\text{Bpin}$ (Product 01) as expected, with a peak for hydrogen gas at 4.47 ppm in d_6 -benzene.

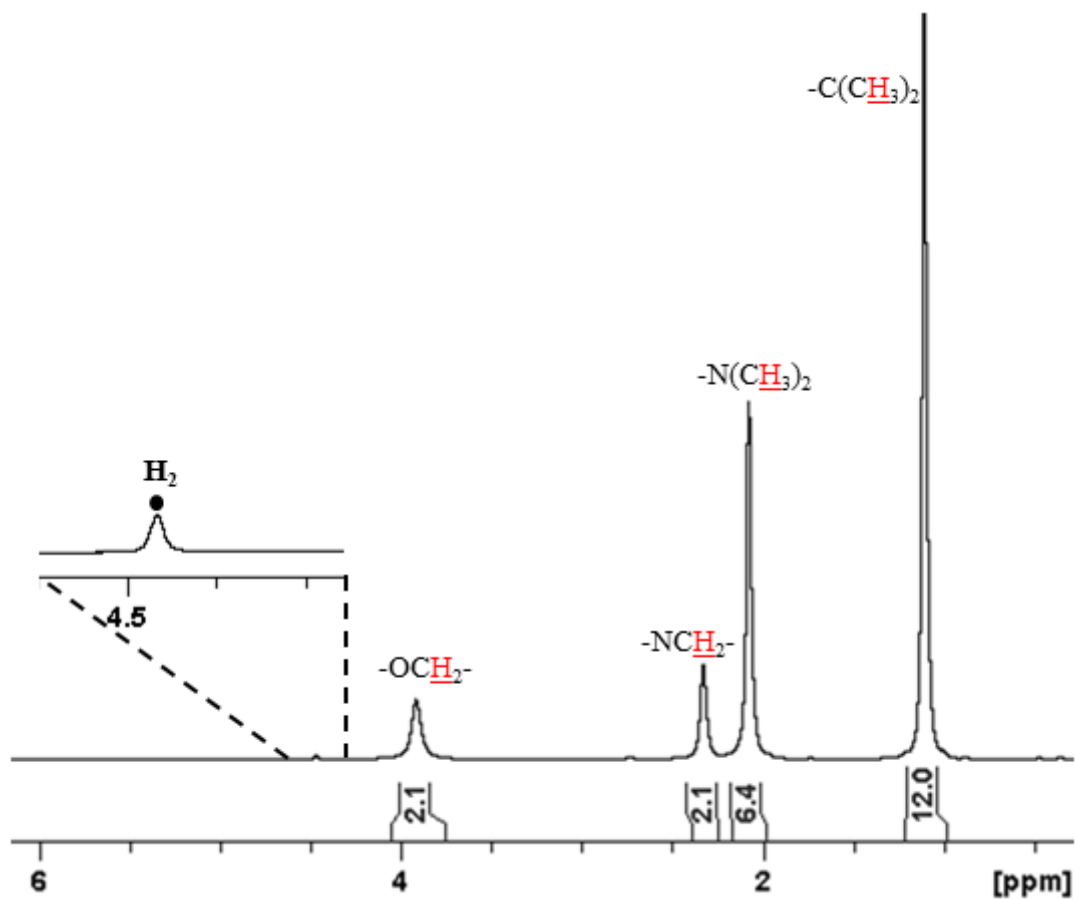


Figure 3.20: The proton NMR spectrum of the 1:2 reaction of $\text{Ge}(\text{OCH}_2\text{CH}_2\text{NMe}_2)_2$ with HBpin in d_6 -benzene, collected after 24 hours at room temperature. The circle indicates the hydrogen gas.

Further characterization, the thermal stability, and the crystal structure of $(\text{Me}_2\text{NCH}_2\text{CH}_2\text{O})\text{Bpin}$ is discussed in detail in Section 3.5. The orange precipitate formed in the reaction was collected as follows. Solvents were removed by centrifugation and the precipitate was washed several times with toluene and then hexanes. The X-ray diffractogram of the precipitate indicates that it is an amorphous solid. (Figure 3.21).

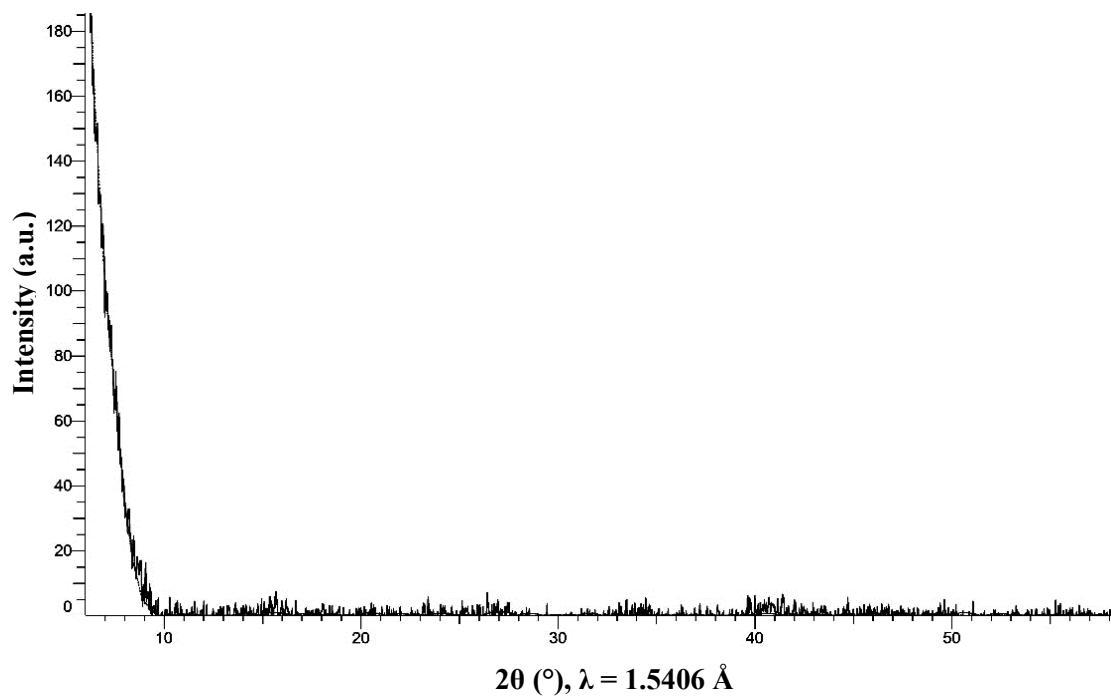
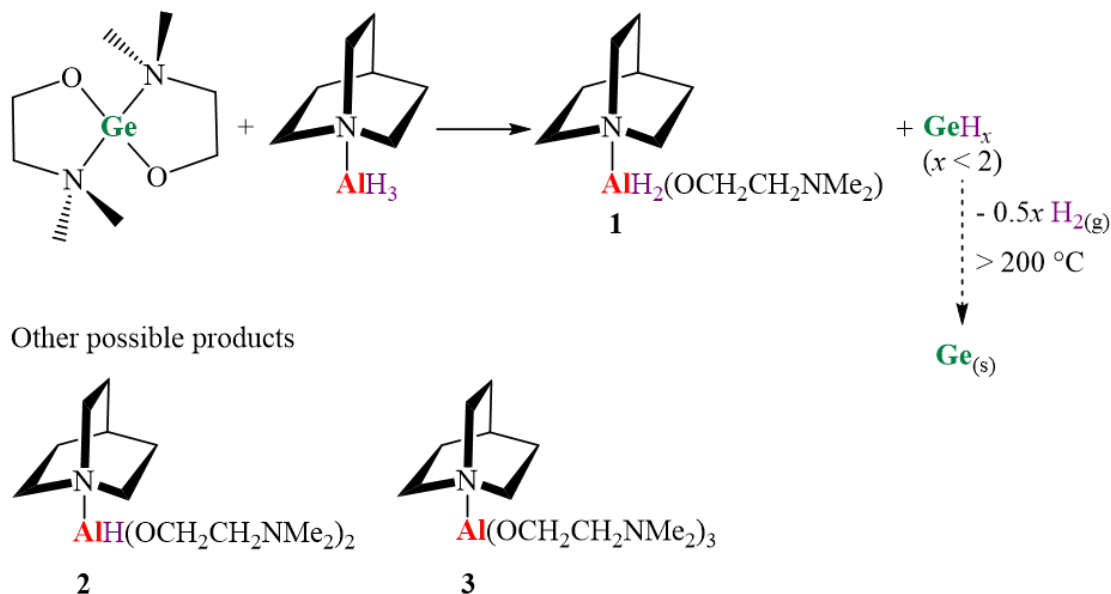


Figure 3.21: Powder X-ray diffractogram (PXRD) of the orange precipitate GeH_x formed from the 1:1 reaction of $\text{Ge}(\text{OCH}_2\text{CH}_2\text{NMe}_2)_2$ and HBpin in d_6 -benzene, 24 h, RT.

3.3.3.3 Reaction of $\text{Ge}(\text{OCH}_2\text{CH}_2\text{NMe}_2)_2$ with AlH_3 (Quinuclidine)



Scheme 3.14: Possible by-products predicted for the reaction of $\text{Ge}(\text{OCH}_2\text{CH}_2\text{NMe}_2)_2$ and AlH_3 (Quinuclidine).

Three different by-products indicated in the Scheme 3.14 can be formed during a solution reaction between $\text{Ge}(\text{OCH}_2\text{CH}_2\text{NMe}_2)_2$ and AlH_3 (Quinuclidine), depending on how many hydride groups are replaced. Product 01 is formed from exchange of one hydride group, whereas Products 02 and 03 are formed from the exchange of two and three hydride groups, respectively.

Solutions of $\text{Ge}(\text{OCH}_2\text{CH}_2\text{NMe}_2)_2$ and AlH_3 (Quinuclidine) in d_6 -benzene were mixed together in a 1:2 ratio at room temperature. Orange precipitate formation was observed soon after mixing the reagents at room temperature. The proton NMR spectrum of the reaction collected 24 hours after mixing the reagents at room temperature is shown in

Figure 3.22 b along with a proton NMR spectrum of quinuclidine (Figure 3.22 a). The complexity of the spectrum made it difficult to identify all peaks separately. However, the spectrum evidently indicates the formation of free quinuclidine during the reaction, which confirms that Al dissociates from quinuclidine upon reacting with $\text{Ge}(\text{OCH}_2\text{CH}_2\text{NMe}_2)_2$.

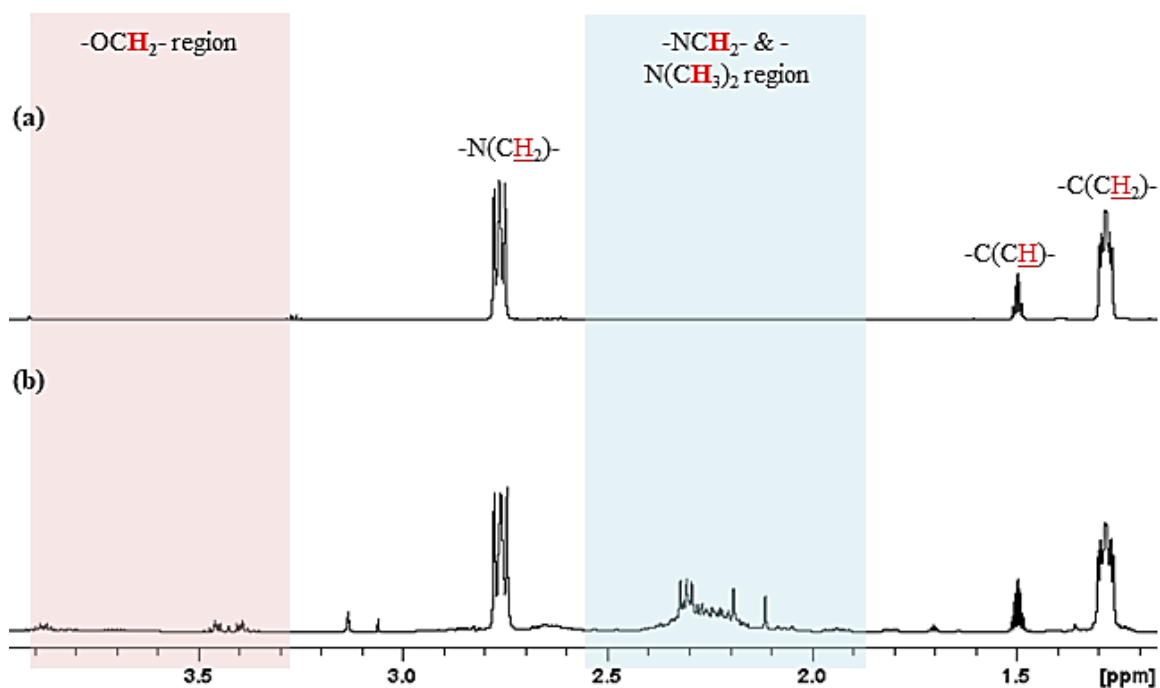


Figure 3.22: The proton NMR spectra in d_6 -benzene of a) Quinuclidine and b) the 1:2 reaction between $\text{Ge}(\text{OCH}_2\text{CH}_2\text{NMe}_2)_2$ and $\text{AlH}_3(\text{Quinuclidine})$ collected after 24 hours at room temperature.

The orange precipitate formed in the reaction was collected by removing solvents using centrifugation followed by washings with toluene and the hexanes. The powder X-ray diffractogram of the precipitate collected revealed that it was amorphous (Figure 3.23).

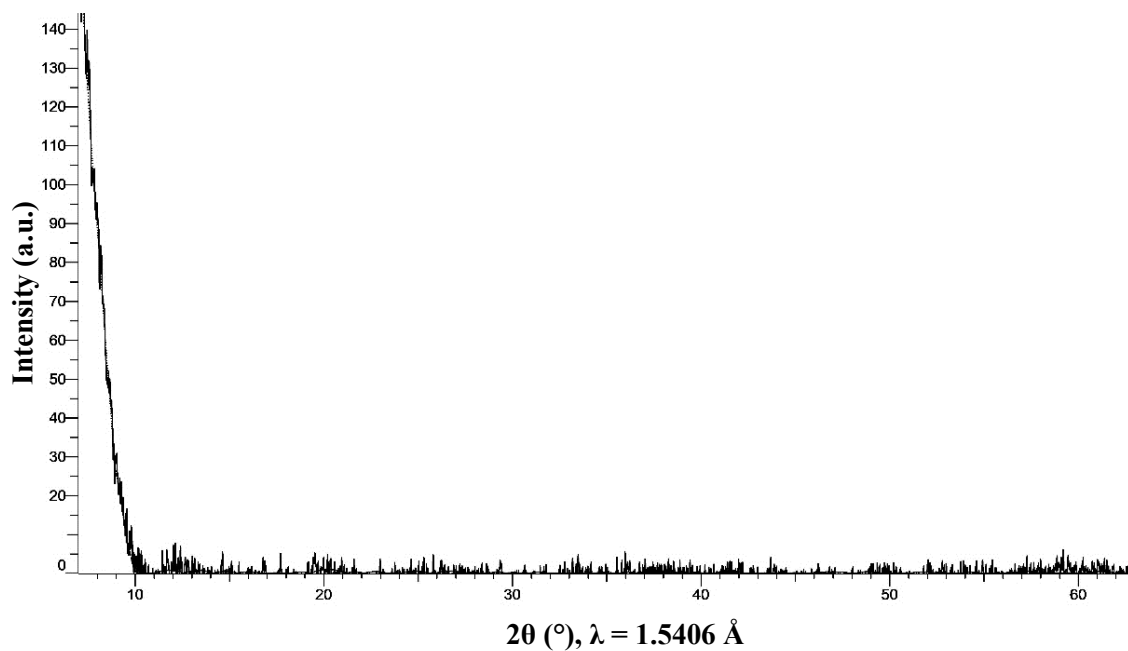
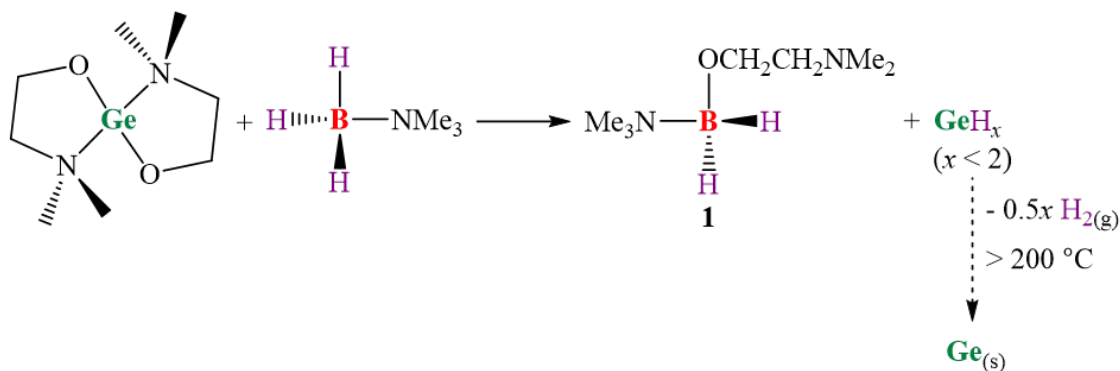
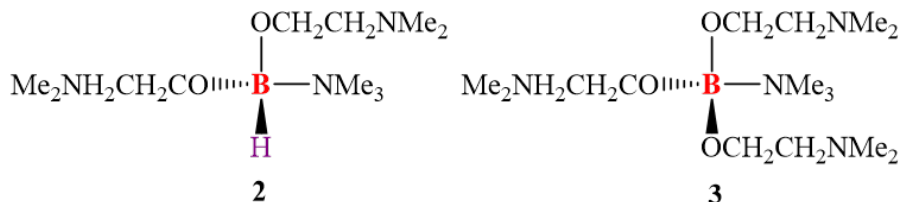


Figure 3.23: Powder X-ray diffractogram (PXRD) of the orange precipitate GeH_x formed from the 1:2 reaction of $\text{Ge}(\text{OCH}_2\text{CH}_2\text{NMe}_2)_2$ and $\text{AlH}_3(\text{Quinuclidine})$ in d_6 -benzene, 24 h, RT.

3.3.3.4 Reaction of $\text{Ge}(\text{OCH}_2\text{CH}_2\text{NMe}_2)_2$ with $\text{BH}_3(\text{NMe}_3)$



Other possible products



Scheme 3.15: Possible by-products predicted for the reaction of $\text{Ge}(\text{OCH}_2\text{CH}_2\text{NMe}_2)_2$ and $\text{BH}_3(\text{NMe}_3)$.

$\text{BH}_2(\text{OCH}_2\text{CH}_2\text{NMe}_2)(\text{NMe}_3)$ (Product 01), $\text{BH}(\text{OCH}_2\text{CH}_2\text{NMe}_2)_2(\text{NMe}_3)$ (Product 02) or $\text{B}(\text{OCH}_2\text{CH}_2\text{NMe}_2)_3(\text{NMe}_3)$ (Product 03) are the possible by-products of the ligand exchange reaction between $\text{Ge}(\text{OCH}_2\text{CH}_2\text{NMe}_2)_2$ and $\text{BH}_3(\text{NMe}_3)$, as illustrated in Scheme 3.15. In order to study the solution reactivity of $\text{Ge}(\text{OCH}_2\text{CH}_2\text{NMe}_2)_2$ with $\text{BH}_3(\text{NMe}_3)$, a solution of $\text{Ge}(\text{OCH}_2\text{CH}_2\text{NMe}_2)_2$ in d_6 -benzene was mixed with a solution of $\text{BH}_3(\text{NMe}_3)$ in d_6 -benzene in a 1:1 ratio at room temperature. No immediate reaction was observed after mixing the reagents. However, after 24 hours at room temperature an orange-brown precipitate was observed.

The proton NMR spectrum of the reaction was collected 24 hours after mixing the reagents at room temperature, and is shown in Figure 3.24. Formation of hydrogen gas was confirmed from the proton NMR spectrum (Labelled with a circle). Based on peak integrations, the spectrum suggests the formation of $\text{B}(\text{OCH}_2\text{CH}_2\text{NMe}_2)_3(\text{NMe}_3)$ (Product 03) as the only by-product of the reaction. This is further confirmed by the absence of equal-intensity quartet peaks for H attached to ^{11}B . It is also possible for the trimethylamine group to dissociate, producing $\text{B}(\text{OCH}_2\text{CH}_2\text{NMe}_2)_3$ and NMe_3 , which would give rise to the same peak pattern in the proton NMR spectrum. Some unreacted $\text{BH}_3(\text{NMe}_3)$ can also be seen in the spectrum which is labelled with an asterisk.

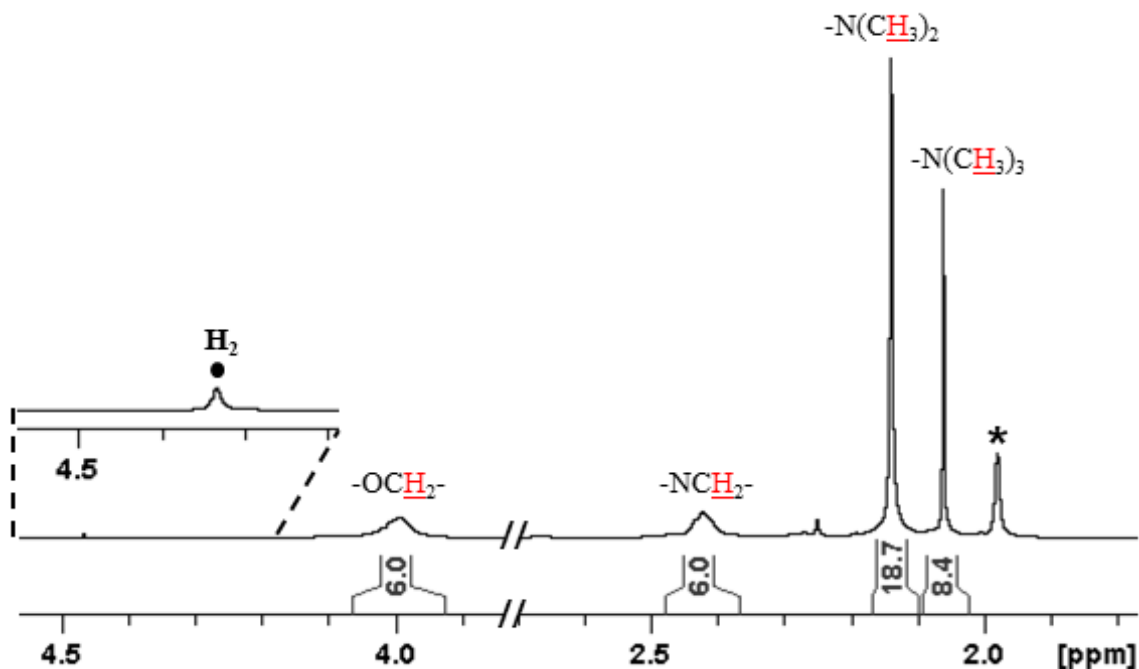
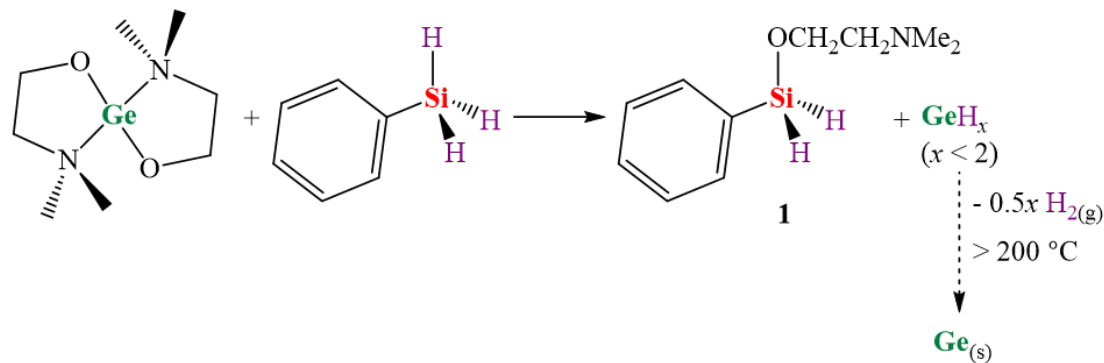
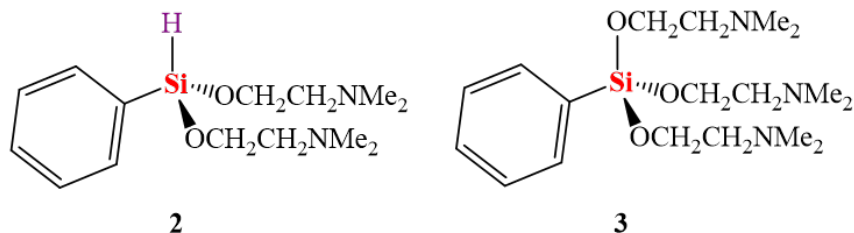


Figure 3.24: The proton NMR spectra of the 1:1 reaction solution of $\text{Ge}(\text{OCH}_2\text{CH}_2\text{NMe}_2)_2$ and $\text{BH}_3(\text{NMe}_3)$ in d_6 -benzene, collected at room temperature after 24 hours. Unreacted $\text{BH}_3(\text{NMe}_3)$ is labelled with an asterisk and the hydrogen peak is indicated with a circle.

3.3.3.5 Reaction of $\text{Ge}(\text{OCH}_2\text{CH}_2\text{NMe}_2)_2$ with PhSiH_3



Other possible products



Scheme 3.16: Possible by-products predicted for the reaction of $\text{Ge}(\text{OCH}_2\text{CH}_2\text{NMe}_2)_2$ and PhSiH_3 .

As illustrated in the Scheme 3.16, the reaction between $\text{Ge}(\text{OCH}_2\text{CH}_2\text{NMe}_2)_2$ and PhSiH_3 can produce three different by-products. Exchange of one hydride group on PhSiH_3 with a $\text{OCH}_2\text{CH}_2\text{NMe}_2$ group on $\text{Ge}(\text{OCH}_2\text{CH}_2\text{NMe}_2)_2$ will produce $\text{PhSiH}_2(\text{OCH}_2\text{CH}_2\text{NMe}_2)$ (Product 01) and subsequent loss of hydride groups will produce $\text{PhSiH}(\text{OCH}_2\text{CH}_2\text{NMe}_2)_2$ (Product 02) and $\text{PhSi}(\text{OCH}_2\text{CH}_2\text{NMe}_2)_3$ (Product 03) respectively.

To study the reactivity of $\text{Ge}(\text{OCH}_2\text{CH}_2\text{NMe}_2)_2$ towards PhSiH_3 in solution, a solution of PhSiH_3 was added to a stirring solution of $\text{Ge}(\text{OCH}_2\text{CH}_2\text{NMe}_2)_2$ in d_6 -benzene in a 1:5 ratio at room temperature. An orange-coloured precipitate was observed immediately after

mixing the reagents at room temperature. The proton NMR spectrum of the reaction solution collected 24 hours after mixing reagents at room temperature is shown in Figure 3.25. The proton NMR spectrum of the reaction confirms the formation of hydrogen gas (Figure 3.25-Labelled with a circle). Based on the proton NMR spectrum, the reaction seems to produce $\text{PhSiH}(\text{OCH}_2\text{CH}_2\text{NMe}_2)_2$ (Product 02) (Figure 3.25-Labelled with squares) and $\text{PhSi}(\text{OCH}_2\text{CH}_2\text{NMe}_2)_3$ (Product 03) (Figure 3.25-Labelled with triangles). No signs of $\text{PhSiH}_2(\text{OCH}_2\text{CH}_2\text{NMe}_2)$ (Product 01) were observed from the spectrum.

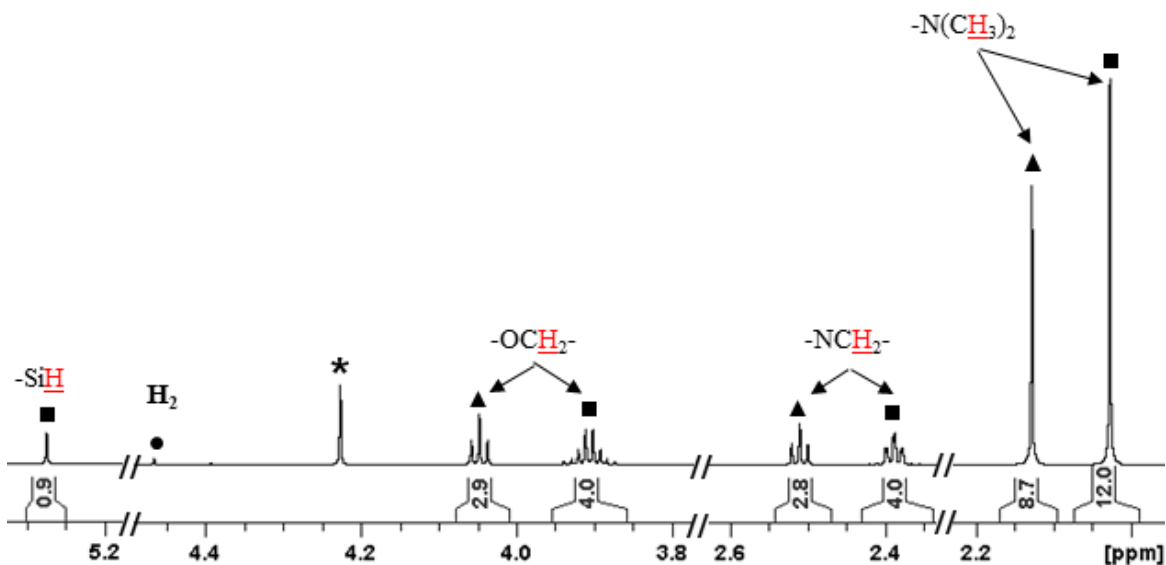


Figure 3.25: The proton NMR spectrum of the 1:5 reaction of $\text{Ge}(\text{OCH}_2\text{CH}_2\text{NMe}_2)_2$ and PhSiH_3 in d_6 -benzene, collected at room temperature after 24 hours. A delay time of 15s was used to ensure proper integration of SiH signals. $\text{PhSiH}(\text{OCH}_2\text{CH}_2\text{NMe}_2)_2$ is labelled with squares and $\text{PhSi}(\text{OCH}_2\text{CH}_2\text{NMe}_2)_3$ is labelled with stars. The circle indicates the peak of the hydrogen gas.

$\text{Ge}(\text{OCH}_2\text{CH}_2\text{NMe}_2)_2$ and PhSiH_3 were mixed in several different ratios to explore the ability to produce only one by-product during the reaction. Regardless of the stoichiometric ratios between $\text{Ge}(\text{OCH}_2\text{CH}_2\text{NMe}_2)_2$ and PhSiH_3 , all reactions continually produced both $\text{PhSiH}(\text{OCH}_2\text{CH}_2\text{NMe}_2)_2$ (Product 02) and $\text{PhSi}(\text{OCH}_2\text{CH}_2\text{NMe}_2)_3$ (Product 03). However, the distribution between these two products were changing when varying the stoichiometric ratios between two reagents. In order to further understand the product distribution reactant solutions of PhSiH_3 and $\text{HOCH}_2\text{CH}_2\text{NMe}_2$ in d_6 -benzene were mixed together in 1:1, 1:2, and 1:3 ratios at room temperature. Figure 3.26 illustrates a comparison of proton NMR spectra collected for reaction solutions of 1:1, 1:2, and 1:3 (Figure 3.26 a, Figure 3.26 b, and Figure 3.26 c respectively). Comparison of these spectra reveals that increasing $\text{HOCH}_2\text{CH}_2\text{NMe}_2$ in the reaction favours the formation of $\text{PhSi}(\text{OCH}_2\text{CH}_2\text{NMe}_2)_3$ (Product 03).

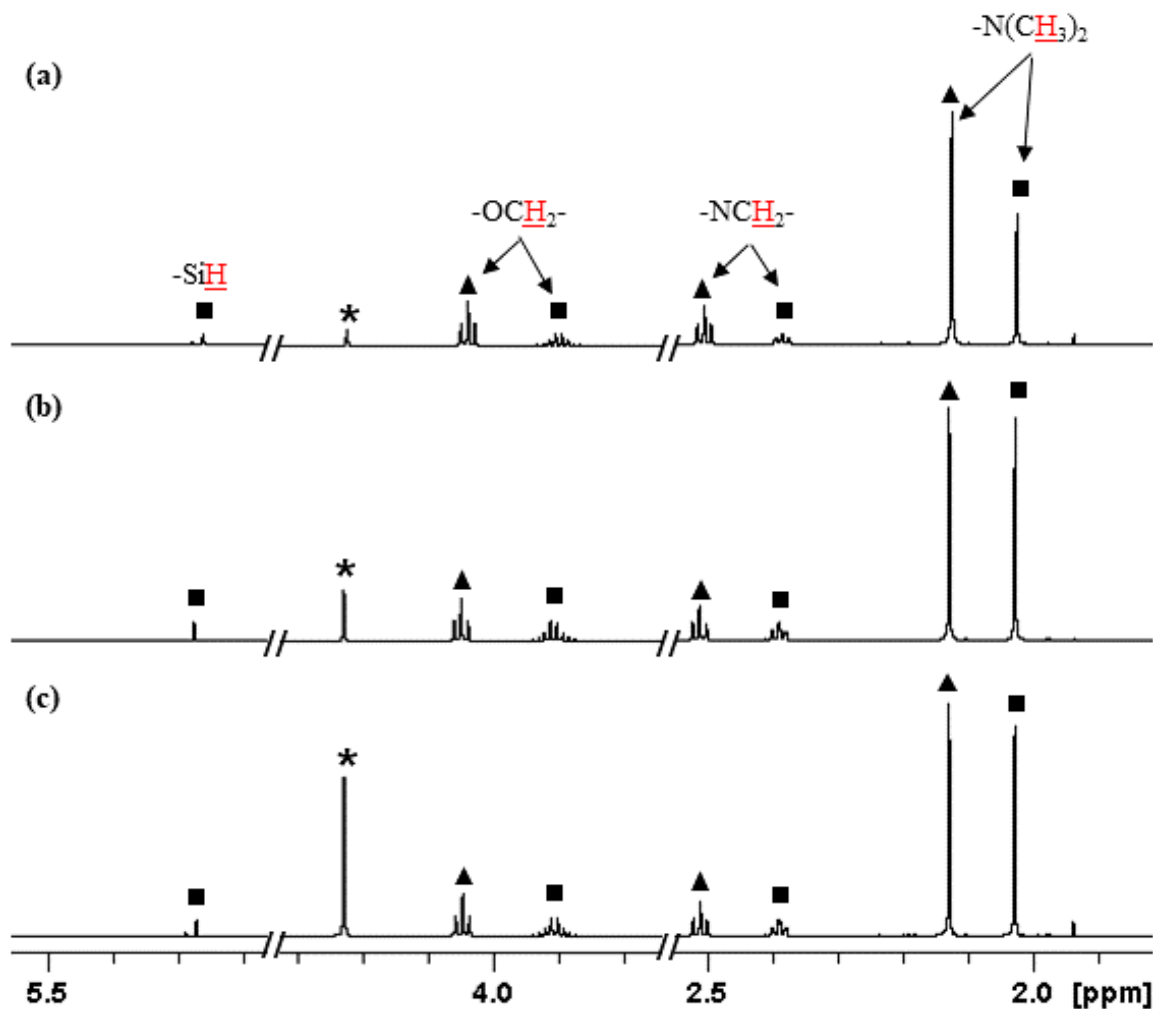


Figure 3.26: Proton NMR spectra collected for reactions between PhSiH₃ and HOCH₂CH₂NMe₂ in d₆-benzene at room temperature, a) 1:3 reaction, b) 1:2 reaction, and c) 1:1 reaction. Delay time of 15s was used to ensure proper integration of SiH signals. PhSiH(OCH₂CH₂NMe₂)₂ is labelled with squares and PhSi(OCH₂CH₂NMe₂)₃ is labelled with triangles.

Figure 3.27 shows the X-ray diffractogram collected for the orange precipitate $(\text{GeH})_x$ formed from the reaction. As is evident from the diffractogram, the precipitate was found to be amorphous, as expected.

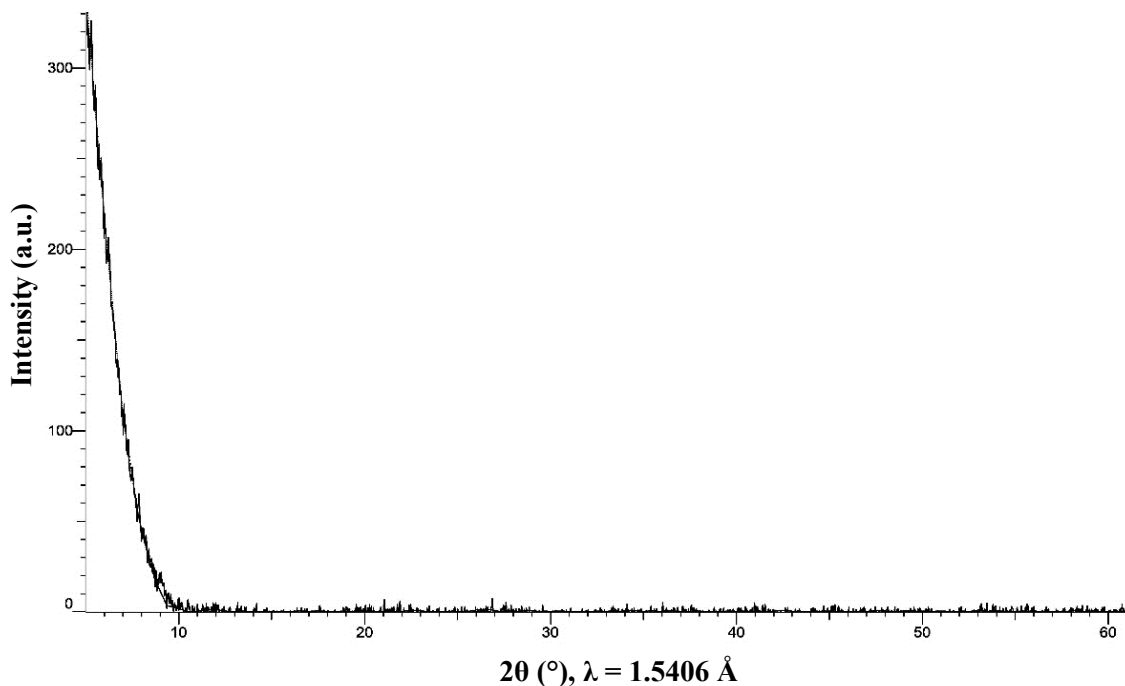


Figure 3.27: Powder X-ray diffractogram (PXRD) of the orange precipitate GeH_x formed from the 1:5 reaction of $\text{Ge}(\text{OCH}_2\text{CH}_2\text{NMe}_2)_2$ and PhSiH_3 in d_6 -benzene, 24 h, RT.

3.4 Attempts to obtain Ge from GeH_x precipitates

All of the reactions of Ge precursors and reducing reagents gave a precipitate, which was a fine powder with colours ranging from yellow to dark orange. According to information available on literature, this yellow coloured amorphous solid is believed to be a polymeric germanium hydride with the formula of GeH_x, where x is close to 1 (values between 0.95 to 1.10 had been found), giving the formula (GeH)_x.¹³⁹ GeH_x has been reported to decompose into its elements upon heating, following the reaction equation mentioned in the Scheme 3.17.^{136 137} However, information regarding the decomposition temperature is somewhat controversial, and dependent on the method of synthesis. According to Dennis and Skow, dissolving NaGe alloy in cold water or concentrated HCl_(aq) resulted in GeH_x as brown powder, which decomposed into its elements at 165 °C.¹³⁶ Kraus, C. A et al, produced GeH_x as a brownish solid from the reaction of NaGe alloy with NH₄Br in liquid NH₃, and upon heating GeH_x after evaporating NH₃, hydrogen gas evolution was observed at or above 100 °C.¹³⁷ They found that most of the hydrogen was given off between 100-200 °C yet small quantities of hydrogen were evolved until 500 °C.¹³⁷



Scheme 3.17: Decomposition of (GeH)_x into its elements.^{136 137}

The polymeric GeH_x does not dissolve in any inorganic or organic solvents without a reaction.¹³⁶ Characterization of GeH_x using IR spectroscopy was found to produce three major Ge-H bands at 2062 cm⁻¹, 833 cm⁻¹, and 775 cm⁻¹.¹³⁹

To determine the accurate temperature and the duration of heat required for GeH_x to decompose into elemental Ge and hydrogen gas, several different GeH_x precipitates collected from 1:10 reactions of $\text{Ge}(\text{OCH}_2\text{CH}_2\text{NMe}_2)_2$ with HBpin and PhSiH_3 were heated under a dynamic argon flow. These X-ray diffractograms were then compared against the diffraction pattern produced by elemental Ge to find out if any reactions were able to produce elemental Ge. Figure 3.28 indicates the X-ray diffractogram of elemental Ge.

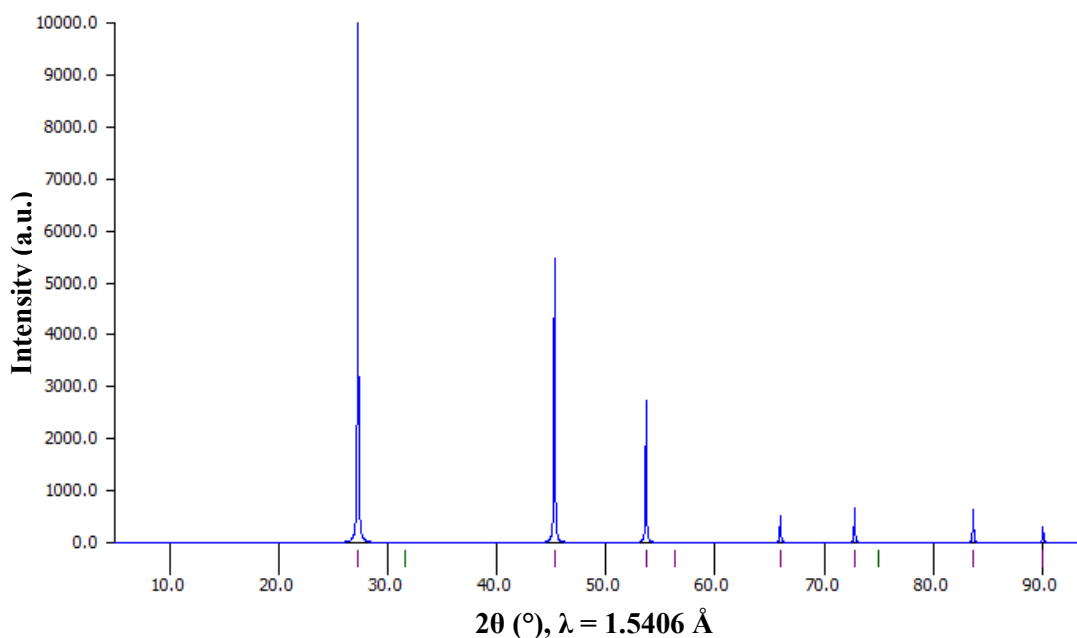


Figure 3.28: Powder X-ray diffraction (PXRD) pattern of elemental Germanium.¹⁴⁰

The orange precipitate GeH_x was collected from the 1:10 reaction of $\text{Ge}(\text{OCH}_2\text{CH}_2\text{NMe}_2)_2$ with HBpin in toluene. The resulting GeH_x was separated by centrifugation and washed with toluene followed by hexanes. GeH_x was heated at 200 °C for 24 hours under a dynamic argon flow. The orange powder turned a grey/black colour upon heating. Figure 3.29 indicates the X-ray diffractogram obtained for the grey precipitate. With comparison to the

X-ray diffractogram of elemental Ge (Figure 3.28), only a little hump around $2\theta = 27^\circ$ was observed, which corresponds to the most prominent 111 peak for elemental germanium.

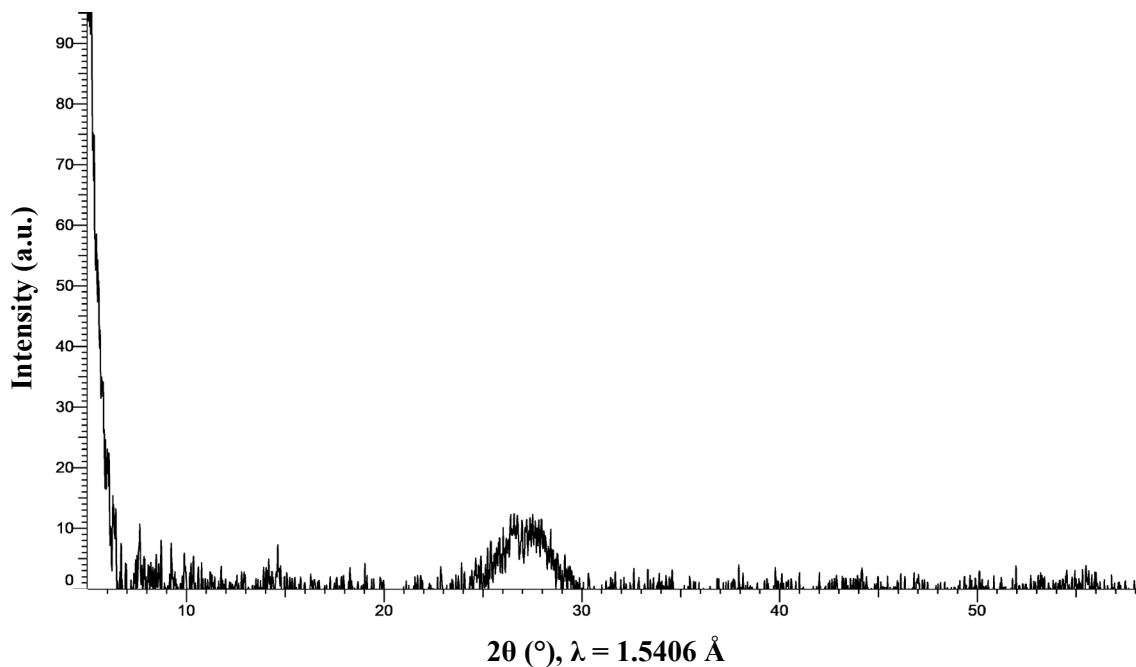


Figure 3.29: X-ray diffractogram of the grey-black solid obtained after heating (200 °C, 24 h) the orange GeH_x precipitate from the 1:10 reaction between $\text{Ge}(\text{OCH}_2\text{CH}_2\text{NMe}_2)_2$ and HBpin.

The broad hump at around $2\theta = 27^\circ$ does not provide sufficient evidence to confirm the formation of elemental Ge. However, it is not inconsistent with the formation of this product; peak broadening can be produced by Ge with low crystallinity, or very small particle size.

In another attempt, the orange-coloured GeH_x precipitate collected from the same reaction was heated at $200\text{ }^\circ\text{C}$ for 48 hours. Similar to the previous reaction, upon heating the precipitate turned grey/black in colour. Figure 3.30 illustrates the X-ray diffractogram collected for the precipitate, which again indicates a small hump at around $2\theta = 27^\circ$.

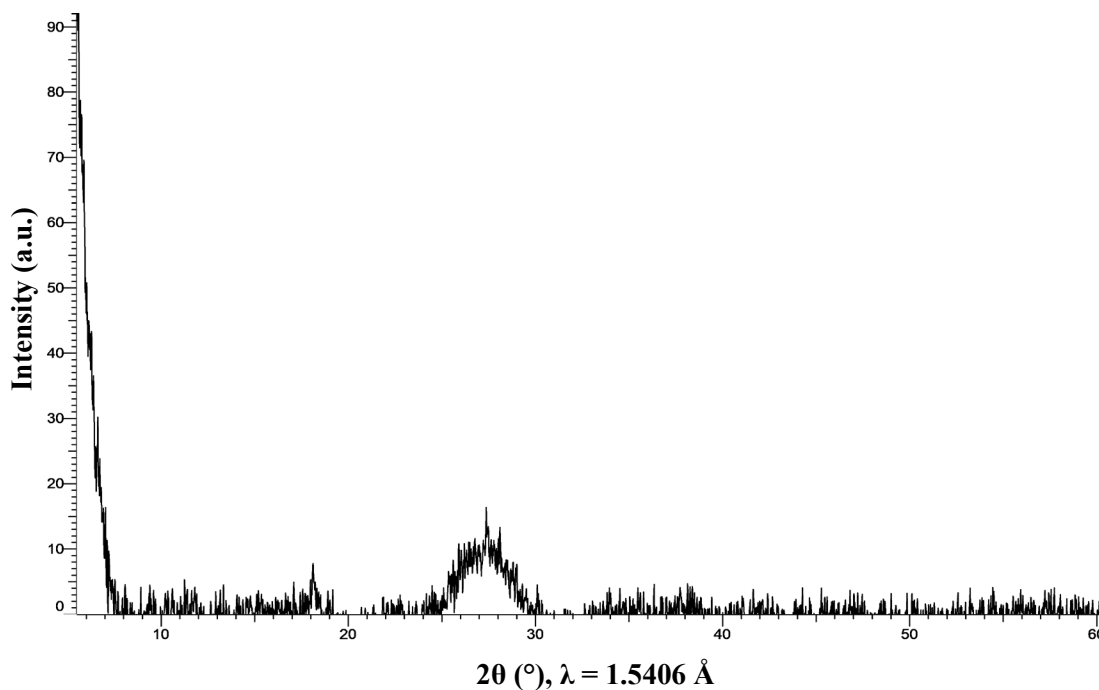


Figure 3.30: X-ray diffractogram of the grey-black solid obtained after heating ($200\text{ }^\circ\text{C}$, 48 h) the orange GeH_x precipitate from the 1:10 reaction between $\text{Ge}(\text{OCH}_2\text{CH}_2\text{NMe}_2)_2$ and HBpin.

The orange precipitate GeH_x was then heated at $230\text{ }^\circ\text{C}$ for 48 hours under a dynamic argon flow and the X-ray diffractogram was collected (Figure 3.31). Once More, the diffractogram indicates only the little hump at around $2\theta = 27^\circ$. In summary, heating the orange precipitate collected from the reaction between $\text{Ge}(\text{OCH}_2\text{CH}_2\text{NMe}_2)_2$ and HBpin afforded a grey/black powder. PXRD on this product provided some support for the formation of elemental Ge, but additional characterization would be required to confirm whether this is the case.

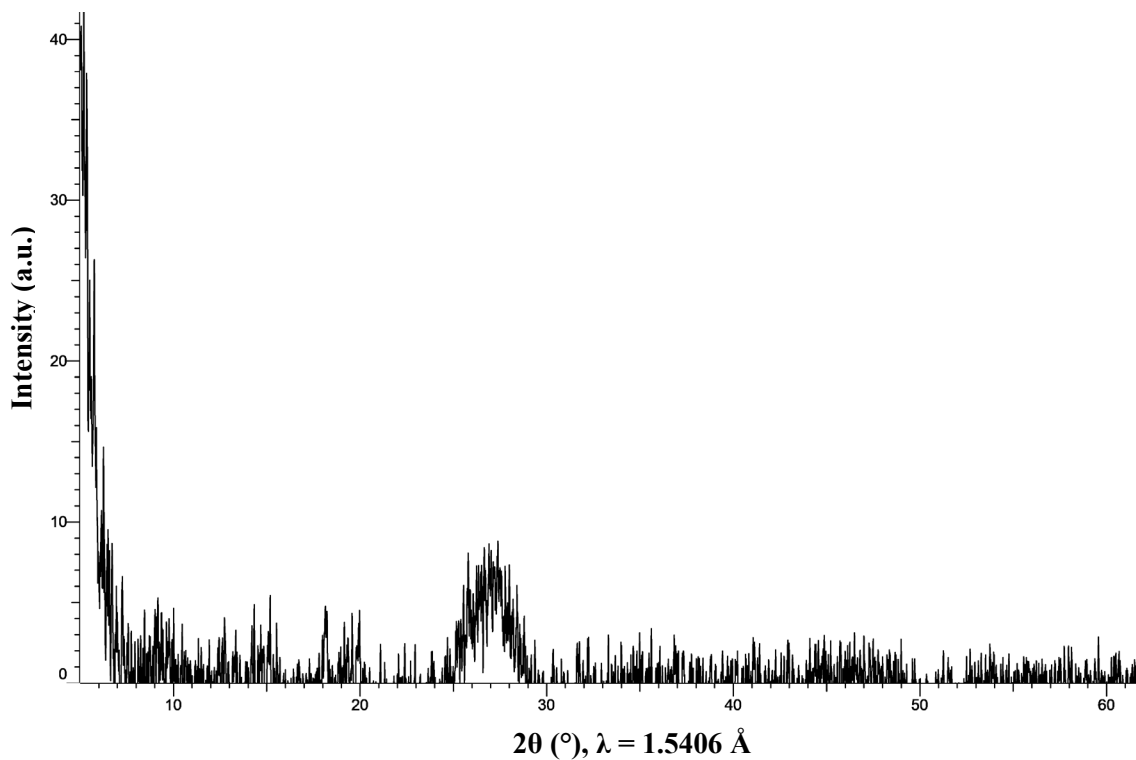


Figure 3.31: X-ray diffractogram of the grey-black solid obtained after heating ($230\text{ }^\circ\text{C}$, 48 h) the orange GeH_x precipitate from the 1:10 reaction between $\text{Ge}(\text{OCH}_2\text{CH}_2\text{NMe}_2)_2$ and HBpin.

A 1:10 reaction of $\text{Ge}(\text{OCH}_2\text{CH}_2\text{NMe}_2)_2$ with PhSiH_3 was carried out in toluene at room temperature. The orange precipitate of GeH_x was collected after few hours by centrifugation and washing with toluene followed by hexanes. The orange GeH_x powder turned grey/black upon heating at $200\text{ }^\circ\text{C}$ for 24 hours. Figure 3.32 indicates the X-ray diffractogram of the grey precipitate, and only a little hump at around $2\theta = 27^\circ$ can be seen in the diffractogram.

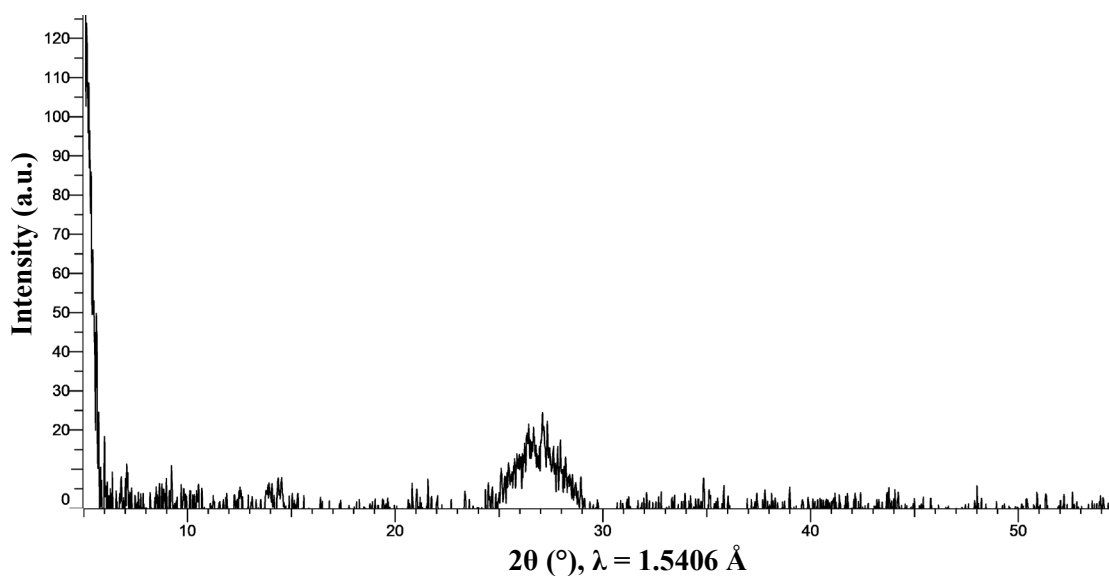


Figure 3.32: X-ray diffractogram of the grey-black solid obtained after heating ($200\text{ }^\circ\text{C}$, 24 h) the orange GeH_x precipitate from the 1:10 reaction between $\text{Ge}(\text{OCH}_2\text{CH}_2\text{NMe}_2)_2$ and PhSiH_3 .

Another sample of the orange precipitate collected from the same reaction was then heated for 48 hours at 200 °C under a dynamic argon flow. The precipitate turned grey/black in colour upon heating and the X-ray diffractogram of the precipitate was collected. A little hump at around $2\theta = 27^\circ$ is observed in the X-ray diffractogram (Figure 3.33).

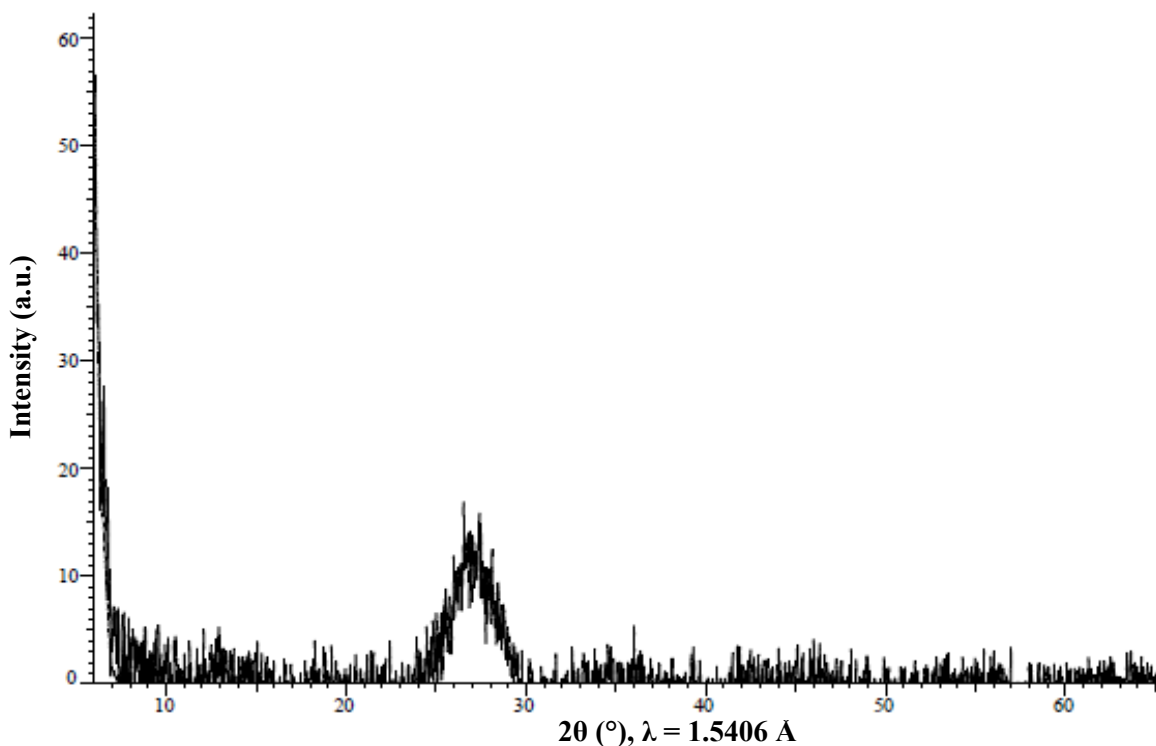


Figure 3.33: X-ray diffractogram of the grey-black solid obtained after heating (200 °C, 48 h) the orange GeH_x precipitate from the 1:10 reaction between $\text{Ge}(\text{OCH}_2\text{CH}_2\text{NMe}_2)_2$ and PhSiH_3 .

In another attempt the orange GeH_x precipitate was heated at 230 °C for 48 hours and the X-ray diffractogram was collected (Figure 3.34). The diffractogram indicates the formation of pure elemental Ge as it aligns well with diffraction pattern of elemental Ge. However, two other attempts were taken to investigate the reproducibility of the results observed and

both X-ray diffractograms collected only indicated a small hump at around $2\theta = 27^\circ$. It is not clear why this one experiment yielded a sample of crystalline Ge with sufficient particle size to avoid peak broadening. However, this result provides some support to the idea that broad peak at $2\theta = 27^\circ$, which was observed for most samples, may indeed be due to elemental germanium.

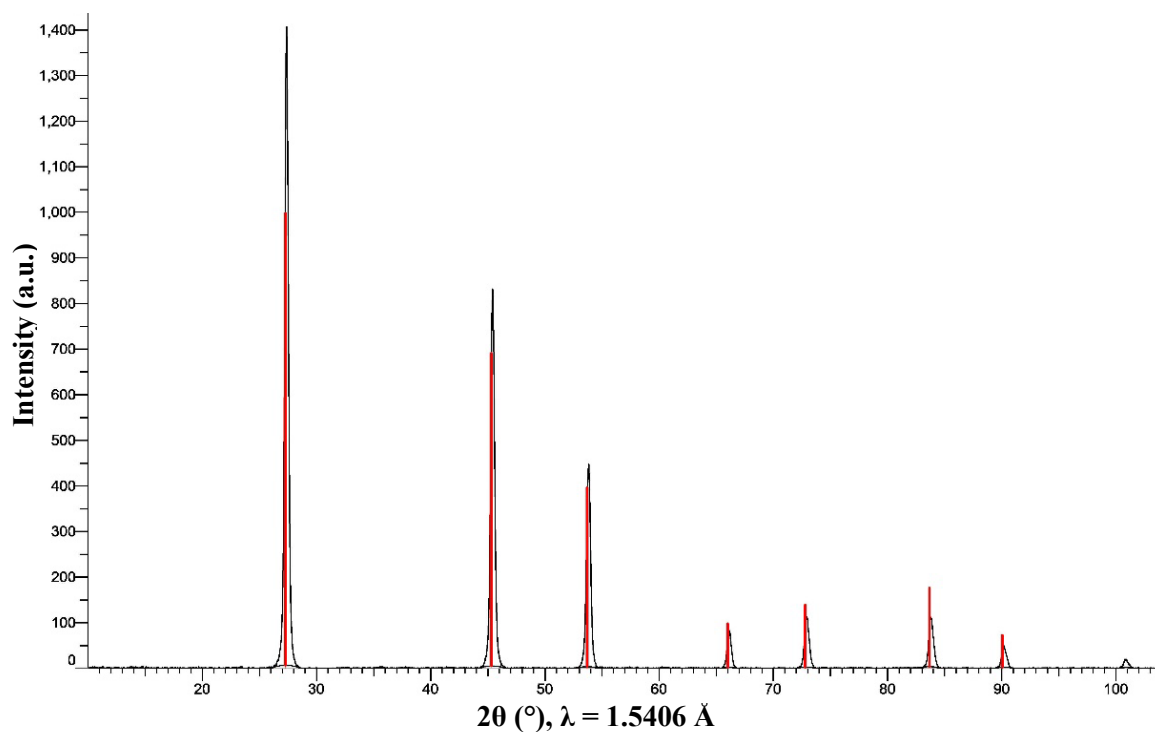


Figure 3.34: X-ray diffractogram of the grey-black solid obtained after heating (230 °C, 48 h) the orange GeH_x precipitate from the 1:10 reaction between $\text{Ge}(\text{OCH}_2\text{CH}_2\text{NMe}_2)_2$ and PhSiH_3 .

3.5 Further characterization of products formed in the solution reactions

Some solution reactions of Ge precursors with reducing reagents produced only one by-product. Attempts were taken to isolate or separately synthesize these by-products and to characterize them using relevant methods.

3.5.1 (*t*-BuNCH₂CH₂NMe₂)AlCl₂ (LAICl₂)

An equimolar reaction of GeCl₂(Dioxane) with LAIH₂ in d₆-benzene at room temperature produced LAICl₂ as evident from the proton NMR spectrum. LAICl₂ has previously been produced in a reaction between LAIH₂ and AlCl₃.¹¹⁰ ¹H and ¹³C{¹H} NMR spectra of LAICl₂ (prepared via the 1:1 reaction of GeCl₂(Dioxane) with LAIH₂) were collected and they were compared against the spectral data found in the literature, as shown in Figures 3.35 and 3.36.¹¹⁰ These 1D spectra confirm the formation of LAICl₂ in the reaction of GeCl₂(Dioxane) with LAIH₂, and the expected correlations were observed in the HSQC NMR spectrum (Figure 3.37).

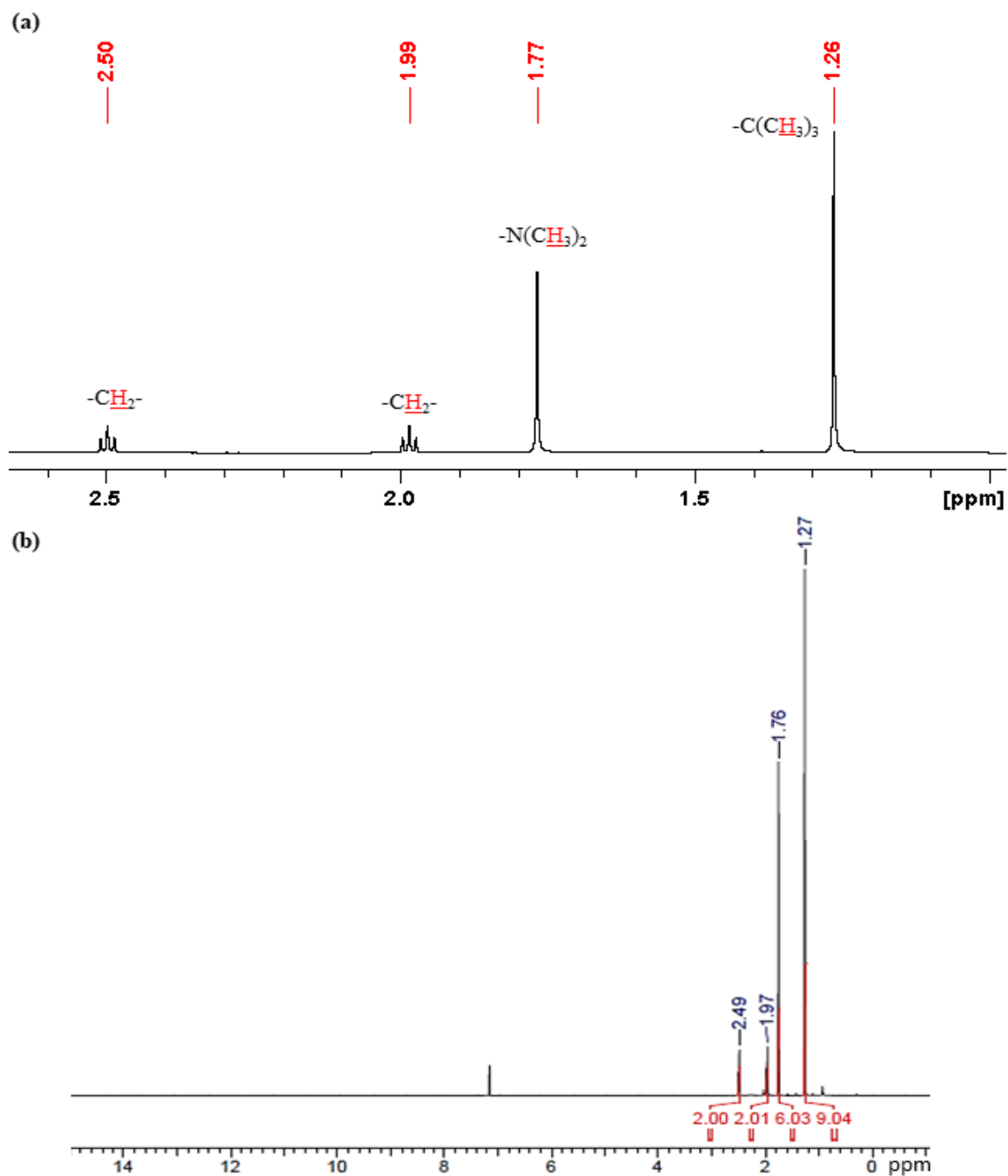


Figure 3.35: ¹H NMR spectra in d₆-benzene collected for, a) The 1:1 solution reaction between GeCl₂(Dioxane) and LAIH₂ (24 h, RT) and b) LAICl₂. Reprinted with permission from ref. 110. Copyright 2018 American Chemical Society.

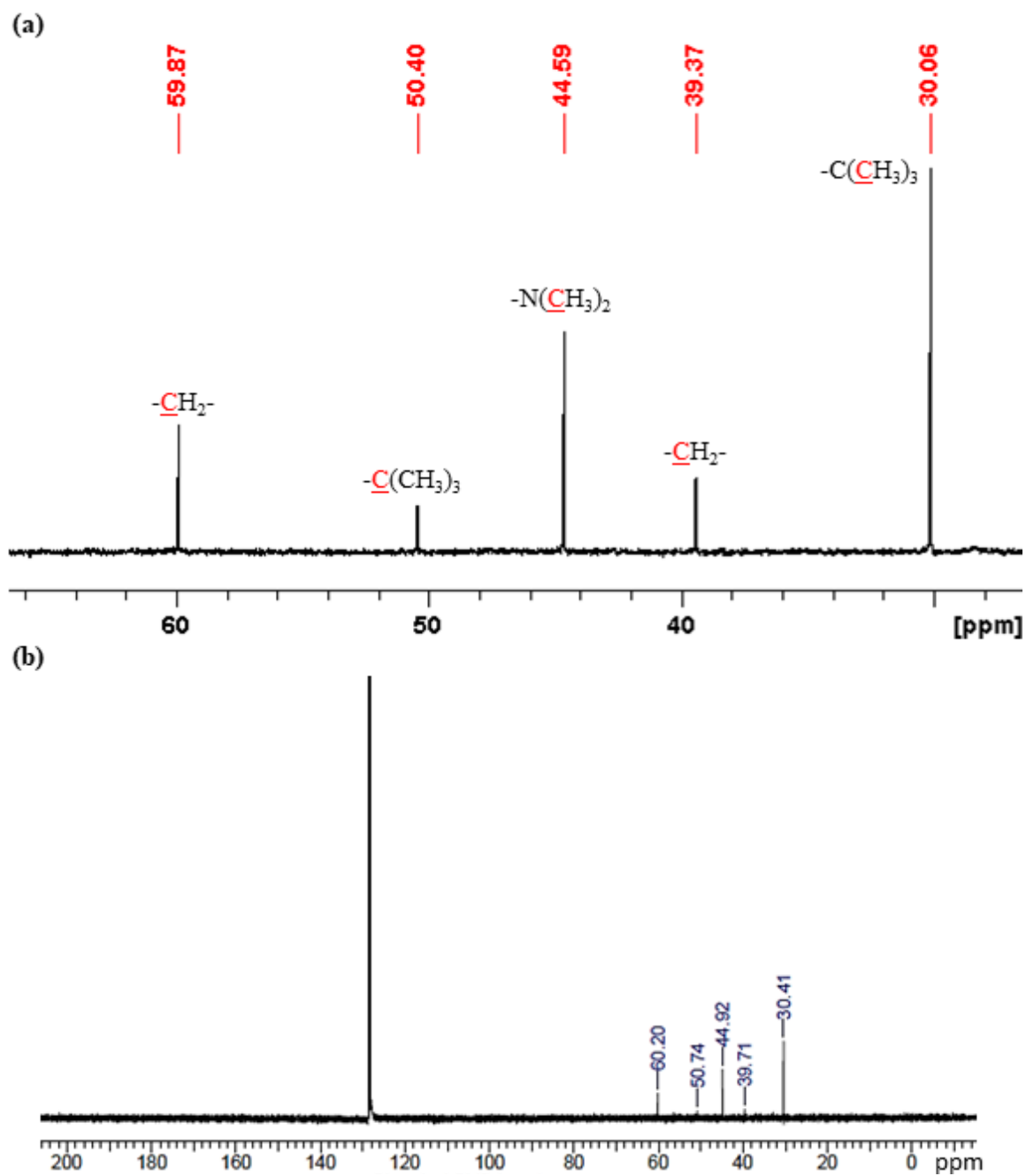


Figure 3.36: $^{13}\text{C}\{^1\text{H}\}$ NMR spectra in d_6 -benzene collected for, a) The 1:1 solution reaction between $\text{GeCl}_2(\text{Dioxane})$ and LAIH_2 (24 h, RT) and b) LAICl_2 . Reprinted with permission from ref. 110. Copyright 2018 American Chemical Society.

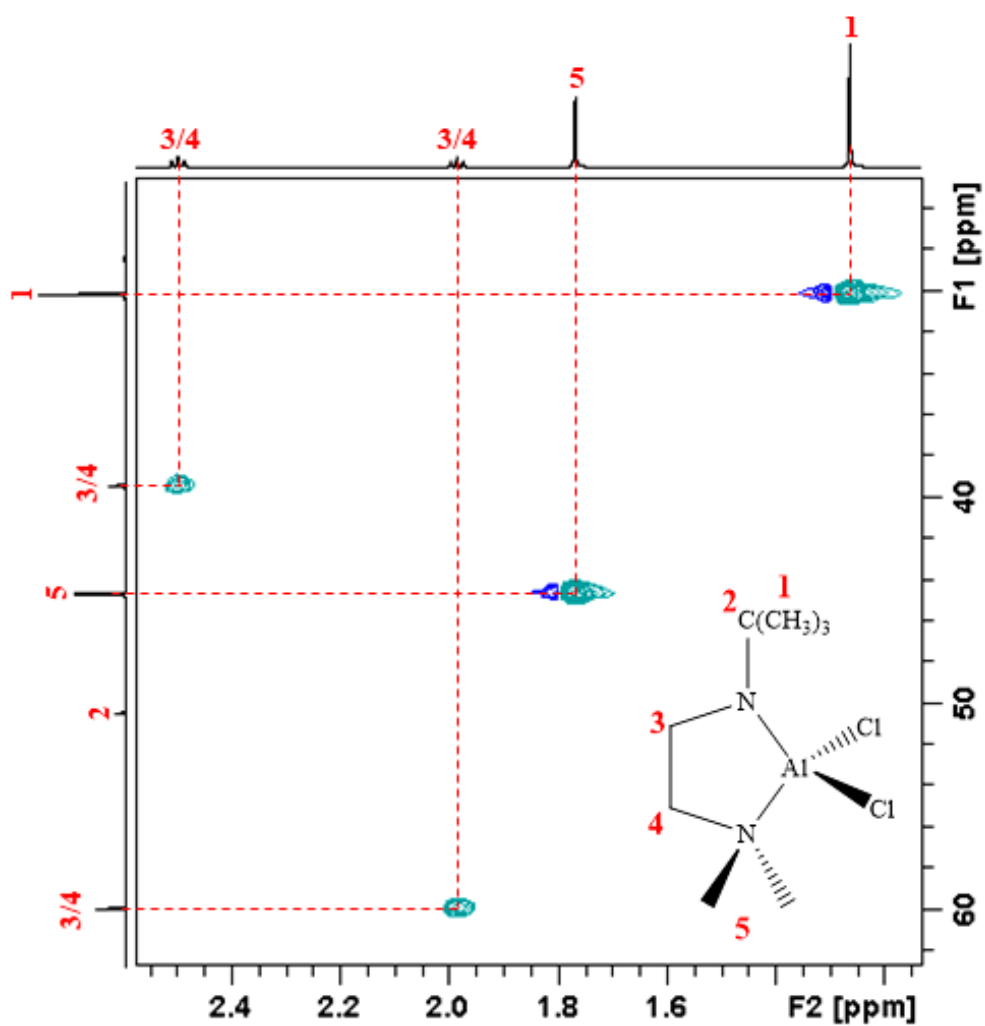


Figure 3.37: Heteronuclear single quantum correlation (HSQC) NMR spectrum in d_6 -benzene collected for the 1:1 solution reaction between $\text{GeCl}_2(\text{Dioxane})$ and $\text{LA}(\text{H}_2)$ (24 h, RT).

3.5.2 (Me₂NCH₂CH₂O)Bpin

The reaction between Ge(OCH₂CH₂NMe₂)₂ and HBpin seemed to produce (Me₂NCH₂CH₂O)Bpin as the only by-product, as evident from the proton NMR spectrum collected. Once the reaction was complete, the orange-coloured precipitate GeH_x was separated by centrifugation, and solvent was removed from the supernatant in vacuo. The residue was then dissolved in hexanes and cooled to -30 °C to afford crystals of (Me₂NCH₂CH₂O)Bpin.

The X-ray structure of (Me₂NCH₂CH₂O)Bpin is shown in Figure 3.38. The structure was solved under the space group P2₁/c with an R1 value of 4.86. In the structure, boron is four coordinated with a B ← N coordinate bond and adopts a distorted tetrahedral geometry around the B atom. The B(1)–N(1) bond distance is 1.695(4) Å which is longer than all B–O bonds (1.453(4)-1.499(3) Å).

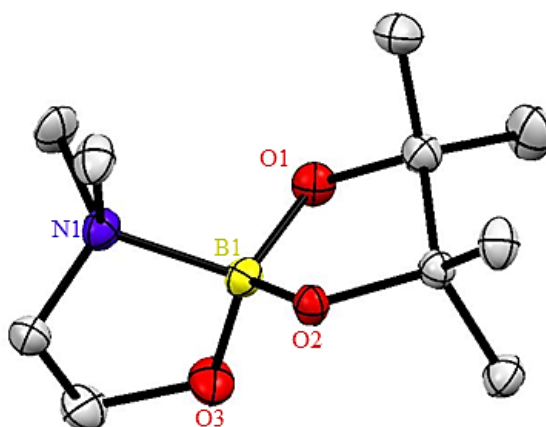
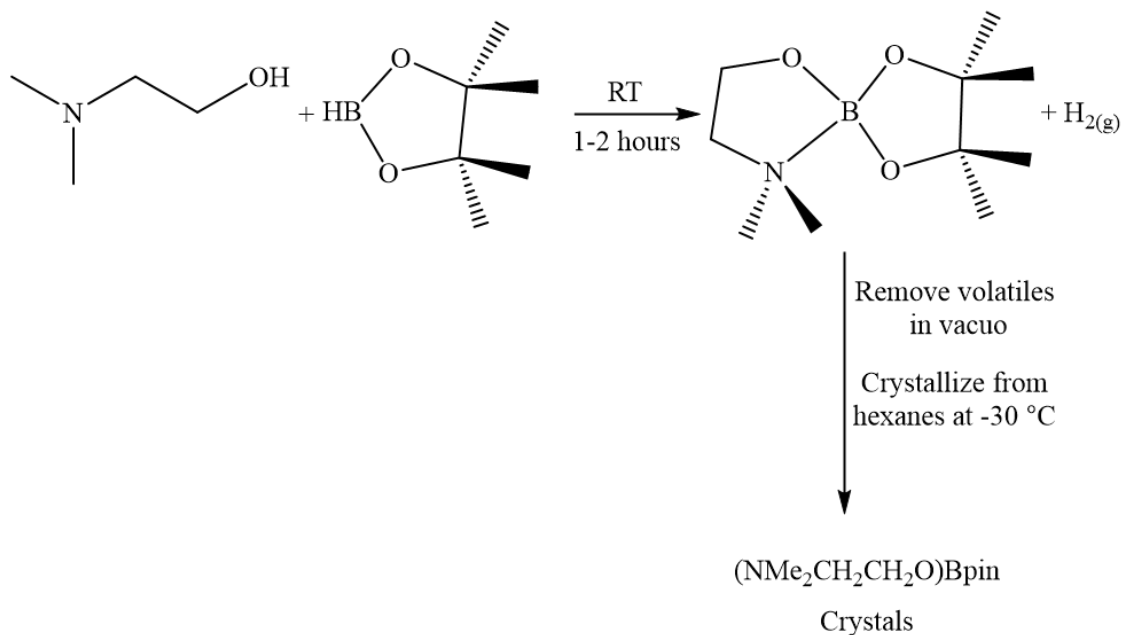


Figure 3.38: X-ray crystal structure of (Me₂NCH₂CH₂O)Bpin, with thermal ellipsoids drawn at 50% probability. Hydrogen atoms have been omitted for clarity.

Table 3.1: Selected bond angles ($^{\circ}$) and Bond lengths for $(\text{Me}_2\text{NCH}_2\text{CH}_2\text{O})\text{Bpin}$ with estimated standard deviations in parentheses.

| | |
|----------------|-----------------------|
| O(1)–B(1)–O(2) | 106.6(2) $^{\circ}$ |
| O(1)–B(1)–O(3) | 117.6(2) $^{\circ}$ |
| O(1)–B(1)–N(1) | 107.7(2) $^{\circ}$ |
| O(2)–B(1)–O(3) | 112.1(2) $^{\circ}$ |
| O(2)–B(1)–N(1) | 112.8(2) $^{\circ}$ |
| O(3)–B(1)–N(1) | 100.0(2) $^{\circ}$ |
| N(1)–B(1) | 1.695(4) \AA |
| O(1)–B(1) | 1.499(3) \AA |
| O(2)–B(1) | 1.453(4) \AA |
| O(3)–B(1) | 1.460(4) \AA |

To characterize and to study the thermal stability and volatility of $(\text{Me}_2\text{NCH}_2\text{CH}_2\text{O})\text{Bpin}$, this product was independently synthesized using the reaction between $\text{Me}_2\text{NCH}_2\text{CH}_2\text{OH}$ and HBpin. Scheme 3.18 illustrates the reaction pathway involved in the synthesis. $\text{Me}_2\text{NCH}_2\text{CH}_2\text{OH}$ and HBpin were mixed together in 1:1 ratio at room temperature. The reaction was complete after a few hours, volatiles were removed in vacuo, and $(\text{Me}_2\text{NCH}_2\text{CH}_2\text{O})\text{Bpin}$ was crystallized from hexanes at $-30\text{ }^{\circ}\text{C}$ with a yield of 70%. $(\text{Me}_2\text{NCH}_2\text{CH}_2\text{O})\text{Bpin}$ could be sublimed at $60\text{ }^{\circ}\text{C}/9\text{ mTorr}$.



Scheme 3.18: Reaction pathway for the synthesis of $(\text{Me}_2\text{NCH}_2\text{CH}_2\text{O})\text{Bpin}$.

Figure 3.39 shows NMR spectra collected for $(\text{Me}_2\text{NCH}_2\text{CH}_2\text{O})\text{Bpin}$. ^1H , $^{13}\text{C}\{^1\text{H}\}$, and $^{11}\text{B}\{^1\text{H}\}$ NMR spectra confirm that $(\text{Me}_2\text{NCH}_2\text{CH}_2\text{O})\text{Bpin}$ is free of impurities, and observation of a single peak for the pinacolate CMe_2 groups (in the ^1H and ^{13}C NMR spectra) indicates that the amine of the $\text{OCH}_2\text{CH}_2\text{NMe}_2$ ligand rapidly dissociates and re-associates in solution. The HSQC NMR spectrum of $(\text{Me}_2\text{NCH}_2\text{CH}_2\text{O})\text{Bpin}$ (Figure 3.40) further confirms the C–H connectivity of the CH_3 and CH_2 groups in $(\text{Me}_2\text{NCH}_2\text{CH}_2\text{O})\text{Bpin}$.

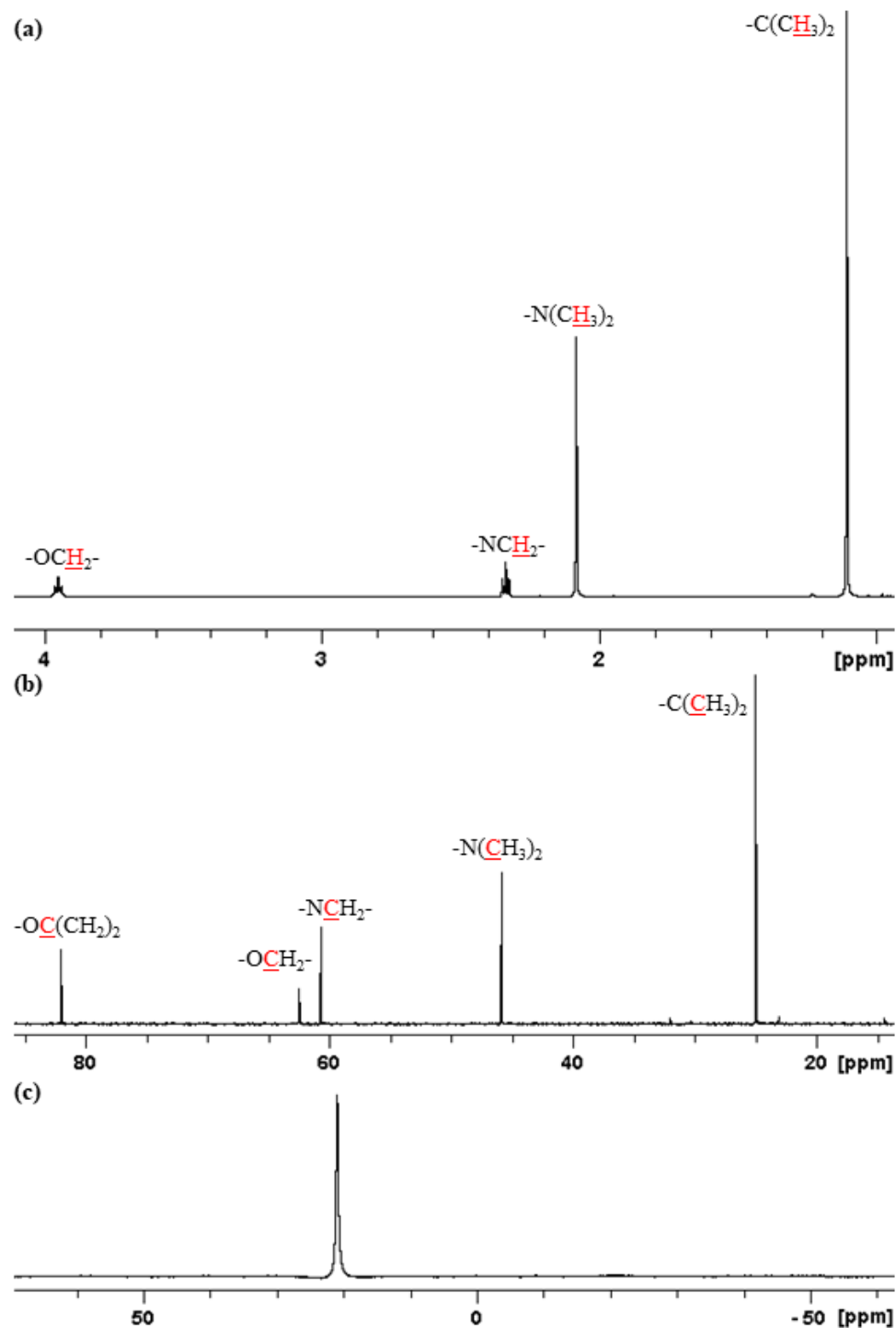


Figure 3.39: a) ^1H , b) $^{13}\text{C}\{^1\text{H}\}$, and c) $^{11}\text{B}\{^1\text{H}\}$ NMR spectra of $(\text{Me}_2\text{NCH}_2\text{CH}_2\text{O})\text{Bpin}$ in d_6 -benzene.

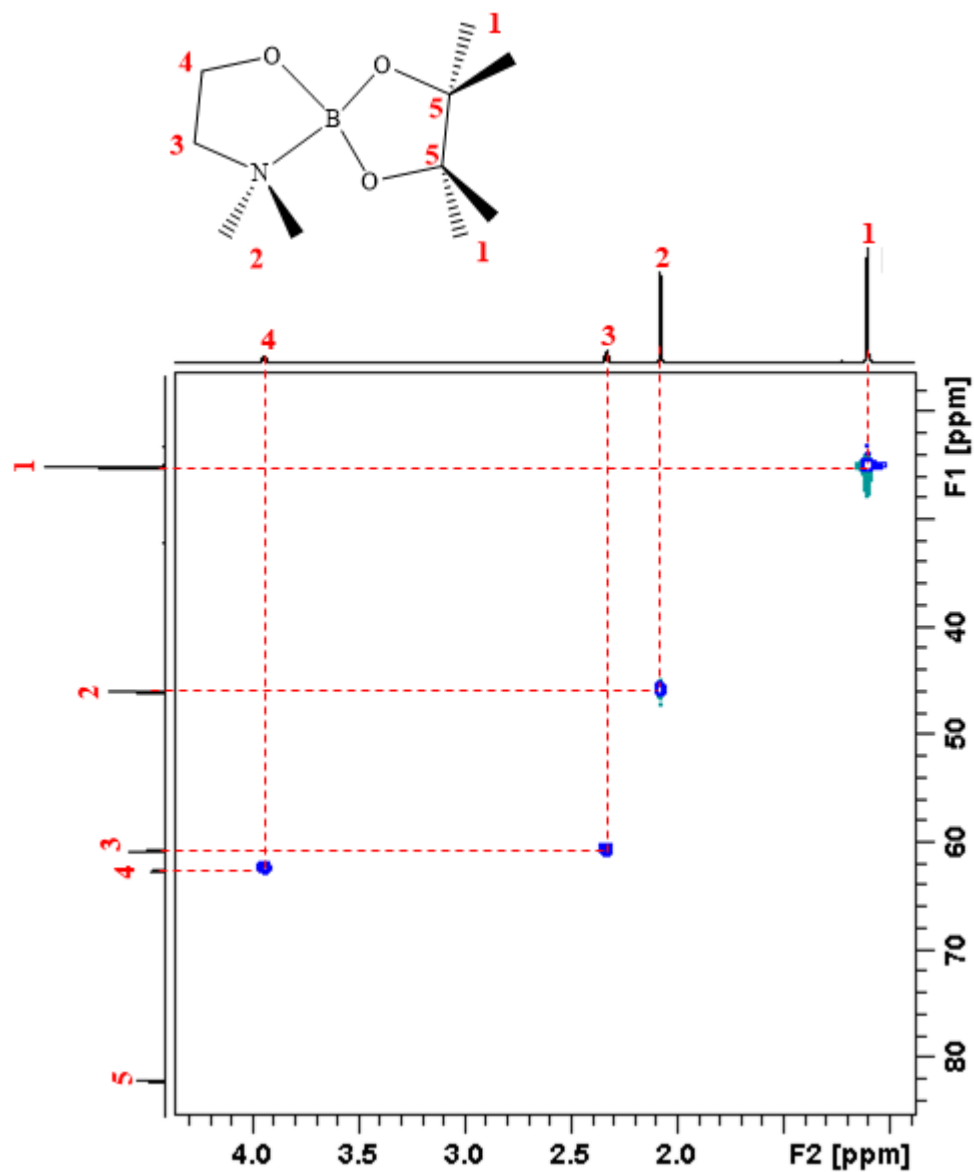


Figure 3.40: Heteronuclear single quantum correlation (HSQC) NMR spectrum collected for (Me₂NCH₂CH₂O)Bpin in d₆-benzene.

The thermal stability of (Me₂NCH₂CH₂O)Bpin was studied by heating a solid sample of (Me₂NCH₂CH₂O)Bpin under a dynamic argon flow for 24 hours at different temperatures ranging from 100-140 °C. No visual change was observed at these temperatures, and

comparison of proton NMR spectra further confirm that $(\text{Me}_2\text{NCH}_2\text{CH}_2\text{O})\text{Bpin}$ is stable up to $140\text{ }^\circ\text{C}$ (Figure 3.41).

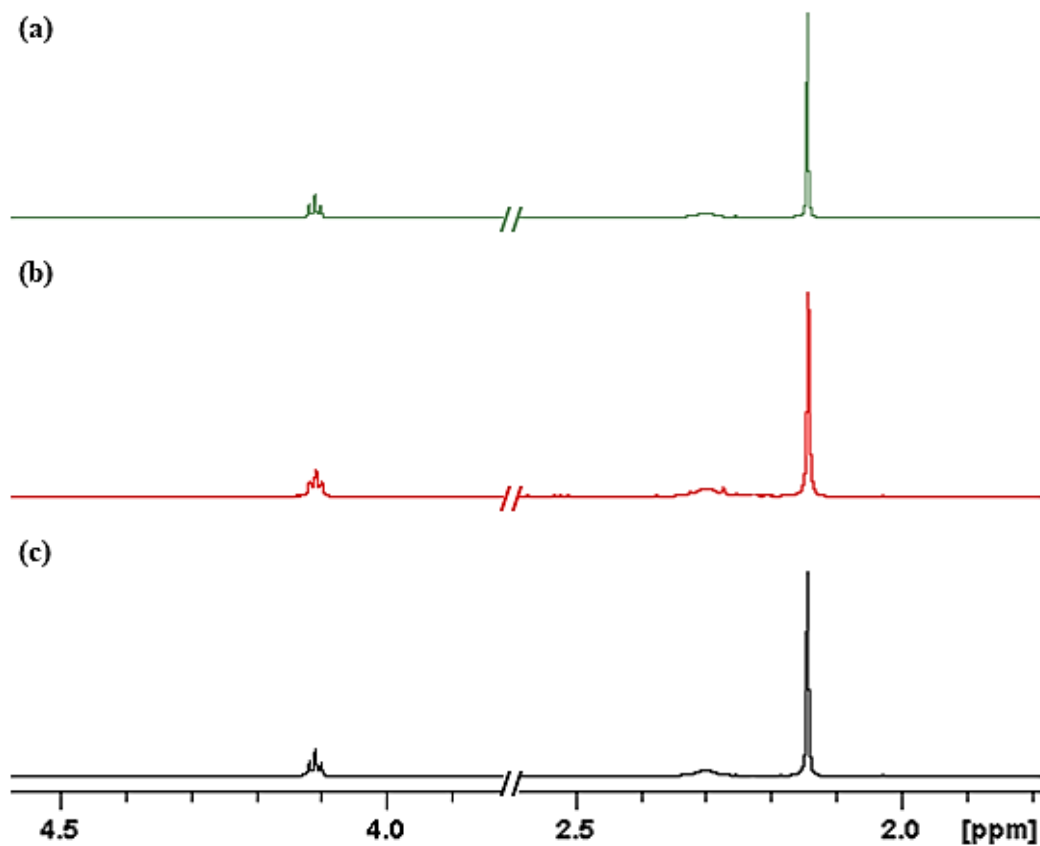


Figure 3.41: Proton NMR spectra collected for thermal stress testing of $(\text{Me}_2\text{NCH}_2\text{CH}_2\text{O})\text{Bpin}$ in d_6 -benzene, a) at RT, b) heated at $100\text{ }^\circ\text{C}/24\text{ h}$ under a dynamic argon flow, and c) heated at $140\text{ }^\circ\text{C}/24\text{ h}$ under a dynamic argon flow.

3.5.3 $\{(Me_3Si)_2N\}Bpin$

The 1:4 reaction between $Ge\{N(SiMe_3)_2\}_2$ and HBpin in d_6 -benzene produced $\{(Me_3Si)_2N\}Bpin$ as the only by-product judged by the proton NMR spectrum. In order to confirm the formation of $\{(Me_3Si)_2N\}Bpin$, $^{13}C\{^1H\}$ and $^{11}B\{^1H\}$ NMR spectra of the reaction solution were collected (Figure 3.42). The proton NMR spectrum indicates two singlets as expected for $\{(Me_3Si)_2N\}Bpin$. The singlet at 0.3 ppm is for the methyl groups connected to the Si atom of the $(Me_3Si)_2N$ group, and the singlet at 1.03 ppm is for the methyl groups attached to the C atoms of the Bpin group. The $^{13}C\{^1H\}$ NMR spectrum indicates methyl groups attached to Si at 3.8 ppm and methyl groups attached to C at 24.7 ppm. Carbons directly connected to the O atom appear at 81.7 ppm. Both the 1H and $^{13}C\{^1H\}$ NMR spectra indicate peaks believed to be from $N(SiMe_3)_2$ group of $GeH_x\{N(SiMe_3)_2\}_y$ ($x \geq 0$; $y < 2$) (Figure 3.42: labelled with triangles). In the $^{11}B\{^1H\}$ NMR spectrum, there are only two peaks, one is from unreacted excess HBpin and the other is from $\{(Me_3Si)_2N\}Bpin$. In summary, comparison of 1H , $^{13}C\{^1H\}$, and $^{11}B\{^1H\}$ NMR spectra of the solution formed from the reaction of $Ge\{N(SiMe_3)_2\}_2$ with HBpin confirms the formation of $\{(Me_3Si)_2N\}Bpin$.

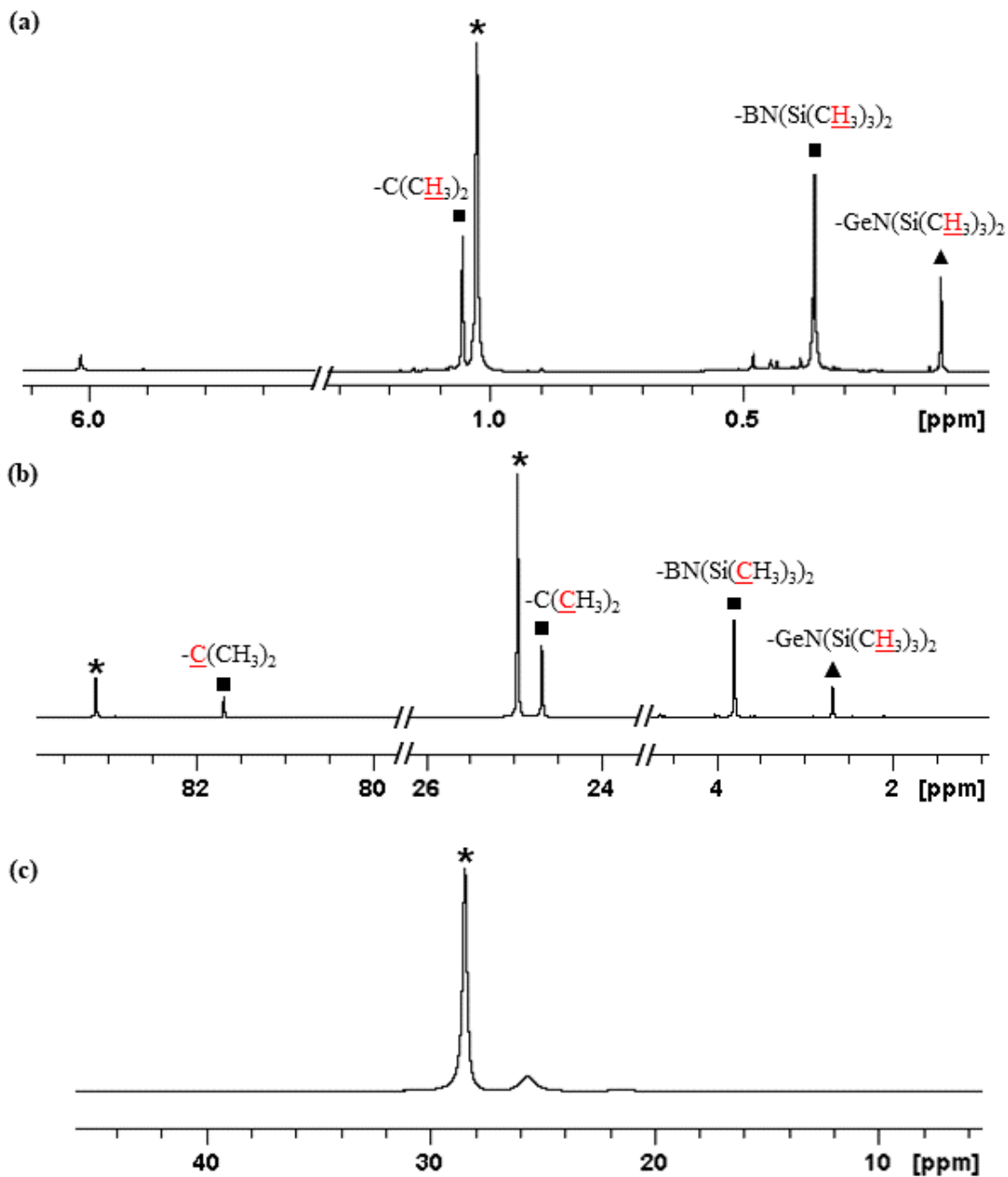


Figure 3.42: a) ^1H , b) $^{13}\text{C}\{^1\text{H}\}$, and c) $^{11}\text{B}\{^1\text{H}\}$ NMR spectra collected for the 1:4 reaction solution of $\text{Ge}\{\text{N}(\text{SiMe}_3)_2\}_2$ and HBpin in d_6 -benzene. $\text{GeH}_x\{\text{N}(\text{SiMe}_3)_2\}_y$ ($x \geq 0$; $y < 2$), $\{(\text{Me}_3\text{Si})_2\text{N}\}$ Bpin, and unreacted HBpin is labelled with triangles, squares, and with an asterisk, respectively.

3.6 Summary, conclusions, and future work

Solution reactions of all germanium precursors are expected to follow a reaction pathway in which both ligands are replaced with hydride groups to produce polymeric GeH_x and H_2 gas. Hence, a positive reaction would be indicated by the observation of hydrogen gas in the proton NMR spectrum at 4.47 ppm in d_6 -benzene. However, none of the reactions of $\text{Ge}\{\text{N}(\text{SiMe}_3)_2\}_2$ produced H_2 as evident from the proton NMR spectra collected. By contrast, H_2 formation was observed in all solution reactions of $\text{GeCl}_2(\text{Dioxane})$ and $\text{Ge}(\text{OCH}_2\text{CH}_2\text{NMe}_2)_2$. In order to confirm the formation of H_2 , the J-young tube was left open for few hours at room temperature and the NMR spectrum was collected again which indicated the disappearance of the peak at 4.47 ppm.

Table 2.2 indicates a summary of results obtained for solution reactivity studies for all three Ge precursors with hydride co-reactants along with the stoichiometric ratios between reagents. In summary, $\text{Ge}\{\text{N}(\text{SiMe}_3)_2\}_2$ only reacted with LiAlH_2 and HBpin and none of these reactions produced a precipitate. Based on the NMR spectra collected, it was found that only one $\text{N}(\text{SiMe}_3)_2$ group on $\text{Ge}\{\text{N}(\text{SiMe}_3)_2\}_2$ is replaced with a hydride group even in the presence of excess co-reactant.

For solution reactions of $\text{GeCl}_2(\text{Dioxane})$, LiAlH_2 produced an orange precipitate upon mixing the reagents at room temperature. Reactions with both $\text{AlH}_3(\text{Quinuclidine})$ and $\text{BH}_3(\text{NMe}_3)$ produced yellow solutions upon mixing reagents, which then produced orange precipitates in about 30 minutes and in 24 hours, respectively. The reaction with PhSiH_3 only produced a precipitate upon heating at $60\text{ }^\circ\text{C}$ for 24 hours. Hence, the reactivity of

$\text{GeCl}_2(\text{Dioxane})$ with co-reactants can be arranged as follows from highest reactivity to lowest reactivity; $\text{LiAlH}_2 > \text{AlH}_3(\text{Quinuclidine}) > \text{BH}_3(\text{NMe}_3) > \text{PhSiH}_3 > \text{HBpin}$ (no precipitate).

All solution reactions of $\text{Ge}(\text{OCH}_2\text{CH}_2\text{NMe}_2)_2$ produced yellow-orange precipitates at room temperature immediately upon mixing reagents together, except for the reaction with $\text{BH}_3(\text{NMe}_3)$ where a precipitate was only observed after 24 hours. Comparing the reactivities of all Ge precursors indicate that $\text{Ge}\{\text{N}(\text{SiMe}_3)_2\}_2$ has the lowest reactivity with the selected reducing reagents compared to $\text{GeCl}_2(\text{Dioxane})$ and $\text{Ge}(\text{OCH}_2\text{CH}_2\text{NMe}_2)_2$. From the reducing reagents studied, LiAlH_2 and HBpin reacted with all Ge precursors.

Precipitates produced in reactions ranged in colours from yellow to dark orange. The precipitate was found to be amorphous based on X-ray diffraction data. This precipitate is hypothesized to be the germanium monohydride polymer; $(\text{GeH})_x$ which decomposes into its elements, elemental Germanium, and hydrogen gas upon heating at temperatures above $200\text{ }^\circ\text{C}$.

Considering the overall reactivity shown by the Ge precursors, $\text{Ge}(\text{OCH}_2\text{CH}_2\text{NMe}_2)_2$ indicates highest reactivity with all reducing agents, hence would be an ideal candidate for reactor studies. Furthermore, $\text{Ge}(\text{OCH}_2\text{CH}_2\text{NMe}_2)_2$ can be easily synthesized and possesses good volatility and thermal stability.

To investigate the heating temperature and duration of heating for the thermal decomposition of GeH_x , in to its elements, the orange colour precipitates formed from the reactions of $\text{Ge}(\text{OCH}_2\text{CH}_2\text{NMe}_2)_2$ with HBpin and PhSiH_3 were heated between $200\text{ }^\circ\text{C}$

and 230 °C for different time durations under a dynamic argon flow. For all reactions to prepare GeH_x for this purpose, a large excess of the co-reactant was used to ensure the complete conversion of Ge(OCH₂CH₂NMe₂)₂ into GeH_x. All but one of the X-ray diffractograms collected upon heating the precipitate from reactions of Ge(OCH₂CH₂NMe₂)₂ with HBpin and PhSiH₃ indicated a small hump at around $2\theta = 27^\circ$ for the different temperatures and heating time durations studied. However, on one occasion, heating the precipitate (230 °C, 48 h) formed in the reaction between Ge(OCH₂CH₂NMe₂)₂ and PhSiH₃ produced an X-ray diffractogram with sharp peaks identical to elemental Ge. Hence, more characterization steps will be required to confirm the formation of elemental Ge during heating of the GeH_x precipitate.

Future studies should focus on (a) additional characterization of the polymeric GeH_x precipitate, to fully understand its structure, and (b) characterization of the grey/black precipitate formed upon heating GeH_x to confirm the formation elemental Ge during the thermal decomposition. Potential characterization methods include combustion elemental analysis, X-ray photo electron spectroscopy (XPS), and solid-state NMR spectroscopy. ALD reactor studies using the reactions of Ge(OCH₂CH₂NMe₂)₂ would be of high interest, especially with PhSiH₃ considering its low cost and availability. Reactions with LAIH₂ and HBpin would also be of interest due to high reactivity with Ge(OCH₂CH₂NMe₂)₂. Another interesting reaction would be the reaction of GeCl₂(Dioxane) with LAIH₂ as it forms LAICl₂ as the only by-product of the reaction.

Table 3.2: Summary of solution reactivity studies of Ge(II) precursors.

| Precursors | Co-reactants | | | | |
|--|---|--|--|--|--|
| | LAIH ₂ | HBpin | AlH ₃ (Quin.) | BH ₃ (NMe ₃) | PhSiH ₃ |
| Precursor: Co-reactant ratio | 1:1 | 1:2 | 2:1 | 3:2 | 3:2 |
| GeCl₂(Dioxane) | Orange-brown precipitate; (GeH) _x forms immediately at RT. | Clear yellow solution forms immediately. No precipitate. | Yellow solution forms immediately. Orange precipitate; (GeH) _x after 30 min., RT | Yellow solution forms immediately. Orange precipitate; (GeH) _x at 24 h, RT | Yellow solution forms immediately Yellow precipitate; (GeH) _x at 40 °C, 24 h |
| Precursor: Co-reactant ratio | 1:1 | 1:4 | 1: 4 | 1: 5 | 1: 4 |
| Ge{N(SiMe₃)₂}₂ | Clear pale-yellow solution. Formation of LAIH(N(SiMe ₃) ₂) | Clear pale-yellow solution at 60 °C, 24 h. Formation of (SiMe ₃) ₂ NBpin | No reaction | No reaction | No reaction |

| Precursors | Co-reactants | | | | |
|--|---|---|---|--|---|
| | LAH_2 | HBpin | $\text{AlH}_3(\text{Quin.})$ | $\text{BH}_3(\text{NMe}_3)$ | PhSiH_3 |
| Precursor: Co-reactant ratio | 1:1 | 1:2 | 1:2 | 1:1 | 1:5 |
| $\text{Ge}(\text{O}(\text{CH}_2)_2\text{NMe}_2)_2$ | Orange-brown precipitate; $(\text{GeH})_x$ forms immediately at RT. | Orange precipitate; $(\text{GeH})_x$ forms immediately at RT. | Orange precipitate; $(\text{GeH})_x$ forms immediately at RT. | No immediate change. Orange precipitate; GeH_x at RT, 24 h | Orange precipitate; $(\text{GeH})_x$ forms immediately at RT. |

CHAPTER 4 – EXPERIMENTAL

4.1 General Procedures

All air-sensitive operations were performed in a purified argon atmosphere using glovebox or standard Schlenk line techniques. LiAlH_4 in Et_2O , LiAlH_4 , quinuclidine hydrochloride, 4,4,5,5-tetramethyl-1,3,2-dioxaborolane (HBpin), 2-isopropoxy-4,4,5,5-tetramethyl-1,3,2-dioxaborolane (PrO^iBpin), $\text{BH}_3(\text{NMe}_3)$, PhSiH_3 , 2-Chloro-N,N, dimethylamine hydrochloride, tertiary-butylamine, 2-dimethylaminoethanol, NaCl , anhydrous MgSO_4 , AlCl_3 , and isopropanol were purchased from Sigma Aldrich. $\text{Zn}(\text{O}^i\text{Pr})_2$, ZnEt_2 , and dimethylzinc (1 M, heaxnes) were purchased from Strem Chemicals. $\text{Ge}\{\text{N}(\text{SiMe}_3)_2\}_2$ and $\text{GeCl}_2(\text{Dioxane})$ were purchased from Gelest. 2,4,4,5,5-pentamethyl-1,3,2-dioxaborolane (MeBpin) and 2-ethyl-4,4,5,5-tetramethyl-1,3,2-dioxaborolane (EtBpin) were purchased from TCI chemicals. Hexanes, toluene, and benzene were purchased from Caledon and diethyl ether was purchased from Sigma. Deuterated benzene (d_6 -benzene) was purchased from ACP chemicals. 2-dimethylaminoethanol and isopropanol were dried over molecular sieves and distilled under reduced pressure prior to use. 4,4,5,5-tetramethyl-1,3,2-dioxaborolane (HBpin) and PhSiH_3 were distilled under reduced pressure. AlCl_3 was sublimed prior to use. Hexanes, diethyl ether, and benzene, were dried and distilled at atmospheric pressure from sodium/benzophenone, while toluene was dried and distilled at atmospheric pressure from sodium. Deuterated solvent (d_6 -benzene) was dried and distilled from sodium/benzophenone. MeZnO^iPr ,⁶⁹ $[\text{H}_2\text{Al}(^i\text{BuNCH}_2\text{CH}_2\text{NMe}_2)]$ (LAiH_2),¹¹⁰

$\text{Ge}(\text{OCH}_2\text{CH}_2\text{NMe}_2)_2$,¹³⁵ and $\text{AlH}_3(\text{Quinuclidine})$ ¹²⁰ were synthesized following literature procedures.

NMR spectra were collected in dry, oxygen-free d_6 -benzene. ^1H , $^{13}\text{C}\{^1\text{H}\}$, $^{11}\text{B}\{^1\text{H}\}$, and HSQC NMR spectroscopy experiments were performed on Bruker AV-500 and AV-600 spectrometers at 298 K. Chemical shift values are given relative to SiMe_4 for ^1H and ^{13}C NMR spectra, and indirect referencing was used for ^{11}B NMR spectra. All ^1H and ^{13}C NMR spectra were referenced to SiMe_4 through the resonance of the employed deuterated solvent; d_6 -benzene ($\delta = 7.16$ ppm for ^1H NMR) or ($\delta = 128.06 \pm 0.02$ ^{13}C NMR). X-ray crystallographic analyses of powder samples were performed on a Bruker D8 Davinci diffractometer, equipped with a Vantec 500 area detector, with a focused Cu X-ray source. Reference patterns were obtained via Mercury software using data retrieved from the Cambridge Crystallographic Structure Database. X-ray crystallographic analysis of crystals were performed with crystals covered in Paratone oil and mounted on a SMART APEX II diffractometer with 3 kW sealed tube Mo generator in the McMaster Analytical X-ray (MAX) Diffraction facility.

4.2 Solution reactions of Zinc

4.2.1 The 1:1 reaction of MeZnO^iPr with LAlH_2

18.3 mg (0.143 mmol) of MeZnO^iPr in ~ 0.3 mL of d_6 -benzene was added to 25.0 mg (0.143 mmol) of LAlH_2 in ~ 0.3 mL of d_6 -benzene at room temperature. Proton NMR spectra of the reaction solution were collected within 10 minutes of mixing the reagents at RT and

after 24 hours at RT, 40 °C, 60 °C, and 80 °C, respectively. All other reactions of MeZnO^{*i*}Pr and ZnEt₂ were carried out analogously, with details provided in the Table 4.1.

Table 4.1: Amounts of Zn precursors and co-reactants used in solution reactions of MeZnO^{*i*}Pr and ZnEt₂.

| Precursor name and amount | Co-reactant name and amount | Precursor-co-reactant ratio |
|---|--|-----------------------------|
| MeZnO ^{<i>i</i>} Pr 19.8 mg (0.155 mmol) | HBpin 39.6 mg (0.310 mmol) | 1:2 |
| MeZnO ^{<i>i</i>} Pr 8.9 mg (0.070 mmol) | AlH ₃ (Quinuclidine) 10.0 mg (0.070 mmol) | 1:1 |
| MeZnO ^{<i>i</i>} Pr 12.0 mg (0.094 mmol) | BH ₃ (NMe ₃) 6.9 mg (0.090 mmol) | 1:1 |
| ZnEt ₂ 20.0 mg (0.160 mmol) | LAIH ₂ 27.6 mg (0.160 mmol) | 1:1 |
| ZnEt ₂ 20.0 mg (0.160 mmol) | HBpin 41.5 mg (0.320 mmol) | 1:2 |
| ZnEt ₂ 20.0 mg (0.160 mmol) | BH ₃ (NMe ₃) 11.7 mg (0.160 mmol) | 1:1 |
| ZnEt ₂ 20.0 mg (0.160 mmol) | PhSiH ₃ 21.8 mg (0.160 mmol) | 1:1 |

4.2.2 The 1:1 reaction of Zn(O^{*i*}Pr)₂ with LAIH₂

15.8 mg (0.086 mmol) of Zn(O^{*i*}Pr)₂ was added to a solution of 15.0 mg (0.086 mmol) of LAIH₂ in ~0.6 mL of d₆-benzene at room temperature. Proton NMR spectra of the reaction solution were collected within 10 minutes of mixing the reagents at RT and after 24 hours at RT, 40 °C, 60 °C, and 80 °C, respectively. All other reactions of Zn(O^{*i*}Pr)₂ were carried out analogously, with details provided in the Table 4.2.

Table 4.2: Amounts of Zn precursors and co-reactants used in solution reactions of $\text{Zn}(\text{O}^i\text{Pr})_2$.

| Precursor name and amount | Co-reactant name and amount | Precursor-co-reactant ratio |
|---|--|-----------------------------|
| $\text{Zn}(\text{O}^i\text{Pr})_2$ 10.0 mg (0.054 mmol) | HBpin 34.5 mg (0.270 mmol) | 1:5 |
| $\text{Zn}(\text{O}^i\text{Pr})_2$ 6.4 mg (0.035 mmol) | $\text{AlH}_3(\text{Quinuclidine})$ 10.0 mg (0.071 mmol) | 1:2 |
| $\text{Zn}(\text{O}^i\text{Pr})_2$ 10.0 mg (0.054 mmol) | $\text{BH}_3(\text{NMe}_3)$ 4.0 mg (0.054 mmol) | 1:1 |
| $\text{Zn}(\text{O}^i\text{Pr})_2$ 10.0 mg (0.054 mmol) | PhSiH_3 14.9 mg (0.109 mmol) | 1:2 |

4.2.3 Powder X-ray diffraction (PXRD) sample preparation

The following reaction solutions were selected to collect grey precipitates for powder X-ray diffraction studies: (a) 1:1 reaction of MeZnO^iPr with LAlH_2 24 h, RT, (b) 1:2 reaction of MeZnO^iPr with HBpin 24 h, RT, (c) MeZnO^iPr with $\text{AlH}_3(\text{Quinuclidine})$ 24 h, 40 °C, (d) 1:1 reaction of $\text{Zn}(\text{O}^i\text{Pr})_2$ with LAlH_2 24 h, RT, (e) 1:5 reaction of $\text{Zn}(\text{O}^i\text{Pr})_2$ with HBpin 24 h, 40 °C, (f) 1:2 reaction of $\text{Zn}(\text{O}^i\text{Pr})_2$ with $\text{AlH}_3(\text{Quinuclidine})$ 24 h, RT, (g) 1:2 reaction of $\text{Zn}(\text{O}^i\text{Pr})_2$ with PhSiH_3 , 24 h, 60 °C, (h) 1:1 reaction of ZnEt_2 with LAlH_2 , and (i) 1:2 reaction of ZnEt_2 with HBpin after 24 h, RT. Precipitates were collected from each reaction solution by centrifugation. Precipitates were washed two times with toluene followed by two times with hexanes and dried in vacuo.

4.3 Solution reactions of Germanium

4.3.1 The 1:1 reaction of GeCl₂(Dioxane) with LAIH₂

32.7 mg (0.141 mmol) of GeCl₂(Dioxane) was added to a solution of 20.0 mg (0.141 mmol) of LAIH₂ in ~0.6 mL of d₆-benzene at room temperature. Proton NMR spectra of the reaction solution were collected within 10 minutes of mixing the reagents at RT and after 24 hours at RT, 40 °C, 60 °C, and 80 °C respectively. All other reactions of GeCl₂(Dioxane), Ge{N(SiMe₃)₂}₂, and Ge(OCH₂CH₂NMe₂)₂ were carried out analogously, with details provided in the Table 4.3.

Table 4.3: Amounts of GeCl₂(Dioxane) and co-reactants used in solution reactions of GeCl₂(Dioxane).

| Precursor name and amount | Co-reactant name and amount | Precursor-co-reactant ratio |
|---|---|-----------------------------|
| GeCl ₂ (Dioxane) 19.2 mg (0.083 mmol) | HBpin 21.2 mg (0.166 mmol) | 1:2 |
| GeCl ₂ (Dioxane) 32.8 mg (0.142 mmol) | AlH ₃ (Quinuclidine) 10.0 mg (0.071 mmol) | 2:1 |
| GeCl ₂ (Dioxane) 25.0 mg (0.108 mmol) | BH ₃ (NMe ₃) 5.4 mg (0.072 mmol) | 3:2 |
| GeCl ₂ (Dioxane) 30.0 mg (0.130 mmol) | PhSiH ₃ 11.8 mg (0.086 mmol) | 3:2 |

4.3.2 The 1:1 reaction of $\text{Ge}\{\text{N}(\text{SiMe}_3)_2\}_2$ with LiAlH_2

22.8 mg (0.058 mmol) of $\text{Ge}\{\text{N}(\text{SiMe}_3)_2\}_2$ in ~0.3 mL of d_6 -benzene was added to 10.0 mg (0.058 mmol) of LiAlH_2 in ~0.3 mL of d_6 -benzene at room temperature. Proton NMR spectra of the reaction solution were collected within 10 minutes of mixing the reagents at RT and after 24 hours at RT, 40 °C, 60 °C, and 80 °C, respectively. All other reactions of $\text{Ge}\{\text{N}(\text{SiMe}_3)_2\}_2$, and $\text{Ge}(\text{OCH}_2\text{CH}_2\text{NMe}_2)_2$ were carried out analogously, with details provided in the Table 4.4.

Table 4.4: Amounts of Ge precursors and co-reactants used in solution reactions of $\text{Ge}\{\text{N}(\text{SiMe}_3)_2\}_2$, and $\text{Ge}(\text{OCH}_2\text{CH}_2\text{NMe}_2)_2$.

| Precursor name and amount | Co-reactant name and amount | Precursor-co-reactant ratio |
|---|--|-----------------------------|
| $\text{Ge}\{\text{N}(\text{SiMe}_3)_2\}_2$ 19.2 mg (0.049 mmol) | HBpin 25.0 mg (0.195 mmol) | 1:4 |
| $\text{Ge}\{\text{N}(\text{SiMe}_3)_2\}_2$ 13.9 mg (0.036 mmol) | $\text{AlH}_3(\text{Quinuclidine})$ 20.0 mg (0.142 mmol) | 1:4 |
| $\text{Ge}\{\text{N}(\text{SiMe}_3)_2\}_2$ 33.7 mg (0.086 mmol) | $\text{BH}_3(\text{NMe}_3)$ 25.0 mg (0.343 mmol) | 1:4 |
| $\text{Ge}\{\text{N}(\text{SiMe}_3)_2\}_2$ 14.4 mg (0.037 mmol) | PhSiH_3 25.0 mg (0.183 mmol) | 1:5 |
| $\text{Ge}(\text{OCH}_2\text{CH}_2\text{NMe}_2)_2$ 28.9 mg (0.116 mmol) | LAlH_2 20.0 mg (0.116 mmol) | 1:1 |
| $\text{Ge}(\text{OCH}_2\text{CH}_2\text{NMe}_2)_2$ 24.3 mg (0.098 mmol) | HBpin 25.0 mg (0.195 mmol) | 1:2 |
| $\text{Ge}(\text{OCH}_2\text{CH}_2\text{NMe}_2)_2$ 22.0 mg (0.090 mmol) | $\text{AlH}_3(\text{Quinuclidine})$ 25.0 mg (0.177 mmol) | 1:2 |
| $\text{Ge}(\text{OCH}_2\text{CH}_2\text{NMe}_2)_2$ 34.1 mg (0.137 mmol) | $\text{BH}_3(\text{NMe}_3)$ 10.0 mg (0.137 mmol) | 1:1 |
| $\text{Ge}(\text{OCH}_2\text{CH}_2\text{NMe}_2)_2$ 18.3 mg (0.070 mmol) | PhSiH_3 50.0 mg (0.370 mmol) of | 1:5 |

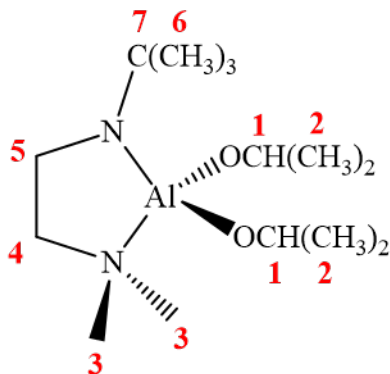
4.3.3 Powder X-ray diffraction (PXRD) sample preparation

The following reaction solutions (24 hours after mixing the reagents at room temperature) were used to collect orange precipitates for powder X-ray diffraction studies: (a) 1:1 reaction of $\text{GeCl}_2(\text{Dioxane})$ with LiAlH_2 , (b) 1:1 reaction of $\text{Ge}(\text{OCH}_2\text{CH}_2\text{NMe}_2)_2$ with LiAlH_2 , (c) 1:2 reaction of $\text{Ge}(\text{OCH}_2\text{CH}_2\text{NMe}_2)_2$ with HBpin , (d) 1:2 reaction of $\text{Ge}(\text{OCH}_2\text{CH}_2\text{NMe}_2)_2$ with $\text{AlH}_3(\text{Quinuclidine})$, and (e) 1:5 reaction of $\text{Ge}(\text{OCH}_2\text{CH}_2\text{NMe}_2)_2$ with PhSiH_3 . Precipitates were collected from each reaction solution by centrifugation. Precipitates were washed two times with toluene followed by two times with hexanes and dried in vacuo.

4.3.4 Sample preparation for GeH_x studies

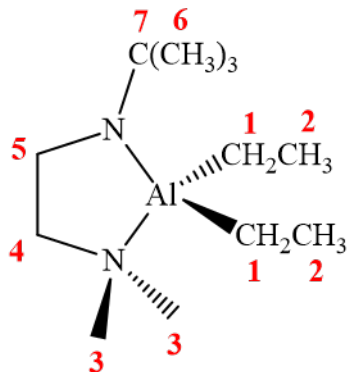
130.0 mg (0.5 mmol) of $\text{Ge}(\text{OCH}_2\text{CH}_2\text{NMe}_2)_2$ and 700.0 mg (5.0 mmol) of PhSiH_3 were dissolved in ~ 5 mL of toluene. The reagents were mixed together at room temperature and the solution was stirred for 1 hour at room temperature. The resulting precipitate was separated by centrifugation, washed two times with toluene (~2.5 mL each time) followed by two times with hexanes (~2.5 mL each time). The precipitate was then dried in vacuo. 30.0 mg (82% yield if $x = 1$) of an orange colour solid of GeH_x was obtained. Portions of the precipitate were heated under dynamic argon for (a) 24 hours at 200 °C, (b) 24 hours at 230 °C and (c) 48 hours at 230 °C in a sealed Schlenk tube in a silicon oil bath. Powder X-ray diffractograms of the precipitates were collected. The same reaction was repeated with 50.00 mg (0.2 mmol) of $\text{Ge}(\text{OCH}_2\text{CH}_2\text{NMe}_2)_2$ and 256 mg (2.0 mmol) of HBpin where 13.5 mg (92% yield if $x = 1$) of GeH_x was obtained.

4.4 (^tBuNCH₂CH₂NMe₂)Al(OⁱPr)₂ (LAl(OⁱPr)₂)



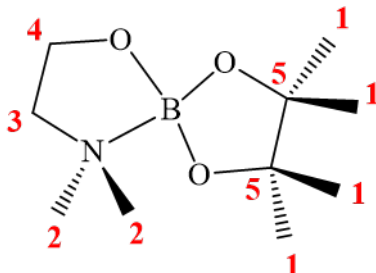
10.0 mg (0.057 mmol) of AlH_2 was dissolved in ~ 2.0 mL of d_6 -benzene. 21.0 mg (0.114 mmol) of $\text{Zn}(\text{O}^i\text{Pr})_2$ was added to the solution of AlH_2 and stirred at room temperature for 4 hours. Zn precipitates and undissolved $\text{Zn}(\text{O}^i\text{Pr})_2$ were removed by centrifugation. Attempts to collect $\text{LAl}(\text{O}^i\text{Pr})_2$ by pumping down the solvent were unsuccessful as it was too volatile and evaporated in vacuo. To obtain an appropriate volume for NMR experiments, the remaining solution was concentrated in vacuo and NMR spectra were collected. **^1H NMR (500.25 MHz, d_6 -benzene):** $\delta = 4.41$ (sept, $J_{\text{H-H}} = 6.0$ Hz, 2H, H^1), 2.68 (t, $J_{\text{H-H}} = 5.8$ Hz, 2H, H^4/H^5), 2.16 (t, $J_{\text{H-H}} = 5.8$ Hz, 2H, H^4/H^5), 1.91 (s, 6H, H^3), 1.35 (broad/overlapped, 12H, H^2 and 9H, H^6). **$^{13}\text{C}\{^1\text{H}\}$ NMR (125.78 MHz, d_6 -benzene):** $\delta = 63.48$ (C^1), 59.40 (C^4/C^5), 50.10 (C^7), 44.20 (C^3), 40.04 (C^4/C^5), 30.24 (C^6), 28.60 (C^2), 28.46 (C^2).

4.5 (ⁱBuNCH₂CH₂NMe₂)AlEt₂ (LAlEt₂)



54.0 mg (0.44 mmol) of ZnEt₂ in ~2 mL benzene and 75.0 mg (0.44 mmol) of LAlH₂ in ~2 mL benzene were mixed together at room temperature. The solution was stirred for 2 hours at room temperature and Zn precipitates were removed by centrifugation. The remaining solution was dried in vacuo to collect a clear, colourless oil 50.0 mg with a 50% yield. Attempts to grow crystals from hexanes at -30 °C were unsuccessful. **¹H NMR (500.25 MHz, d₆-benzene):** δ = 2.75 (t, *J*_{H-H} = 5.8 Hz, 2H, *H*⁴/*H*⁵), 2.14 (t, *J*_{H-H} = 5.8 Hz, 2H, *H*⁴/*H*⁵), 1.73 (s, 6H, *H*³), 1.37 (t, *J*_{H-H} = 8.1 Hz, 6H, *H*²), 1.30 (s, 9H, *H*⁶), 0.08 (q, *J*_{H-H} = 8.0 Hz, 4H, *H*¹). **¹³C{¹H} NMR (125.78 MHz, d₆-benzene):** δ = 61.06 (*C*⁴/*C*⁵), 50.23 (*C*⁷), 44.08 (*C*³), 41.36 (*C*⁴/*C*⁵), 30.55 (*C*⁶), 10.59 (*C*²), 1.89 (*C*¹).

4.6 (NMe₂CH₂CH₂O)Bpin



0.59 g (4.6 mmol) of HBpin was dissolved in ~2 mL hexanes and 0.41 g (4.6 mmol) of 2-dimethylaminoethanol was dissolved in ~2 mL hexanes. The reagents were mixed together at room temperature. The solution was then stirred at room temperature for 2 hours and solvent was removed in vacuo to collect a white solid. The solid was then dissolved in a small amount of hexanes and stored in the freezer at -30 °C to obtain a colourless crystals 0.72 g with a 72% yield. Sublimation temperature 60 °C/ 9 mTorr. **¹H NMR (500.25 MHz, d₆-benzene):** δ = 3.95 (t, *J*_{H-H} = 6.0 Hz, 2H, *H*⁴), 2.34 (t, *J*_{H-H} = 6.0 Hz, 2H, *H*³), 2.08 (s, 6H, *H*²), 1.11 (s, 12H, *H*¹). **¹³C{¹H} NMR (125.78 MHz, d₆-benzene):** δ = 82.00 (*C*⁵), 62.45 (*C*⁴), 60.67 (*C*³), 45.82 (*C*²), 24.96 (*C*¹). **¹¹B{¹H} NMR (160.50 MHz, d₆-benzene):** δ = 20.85 (B).

REFERENCES

- (1) Razavi, B. In *Fundamentals of Microelectronics*; John Wiley & Sons: New York, 2013; pp 2–10.
- (2) Schaller, R. R. Moore's Law: Past, Present and Future. *IEEE Spectr.* **1997**, *34* (6), 52–59.
- (3) Moore's Law: Transistors per microprocessor <https://ourworldindata.org/grapher/transistors-per-microprocessor> (accessed Oct 21, 2020).
- (4) Mujtaba, H. AMD EPYC Rome CPUs Feature 39.54 Billion Transistors, IOD Detailed. *Wccftech*, 2019.
- (5) Seon, Y.; Chang, J.; Yoo, C.; Jeon, J. Device and Circuit Exploration of Multi-Nanosheet Transistor for Sub-3 Nm Technology Node. *Electronics* **2021**, *10* (2), 180.
- (6) About - IEEE International Roadmap for Devices and Systems™ <https://irds.ieee.org/> (accessed Nov 17, 2020).
- (7) Marvell and TSMC Collaborate to Deliver Data Infrastructure Portfolio on 5nm Technology <https://www.hpwire.com/off-the-wire/marvell-and-tsmc-collaborate-to-deliver-data-infrastructure-portfolio-on-5nm-technology/> (accessed Nov 17, 2020).
- (8) Cutress, D. I. Where are my GAA-FETs? TSMC to Stay with FinFET for 3nm <https://www.anandtech.com/show/16041/where-are-my-gaafets-tsmc-to-stay-with-finfet-for-3nm> (accessed Nov 17, 2020).
- (9) Balling, P.; Schou, J. Femtosecond-Laser Ablation Dynamics of Dielectrics: Basics and Applications for Thin Films. *Rep. Prog. Phys.* **2013**, *76* (3), 1–39.
- (10) Emslie, D. J. H.; Chadha, P.; Price, J. S. Metal ALD and Pulsed CVD: Fundamental Reactions and Links with Solution Chemistry. *Coord. Chem. Rev.* **2013**, *257* (23–24), 3282–3296.
- (11) Seshan, K. In *Handbook of Thin Film Deposition Processes and Techniques*; Noyes Publications: New York, 2001; pp 1–100.
- (12) Knoops, H. C. M.; Potts, S. E.; Bol, A. A.; Kessels, W. M. M. Atomic Layer Deposition. In *Handbook of Crystal Growth*; Kuech, T., Ed.; Elsevier: Amsterdam, 2015; pp 1101–1134.
- (13) Rossnagel, S. M. Thin Film Deposition with Physical Vapor Deposition and Related Technologies. *J. Vac. Sci. Technol., A* **2003**, *21* (5), S74–S87.
- (14) Mattox, D. M. In *Handbook of Physical Vapor Deposition (PVD) Processing*; Elsevier: Massachusetts, 2010; pp 1–45.
- (15) Pierson, H. O. In *Handbook of Chemical Vapor Deposition: Principles, Technology and Applications*; William Andrew Inc: New Jersey, 1999; pp 20–100.
- (16) Creighton, J. R.; Ho, P. In *Chemical Vapor Deposition*; Park, J.-H., Sudarshan, T. S., Eds.; ASM International: Ohio, 2001; Vol. 2, pp 1–22.

- (17) Wang, D.; Chang, Y.-L.; Wang, Q.; Cao, J.; Farmer, D. B.; Gordon, R. G.; Dai, H. Surface Chemistry and Electrical Properties of Germanium Nanowires. *J. Am. Chem. Soc.* **2004**, *126* (37), 11602–11611.
- (18) In *Chemical Vapour Deposition: Precursors, Processes and Applications*; Jones, A. C., Hitchman, M. L., Eds.; Royal Society of Chemistry: Cambridge, UK, 2009; pp 207–345.
- (19) Gates, S. M. Surface Chemistry in the Chemical Vapor Deposition of Electronic Materials. *Chem. Rev.* **1996**, *96* (4), 1519–1532.
- (20) Knisley, T. J.; Kalutarage, L. C.; Winter, C. H. Precursors and Chemistry for the Atomic Layer Deposition of Metallic First Row Transition Metal Films. *Coord. Chem. Rev.* **2013**, *257* (23–24), 3222–3231.
- (21) Johnson, R. W.; Hultqvist, A.; Bent, S. F. A Brief Review of Atomic Layer Deposition: From Fundamentals to Applications. *J. Chem. Soc.* **2014**, *17* (5), 236–246.
- (22) Leskelä, M.; Ritala, M. Atomic Layer Deposition Chemistry: Recent Developments and Future Challenges. *Angew. Chem. Int. Ed.* **2003**, *42* (45), 5548–5554.
- (23) Ahn, J.; Ahn, C.; Jeon, S.; Park, J. Atomic Layer Deposition of Inorganic Thin Films on 3D Polymer Nanonetworks. *Appl. Sci.* **2019**, *9* (10), 1–17.
- (24) Hagen, D. J.; Pemble, M. E.; Karppinen, M. Atomic Layer Deposition of Metals: Precursors and Film Growth. *Appl. Phys. Rev.* **2019**, *6* (4), 1–63.
- (25) George, S. M. Atomic Layer Deposition: An Overview. *Chem. Rev.* **2010**, *110* (1), 111–131.
- (26) Profijt, H. B.; Potts, S. E.; van de Sanden, M. C. M.; Kessels, W. M. M. Plasma-Assisted Atomic Layer Deposition: Basics, Opportunities, and Challenges. *J. Vac. Sci. Technol., A* **2011**, *29* (5), 1–26.
- (27) Schmidt, J.; Veith-Wolf, B.; Werner, F.; Zielke, D.; Brendel, R. Silicon Surface Passivation by Ultrathin Al₂O₃ Films and Al₂O₃/SiN_x Stacks; IEEE Photovoltaic Specialists Conference: Honolulu, HI, USA, 2010; pp 885–890.
- (28) Oviroh, P. O.; Akbarzadeh, R.; Pan, D.; Coetzee, R. A. M.; Jen, T.-C. New Development of Atomic Layer Deposition: Processes, Methods and Applications. *Sci. Technol. Adv. Mater.* **2019**, *20* (1), 465–496.
- (29) Kim, H.; Oh, I.-K. Review of Plasma-Enhanced Atomic Layer Deposition: Technical Enabler of Nanoscale Device Fabrication. *Jpn. J. Appl. Phys.* **2014**, *53* (3S2), 03DA01-1–7.
- (30) Sønsteby, H. H.; Yanguas-Gil, A.; Elam, J. W. Consistency and Reproducibility in Atomic Layer Deposition. *J. Vac. Sci. Technol., A* **2020**, *38* (2), 020804-1–14.
- (31) In *Handbook of Manufacturing Engineering and Technology*; Nee, A. Y. C., Ed.; Springer London: London, 2015; pp 1–100.
- (32) Fang, G.; Xu, L.; Cao, Y.; Li, A. Theoretical Design and Computational Screening of Precursors for Atomic Layer Deposition. *Coord. Chem. Rev.* **2016**, *322*, 94–103.
- (33) Johnson, A. L.; Parish, J. D. Recent Developments in Molecular Precursors for Atomic Layer Deposition. *Organomet. Chem.* **2018**, *42*, 1–53.

- (34) Gordon, R. G. ALD Precursors and Reaction Mechanisms. In *Atomic Layer Deposition for Semiconductors*; Hwang, C. S., Ed.; Springer US: Boston, MA, 2014; pp 15–46.
- (35) Devi, A. ‘Old Chemistries’ for New Applications: Perspectives for Development of Precursors for MOCVD and ALD Applications. *Coordination Chemistry Reviews* **2013**, *257* (23), 3332–3384.
- (36) Hatanpää, T.; Ritala, M.; Leskelä, M. Precursors as Enablers of ALD Technology: Contributions from University of Helsinki. *Coord. Chem. Rev.* **2013**, *257* (23), 3297–3322.
- (37) Miiikkulainen, V.; Leskelä, M.; Ritala, M.; Puurunen, R. L. Crystallinity of Inorganic Films Grown by Atomic Layer Deposition: Overview and General Trends. *J. Appl. Phys.* **2013**, *113* (2), 021301-1–101.
- (38) Baer, D. R. In *Handbook of Deposition Technologies for Films and Coatings: Science, Applications and Technology*; Martin, P. M., Ed.; Elsevier: Amsterdam, 2009; pp 20–57.
- (39) Doll, G. L.; Mensah, B. A.; Mohseni, H.; Scharf, T. W. Chemical Vapor Deposition and Atomic Layer Deposition of Coatings for Mechanical Applications. *J. Therm. Spray Technol.* **2010**, *19* (1–2), 510–516.
- (40) Gaskins, J. T.; Hopkins, P. E.; Merrill, D. R.; Bauers, S. R.; Hadland, E.; Johnson, D. C.; Koh, D.; Yum, J. H.; Banerjee, S.; Nordell, B. J.; Paquette, M. M.; Caruso, A. N.; Lanford, W. A.; Henry, P.; Ross, L.; Li, H.; Li, L.; French, M.; Rudolph, A. M.; King, S. W. Review—Investigation and Review of the Thermal, Mechanical, Electrical, Optical, and Structural Properties of Atomic Layer Deposited High-*k* Dielectrics: Beryllium Oxide, Aluminum Oxide, Hafnium Oxide, and Aluminum Nitride. *ECS J. Solid State Sci. Technol.* **2017**, *6* (10), N189–N208.
- (41) Jeon, W. Recent Advances in the Understanding of High-*k* Dielectric Materials Deposited by Atomic Layer Deposition for Dynamic Random-Access Memory Capacitor Applications. *J. Mater. Res.* **2020**, *35* (7), 775–794.
- (42) Park, B.-E.; Oh, I.-K.; Mahata, C.; Lee, C. W.; Thompson, D.; Lee, H.-B.-R.; Maeng, W. J.; Kim, H. Atomic Layer Deposition of Y-Stabilized ZrO₂ for Advanced DRAM Capacitors. *J. Alloys Compd.* **2017**, *722*, 307–312.
- (43) Wen, L. G.; Roussel, P.; Pedreira, O. V.; Briggs, B.; Groven, B.; Dutta, S.; Popovici, M. I.; Heylen, N.; Ciofi, I.; Vanstreels, K.; Østerberg, F. W.; Hansen, O.; Petersen, D. H.; Opsomer, K.; Detavernie, C.; Wilson, C. J.; Elshocht, S. V.; Croes, K.; Bömmels, J.; Tökei, Z.; Adelman, C. Atomic Layer Deposition of Ruthenium with TiN Interface for Sub-10 Nm Advanced Interconnects beyond Copper. *ACS Appl. Mater. Interfaces* **2016**, *8* (39), 26119–26125.
- (44) Zhao, C.; Xiang, J. Atomic Layer Deposition (ALD) of Metal Gates for CMOS. *Appl. Sci.* **2019**, *9* (11), 2388-1–24.
- (45) Maina, J. W.; Merenda, A.; Weber, M.; Pringle, J. M.; Bechelany, M.; Hyde, L.; Dumée, L. F. Atomic Layer Deposition of Transition Metal Films and Nanostructures for Electronic and Catalytic Applications. *Crit. Rev. Solid State Mater. Sci.* **2020**, *45*, 1–22.

- (46) Kessels, E. Overview of All Materials Prepared by Atomic Layer Deposition (ALD) – An up-to-Date and Colorful Periodic Table (to Download) – Atomic Limits.
- (47) Higashi, G. S.; Fleming, C. G. Sequential Surface Chemical Reaction Limited Growth of High Quality Al₂O₃ Dielectrics. *Appl. Phys. Lett.* **1989**, *55* (19), 1963–1965.
- (48) Zaera, F. The Surface Chemistry of Thin Film Atomic Layer Deposition (ALD) Processes for Electronic Device Manufacturing. *J. Mater. Chem.* **2008**, *18* (30), 3521–3526.
- (49) Ponraj, J. S.; Attolini, G.; Bosi, M. Review on Atomic Layer Deposition and Applications of Oxide Thin Films. *Crit. Rev. Solid State Mater. Sci.* **2013**, *38* (3), 203–233.
- (50) Shan, C. X.; Hou, X.; Choy, K.-L. Corrosion Resistance of TiO₂ Films Grown on Stainless Steel by Atomic Layer Deposition. *Surf. Coat. Technol.* **2008**, *202* (11), 2399–2402.
- (51) Leskelä, M.; Ritala, M. Rare-Earth Oxide Thin Films as Gate Oxides in MOSFET Transistors. *J. Solid State Chem.* **2003**, *171* (1), 170–174.
- (52) Leskelä, M.; Ritala, M. Atomic Layer Deposition (ALD): From Precursors to Thin Film Structures. *Thin Solid Films* **2002**, *409* (1), 138–146.
- (53) Ritala, M.; Kalsi, P.; Riihelä, D.; Kukli, K.; Leskelä, M.; Jokinen, J. Controlled Growth of TaN, Ta₃N₅, and TaO_xN_y Thin Films by Atomic Layer Deposition. *Chem. Mater.* **1999**, *11* (7), 1712–1718.
- (54) Juppo, M.; Alén, P.; Ritala, M.; Leskelä, M. Trimethylaluminum as a Reducing Agent in the Atomic Layer Deposition of Ti(Al)N Thin Films. *Chem. Vap. Deposition* **2001**, *7* (5), 211–217.
- (55) Juppo, M.; Ritala, M.; Leskelä, M. Use of 1,1-Dimethylhydrazine in the Atomic Layer Deposition of Transition Metal Nitride Thin Films. *J. Electrochem. Soc.* **2000**, *147* (9), 3377–3381.
- (56) Lee, B. H.; Hwang, J. K.; Nam, J. W.; Lee, S. U.; Kim, J. T.; Koo, S.-M.; Baunemann, A.; Fischer, R. A.; Sung, M. M. Low-Temperature Atomic Layer Deposition of Copper Metal Thin Films: Self-Limiting Surface Reaction of Copper Dimethylamino-2-propoxide with Diethylzinc. *Angew. Chem. Int. Ed.* **2009**, *121* (25), 4606–4609.
- (57) Guziewicz, E.; Godlewski, M.; Krajewski, T.; Wachnicki, Ł.; Szczepanik, A.; Kopalko, K.; Wójcik-Głodowska, A.; Przeździecka, E.; Paszkowicz, W.; Łusakowska, E.; Kruszewski, P.; Huby, N.; Tallarida, G.; Ferrari, S. ZnO Grown by Atomic Layer Deposition: A Material for Transparent Electronics and Organic Heterojunctions. *J. Appl. Phys.* **2009**, *105* (12), 122413-1–5.
- (58) Na, J.-S.; Scarel, G.; Parsons, G. N. In Situ Analysis of Dopant Incorporation, Activation, and Film Growth during Thin Film ZnO and ZnO:Al Atomic Layer Deposition. *J. Phys. Chem. C* **2010**, *114* (1), 383–388.
- (59) Jensen, J. M.; Oelkers, A. B.; Toivola, R.; Johnson, D. C.; Elam, J. W.; George, S. M. X-Ray Reflectivity Characterization of ZnO/Al₂O₃ Multilayers Prepared by Atomic Layer Deposition. *Chem. Mater.* **2002**, *14* (5), 2276–2282.

- (60) Gu, D.; Baumgart, H.; Abdel-Fattah, T. M.; Namkoong, G. Synthesis of Nested Coaxial Multiple-Walled Nanotubes by Atomic Layer Deposition. *ACS Nano* **2010**, *4* (2), 753–758.
- (61) Kim, D. S.; Lee, S.-M.; Scholz, R.; Knez, M.; Gösele, U.; Fallert, J.; Kalt, H.; Zacharias, M. Synthesis and Optical Properties of ZnO and Carbon Nanotube Based Coaxial Heterostructures. *Appl. Phys. Lett.* **2008**, *93* (10), 103108-1–3.
- (62) Kopalko, K.; Wójcik, A.; Godlewski, M.; Łusakowska, E.; Paszkowicz, W.; Domagała, J. Z.; Godlewski, M. M.; Szczerbakow, A.; Świątek, K.; Dybko, K. Growth by Atomic Layer Epitaxy and Characterization of Thin Films of ZnO. *Phys. Stat. Sol. (c)* **2005**, *2* (3), 1125–1130.
- (63) King, D. M.; Johnson, S. I.; Li, J.; Du, X.; Liang, X.; Weimer, A. W. Atomic Layer Deposition of Quantum-Confined ZnO Nanostructures. *Nanotechnology* **2009**, *20* (19), 1–8.
- (64) Keun Kim, S.; Seong Hwang, C.; Ko Park, S.-H.; Jin Yun, S. Comparison between ZnO Films Grown by Atomic Layer Deposition Using H₂O or O₃ as Oxidant. *Thin Solid Films* **2005**, *478* (1), 103–108.
- (65) Lin, Y.-T.; Chung, P.-H.; Lai, H.-W.; Su, H.-L.; Lyu, D.-Y.; Yen, K.-Y.; Lin, T.-Y.; Kung, C.-Y.; Gong, J.-R. Self-Limiting Growth of ZnO Films on (0001) Sapphire Substrates by Atomic Layer Deposition at Low Temperatures Using Diethyl-Zinc and Nitrous Oxide. *Appl. Surf. Sci.* **2009**, *256* (3), 819–822.
- (66) Janocha, E.; Pettenkofer, C. ALD of ZnO Using Diethylzinc as Metal-Precursor and Oxygen as Oxidizing Agent. *Appl. Surf. Sci.* **2011**, *257* (23), 10031–10035.
- (67) Stuyven, G.; De Visschere, P.; Hikavy, A.; Neyts, K. Atomic Layer Deposition of ZnS Thin Films Based on Diethyl Zinc and Hydrogen Sulfide. *J. Cryst. Growth* **2002**, *234* (4), 690–698.
- (68) An, K.-S.; Cho, W.; Lee, B. K.; Lee, S. S.; Kim, C. G. Atomic Layer Deposition of Undoped and Al-Doped ZnO Thin Films Using the Zn Alkoxide Precursor Methylzinc Isopropoxide. *J. Nanosci. Nanotechnol.* **2008**, *8* (9), 4856–4859.
- (69) Auld, J.; Houlton, D. J.; Jones, A. C.; Rushworth, S. A.; Malik, M. A.; O'Brien, P.; Critchlow, G. W. Growth of ZnO by MOCVD Using Alkylzinc Alkoxides as Single-Source Precursors. *J. Mater. Chem.* **1994**, *4* (8), 1249–1253.
- (70) Mai, L.; Mitschker, F.; Bock, C.; Niesen, A.; Ciftiyurek, E.; Rogalla, D.; Mickler, J.; Erig, M.; Li, Z.; Awakowicz, P.; Schierbaum, K.; Devi, A. From Precursor Chemistry to Gas Sensors: Plasma-Enhanced Atomic Layer Deposition Process Engineering for Zinc Oxide Layers from a Nonpyrophoric Zinc Precursor for Gas Barrier and Sensor Applications. *Small* **2020**, *16* (22), 1–12.
- (71) Thiandoume, C.; Sallet, V.; Triboulet, R.; Gorochoy, O. Decomposition Kinetics of Tertiarybutanol and Diethylzinc Used as Precursor Sources for the Growth of ZnO. *J. Cryst. Growth* **2009**, *311*, 1411–1415.
- (72) Makino, H.; Miyake, A.; Yamada, T.; Yamamoto, N.; Yamamoto, T. Influence of Substrate Temperature and Zn-Precursors on Atomic Layer Deposition of Polycrystalline ZnO Films on Glass. *Thin Solid Films* **2009**, *517* (10), 3138–3142.
- (73) Hsu, C. T. Epitaxial Growth of II–VI Compound Semiconductors by Atomic Layer Epitaxy. *Thin Solid Films* **1998**, *335* (1), 284–291.

- (74) Kaiya, K.; Yoshii, N.; Takahashi, N.; Nakamura, T. Atmospheric Pressure Atomic Layer Epitaxy of ZnO on a Sapphire (0001) Substrate by Alternate Reaction of ZnCl₂ and O₂. *J. Mater. Sci. Lett.* **2000**, *19* (23), 2089–2090.
- (75) Kopalko, K.; Godlewski, M.; Domagala, J. Z.; Lusakowska, E.; Minikayev, R.; Paszkowicz, W.; Szczerbakow, A. Monocrystalline ZnO Films on GaN/Al₂O₃ by Atomic Layer Epitaxy in Gas Flow. *Chem. Mater.* **2004**, *16* (8), 1447–1450.
- (76) Ihanus, J.; Lankinen, M. P.; Kemell, M.; Ritala, M.; Leskelä, M. Aging of Electroluminescent ZnS:Mn Thin Films Deposited by Atomic Layer Deposition Processes. *J. of Appl. Phys.* **2005**, *98* (11), 1–8.
- (77) Arii, T.; Kishi, A. The Effect of Humidity on Thermal Process of Zinc Acetate. *Thermochim. Acta* **2003**, *400* (1), 175–185.
- (78) Wójcik, A.; Godlewski, M.; Guzewicz, E.; Minikayev, R.; Paszkowicz, W. Controlling of Preferential Growth Mode of ZnO Thin Films Grown by Atomic Layer Deposition. *J. Cryst. Growth* **2008**, *310* (2), 284–289.
- (79) Tammenmaa, M.; Koskinen, T.; Hiltunen, L.; Niinistö, L.; Leskelä, M. Zinc Chalcogenide Thin Films Grown by the Atomic Layer Epitaxy Technique Using Zinc Acetate as Source Material. *Thin Solid Films* **1985**, *124* (2), 125–128.
- (80) Ylilammi, M.; Ranta-aho, T. Metal Fluoride Thin Films Prepared by Atomic Layer Deposition. *J. Electrochem. Soc.* **1994**, *141* (5), 1278–1284.
- (81) Polarz, S.; Roy, A.; Merz, M.; Halm, S.; Schröder, D.; Schneider, L.; Bacher, G.; Kruis, F. E.; Driess, M. Chemical Vapor Synthesis of Size-Selected Zinc Oxide Nanoparticles. *Small* **2005**, *1* (5), 540–552.
- (82) Rees, W. S.; Green, D. M.; Anderson, T. J.; Bretschneider, E.; Pathangey, B.; Park, C.; Kim, J. Evaluation of Zn{N[Si(CH₃)₃]₂}₂ as Ap-Type Dopant in OMVPE Growth of ZnSe. *J. Electron. Mater.* **1992**, *21* (3), 361–366.
- (83) Rudolph, G.; Henry, M. C. The Thermal Decomposition of Zinc Acetylacetonate Hydrate. *Inorg. Chem.* **1964**, *3* (9), 1317–1318.
- (84) Hosono, E.; Fujihara, S.; Onuki, M.; Kimura, T. Low-Temperature Synthesis of Nanocrystalline Zinc Titanate Materials with High Specific Surface Area. *J. Am. Ceram. Soc.* **2004**, *87* (9), 1785–1788.
- (85) Minami, T.; Sato, H.; Sonohara, H.; Takata, S.; Miyata, T.; Fukuda, I. Preparation of Milky Transparent Conducting ZnO Films with Textured Surface by Atmospheric Chemical Vapour Deposition Using Zn (C₅H₇O₂)₂. *Thin Solid Films* **1994**, *253* (1–2), 14–19.
- (86) Suh, S.; Miinea, L.; Hoffman, D.; Zhang, Z.; Chu, W.-K. Atmospheric Pressure Chemical Vapor Deposition of Undoped Zinc Oxide Films from a Zinc Amide Precursor. *J. Mater. Sci. Lett.* **2001**, *20*, 115–118.
- (87) Rees, W. S.; Just, O.; Schumann, H.; Weimann, R. First Structural Characterization of a Zinc-Bis(Dialkylamide) Compound: *Polyhedron* **1998**, *17* (5–6), 1001–1004.
- (88) Bekermann, D.; Rogalla, D.; Becker, H.-W.; Winter, M.; Fischer, R. A.; Devi, A. Volatile, Monomeric, and Fluorine-Free Precursors for the Metal Organic Chemical Vapor Deposition of Zinc Oxide. *Eur. J. Inorg. Chem.* **2010**, *2010* (9), 1366–1372.
- (89) Du, L.; Wang, H.; Ding, Y. A Germanium(II) Aminopyridinato Compound and Its Potential as a CVD Precursor. *Polyhedron* **2017**, *134*, 282–286.

- (90) Ritala, M.; Pore, V.; Hatanpää, T.; Heikkilä, M.; Leskelä, M.; Mizohata, K.; Schrott, A.; Raoux, S.; Rossnagel, S. M. Atomic Layer Deposition of Ge₂Sb₂Te₅ Thin Films. *Microelectron. Eng.* **2009**, *86* (7–9), 1946–1949.
- (91) Leskelä, M.; Pore, V.; Hatanpää, T.; Heikkilä, M.; Ritala, M.; Schrott, A.; Raoux, S.; Rossnagel, S. Atomic Layer Deposition of Materials for Phase-Change Memories. *ECS Trans.* **2019**, *25* (4), 399–407.
- (92) Park, E.-S.; Yoo, C.; Kim, W.; Ha, M.; Jeon, J. W.; Lee, Y. K.; Hwang, C. S. Developing Precursor Chemistry for Atomic Layer Deposition of High-Density, Conformal GeTe Films for Phase-Change Memory. *Chem. Mater.* **2019**, *31* (21), 8663–8672.
- (93) Kim, S. B.; Sinsersuksakul, P.; Hock, A. S.; Pike, R. D.; Gordon, R. G. Synthesis of N-Heterocyclic Stannylene (Sn(II)) and Germylene (Ge(II)) and a Sn(II) Amidinate and Their Application as Precursors for Atomic Layer Deposition. *Chem. Mater.* **2014**, *26* (10), 3065–3073.
- (94) Kawamura, H.; Tachikawa, K. Preparation of the Superconducting Nb₃Ge Tape by a Continuous CVD Process. *Jpn. J. Appl. Phys.* **1977**, *16* (11), 2037–2041.
- (95) Gynane, M. J. S.; Harris, D. H.; Lappert, M. F.; Power, P. P.; Rividre, P.; Rividre-Baudet, M. Subvalent Group 4B Metal Alkyls and Amides. *J. Chem. Soc., Dalton Trans.* **1977**, No. 20, 2004–2009.
- (96) Baxter, D. V.; Chisholm, M. H.; Gama, G. J.; Hector, A. L.; Parkin, I. P. Low Pressure Chemical Vapor Deposition of Metallic Films of Iron, Manganese, Cobalt, Copper, Germanium and Tin Employing Bis(Trimethyl)silylamido Complexes, M(N(SiMe₃)₂)_n. *Chem. Vap. Deposition* **1995**, *1* (2), 49–51.
- (97) Chen, T.; Xu, C.; Hunks, W.; Stender, M.; Stauf, G. T.; Chen, P. S.; Roeder, J. F. Low Temperature Deposition of Ge Thin Films for Phase Change Memory. *ECS Trans.* **2019**, *11* (7), 269–278.
- (98) Roskamp, C. A.; Roskamp, E. J. Germanium Dichloride–Dioxane Complex. In *Encyclopedia of Reagents for Organic Synthesis*; John Wiley & Sons: New Jersey, 2001; pp 200–250.
- (99) Kang, S.-W.; Kim, J.-T.; Yun, J.-Y.; Seo, K.-C.; Shin, J.-S.; Yang, I.-D. Growth of Germanium Islands, Wires, or Films from CVD with a New Precursor. *Chem. Vap. Deposition* **2009**, *15* (7–9), 175–178.
- (100) Kim, R.-Y.; Kim, H.-G.; Yoon, S.-G. Ge Film Growth in the Presence of Sb by Metal Organic Chemical Vapor Deposition. *J. Appl. Phys.* **2007**, *102* (8), 1–5.
- (101) Bernal Ramos, K.; Saly, M. J.; Chabal, Y. J. Precursor Design and Reaction Mechanisms for the Atomic Layer Deposition of Metal Films. *Coord. Chem. Rev.* **2013**, *257* (23), 3271–3281.
- (102) Mårtensson, P.; Carlsson, J.-O. Atomic Layer Epitaxy of Copper on Tantalum. *Chem. Vap. Deposition* **1997**, *3* (1), 45–50.
- (103) Klaus, J. W.; Ferro, S. J.; George, S. M. Atomic Layer Deposition of Tungsten Using Sequential Surface Chemistry with a Sacrificial Stripping Reaction. *Thin Solid Films* **2000**, *360* (1), 145–153.

- (104) Hukka, I.; Rawles, E.; D'Evelyn, P. Novel Method for Chemical Vapor Deposition and Atomic Layer Epitaxy Using Radical Chemistry. *Thin Solid Films* **1993**, 225 (1–2), 212–218.
- (105) Komarov, S. F.; Lee, J.-J.; Hudson, J. B.; D'Evelyn, M. P. Self-Limiting Diamond Growth from Alternating CF_x and H Fluxes. *Diamond Relat. Mater.* **1998**, 7 (8), 1087–1094.
- (106) Yarmoff, J. A.; Shuh, D. K.; Durbin, T. D.; Lo, C. W.; Lapiano-Smith, D. A.; McFeely, F. R.; Himpsel, F. J. Atomic Layer Epitaxy of Silicon by Dichlorosilane Studied with Core Level Spectroscopy. *J. Vac. Sci. Technol., A* **1992**, 10 (4), 2303–2307.
- (107) Koleske, D. D.; Gates, S. M. Atomic Layer Epitaxy of Si on Ge(100): Direct Recoiling Studies of Film Morphology. *J. Appl. Phys.* **1994**, 76 (3), 1615–1621.
- (108) Koleske, D. D.; Gates, S. M. Atomic Layer Epitaxy of Si on Ge(100) Using Si_2Cl_6 and Atomic Hydrogen. *Appl. Phys. Lett.* **1994**, 64 (7), 884–886.
- (109) Yokoyama, S.; Ohba, K.; Nakajima, A. Self-Limiting Atomic-Layer Deposition of Si on SiO_2 by Alternate Supply of Si_2H_6 and $SiCl_4$. *Appl. Phys. Lett.* **2001**, 79 (5), 617–619.
- (110) Blakeney, K. J.; Winter, C. H. Atomic Layer Deposition of Aluminum Metal Films Using a Thermally Stable Aluminum Hydride Reducing Agent. *Chem. Mater.* **2018**, 30 (6), 1844–1848.
- (111) Cheon, J.; Dubois, L. H.; Girolami, G. S. Chemical Vapor Deposition of Zinc from Diallyl Zinc Precursors. *Chem. Mater.* **1994**, 6 (12), 2279–2287.
- (112) James, W. J.; Tseng, P. Synthesis and Characterization of Zinc Thin Films Formed in a Glow Discharge. *J. Vac. Sci. Technol., A* **1985**, 3 (6), 2634–2638.
- (113) Lindley, D. Landmarks: Birth of Modern Electronics. *Phys. Rev. Focus* **2009**, 23 (16).
- (114) Bosi, M.; Attolini, G. Germanium: Epitaxy and Its Applications. *Prog. Cryst. Growth Charact. Mater.* **2010**, 56 (3), 146–174.
- (115) Wu, H.; Ye, P. D. Fully Depleted Ge CMOS Devices and Logic Circuits on Si. *IEEE Trans. Electron Devices* **2016**, 63 (8), 3028–3035.
- (116) Hall, L. H. The Thermal Decomposition of Germane. *J. Electrochem. Soc.* **1972**, 119 (11), 1593–1596.
- (117) Ishii, H.; Takahashi, Y. Growth and Etching of Germanium Films by Chemical Vapor Deposition in a $GeCl_4$ - H_2 Gas System. *J. Electrochem. Soc.* **1988**, 135 (6), 1539–1543.
- (118) Woelk, E.; Shenai-Khatkhate, D. V.; DiCarlo, R. L.; Amamchyan, A.; Power, M. B.; Lamare, B.; Beaudoin, G.; Sagnes, I. Designing Novel Organogermanium OMVPE Precursors for High-Purity Germanium Films. *J. Cryst. Growth* **2006**, 287 (2), 684–687.
- (119) Sugahara, S.; Kitamura, T.; Imai, S.; Matsumura, M. Atomic Layer Epitaxy of Germanium. *Appl. Surf. Sci.* **1994**, 82–83, 380–386.
- (120) Greenwood, N. N.; Thomas, B. S. Investigation of the Properties and Thermochemistry of Some Complexes of Aluminium Hydride with Tertiary Amines and Diamines. *J. Chem. Soc., A* **1971**, 22 (17), 4844–4853.

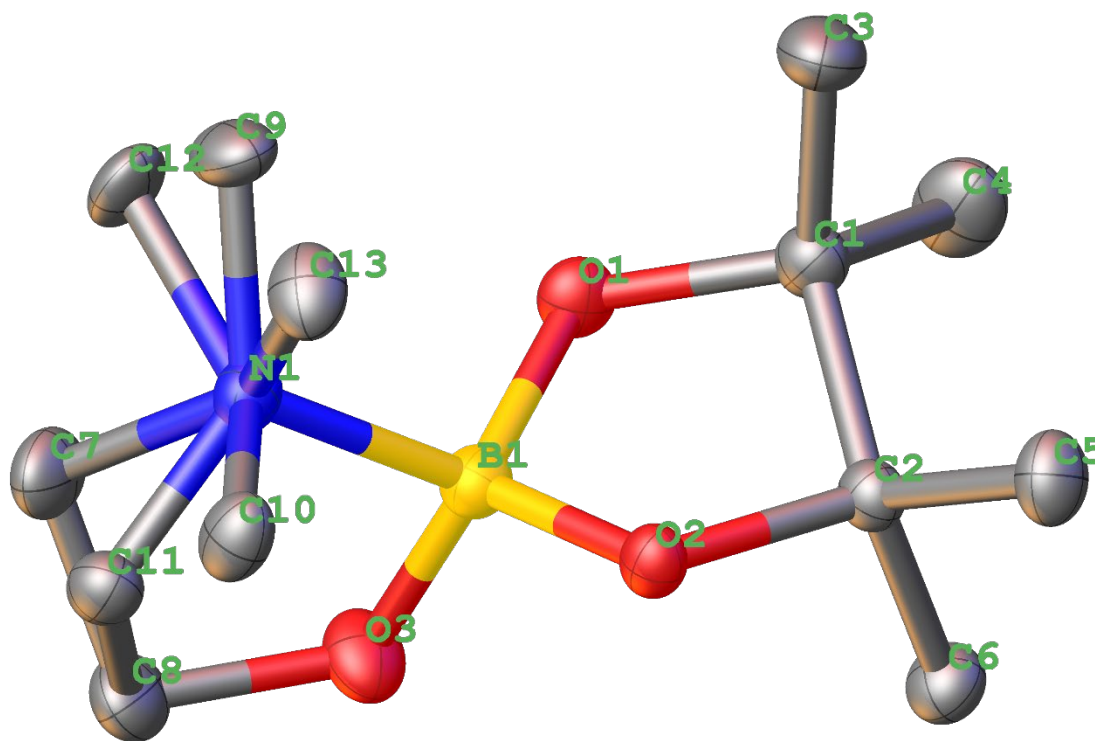
- (121) Vidjayacoumar, B.; Emslie, D. J. H.; Clendenning, S. B.; Blackwell, J. M.; Britten, J. F.; Rheingold, A. Investigation of AlMe_3 , BEt_3 , and ZnEt_2 as Co-Reagents for Low-Temperature Copper Metal ALD/Pulsed-CVD. *Chem. Mater.* **2010**, *22* (17), 4844–4853.
- (122) Mehrotra, R. C.; Aroda, M. Alkoxides and Double Alkoxides of Zinc. *Z. Anorg. Allg. Chem.* **1969**, *370* (5–6), 300–309.
- (123) Ashby, E. C.; Willard, G. F.; Goel, A. B. New, Convenient, and Stereospecific Method for the Dehydration of Alcohols. Thermal Decomposition of Magnesium, Zinc, and Aluminum Alkoxides. *J. Org. Chem.* **1979**, *44* (8), 1221–1232.
- (124) Włodarski, M.; Chodorow, U.; Jóźwiak, S.; Putkonen, M.; Durejko, T.; Sajavaara, T.; Norek, M. Structural and Optical Characterization of ZnS Ultrathin Films Prepared by Low-Temperature ALD from Diethylzinc and 1,5-Pentanedithiol after Various Annealing Treatments. *Materials* **2019**, *12* (19), 1–16.
- (125) Cai, J.; Ma, Z.; Wejinya, U.; Zou, M.; Liu, Y.; Zhou, H.; Meng, X. A Revisit to Atomic Layer Deposition of Zinc Oxide Using Diethylzinc and Water as Precursors. *J. Mater. Sci.* **2019**, *54* (7), 5236–5248.
- (126) Lancaster, D. K.; Sun, H.; George, S. M. Atomic Layer Deposition of Zn (O, S) Alloys Using Diethylzinc with H_2O and H_2S : Effect of Exchange Reactions. *J. Phys. Chem. C* **2017**, *121* (34), 18643–18652.
- (127) Coates, G. E.; Ridley, D. Alkoxy-, Thio-, and Amino-Derivatives of Methylzinc. *J. Chem. Soc.* **1965**, 1870–1877.
- (128) Hikov, T.; Rittermeier, A.; Luedemann, M.-B.; Herrmann, C.; Muhler, M.; Fischer, R. A. Preparation of ZnO Colloids by Pyrolysis of $[\text{MeZnO}^i\text{Pr}]_4$ in the Presence of Hexadecylamine and Probing the Surface Chemistry of the Nanoparticles by CO/ CO_2 Adsorption Studies Followed by FTIR. *J. Mater. Chem.* **2008**, *18* (28), 3325–3331.
- (129) Lummis, P. A.; Momeni, M. R.; Lui, M. W.; McDonald, R.; Ferguson, M. J.; Miskolzie, M.; Brown, A.; Rivard, E. Accessing Zinc Monohydride Cations through Coordinative Interactions. *Angew. Chem. Int. Ed.* **2014**, *126* (35), 9501–9505.
- (130) Bolton, P. D.; Clot, E.; Cowley, A. R.; Mountford, P. AlMe_3 and ZnMe_2 Adducts of a Titanium Imido Methyl Cation: A Combined Crystallographic, Spectroscopic, and DFT Study. *J. Am. Chem. Soc.* **2006**, *128* (46), 15005–15018.
- (131) Mizuhata, Y.; Sasamori, T.; Tokitoh, N. Stable Heavier Carbene Analogues. *Chem. Rev.* **2009**, *109* (8), 3479–3511.
- (132) Denk, M. K.; Khan, M.; Lough, A. J.; Shuchi, K. Redetermination of the Germanium Dichloride Complex with 1,4-Dioxane at 173K. *Acta Crystallogr., Sect. C: Cryst. Struct. Commun.* **1998**, *54* (12), 1830–1832.
- (133) Sutrisno, A.; A. Hanson, M.; A. Rupal, P.; V. Terskikh, V.; M. Baines, K.; Huang, Y. Exploring the Limits of ^{73}Ge Solid-State NMR Spectroscopy at Ultrahigh Magnetic Field. *Chem. Commun.* **2010**, *46* (16), 2817–2819.
- (134) Chorley, W.; Hitchcock, B.; Lappert, F.; Power, P.; Olmstead, M. Subvalent Group 14 Metal Compounds XIV*. The X-Ray Crystal Structures of Two Monomeric Group 14 Metal Bisamides, $\text{Ge}[\text{N}(\text{SiMe}_3)_2]_2$ and $\text{Sn}[\text{NC}(\text{Me})_2(\text{CH}_2)_3\text{CMe}_2]_2$. *Inorg. Chim. Acta* **1992**, *198–200*, 203–209.

- (135) Zemlyansky, N. N.; Borisova, I. V.; Kuznetsova, M. G.; Khrustalev, V. N.; Ustynyuk, Y. A.; Nechaev, M. S.; Lunin, V. V.; Barrau, J.; Rima, G. New Stable Germylenes, Stannylenes, and Related Compounds. 1. Stable Germanium(II) and Tin(II) Compounds $M(OCH_2CH_2NMe_2)_2$ ($M = Ge, Sn$) with Intramolecular Coordination Metal–Nitrogen Bonds. Synthesis and Structure. *Organometallics* **2003**, 22 (8), 1675–1681.
- (136) Dennis, L. M.; Skow, N. A. GERMANIUM. XXIX. GERMANIUM MONOHYDRIDE1. *J. Am. Chem. Soc.* **1930**, 52, 2369–2372.
- (137) Kraus, C. A.; Carney, E. S. Compounds of Germanium and Hydrogen: Some of Their Reactions and Derivatives. I. Preparation of Monogermane. II. Sodium Trihydrogermanides. *J. Am. Chem. Soc.* **1934**, 56 (4), 765–768.
- (138) Zwettler, N.; Dupé, A.; Klokić, S.; Milinković, A.; Rodić, D.; Walg, S.; Neshchadin, D.; Belaj, F.; Mösch-Zanetti, N. C. Hydroalkylation of Aryl Alkenes with Organohalides Catalyzed by Molybdenum Oxido Based Lewis Pairs. *Adv. Synth. Catal.* **2020**, 362 (15), 3170–3182.
- (139) Jolly, W. L.; Drake, J. E.; Rudolph, R.; Wartik, T. Hydrides of Germanium, Tin, Arsenic, and Antimony. In *Inorganic Syntheses*; Kleinberg, J., Ed.; John Wiley & Sons, Inc.: Hoboken, NJ, USA, 2007; pp 34–44.
- (140) Hom, T.; Kiszénick, W.; Post, B. Accurate lattice constants from multiple reflection measurements II. lattice constants of germanium, silicon, and diamond Locality: synthetic Sample: at $T = 25\text{ }^\circ\text{C}$. *J. Appl. Crystallogr.* **1975**, 8, 457-458.

APPENDIX

Molecular Structure and Crystallographic Data for (Me₂NCH₂CH₂O)Bpin.

C(7), C(9), and C(10) 68.3(2)% / C(11), C(12), and C(13) 31.7(2)%



Crystal data and structure refinement for Me₂NCH₂CH₂OBpin.

| | | |
|----------------------|--|-----------------|
| Empirical formula | C ₁₀ H ₂₂ BNO ₃ | |
| Formula weight | 215.09 | |
| Temperature/K | 100.00(10) | |
| Crystal system | monoclinic | |
| Space group | P2 ₁ /c | |
| Unit cell dimensions | a = 12.095(2) Å | α = 90° |
| | b = 8.8825(15) Å | β = 103.654(3)° |
| | c = 11.5421(19) Å | γ = 90° |

| | |
|---|---|
| Volume/Å ³ | 1205.0(3) |
| Z | 4 |
| Density (calculated)/cm ³ | 1.186 |
| Absorption coefficient/mm ⁻¹ | 0.084 |
| F(000) | 472.0 |
| Crystal size/mm ³ | 0.2 × 0.2 × 0.2 |
| Radiation | Mo Kα (λ = 0.71073) |
| 2θ range for data collection/° | 3.46 to 61.01 |
| Index ranges | -17 ≤ h ≤ 17, -12 ≤ k ≤ 12, -16 ≤ l ≤ 16 |
| Reflections collected | 30551 |
| Independent reflections | 3689 [R _{int} = 0.0615, R _{sigma} = 0.0462] |
| Data/restraints/parameters | 3689/0/172 |
| Goodness-of-fit on F ² | 1.011 |
| Final R indexes [I ≥ 2σ (I)] | R ₁ = 0.0487, wR ₂ = 0.1094 |
| Final R indexes [all data] | R ₁ = 0.0770, wR ₂ = 0.1229 |
| Largest diff. peak/hole / e Å ⁻³ | 0.41/-0.16 |

Bond lengths (Å) and bond angles (°) for Me₂NCH₂CH₂OBpin.

| | | | |
|------------|------------|------------|------------|
| O(2)–C(2) | 1.4385(13) | N(1)–C(11) | 1.394(4) |
| O(2)–B(1) | 1.4517(16) | N(1)–C(12) | 1.579(4) |
| O(1)–C(1) | 1.4414(15) | N(1)–C(13) | 1.523(4) |
| O(1)–B(1) | 1.4482(15) | C(2)–C(6) | 1.5350(16) |
| O(3)–C(8) | 1.4147(16) | C(2)–C(1) | 1.5678(17) |
| O(3)–B(1) | 1.4619(16) | C(2)–C(5) | 1.5273(17) |
| N(1)–B(1) | 1.6925(16) | C(1)–C(3) | 1.5329(18) |
| N(1)–C(9) | 1.437(2) | C(1)–C(4) | 1.5299(17) |
| N(1)–C(10) | 1.531(2) | C(8)–C(7) | 1.498(2) |
| N(1)–C(7) | 1.512(2) | C(8)–C(11) | 1.639(4) |

| | | | |
|------------------|-------------|-----------------|-------------|
| C(2)–O(2)–B(1) | 106.75 (9) | C(5)–C(2)–C(6) | 109.17 (10) |
| C(1)–O(1)–B(1) | 109.20 (9) | C(5)–C(2)–C(1) | 114.94 (10) |
| C(8)–O(3)–B(1) | 114.28 (10) | O(1)–C(1)–C(2) | 102.41 (9) |
| C(9)–N(1)–B(1) | 117.29 (11) | O(1)–C(1)–C(3) | 109.51 (10) |
| C(9)–N(1)–C(10) | 109.32 (13) | O(1)–C(1)–C(4) | 108.77 (10) |
| C(9)–N(1)–C(7) | 112.14 (13) | C(3)–C(1)–C(2) | 112.92 (10) |
| C(10)–N(1)–B(1) | 109.55 (10) | C(4)–C(1)–C(2) | 114.23 (10) |
| C(7)–N(1)–B(1) | 101.27 (10) | C(4)–C(1)–C(3) | 108.73 (11) |
| C(7)–N(1)–C(10) | 106.60 (12) | O(3)–C(8)–C(7) | 104.20 (12) |
| C(11)–N(1)–B(1) | 104.40 (17) | O(3)–C(8)–C(11) | 103.22 (16) |
| C(11)–N(1)–C(12) | 112.0 (2) | O(2)–B(1)–O(3) | 117.22 (10) |
| C(11)–N(1)–C(13) | 114.1 (2) | O(2)–B(1)–N(1) | 107.53 (9) |
| C(12)–N(1)–B(1) | 108.78 (17) | O(1)–B(1)–O(2) | 106.81 (10) |
| C(13)–N(1)–B(1) | 115.32 (17) | O(1)–B(1)–O(3) | 112.20 (10) |
| C(13)–N(1)–C(12) | 102.4 (2) | O(1)–B(1)–N(1) | 113.12 (9) |
| O(2)–C(2)–C(6) | 108.41 (9) | O(3)–B(1)–N(1) | 99.95 (9) |
| O(2)–C(2)–C(1) | 102.26 (9) | C(8)–C(7)–N(1) | 103.85 (13) |
| O(2)–C(2)–C(5) | 109.01 (9) | N(1)–C(11)–C(8) | 102.5 (2) |
| C(6)–C(2)–C(1) | 112.64 (10) | | |